First Principles Modelling of Thermoelectric Materials

Genadi Antonov Naydenov

Doctor of Philosophy

University of York
Physics

May 2019

Abstract

Thermoelectric semiconductor materials possess the unique ability to convert temperature differential into electricity or *vice versa*. This presents excellent opportunities for harvesting waste heat or cooling. Thermoelectric applications are found in many different areas ranging from medicine to space programs. The quality of the materials is determined by their thermoelectric properties like the Seebeck coefficient, electrical and thermal conductivity.

In this thesis we model the thermoelectric properties from first principles. The materials of interest include Fe_2VAl, NbFeSb, TaFeSb and Bi_2Te_3. The thermoelectric properties are analysed by considering the effects of doping, point defects, grain boundaries and size reduction.

A number of key results are found. We show that the experimentally observed behaviour of the Seebeck coefficient in Fe_2VAl can be theoretically modelled by enhancing the localisation of V electrons with the Hubbard model.

We establish TaFeSb as a new thermoelectric material which exhibits 50% better *p*-type thermoelectric properties than NbFeSb due to an increased scattering strength between Ta and potential dopants. We also note that mixing NbFeSb and TaFeSb does not have a negative impact on the electronic properties and could potentially lead to further improvements in the thermoelectric performance.

We investigate the electronic thermoelectric properties of Bi_2Te_3 thin films. We find that the Seebeck coefficient increases dramatically when the film thickness is reduced to 1–2 nm. This leads to an overall increase in the power factor of the material and enhanced *p*-type thermoelectric performance.

The successful calculation of the properties for a wide range of materials also shows that the developed in this project computational framework can be reliably used for further research on thermoelectrics.

Contents

List of Figures

List of Tables

List of Listings

Acknowledgements

First of all, I would like to thank my supervisors Phil Hasnip, Vlado Lazarov and Matt Probert. I am extremely grateful to them for making this project possible and for giving me the opportunity to spend a lot of time with them. Believe me, they are not only fantastic academics, but also amazing people! Many thanks to all of them for being so responsive, supportive and friendly. I will never forget what you have done for me!

I would like to thank the guys with whom I shared an office in the Nanocentre: Barat Kurbanjan, Arsham Ghasemi, Zlatko Nedelkoski, David Lloyd and Adam Kerrigan. I learnt so much from them about different places, customs and people. It was also a pleasure to chat with them about science, physics and... football. Discussing the latest football news was a crucial activity which helped us bond as a group and lift our spirits. Too bad we were not supporting the same teams. It was a joy to work in one room with you and that is something which I will really miss!

I wish to thank Jacob Wilkins, Ed Higgins and Peter Byrne for giving me useful advice and asking great questions during the group meeting talks. I often went over the allocated time but did not hear a single complaint by them. The level of endurance of these guys is incredible, true heroes! I am also very happy and thankful for having Alban D'Harcourt in the group. During our conversations on thermoelectrics his level of enthusiasm felt inspiring and reassuring. Neville Yee is another person I am thankful for knowing. It is always possible to learn something new while you are around him. You guys are all great!

I would like to thank Luke Abraham for making the LaTeX thesis template and Paul Sharp for filling it with content and showing what the final product would look like. Special thanks to the Physics staff who were always ready to help, assist with and resolve any issues that might occur!

Thousands of thanks to the Vanbrugh College staff members. They are absolutely fantastic! Making you feel at home in a foreign place sounds like an impossible task but Georgina Heath and Lenore Klassen truly did it. There are no words to express how grateful I am for their help during my undergraduate and postgraduate studies. You made Vanbrugh feel like family!

Finally, and most importantly, I wish to express my gratitude to my beloved parents Mariana and Anton. I feel truly blessed for having you! I would like to thank you for believing in me and supporting me throughout the years. I would not have been able to follow this path and be where I am today without your help and dedication. Thank you!

Declarations

I declare that the work presented in this thesis, except where otherwise stated, is based on my own research and has not been submitted previously for a degree in this or any other university. I declare that I fully participated in the formulation of the research, to the associated calculations and the final interpretation of the results presented in Chapter 4, 5 and 6 and Appendix A. Parts of the work reported in this thesis have been published in Journal of Physics: Materials and APL Materials.

Chapter 4 describes collaborative work which is in preparation for submission. Manuscript: www-users.york.ac.uk/~gan503/FVA-manuscript.pdf;

Chapter 5 describes collaborative work that has been published:
G. A. Naydenov, P. J. Hasnip, V. K. Lazarov, and M. I. J. Probert, "Huge power factor in p-type half-Heusler alloys NbFeSb and TaFeSb," *J. Phys. Mater.* **2**, 035002, (2019), DOI: 10.1088/2515-7639/ab16fb;

Appendix A describes collaborative work that has been published:
A. Ghasemi, D. Kepaptsoglou, A. I. Figueroa, G. A. Naydenov, P. J. Hasnip, M. I. J. Probert, Q. Ramasse, G. van der Laan, T. Hesjedal and V. K. Lazarov, "Experimental and density functional study of Mn doped Bi_2Te_3 topological insulator," *APL Materials* **4**, 126103, (2016), DOI: 10.1063/1.4971354.

I declare that the software in the form of interfaces and loaders needed to enable the thermoelectric calculations, except where otherwise stated, has been developed as part of the research. I participated fully in the development of the code and an explicit list of the developed programs by me is given in Section 3.5, whereas code examples are shown in Appendix B.

Prologue

We can start by talking about the world energy crisis, how important it is to have renewable energy sources and how thermoelectric devices can solve this problem. Yes, it is all true but not the main reason why people are investigating thermoelectric properties. Thermoelectricity is an interesting phenomenon. That is the main reason, plain and simple.

I doubt anyone has ever done a research on thermoelectricity and has not had the chance to hold a thermoelectric plate in their hands. Imagine we are in that position and holding the thermoelectric is just not enough. We would like to see what it can do. A few moments later we have an electric circuit which is ready for testing, with a 3 V DC motor or a small bulb wired to the plate. Then we attach an ice cube to one side of the thermoelectric plate. The other side we touch with our fingers, and almost instantaneously, the motor starts spinning, the bulb is shining.

The whole process feels surreal and counter-intuitive. We have managed to run a motor with the help of an ice cube and a small plate made of semiconductors. We have converted a temperature difference into electricity. Suddenly, we realise how much more we can do with the thermoelectric plate. What if it is possible to make the device bigger, or smaller, or more efficient? The possibilities are countless but for that purpose we need to investigate the thermoelectric effect into more details. Remember when I told you that the main motivation behind thermoelectric investigations is not the energy crisis. I hope I have managed to convince you by now.

Chapter 1

Introduction

1.1 What is a thermoelectric?

A thermoelectric module is a device which is made of series of p- and n-type semiconductors. They work together to generate electricity due to a temperature gradient or transport heat due to an electric current. Thermoelectric modules are referred to as TEG or TEC depending on whether they are used as generators or coolers. The most important properties of a thermoelectric semiconductor are its electrical conductivity σ, thermal conductivity κ and Seebeck coefficient S. The quality of the thermoelectric material is determined by the relation between the above quantities ($ZT = S^2\sigma T/\kappa$), where ZT is the thermoelectric figure of merit and T denotes temperature. Our goal is to maximise ZT by achieving low thermal conductivity and high power factor $S^2\sigma$. Larger ZT means that our thermoelectric is more efficient, and larger power factor means that it is capable of doing more work. That is a very concise summary of the thermoelectric effect but if you are interested in understanding more details about the phenomenon, different devices, their applications, how to model the thermoelectric properties on a computer or how to optimise the thermoelectric efficiency I hope you will find this and the next few chapters very interesting.

1.2 Design of thermoelectric devices

The choice of a clever architecture is mandatory when designing a thermoelectric device. A compromise between thermoelectric conversion direction, geometric shape, size and flexibility is essential for the longevity, efficiency and applicability of the TEG (TEC) module.

1.2.1 Flat bulk thermoelectric devices

The flat bulk TEG (TEC) module, as shown in Fig. 1.1 [1], is the most common architecture in which the electrical current and thermal current are parallel to each other. The module has a cuboid shape and is made of multiple altering legs of *p*- and *n*-type thermoelectric semiconductors. The tops and the bottoms of the legs are connected via several metallic layers. The shape of a single *pn*-pair looks like a gate. All gates are wired in series and enclosed between two ceramic plates, which form the cold and hot side of the TEG. On a macro scale it looks like the electricity runs within a plane parallel to the plates, while the heat is transferred in a perpendicular direction. To harvest the energy, a heat source and a heat sink need to be brought into contact with the two sides of the module.

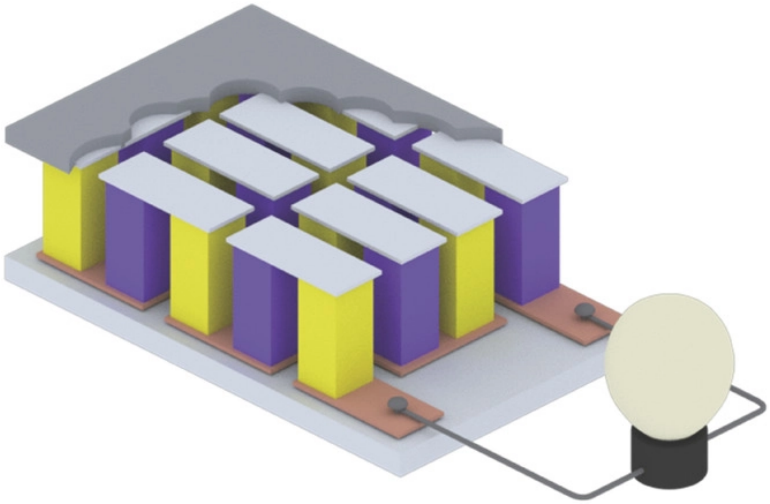

Figure 1.1: Flat bulk architecture of a TEG in which *p*-type and *n*-type semiconductor legs (coloured in yellow and purple) are wired in series using metallic layers. The hot and cold side plates are typically made of ceramics. All other architectures are derived from this design. [Image taken from He *et al*. [1]]

It becomes apparent that the arrangement and the shape of the legs have an impact upon the performance of the device. Studies try to find a relation between the number and height of thermoelectric legs [2]. Different shapes such as cuboid, pyramid [3, 4], exponential [5, 6], and quadratic [7] are also being tested and compared. Pyramidal legs are suggested to exhibit higher power density than the rest. A recent TEG prototype based on pyramidal legs shows they make it easier to maintain the temperature gradient across the module by decreasing the thermal conductance of the legs [8]. The measured output in the pyramid structure shows an incredible improvement of approximately 70% when compared to the cuboid counterpart. Thus, illustrating how important the geometrical configuration of the thermoelectric legs is for the device

performance.

1.2.2 Thin-film thermoelectric devices

The cooling of power electronics is a very delicate task due to the dimensions of the system. Thermoelectric devices with a microscopic size are excellent candidates for both cooling and harvesting the wasted heat in an electronic device. In this case, the thickness of the thermoelectric materials need to be in the micrometer to sub-millimeter range. Due to the small thickness, thin films allow for low thermal resistances and very high heat fluxes which yield much higher power densities compared with conventional modules [9].

The problem associated with the thin film architecture lies in the control of the growth process. The most preferable fabrication technique is electrochemical deposition in which the micrometer or sub-millimeter thick legs are deposited into cavities [1]. For example, in a template-assisted local electrochemical deposition the *p*- and *n*-type material is deposited on a silicon wafer in a sequence. The fabrication process includes patterning and depositing the bottom contact layer, then constructing the cavities for the legs and then subsequent deposition of the first thermoelectric material. The second material need to be deposited in the same way while protecting the first deposit. A top contact is deposited at the end of the process [10].

Aside from electrochemical deposition methods, physical deposition methods and lithographical structuring were also successfully applied. For instance, a thin-film TEG was realised by molecular beam epitaxy [11]. Employing sputtering methods, *n*- and *p*-type legs were formed on two separate substrates and then mechanically joined by soldering [12]. In all cases, the manufacturing process requires several deposition or lithography steps. In addition, any further mechanical polishing and handling needs to be conducted in a clean laboratory environment in order to avoid ruining the thermoelectric properties by sample contamination [10]. Despite the benefits of the micro thermoelectric devices, their manufacturing process presents multiple challenges which limit their applicability.

1.2.3 Flexible thermoelectric devices

Flexible electronic devices such as rollable TV panels and foldable phones are a very trendy topic. While the advantages of such technology are not always immediately obvious, the interest in flexible thermoelectric devices is not surprising. Innovative manufacturing techniques aim to mitigate the typical in-

flexible design. The fabrication process can include techniques such as printing, additive manufacturing, thermal spraying, melt-mixing of composites and laser-aided restructuring [1].

The flexible effect is achieved with the help of organic components. Unlike traditional thermoelectric materials polymers are widely available as they are made of more abundant elements. Polymers have intrinsically low thermal conductivity and can be easily processed in different shapes. There are several intrinsically conductive polymers, like poly(3,4-ethylenedioxythiophene), poly(styrenesulfonate) and polyaniline, which are regarded as suitable for thermoelectric applications. The good thermoelectric properties believed to be due to the semimetal nature of the compounds [13, 14].

1.2.4 Wearable thermoelectric devices

Another interesting device is the wearable TEG. It utilises the heat from the human body and faces some additional challenges [15]. Wearable TEG devices need to be aesthetically appealing, lightweight and comfortable. In terms of operation, they rely only on the temperature difference between the body and the environment, with the cold side being cooled down by air convection.

Due to the large thermal resistance between the skin and the device, the hot and cold side need to be designed carefully in order to increase the harvested power density [16]. Implementations in wrist bands or designs with head spreaders made of Y-shaped copper fins show promise in that direction [15]. Nevertheless the power density of a wearable TEG remains around 3 times less than that of a piezoelectric based generator when a person is running at a speed of 10 km/h [17]. The benefit of thermoelectric devices, however, is that they are not affected by the state of the activity and that they generate more energy over long period of time.

1.2.5 Notable mentions

There are a few other architectures which are worth mentioning. Among them is the cylindrical bulk thermoelectric architecture [18]. The module looks like a cylinder with a very thick wall which hosts the thermoelectric legs. This design works similarly to the flat architecture but the module shape is beneficial for applications where the heat flows in radical direction.

The last design considers the case in which the heat and electrical currents in the thermoelectric compound are orthogonal to each other, which is use-

ful for materials which exhibit anisotropic transport properties. In this architecture the *p*-type and *n*-type materials are stacked with an isolating layer in between [19]. In such a configuration, the electrical and thermal currents are disentangled because the isolating layers guide the electrical current towards transversely arranged contact points.

1.3 Applications of thermoelectrics

In the previous section we talked about the different architectures and how different design solutions try to maximise efficiency. Now we proceed by discussing the applications of TEG (TEC) modules. The ability to operate for long periods of time with almost no maintenance makes thermoelectric generators and coolers technically attractive. Thermoelectric devices have been utilised or attempted to be used in a lot of different areas like medicine, the car industry, aerospace programs, electronics, industrial factories and households [9].

1.3.1 Medical applications

The most common and accessible thermoelectric application is the portable thermoelectric cooler. It is basically a solid-state fridge, which runs silently and does not have any moving parts or fluids which can leak away. If carefully designed and constructed, the devices can be very reliable with a long lifetime. The most important feature of thermoelectric coolers is their ability to control the temperature proportionally rather than with an on-off cycle. This is useful for food transportation and storage, but more importantly it is crucial for medical services.

It is very important to keep biological products like a vaccine or blood serum within a certain temperature range under transportation. An example for such application is a portable thermoelectric medical cooling kit controlled by a microprocessor. It was developed for preserving human blood during transportation and operates at 12 V [20]. In remote areas or places with hot weather portable coolers make it possible for doctors to transport products and treat urgent health issues on-site.

Another extremely important medical application of TEG modules involves harvesting energy from the temperature difference in the human body and powering a heart pacemaker [21]. Pacemakers require a power source to operate, which is usually a battery which needs to be replaced every 10 years. However, every surgery poses a further risk to the patient. A TEG power

source would eliminate that problem since it does not require maintenance or replacement. A recent report from 2018, shows a clever TEG design which allows the circuit to start up from very low input voltages of 40 mV. Then the harvested energy is passed to a low-voltage oscillator and then to a low-voltage charge pump. A voltage of 1.2 V is produced by the pump. The final output voltage is increased to 2.4 V with the help of boost converters [22]. It cannot be highlighted enough how remarkable the realisation of this concept is.

1.3.2 Vehicle applications

From a commercial point of view the most attractive application of thermoelectric devices is decreasing the fuel consumption in vehicles. At first glance, the idea seems straightforward. A generator mounted in the exhaust system can harvest the waste heat from the exhaust gases while the cold side being cooled by ambient air or the engine coolant. The design of the module can be flat or cylindrical depending on how the exhaust gases are guided through the module.

On second thought, however, the working temperature in the vehicle is not constant. Under normal conditions, the vehicle goes through many cycles of acceleration and braking, which causes temperature fluctuations in the engine and exhaust system. Thus, different driving conditions, which lead to a broad exhaust gases temperature range, require either a thermoelectric material which can operate at a wide temperature range, or different types of TEG modules which need to be spread throughout the exhaust system. In addition, temperature fluctuations can also lead to mechanical stress and malfunctioning.

Despite the aforementioned hurdles, the constant race for reduced greenhouse gas emissions and improved fuel saving led to many studies on the effect of thermoelectric applications in trucks [23] and cars [24, 25]. An example of TEG module in a BMW car is given in Fig. 1.2. A joint effort of BMW, BSST and Visteon [26] focused on recovering waste heat from the exhaust gas system and engine radiator. The reported reduction in the fuel consumption was between 8–12.5%. This implementation uses a closed liquid loop as a primary heat exchanger to transfer the heat from the exhaust gas to the TEG module. This design aims to deliver higher efficiency compared to a direct attachment. It allows for further control which can minimise problematic thermal fluctuations.

In another application by Hi-Z technologies, Bismuth Telluride was used to

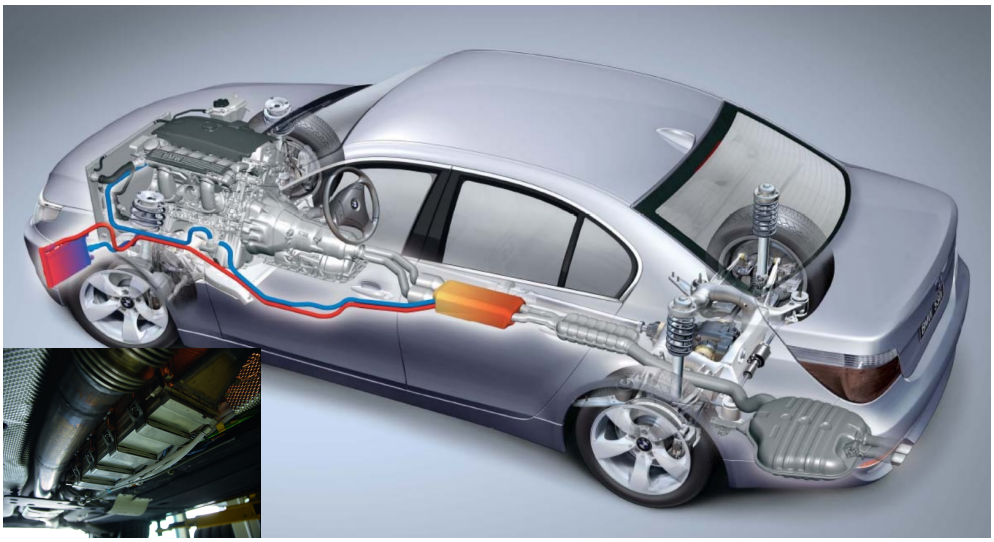

Figure 1.2: Thermoelectric generator module (yellow-orange and inset) in a BMW 530i concept car. [Image taken from [27]]

harvest around 1 kW of power in diesel trucks. The module was placed in the vehicle muffler as it is the component with the lowest temperature, around 250°C. The cooling water from the radiator was used for the cold side of the module [9].

Despite the successful applications, the problem of not having the capability to operate efficiently at a wide temperature range is still present. In a multi-stage heat recovery system different sections are optimised for different working conditions. In such a case, the conversion efficiency would be significantly higher. For example, another material which can be used in cars is Lead Telluride. It is reported to be more suitable for higher temperatures [28]. An automobile exhaust system by Bell utilises that and uses three TEG sections instead of one [29]. The reported performance improvement is more than 90% at low flow rates and over 25% at high flow rates. However, the improved efficiency comes with a cost. The presence of multiple segments which need to work in unison and under different conditions increases the complexity of the system, thus making it less reliable.

1.3.3 Aerospace applications

Our review of thermoelectric applications would not be full if we do not discuss how NASA managed to utilise thermoelectrics. The fact that TEG devices have no no moving parts, no position dependence, more than 100,000 h steady-state operation and precise temperature control makes them an excellent candidate for power supply in space missions [9].

The Voyager 1 space probe was launched by NASA in 1977. It uses a radioisotope thermoelectric generator (RTG), which utilise an array of TEGs to harvest energy from the heat released by the decay of a suitable radioactive material, usually Plutonium 238. Similar implementations have been used in many other space missions like Voyager 3, Cassini, New Horizons, Pioneer 10 and 11, Viking 1 and 2 [30, 31]. The vast range of missions shows that TEG modules can operate under very hostile conditions. In addition, the longevity of the Voyager 1 mission with a lifespan of more than 40 years highlights how incredible reliable thermoelectric devices can be.

On a slightly different note to space programs, commercial and military aeroplanes can utilise thermoelectric devices to capture waste heat from the aircraft engine. Such implementations need to be done with care since they should not compromise the structural stability of the aircraft. The advantage when considering an aeroplane is that the heat from the engine and the relatively low ambient temperature at high altitudes can be used to maintain a constant temperature gradient across the TEG device, thus maximising its performance. The net result could be improved fuel consumption and reduced costs for passenger and cargo airlines.

1.3.4 Thin-film applications

In Section 1.2.2 we discussed thin-film devices and some of the difficulties related to manufacturing them. In this section we will have a look at a very interesting thin-film TEG implementation. It is found in a communication platform at high altitude. This device uses the long wave infrared radiation leaving the Earth's surface as a heat source. The heat sink uses a simple mechanism, which dissipates the heat by radiating it to the space. The temperature difference between the cold and hot side in this case is around 58 K [32]. Another variation utilises heat flow parallel to the film surface and achieves a temperature difference of 85 K [33]. In terms of circuitry, a temperature difference of 80 K can produce a steady current of 0.5 A and a voltage of 3.6 V, which is a considerable amount for an electronic device.

1.3.5 Electronics applications

Voltage regulators and microprocessors are essential part of modern electronics. In some cases, they operate at temperatures which are close to their breaking point. This affects both the performance and the lifetime of the electronic device. The conventional cooling mechanism involves a heat sink which dissi-

pates the heat to the surroundings. Under extreme conditions, when the heat flux is large, liquid and nitrogen cooling solutions are also a viable option. In all cases, the main task is to extract the heat out of the system as efficiently as possible.

Thermoelectric devices are extremely good at transferring heat from one side of the module to the other and can be implemented into electronic devices to help with the cooling. They do not have any moving parts and can operate silently. The advantage of a TEC module is that it can offer a very localised cooling solution. In such application the electronic component is mounted directly onto the cold side of the TEC. Thus, the hot side of the thermoelectric becomes the devices which needs to cooled by convection, a fan or a liquid solution. The benefit of a TEC is that it can reach and maintain a desired temperature by adjusting the input current and voltage.

For example, this concept was successfully applied to an X-ray detector [34, 35]. Only 3 W of electrical power were necessary to bring the temperature of the detector and TEC cold side to -40°C while the hot TEC side was kept constant at around 10°C by a cold water supply. Dramatic improvements were reported for both the energy resolution and the sensitivity of the equipment.

In related areas, thermoelectric heat pumps were used in solar photovoltaic panels and climate control systems. It was reported that better performance and cheaper cost were obtained when the TEC module was used for cooling the solar panel rather than harvesting the waste heat from it [9]. In terms of climate control, TEC modules can work in a similar way to dehumidifiers but with heat. They extract it from the surroundings and pump it into a place, where the heat can be utilised. For example, car manufacturers like Ford, Hyundai and Toyota have been using this approach to cool or heat car seats [36].

1.3.6 Industrial applications

Factories are some of the biggest energy consumers. The manufacturing processes involve multiple chemical or mechanical steps, which all require power. Due to the large scale of the production lines, significant amounts of the energy are lost to the surroundings in the form of exhaust gases, radiation or cooling.

We know that thermoelectrics are very reliable, require low maintenance, have long lifespan and can operate in harsh environment. For all that they look ideal for industrial applications. The type of the thermoelectric materials needs to be selected based on the operation temperature of the facility. For example, in

a combustible solid waste processing plant temperatures can be between 325 K and 1100 K, depending on the operation regime [37]. In terms of energy harvesting, a 60 W thermoelectric module with 4.4% conversion efficiency was installed near the boiler section of an incinerator plant [38]. The expectation was that burning 100 tonnes of waste during a 16 hours working day can generate 426 kW of power [9].

In a steel plant, the furnace can provide a steady source of convenient piped water. This can be utilised and converted by TEG devices into electricity when large amounts of cooling water are discharged at around 90°C. For example, implementation based on the thermoelectric material Bismuth Telluride was employed to produce a total electrical power of 8 MW in major components of a modern steel plant [9, 39]. For comparison, a small coal power plant of 100 MW consumes up to 3 carriages with coals per hour. While the output of the TEG application is only 8% when compared to the power plant, its running costs are essentially close to zero.

1.3.7 Domestic applications

Harvesting the waste heat in the domestic sector is another option which needs to be considered. Thermoelectrics offer an opportunity to increase the power efficiency of households which use burning stoves or other heat sources.

Such application was developed in Sweden in the middle of 1990s [40]. A stove-top thermoelectric module was integrated with a wood burning stove in a remote farm house in the mountains. Being too far away from the electricity grid, farm houses in remote and difficult terrains rely on a gasoline powered electricity generator to provide power supply for basic needs like lighting and small appliances. The downsides of the gasoline motor are that it requires maintenance, make a lot of noise and is expensive to run. A thermoelectric generator offered an attractive alternative. The module was installed in the rear of the stove, where it would not prevent the family from using the appliance and where the temperature was the highest. The cold side was connected to a heat sink and a 12 V (2.2 W) fan which was used to maintain the temperature gradient. The power output of the device varied between 4 W and 10 W depending on the day time, ambient temperature and how often the stove was filled with fuel.

In another application, a system of thermoelectric modules was located between the heat source and the water jacked in a domestic central heating system [9]. The efficiency of the installation was only about 5%, where the remaining 95% of the heat output were used for space heating in the house. Re-

ports suggest that hypothetically the energy efficiency of the household can be increased up to 80% by harvesting the waste heat for space heating and hot water with another thermoelectric system [41, 42].

Other applications include a TEG system which generates electricity and hot water by burning natural gas in a furnace [43], and a cogeneration system which uses solar power and heat from boiler exhaust in residential houses [42, 44]. In all examples, the conversion efficiency is low, however, this does not change the fact that households can benefit from thermoelectric devices and harvest useful electric energy, which otherwise would be lost to the environment.

1.3.8 Summary of applications

Thermoelectric applications can be spilt into two categories, one for cooling and one for power generation. Table 1.1 aims to summarise that. It also shows the thermoelectric materials which are usually used in the discussed application areas. It can be seen that there exist applications for a wide variety of operation temperatures. In the next section, we will focus on the selection criteria for thermoelectric materials and discuss which materials are more suitable for the different temperature regimes.

Category	Application area	Material	Operation temp. (cold/hot)	Ref.
Cooling				
	Medical service	Not specified	283 K/318 K	[20]
	Vehicle	Bi_2Te_3	Not specified	[36]
	Electronics	Not specified	283 K/313 K	[34, 35]
Power generation				
	Medical service	Not specified	$\Delta T = 2-5$ K	[21]
	Automobile	Bi_2Te_3, PbTe	373 K/1073 K	[45]
	Aerospace	PbTe, SiGe	366 K/783−1300 K	[30]
	Thin-films	ZnSb, Bi_2Te_3	$\Delta T = 85$ K	[33]
	Industrial	SiGe	293 K/871 K	[38]
	Domestic	Bi_2Te_3, PbTe	303 K/473−911 K	[40–43]

Table 1.1: Summary of thermoelectric application areas, suitable materials and operation temperature range.

1.4 Overview of thermoelectric materials

Up until now we have looked at different designs and applications but have not talked about which materials are used in the construction of the TEG or TEC modules. It is apparent that different applications require different materials to operate at maximum efficiency. In this section, we will discuss the selection criteria and consider factors like operation temperature range, stability, output efficiency, availability and toxicity for the most common and interesting materials.

1.4.1 Selection criteria for thermoelectric materials

The figure of merit (ZT) should be as large as possible in order to get high thermoelectric efficiency. As explained in Section 1.1, ZT shows the relation between the electrical and thermal transport ($ZT = S^2\sigma T/\kappa$). Thermal conductivity (κ) is the sum of the electronic and lattice thermal conductivity ($\kappa = \kappa_{el} + \kappa_{latt}$). The issue is that the electronic thermal conductivity is related to the electrical conductivity (σ) via the Wiedemann-Franz law ($\kappa_{el} = L\sigma T$). Thus, our ZT equation becomes:

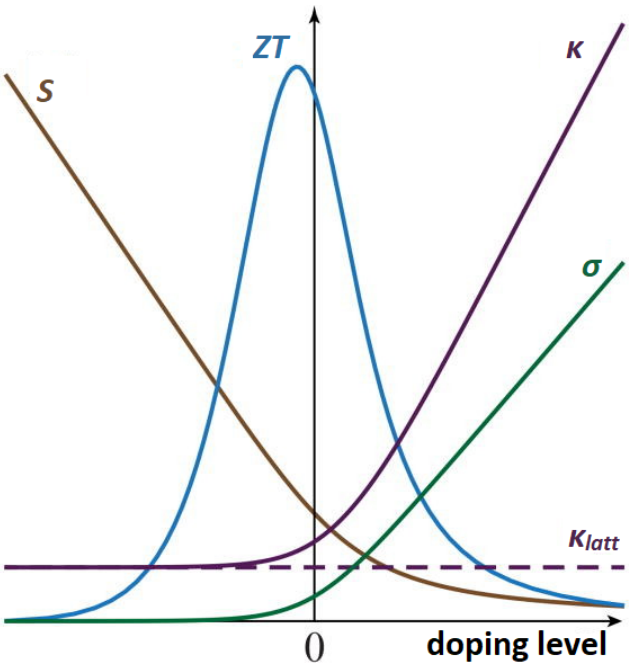

Figure 1.3: Competing processes in thermoelectric optimisation. The Seebeck coefficient decreases with higher doping levels while electrical and thermal conductivity increase, thus making the optimisation of ZT a difficult task.

$$ZT = \frac{S^2/L}{1 + \frac{\kappa_{latt}}{\kappa_{el}}}, \tag{1.1}$$

where L is the Lorenz factor equivalent to 2.4×10^{-8} WΩK^{-2}, S is the Seebeck coefficient and T is the temperature. A high ZT value can be obtained only if the Seebeck coefficient is large or if the ratio $\kappa_{latt}/\kappa_{el}$ is very small. The latter can be achieved when the lattice thermal conductivity is very small or when the electrical conductivity (electron thermal conductivity) is large. It is important to remember that even materials with high ZT and very small κ_{latt} can be inefficient if the power factor ($PF = S^2\sigma$) is not large enough to allow the device to do the needed amount of work.

In summary, the recipe for a good thermoelectric material is having high S and σ, and low κ_{latt}. This turns out to be a very challenging task since these quantities are not fully independent. The competing processes are illustrated in Fig. 1.3 [46].

We can split thermoelectric materials into three sections depending on their ZT. Materials with $ZT < 1$ are considered inefficient, with $ZT \approx 2$ very capable of recovering waste heat and with $ZT \geq 4$ being able to match the efficiency of refrigerators [47]. This point is illustrated very nicely in several studies [27, 48]

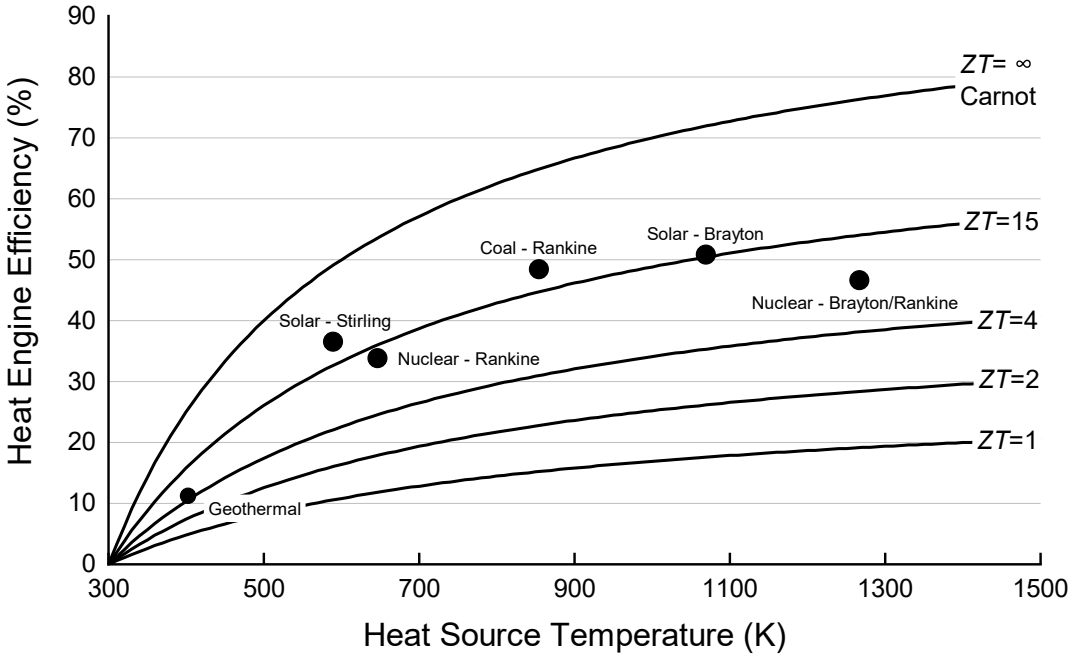

Figure 1.4: The efficiency comparison of thermoelectrics and other energy conversion technologies as a function of the heat source temperature. [Based on [27]]

and shown here in Fig. 1.4. The black dots show some of the common energy-conversion technologies.

Figure 1.5 shows how the thermoelectric figure of merit has improved over the years. It can be seen that there has been a significant increase in the number of investigated materials since 2010. Some of the most promising thermoelectric materials are discussed in the following sections.

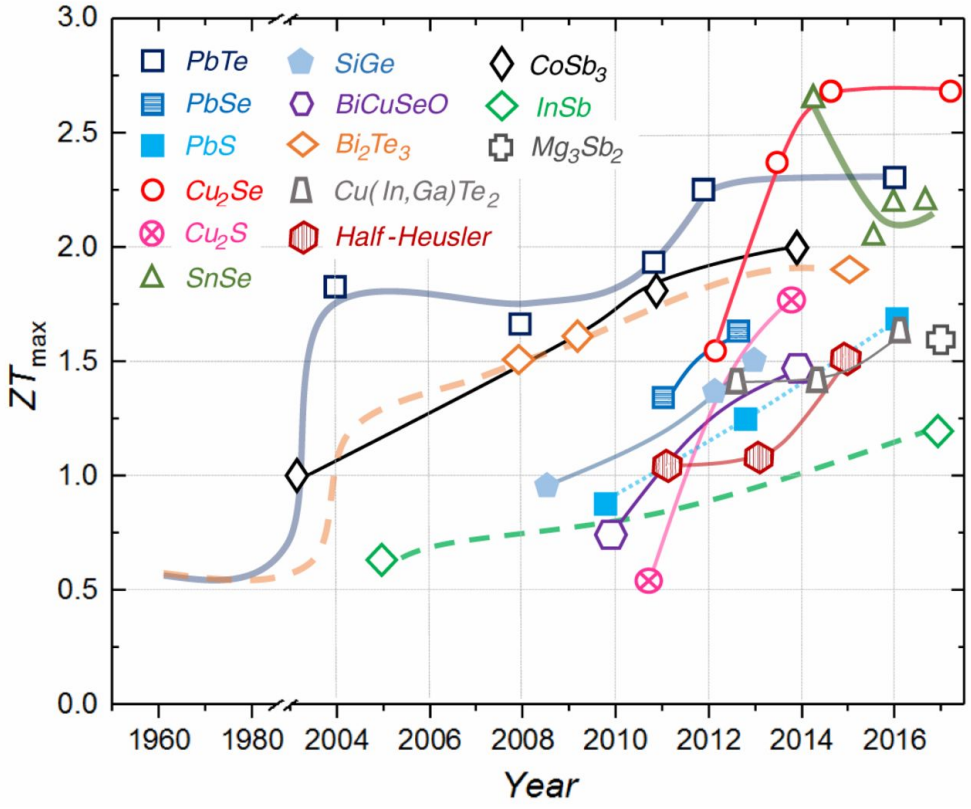

Figure 1.5: The evolution in time of the ZT values for different thermoelectric materials. [Figure taken from He *et al*. [48]]

1.4.2 Chalcogenides: most commonly used thermoelectric materials

We can see in Fig. 1.5 and Table 1.1 that the earliest and most utilised thermoelectric materials are Bi_2Te_3 and PbTe. In fact all bismuth and antimony chalcogenide based materials such as Bi_2Se_3, Bi_2Te_3 and Sb_2Te_3 exhibit good thermoelectric properties. All compounds have an identical rhombohedral crystal structure. It is easier to think of it in terms of a hexagonal cell in which the chemical formula (X_2Y_3) is repeated three times. Each repetition forms a Y(1)-X-Y(2)-X-Y(1) structure, which is known as a quintuple layer. The numbers 1 and 2 denote two different chemical states for the anions.

For a long period of time, the maximum figure of merit of Bi_2Te_3 has been around 1, which for most applications corresponds to efficiency of about 5–7%. The optimal operation temperature of Bi_2Te_3 is relatively low and the efficiency falls off rapidly when the hot side temperature exceeds 500 K [49].

The optimisation of the chalcogenides can be done in several ways. The similarity in the crystal structure allows for mixing the compounds. Fine tuning of the carrier concentration can be achieved by alloying Bi_2Te_3 with Bi_2Se_3 and Sb_2Te_3. Alloying creates defects in the crystal structure, like vacancies, antisites defects and grain boundaries. These give rise to *p*- or *n*-type doping depending on whether the X or Y elements in X_2Y_3 are the ones being mixed. As a results, both the *p*-type compounds close to $(Sb_{0.8}Bi_{0.2})_2Te_3$ and the *n*-type compounds close to Bi_2 $(Te_{0.8}Se_{0.2})_3$ exhibit reduced lattice thermal conductivity due to the presence of more scattering centres [49].

Quintuple layers are weakly bonded to each other via the van der Waals forces and can be easily exfoliated. This can be utilised to make different nanostructures. Oriented *p*-type Sb_2Te_3 and *n*-type Bi_2Te_3 thin films have shown promising properties such as improved Seebeck coefficient and reduced lattice thermal conductivity [49]. This result illustrates that nanostructuring can be successfully used to improve the performance of materials which are needed for thin film applications.

Zinc antimony Zn_4Sb_3 is another material which is classified as one of the better thermoelectrics. Its high efficiency is due to very low thermal conductivity. Reports suggest that Zn_4Sb_3 operates the best between 450 and 670 K and has a ZT of around 1.3 [50, 51].

We have mentioned in Section 1.3.2 that PbTe is more suitable than Bi_2Te_3 for high temperature operation in automobile applications. Materials based on group IV tellurides, such as PbTe, GeTe and SnTe, are usually used for power generation in the temperature range between 500 and 900 K. Alloys with $AgSbTe_2$ have shown promising results and $ZT > 1$ for both *p*- and *n*-type semiconductor. In particular, the *p*-type alloy $(GeTe)_{0.85}(AgSbTe2)_{0.15}$ exhibits a maximum $ZT > 1.2$ and has been successfully implemented in a durable TEG module [49].

1.4.2.1 Other common materials

There are a few other materials which are being studied despite having a relatively low figure of merit ($ZT < 1$). They are either easy to make or that it is believed that their lattice thermal conductivity can be significantly reduced. For example, SiGe alloys are suitable for high temperature ($T > 900$ K) opera-

tions. The advantage of this compound is that both silicon and germanium are well-known semiconducting elements, their growth is a refined process and the combined material can be used for both *p*- and *n*-type semiconductor legs. The main reason for the low ZT in SiGe is the high lattice thermal conductivity of the diamond structure.

Clathrates and skutterudites are materials which are also suitable for mid- and high-temperature applications. The problem with them is their low ZT. The reported ZT of the Al-substituted Ge clathrate compound $Ba_8Al_xGe_{46-x}$ is only around 0.2 despite a good power factor [52], which means that the lattice thermal conductivity ruins the thermoelectric properties of the compound. The most studied skutterudites for thermoelectric applications are based on antimony, like $CoSb_3$. A combination of high carrier mobility, high atomic masses, good Seebeck coefficient and high electrical conductivity is a good premise for excellent electronic thermoelectric properties. However, the thermal conductivity of skutterudites is also high with the best ZT of undoped $CoSb_3$ being only 0.17 at 610 K [53]. The reason why both calthrates and skutterudites are being considered is because of their crystal structures. Both types have empty spaces in their lattices, called cages. These cages can host various guest atoms. That is useful for both doping and decreasing the lattice thermal conductivity.

1.4.3 Emerging materials

The following set of compounds are the new and trending materials which combine excellent electronic properties with acceptable lattice thermal conductivity.

1.4.3.1 Heusler compounds

Heulser compounds are interesting alloys which exhibit good thermoelectric properties. They are split into two different types depending on the chemical composition. The chemical formula X_2YZ denotes full-Heusler alloys (FH) and XYZ denotes half-Heusler alloys (HH), where X stands for a transition metal, Y is a noble metal and Z is a rare-earth element. Both types of alloys have a face-centred cubic crystal structure and are known for their thermal and mechanical stability [48].

Full-Heusler alloys, like Fe_2VAl, are reported to have a substantially higher power factor than Bi_2Te_3 at room temperature [54]. The interesting aspect of Fe_2VAl is that there is a mismatch between experimental results and theoretical prediction regarding the Seebeck coefficient.

Half-Heusler compounds, like NbFeSb, work in the high-temperature regime. They are gaining a lot of popularity at the moment because their power factor can be an order of magnitude higher than that of more conventional materials. One of the main issues with HH compounds is the lack of balance between *n*- and *p*-type performance. A study on the *p*-type properties reached $ZT \approx 1.5$ at 1200 K by doping NbFeSb with Hf. The structure was reported to have excellent mechanical strength and thermal stability [55, 56]. Doping $FeV_{0.6}Nb_{0.4}Sb$ with Ti also yielded promising results due to an increase in the mobility of charge carriers and a decrease in the lattice thermal conductivity [57].

1.4.3.2 SnSe

SnSe is an impressive thermoelectric material. It is characterised by strong anharmonicty and low lattice thermal conductivity [58], which is rather surprising for a binary compound that does not contain any heavy elements like Pb, Bi, Se or Te. This material exhibits a phase transition near 800 K from a lower symmetry crystal structure (*Pnma*) to a higher symmetry one (*Cmcm*). While in the *Cmcm* phase, the energy gap of SnSe is substantially reduced and the mobility of the charge carriers is enhanced. The layered structure of SnSe is also fundamental for obtaining low thermal conductivity. As a result, SnSe has an extremely high $ZT \approx 2.5$ at 900 K. In terms of semiconductor behaviour, good *p*-type thermoelectric properties were reported for Na-doped SnSe [59, 60], whereas Bi-doped SnSe showed promising *n*-type performance [61].

The strongest point of SnSe is that despite the excellent results there are a lot of remaining questions which are yet to be answered. For example, both the effect of native and extrinsic defects on the electrical properties and the performance of polycrystalline SnSe materials need further investigation [48].

1.4.3.3 Oxides

Oxides are another type of material which operates the best at high temperatures. Initially they were regarded as poor thermoelectrics due to the low charge carrier mobility and high lattice thermal conductivity. The low mobility comes from the strong localisation and charge carrier scattering by optical phonons, which comes from the large electronegativity difference among the constituent elements. The high lattice thermal conductivity is due to the high velocity of sound, which is a result of the small mass of oxygen and large bonding energy [48].

The thermoelectric studies of Na_xCoO_2, ZnO, and Ruddlesden-Popper homol-

ogous series $A_{m+1}B_mO_{3m+1}$ are considered groundbreaking as they showed that contrary to expectations, oxides can exhibit useful thermoelectric properties [62, 63]. Among the advantages of oxides are their availability and thermal stability. In addition, operating at high temperatures, above 900 K, ensures that the moderate ZT is compensated by an increased efficiency, as shown in Fig. 1.4. Oxides are also suitable for creating composite structures which are formed by different building layers. In these structures, the layers which contribute to electrical conductivity are different from the layers which act as a phonon glass and stop the phonon propagation. Thus, the electrical and thermal transport are disentangled and can be optimised separately. This concept is known as the phonon glass-electron crystal (PGEC) effect.

1.5 Optimisation mechanisms

The most difficult task in the thermoelectric field is optimising the performance of materials. In terms of chemistry, promising thermoelectric materials possess one or several of the following properties [48]:

- High band degeneracy which increases the density of states near the Fermi level and does not decrease the mobility of charge carriers.
- Complex unit cell with strong anharmonicity and heavy atoms which yield a low intrinsic lattice thermal conductivity.
- Strong spin-orbit coupling effect which leads to topologically protected states.

In all cases, the common goal is to obtain high mobility and low thermal conductivity. The optimisation techniques which try to achieve this goal rely on mechanisms enabled by structural defects, size effects or more exotic nanostructuring.

1.5.1 Defect-enabled optimisation

Structural defects play a significant role in improving the thermoelectric performance. They arise from breaking the symmetry of the perfect crystal lattice. Defects can improve several properties. For example, doping changes the charge carrier concentration and tries to maximise the power factor by finding the optimal combination between the Seebeck coefficient and the electrical conductivity, similar to the ZT behaviour shown in Fig. 1.3. Furthermore, the

induced extrinsic point defects enhance phonon scattering and thus suppress the lattice thermal conductivity. Along with point (intrinsic and extrinsic) defects there exist linear (dislocations) and planar (interfaces and boundaries) defects, all of which will be discussed below.

1.5.1.1 Intrinsic and extrinsic point defects

Determining the role of intrinsic point defects is not an easy task and can often be misleading. As already mentioned, doping is a common technique for tuning the properties of thermoelectric materials. For example, doping Bi_2Te_3 with Sb on the Bi site or Se on the Te site creates a *p*-type or *n*-type thermoelectric, respectively. Although the dopants are extrinsic point defects, they help the formation of intrinsic point defects, like antisites, interstitials and vacancies, which in turn affect the carrier concentration and the thermoelectric performance. The problem with intrinsic defects is that they are difficult to control and depend on the chemistry of the material. A detailed study on V_2VI_3 compounds (V = Group V elements Sb and Bi, and VI = Group VI elements S, Se and Te) showed that the effects of intrinsic point defects can be controlled via chemical composition or temperature [64]. It is reported that the formation of cation antisites and anion vacancies is affected by the electronegativity difference between the cations and anions of the compound. Further investigations on how vacancies, antisite and interstitial defects affect the energy levels near the Fermi level can lead to innovative ways of thermoelectric optimisation.

Extrinsic defects caused by doping can also minimise the lattice thermal conductivity. For example, in caged compounds such as clathrates and skutterudites, the guest atom is situated in the cage. It oscillates with its own low frequency and increases the number of interactions between acoustic and optical phonons. As a result, the anharmonicity of the system is increased, whereas the lattice thermal conductivity is reduced [65]. Nevertheless, doping is never a straightforward process since the dopant atoms can occupy multiple sites. A study on Mn doped Bi_2Te_3 shows that the dopant atoms can accumulate in the van der Waals gap or substitute Bi or Te on their respective sites depending on the concentration of Mn [66]. This is further investigated in Appendix A.

1.5.1.2 Band convergence

In addition to creating intrinsic point defects, doping can be used for band convergence. This mechanism affects the energy levels in a slightly different way. It increases the degeneracy of the bands by aligning them at the valence band

maximum or conduction band minimum. Thus, the amount of available states near the Fermi level is increased and the Seebeck coefficient is enhanced. Band convergence has been tested on PbTe [67–69], $CoSb_3$ [70], Mg_2(Sn, Si) [71] and Te-Ag-Ge-Sb compounds [72]. One of the approaches is to create a pseudo-cubic unit cell; a complex crystal structure, which introduces short-range non-cubic lattice distortions in a long-range cubic framework. The prerequisite for this scheme is a low-symmetry material with a prominent band gap and a low lattice thermal conductivity. The band convergence scheme also proved successful in SnTe. A high $ZT \approx 1.4$ was obtained via In and Cd co-doping and nanostructuring [73].

1.5.1.3 Dislocations

Dislocations are one-dimensional (linear) defects. Their presence results in a lattice strain since the atoms around the dislocation are misaligned. A *p*-type Bi_2Te_3 was synthesised with dense dislocation arrays on low-energy grain boundaries. The presence of the arrays and the point defects within the grains enhanced the phonon scattering and lowered the lattice thermal conductivity, thus, producing an impressive $ZT \approx 1.85$ [74]. Despite not being trivial, the formation and control of dislocation arrays is an interesting topic which is worth further investigation since it can improve the performance of thermoelectric materials by a significant amount.

1.5.1.4 Planar defects

Dislocations lead to the formation of interfaces and grain boundaries when extended to two-dimensions. Planar defects scatter phonons more effectively than charge carriers. They also scatter and filter out low energy and minority charge carriers better than high energy and majority charge carriers, respectively. Such behaviour was reported for nanostructured Bi_2Te_3 in which the majority charge carrier were less affected by scattering due to interfacial defects [75, 76]. In general, interfaces and grain boundaries become a convenient place to implement a carrier-energy filtering scheme [77]. Filtering out the low energy charge carriers can be used to obtain a larger Seebeck coefficient. There are plenty of reports which suggest that a proper intergrain band alignment [78, 79] and coherent or semicoherent grain boundaries [78, 80, 81] tend to retain the mobility of the charge carriers. The lattice thermal conductivity is also suppressed very effectively by rough grain boundaries [82, 83].

In principle, the filtering process aims to 'exclude' some of the bands and is the

exact opposite of the band convergence which we discussed in Section 1.5.1.2. Therefore, when simultaneously used both processes must be properly balanced towards a good power factor.

1.5.2 Reducing the sample size

Size effects play an important role in thermoelectric optimisation and are the main reason for the interest in low dimensional thermoelectric materials like nanocomposites or thin films [80, 84, 85]. Phonons are quasiparticles which carry heat and one of the main mechanisms for suppressing the lattice thermal conductivity is related to limiting their mean free path over a wide temperature range.

Inevitably, classical and quantum size effects are induced when the dimensionality of the sample is reduced. In the classical context, the lattice thermal conductivity can reach its minimum when the phonon mean free path gets close to the interatomic spacing. In that regime and from the phonons point of view, the structure looks amorphous, thus the heat is carrier by random-walking modes.

Charge carriers are affected by the quantum size effect. They become confined in a given direction when the physical size of the material in that direction becomes comparable with the wavelength of the charge carriers. That is used to tweak the density of states and create sharp DOS features near the Fermi level, thus enhancing the Seebeck coefficient [86, 87].

Although it is difficult to differentiate the classical and quantum size effects since they coexist, most promising results obtained via reducing the dimensionality benefit more from scattering the heat carrying phonons rather than increasing the Seebeck coefficient. This suggests that the classical size effect prevails over the quantum one in terms of improving the thermoelectric performance.

1.5.3 Topological insulators optimisation

There is more to the chalcogenides which we discussed in Section 1.4.2. The quantum Hall effect was discovered in 1980 [88] and showed that a strong magnetic field confines the motion of the electrons in the bulk but gives rise to delocalised states on the surface. As a result, a two-dimensional metal subject to a strong magnetic field is a conductor along the surface but an insulator in the bulk. The same idea can be generalised to three-dimensional materials

even in the absence of an external magnetic field due to a nontrivial topology of the occupied bands [89]. These materials are called topological insulators (TI) and are characterised by a bulk band gap and topologically protected conducting edge (surface) states [90]. The requirements for them include large spin-orbit coupling and band inversion. The prerequisites are satisfied by heavy elements which also have low lattice thermal conductivity [91]. Because of that many of the most popular chalcogenide thermoelectric materials such as Bi_2Se_3, Bi_2Te_3 and Sb_2Te_3 are also TIs [92].

The main motivation behind the interest in utilising and optimising TIs as thermoelectric materials is the possibility of leaving the protected conducting states intact while introducing scattering centres for lattice vibrations. As a result, the electrical conductivity of the material should remain the same despite reducing the lattice thermal conductivity. In addition, the curvature of the bands due to the inversion suggests that the charge carriers mobility should be large, yielding good electronic thermoelectric properties. Studies showed that the size of TI thin films directly affects the thermoelectric performance of the materials [93]. An example of that is crossing from the topologically trivial regime to the nontrivial one in a few quintuple layers of Bi_2Te_3 [94]. In addition, stacking nontrivial and trivial layers yields a very low lattice thermal conductivity [95].

1.5.4 Exotic nanostructuring

In this subsection we will discuss some of the more exotic optimisation techniques. These include adding three dimensional structures to our thermoelectric material in hope of improving its performance. It can be considered that we are expanding the concept of one- and two-dimensional defects to nanostructured 3D defects.

1.5.4.1 Nanopores and nanowires

An interesting way of increasing the thermoelectric performance of thin film Bi_2Te_3 is by introducing nanopores in the structure. The idea is relatively simple and can be regarded as adding holes in the thin film. In that way, we create new surface inside the structure, which increases phonon surface scattering. A study shows that pore scattering dominates other mechanisms at around 5% porosity and that the porous structure has a remarkably low lattice thermal conductivity [96]. The best results (300% improvement) are obtained when the pores are evenly distributed across the film. The other notable result is that the

thermal conductivity loses its temperature dependence, which should have a huge impact on low temperature performance.

Nanowires are another interesting way of thermoelectric optimisation. The reported improvements in Bi_2Te_3 are 10- and 20-fold for the thermal conductivity and Seebeck coefficient, respectively [97]. However, in both cases for nanopores and nanowire arrays, the manufacturing process is very challenging due to the stability of the nanostructures.

1.5.4.2 Locally resonant nanophononic optimisation

Placing an array of short wires (pillars) on top of a thermoelectric material is also a proven way of enhancing the thermoelectric performance. The technical term for this configuration is 'locally resonant nanophononic material' and it works in a very clever way. The pillars oscillate mechanically at their own frequency. These vibrations propagate into the substrate and interfere with the lattice vibrations. In practice, the pillars act as a coloured noise generator which affects the phonon spectrum of the base material but leaves the electronic properties untouched. Results in Si based membrane with pillars show an astonishing reduction of the thermal conductivity at room temperature of almost 500 times when compared to bulk Si [98, 99].

The above example combines a Si membrane with Si pillars on one side of the membrane. The success of this technique can be used as a starting point for increasing the complexity of the structure. For example, pillars can be made of different materials and can be placed on both sides of the membrane. It is also not far fetched to assume that we can add nanopores to the membrane and further decrease the thermal conductivity. In general and regardless of the optimisation technique, current results along with the creative ways of combining different optimisation mechanisms make the future of thermoelectric materials look promising.

1.6 Computing thermoelectric properties

People are finding very innovative ways of improving the thermoelectric performance. If Si based materials can achieve such remarkable improvements through thoughtful engineering, then the prospects for other materials look even better. One of the main problems, however, is that the experimental study of multiple complex materials can be a very challenging and expensive task with no guaranteed results. Therefore, having the theoretical means to

investigate different thermoelectric materials and optimisation ideas is becoming more and more important. The theoretical approach can be split into two stages. One computes the electronic thermoelectric properties, while the other estimates the lattice thermal conductivity. In both cases, the initial input data is obtained via first principles calculations.

1.6.1 Software for computing electron transport properties

The first stage solves the semi-classical Boltzmann transport equation (BTE) for electrons and gives information regarding the Seebeck coefficient, electrical conductivity and electron thermal conductivity. There are two packages which can solve the electron BTE – BoltzTraP [100] and BoltzWann [101]. Both programs work in the constant relaxation time approximation, which means that the scattering time of the electrons is fixed. It is provided as a constant which is taken from experimental data or computed via alternative ways such as the deformation potential theory [102]. A new version of BoltzTraP, called BoltzTraP2 [103], allows the users to provide scattering times in a more sophisticated way based on the electron-phonon coupling. BoltzTraP and BoltzWann require knowledge of the electron density of states (DOS) of the material in order to solve the BTE. The difference is that band energies and band derivatives are obtained via Fourier interpolation in BoltzTraP and Wannier interpolation in BoltzWann.

1.6.2 Methods for computing lattice thermal conductivity

The second stage calculates the phonon contribution to the thermal conductivity (κ_{latt}). This part is computationally more demanding. There are several different approaches which can be used to obtain κ_{latt}. These include (i) calculating the phonon DOS from first principles and solving the Boltzmann Transport Equations for phonons [104], (ii) assuming an arbitrary value for κ_{latt} [105], (iii) calculating a theoretical minimum of κ_{latt} for a given compound [106] and (iv) obtaining κ_{latt} via Slack's equation [107], which requires knowledge of the anharmonicity of the system (Grüneisen parameter γ) and the Debye temperature (θ_D). The last two parameters can be calculated either via the bulk and shear moduli[108] or via the quasi-harmonic approximation [109]. The main advantage of the last three approaches (ii-iv) is that they are not computationally intensive and provide a rough estimate of κ_{latt}, which allows the user to obtain a reasonable estimate of ZT. The drawback, however, is that the phonon contribution to κ is derived indirectly via the elastic constants or by considering

only the acoustic phonons. Thus, results neglect the details of the geometry and chemical structure of the material and can often be inaccurate [108].

Option (i) is the contemporary way of calculating κ_{latt}. There exist many open-source packages which are capable of solving the phonon BTE and allow for thermal conductivity calculations. These are ALAMODE [110], almaBTE [111], PhonTS [112], phono3py [113] and ShengBTE [114]. All programs require knowledge of the force constants and anharmonicity of the system. One of the differences is that some packages offer internal, usually less sophisticated, routines for computing the prerequisites. For example, PhonTS can use classical potentials, whereas almaBTE can create virtual mixtures of different compounds. The computation of the phonon mean free path and energy conservation can also vary depending on the program [115]. The main problem of the phonon packages is that they do not support a lot programs which can calculate the force constants and the anharmonicity.

1.6.3 Compatibility with density functional theory codes

The Boltzmann transport equation is a semi-classical one. This means that the components needed for solving it, like density of states, force constants and anharmonicity, need to be computed from first principles via density-functional theory (DFT) codes.

In terms of electronic properties, the program with the best compatibility is BoltzTraP. At the start of this project it could be used along with WIEN2k [116], ABINIT [117], SIESTA [118], VASP [119] and Quantum Espresso [120] programs. In contrast, BoltzWann is implemented in wannier90 [121] and users need to interface other codes to wannier90 first and then use BoltzWann.

The process of calculating the phonon related thermoelectric properties is not as mature as the computation of the electronic thermoelectric properties. The theory needed to predict the phonon properties and the resulting thermal conductivity has been known for decades but it has not been implemented until the second half of the 2000s. Both force constants calculation, based on DFT and density functional perturbation theory (DFPT), and solutions beyond the relaxation time approximation have been enabled by the advancement in the computational power [115]. Therefore, it is no surprise that most programs capable of solving the phonon BTE are developed after 2014 and that their compatibility with DFT codes is limited. For example, ALAMODE, ShengBTE, almaBTE and PhonTS officially work only with VASP and Quantum Espresso. The phono3py package also supports ABINIT and CRYSTAL [122].

The success of the first principles driven framework cannot be denied. In addition to computing the intrinsic thermoelectric properties of materials, DFT codes allow us to investigate the effect of point defects, interfaces or boundaries. More complex nanostructures can also be modelled. In such a case, calculations are just a matter of compatibility (between the transport programs and DFT codes) and scalability (size of the calculation). This leads us to the scope of this thesis, how the project fits into the thermoelectric field and how it can benefit the DFT community.

1.7 Scope and structure of the thesis

Up until now we have looked at the different architectures and applications of thermoelectric devices. We have discussed which materials exhibit good thermoelectric properties and how we can optimise their performance. We have also listed the required software to perform the calculations. In a way, this overview shows how vast the thermoelectric field is and that it is impossible to explore all options in a single project.

In this section we will discuss how the goals of this study fit into the field. One thing which is not immediately obvious is that CASTEP [123], a leading code for calculating the properties of materials from first principles, is not among the supported DFT codes in Section 1.6. While this created an initial obstacle for modelling the thermoelectric properties, it also set a supplementary background goal for the rest of the project. Therefore, in addition to testing different thermoelectric optimisation approaches, the aim of the project was to develop a set of tools which can later be used by the CASTEP community to calculate the thermoelectric properties of any material. The coding details behind the tools are not explicitly discussed throughout the thesis since they are not strictly related to thermoelectric properties. However, all calculations and thermoelectric investigations were carefully considered with respect to the development stage of the tools. The investigated materials include Fe_2VAl, NbFeSb, TaFeSb and Bi_2Te_3 and the theremoelectric optimisations are based on defect-enabled mechanisms, size reduction and utilisation of topological states.

A summary of the rest of the thesis is given below. Materials and optimisation techniques are referenced to the relevant sections in the Introduction.

Chapter 2: Theory – The purpose of the Theory chapter is self-explanatory. It covers the essentials which are needed to understand the first principles calculations, thermoelectric effect and the Boltzmann transport equations.

Chapter 3: Methodology – This chapter serves as a 'how-to' guide on performing thermoelectric calculations. It describes all programs, interfaces, parameters and convergence criteria which have been used throughout the project. If followed correctly, the explained methodology should allow other users to repeat the experiments.

Chapter 4: Computing the electronic thermoelectric properties of Heusler alloys – The first results chapter marks the beginning of the thermoelectric investigations. This period overlaps with the start of the BoltzTraP to CASTEP interface development. It was necessary to choose a material which is easy to simulate for benchmarking purposes and which has interesting electronic thermoelectric properties, preferably a Seebeck coefficient. The material of choice is Fe_2VAl, a full-Heusler compound (mentioned in Section 1.4.3.1). The mismatch between the theoretical and experimental results on the Seebeck coefficient presented an opportunity to test the interface with different settings. We also observed how chemical doping and band structure modifications, like band dispersion (overlaps with the effect in Section 1.5.1.2) and band gap size, affect the Seebeck coefficient.

Chapter 5: Thermoelectric properties of half-Heusler compounds – The next hurdle after finishing the BoltzTraP to CASTEP interface was to calculate the lattice thermal conductivity. This involved making an interface between ShengBTE and CASTEP and using a material with even fewer atoms per unit cell due to phonon calculations being extremely demanding. The half-Heusler compound NbFeSb (mentioned in Section 1.4.3.1) was the perfect candidate. It has a relatively simple crystal structure and exhibits a good reduction in the lattice thermal conductivity when subject to defects (mechanism discussed in Section 1.5.1). Furthermore, we have decided to substitute Nb in NbFeSb with Ta and investigate how the mass difference between the heavier Ta in TaFeSb and potential dopant atoms affects lattice thermal conductivity. This stage of the project also involved enabling a tool which can calculate the effective mass of the charge carriers. Thus, it was possible to compute the constant electron relaxation time from the deformation potential theory.

Chapter 6: Complex optimisation of electronic thermoelectric properties – It is evident that the optimisation techniques used in Chapter 4 and 5 are selected on purpose to be less computationally demanding. In both cases we calculate the intrinsic properties of a material from first principles and then add the supplementary effects in the later stages of the calculation. Therefore, we decided to test more demanding optimisation techniques in Chapter 6. As a compromise between structural complexity and computational costs we focused only on the changes in the electronic thermoelectric properties. The optimisations

include simulating doping on Fe_2VAl and mixing NbFeSb with TaFeSb, investigating the effect of anti-phase grain boundaries (mechanism discussed in Section 1.5.1.4) in Fe_2VAl and Bi_2Te_3 (material mentioned in Section 1.4.2) and testing the size reduction effects in Bi_2Te_3 thin films (mechanism discussed in Section 1.5.2). Some of the interesting properties of topological insulators (discussed in Section 1.5.3) are also investigated in Bi_2Te_3 thin films.

Chapter 7: Conclusions – The last chapter summarises the achieved goals during the project. It also discusses future goals and how the results and interfaces from this study can be used as a starting point for other investigations.

Appendix A: Preferential sites in the van der Waals gaps of Mn-doped Bi_2Te_3 – This appendix presents a study which aimed to support experimental results and determine where Mn prefers to sit in the van der Waals gaps in Bi_2Te_3.

Appendix B: Code snippets from developed software – This appendix shows code examples of the developed software throughout the research.

Chapter 2

Theory

2.1 Density functional theory

Density functional theory (DFT) was developed by Hohenberg and Kohn in 1964 [124] and Kohn and Sham in 1965 [125]. According to them the electron density of any system determines all ground state properties of the system. Kohn and Sham showed that a set of self-consistent one-electron equations can be used to solve the system. The Kohn-Sham equation (Eqn. 2.1) is the Schrödinger equation of a fictitious system of non-interacting particles which generate the same density as any given system of interacting particles:

$$\left(-\frac{\hbar^2}{2m}\nabla^2 + V_{eff}(\mathbf{r})\right)\psi_i(\mathbf{r}) = \varepsilon_i\psi_i(\mathbf{r})\,. \tag{2.1}$$

The first term in Eqn. 2.1 has its usual meaning of the kinetic energy operator, the second term is called the Kohn-Sham potential. It is the effective external potential in which the non-interacting particles move. The energy of particle i is denoted by ε_i and the wavefunction is given by $\psi_i(\mathbf{r})$. Equation 2.2 shows the full form of the effective potential:

$$V_{eff}(\mathbf{r}) = V_{ext}(\mathbf{r}) + \frac{e^2}{4\pi\varepsilon_0}\int\frac{\rho(\mathbf{r}')}{|\mathbf{r}-\mathbf{r}'|}\,\mathrm{d}\mathbf{r}' + \frac{\partial E_{xc}[\rho]}{\partial\rho(\mathbf{r})}. \tag{2.2}$$

Here the first term is the external potential, the second one is the Hartree term describing the electron-electron Coulomb repulsion, while the last term is the exchange-correlation potential, also denoted as V_{xc}. The electron density is labelled as $\rho(\mathbf{r})$ and is found by Eqn. 2.3:

$$\rho(\mathbf{r}) = \sum_{i=1}^{N}|\psi_i(\mathbf{r})|^2. \tag{2.3}$$

The Pauli exclusion principle, which states that two identical fermions cannot occupy the same state at the same time, gives rise to effective repulsion between electrons with parallel spins and causes the exchange interaction. In addition, there is a correlated motion between electrons of anti-parallel spins which arises from their mutual Coulomb repulsion. This is the correlation interaction and means that the probability of finding one electron at a certain position in space depends on the position of others. Therefore, the exchange-correlation potential depends on $\rho(\mathbf{r})$ and since the density depends on the wavefunction which in turn depends on the effective potential, it is necessary to solve the equations in a self-consistent way. This is done with an initial guess of the electron density. As a starting point, V_{xc} needs to be approximated in order to solve the Kohn-Sham equations. Figure 2.1 shows a flowchart of how the solution is reached.

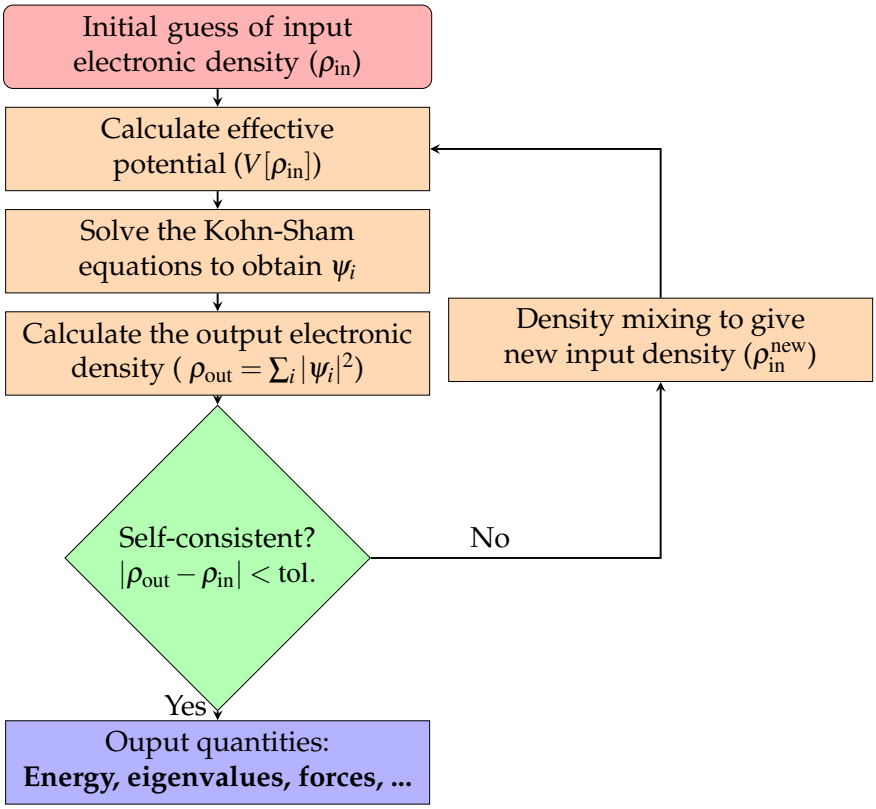

Figure 2.1: Schematic representation of the self-consistent loop for solution of Kohn-Sham equations.

There are two main types of exchange-correlation functional approximations. The first one is the local density approximation (LDA). It takes the density at a point in space and computes the exchange-correlation energy density at that point as if the density is the same everywhere. This works well if the system is homogeneous. A more sophisticated approach is the generalised gradient approximation (GGA). It estimates the contribution of each volume element

based on the magnitude and gradient of the electron density within that element. Perdew, Burke and Ernzerhof proposed a variation of this approximation which is called GGA-PBE [126]. It is widely used nowadays and gives a good compromise between encapsulating the right physics, agreement with experimental results and speed.

2.1.1 Basics of band theory

Although the Kohn-Sham equation is solved for fictitious non-interacting particles, the solution of Eqn. 2.1 gives information about the discrete electron energy levels in a real system. These energy levels, called also eigenenergies, are obtained for a set of **k**-points, which represent positions in the Brillouin zone where the Kohn-Sham equation is solved.

Band structure

Eigenenergy variations along a given **k**-points path form features called bands. The full set of energy levels forms the material's band structure. Although the band structure is simply a plot of lines passing through the three-dimensional Brillouin zone, it can serve as a powerful visual tool which helps explaining the concept of a band gap, electron mobility and density of states.

Types of band gaps

A band gap is present when the space between the top valence and bottom conduction states forms a region in which there are no allowed energy levels. Metals do not have a band gap, semiconductors have a band gap of up to a few electron-volts and insulators have a band gap of anything above that. In spin-polarised materials the band gap of the spin-up and spin-down channels need not be identical. Materials which do not exhibit a band gap in one of the channels are called half-metals.

There are several types of band gaps depending on the position of the valence band maximum (VBM) and conduction band minimum (CBM), as illustrated in Fig. 2.2. If the **k**-vectors of the VBM and the CBM are the same, the band gap is called direct. In a direct band gap an electron can be promoted from the VBM to the CBM by absorbing a photon which has the energy of the band gap. This process is called light absorption. The reverse process is light emission, where an electron in the conduction band annihilates a hole in the valence

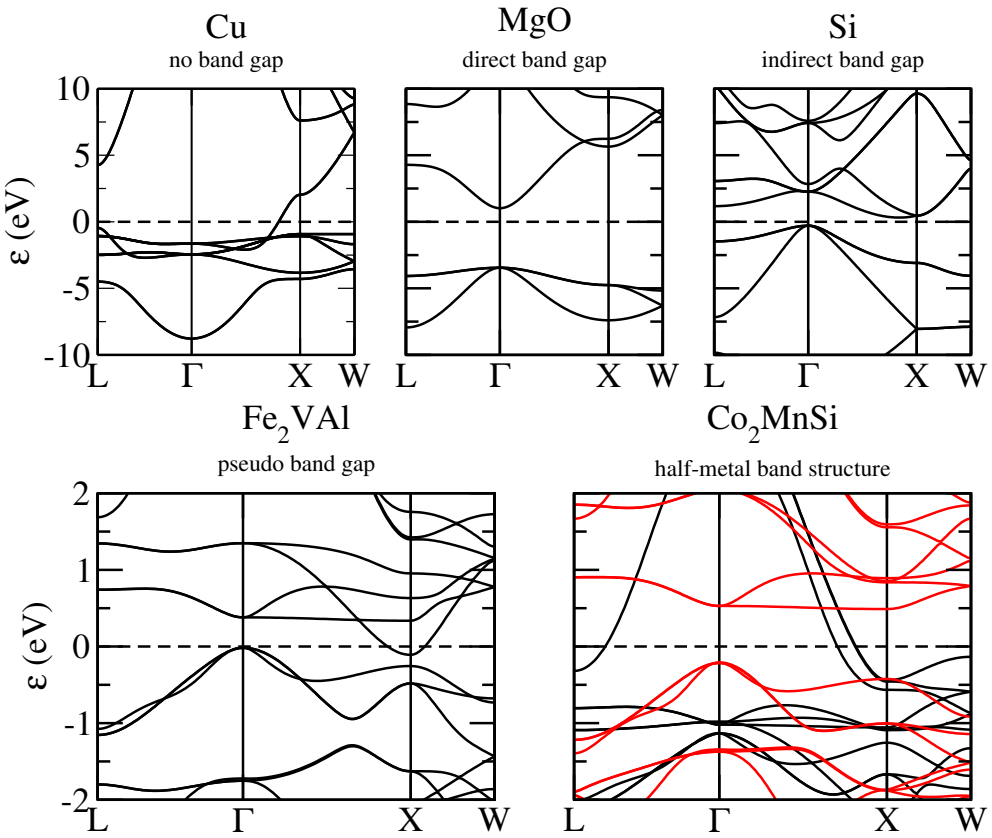

Figure 2.2: Different types of band gaps. Cu is a metal and has no band gap, MgO is a semiconductor which has a wide direct band gap, whereas Si is a semiconductor with an indirect band gap. The semiconductor Fe_2VAl exhibits a pseudo band gap, which is also typical for semi-metals. The band structure of the half-metal Co_2MnSi is typical for metals along the first spin channel (black bands) and typical for semiconductors along the other spin channel (red bands).

band, thus releasing the excess energy as a photon. In these cases the crystal momentum of the electrons and the holes is the same, hence the transitions and the band gap are referred to as direct. An indirect band gap occurs when the **k**-vectors of VBM and CBM are different. In such a case in addition to a photon with the energy of the band gap, light absorption and emission also require the absorption or emission of a phonon, where the phonon momentum equals the difference between the electron and hole momentum. Thus, both energy and crystal momentum are conserved. Since a change in the crystal momentum is also required for the transitions to occur, the band gap is referred to as indirect.

In some cases the energy gap is partial and occurs only in some regions in the Brillouin zone. Such a gap is called a pseudogap and can be thought of as a negative indirect gap. An example is given in Fig. 2.2 for Fe_2VAl, in which case the pseudo gap occurs due to the VBM being at the Γ-point while the CBM is at the X-point. Similar band alignment is associated with semimetallic elements like arsenic, antimony, bismuth and tin.

Band shape determines electron movement

The other useful feature of the band structure is that it illustrates how the band energy changes with respect to momentum space. The group velocity is given by definition as:

$$\mathbf{v}_g = \frac{1}{\hbar}\frac{dE}{d\mathbf{k}}, \tag{2.4}$$

where $\hbar$ is the reduced Planck constant, E is the energy and $\mathbf{k}$ is the position in reciprocal space. Therefore, one can see if the charge carriers are localised or non-localised just by looking at the dispersion of the bands. The projection of the bands along the energy axis results in a density of states plot. Localised (flat) bands yield more states per unit of energy than non-localised (dispersive) bands. Alternatively, it is possible to project atomic orbitals on top of the bands of interest and visualise which species contribute to conduction.

In terms of measurable properties, the quantity which relates the voltage and temperature in materials (Seebeck coefficient) is proportional to the change of the density of states around the Fermi energy [54]. Localised bands yield a larger Seebeck coefficient than the non-localised ones. And while the Seebeck effect is discussed in more details in Section 2.3, it becomes obvious that the band structure is a powerful tool which can allow us to make efficient screening and predictions for material's properties based on bands shape and nature.

2.1.2 Theory of lattice dynamics

In quantum mechanics lattice vibrations are described using quasi-particles called phonons. The uniform oscillations at a given frequency give rise to phonon modes analogous to the normal modes in classical mechanics. Arbitrary lattice vibration can be regarded as a superposition of the different phonon modes.

In order to understand how lattice dynamics is computed from first principles we need to consider a crystal with a unit cell containing N atoms, which are labelled κ. To keep the expressions readable with as few indices as possible we will restrict ourselves to using one unit cell (a). The indices α, β and γ denote Cartesian directions. At the start, the crystal is in mechanical equilibrium with Cartesian coordinates $R_{\kappa\alpha}$. The displacement of an atom from its equilibrium position is then [127]:

$$u_{\kappa\alpha} = r_{\kappa\alpha} - R_{\kappa\alpha}, \tag{2.5}$$

where $r_{\kappa\alpha}$ is the displaced position of the κ-th atom along the α direction. We use the fact that the harmonic lattice dynamics can be obtained from a Taylor expansion of total energy about structural equilibrium coordinates:

$$E^{harmonic} = E_0 + \sum_{\kappa\alpha} \frac{\partial E}{\partial u_{\kappa\alpha}} u_{\kappa\alpha} + \frac{1}{2} \sum_{\kappa\alpha} \sum_{\kappa'\beta} \Phi^{\kappa\kappa'}_{\alpha\beta} u_{\kappa\alpha} u_{\kappa'\beta} + ... \tag{2.6}$$

There is no force acting on the atoms at equilibrium, hence the first derivative of the energy $\partial E/\partial u_{\kappa\alpha}$ vanishes. The deviation from equilibrium is considered to be small, thus the third and higher order terms are neglected. This is called the harmonic approximation. The second order derivative of the energy is the force constants matrix:

$$\Phi^{\kappa\kappa'}_{\alpha\beta} = \frac{\partial^2 E}{\partial u_{\kappa\alpha} \partial u_{\kappa'\beta}}. \tag{2.7}$$

The next step is to write the displacements in terms of a plane wave with respect to cell coordinates:

$$u_{\kappa\alpha} = \varepsilon_{m\mathbf{q},\kappa\alpha}\, e^{i(\mathbf{q}\cdot\mathbf{R}_{\kappa\alpha} - \omega_{m\mathbf{q}} t)}, \tag{2.8}$$

where the index m is for the phonon modes, $\mathbf{q}$ is a phonon wavevector, ω is the angular frequency of the wave and $\varepsilon_{m\mathbf{q},\kappa\alpha}$ is a polarisation vector. Using Newton's force equation (Force = mass $\times$ acceleration) and taking the second time derivative of Eqn. 2.8 and the first derivative Eqn. 2.6 lead us to a diagonalisation problem:

$$D^{\kappa\kappa'}_{\alpha\beta}(\mathbf{q}) \varepsilon_{m\mathbf{q},\kappa\alpha} = \omega^2_{m\mathbf{q}} \varepsilon_{m\mathbf{q},\kappa\alpha}, \tag{2.9}$$

where $D^{\kappa\kappa'}_{\alpha\beta}(\mathbf{q})$ is the dynamical matrix and is defined as:

$$D^{\kappa\kappa'}_{\alpha\beta}(\mathbf{q}) = \frac{1}{\sqrt{M_\kappa M_{\kappa'}}} \sum_a \Phi^{\kappa\kappa'}_{\alpha\beta} e^{i\mathbf{q}\cdot\mathbf{R}_{\kappa\alpha}}, \tag{2.10}$$

where M denotes the mass of an atom. The dynamical matrix is in fact the Fourier transform of the force constants, which can be found either by a finite-displacement method, which involves finding the numerical derivative from two calculations with a small displacement of an atomic coordinate, or by using perturbation theory to evaluate a response wavefunction. Once $D^{\kappa\kappa'}_{\alpha\beta}(\mathbf{q})$ is

known the frequencies of each mode, $3N$ in total, are obtained as the square roots of the eigenvalues of Eqn. 2.9. The phonon eigenvectors correspond to atomic displacements belonging to each mode.

In summary, the first-order force constant is simply a measure of the force on an atom. At equilibrium this is zero. The second-order force constant shows what is the force on a given atom if another atom in the system is moved away from equilibrium. It shows how much atoms affect each other while oscillating. The same logic can be extended to higher order terms. The third-order force constant involves three atoms and can be thought as a measure of the deviation from the harmonic approximation, in other words it shows the anharmonicity of the systems and can be useful in determining scattering rates.

2.2 Beyond density functional theory

While density functional theory is considered to be a very successful level of theory, it does not come without its flaws. For instance, the widely used exchange-correlation functionals LDA and GGA, in their different flavours, fail to predict the insulation behaviour of some strongly correlated materials, like transition metal oxides. Not only is the electronic band gap underestimated, but in some cases, qualitatively wrong metallic ground states are also predicted [128].

2.2.1 Hubbard model

The Hubbard model aims to describe the transition between conducting and insulating systems. Considering a solid with freely moving electrons, the interaction between them is via a screened Coulomb interaction. If we imagine a very simple picture in which there is one atom with a single energy level, then Pauli's exclusion principles tells us that at most two electrons can occupy that single energy state. The interaction is the biggest for two electrons on the same atom and is given by a term with the value of U; in all other cases the interaction term is zero. There is also no interaction between electrons on different atomic sites. Thus, our Hubbard Hamiltonian is governed by the energy scale needed for hopping between adjacent sites and the interaction term if the site is doubly occupied (the on-site repulsion U) [129].

A successful approach based on the Hubbard model, which tackles the problem associated with strongly correlated system, was introduced by Anisimov *et al*. in 1991 [130]. In this model, a small number of localised orbitals is selected

and the electronic correlation associated to them is treated in a special way. The idea is to correct the standard functional by adding an on-site Hubbard-like interaction E_{Hub}:

$$E_{\mathrm{DFT}+U} = E_{\mathrm{DFT}} + E_{\mathrm{Hub}} - E_{\mathrm{dc}} = E_{\mathrm{DFT}} + E_U, \tag{2.11}$$

where E_U is a combination of the Hubbard-like interaction E_{Hub} and the E_{dc} term, which avoids double counting the interactions of the electrons in the Hubbard and DFT terms. Cococcioni and de Gironcoli [128] showed that E_U can be expressed in terms of an effective U_{eff} parameter, which takes into account the screened on-site Coulomb (U) and exchange (J) interactions:

$$E_U = \frac{U_{eff}}{2} \sum_a tr(\rho^a(1-\rho^a)), \tag{2.12}$$

where ρ^a is the atomic orbital occupation matrix with a denoting the atomic site and spin.

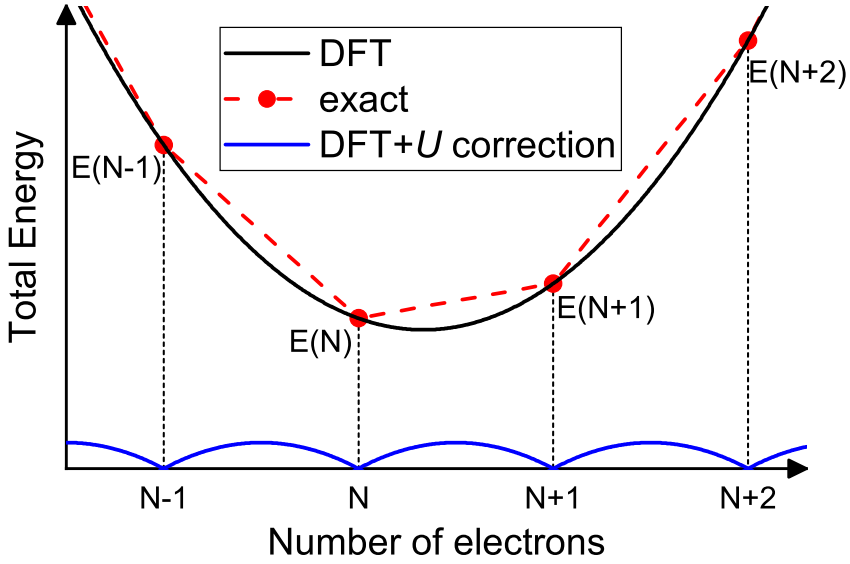

Figure 2.3: Change in the energy profile as a function of number of electrons in a generic atomic system attached to a reservoir. The difference between the exact (red dashed line) and DFT (black curve) energy is given by the bottom curve (blue ripples). Redrawn from [128].

The effect of the "$+U$" correction is visualised in Fig. 2.3. The energy curve of a system with different number of electrons (N) should represent points which are connected by straight lines since the intermediate states with fractional number of electrons are a statistical mixture of the boundary states with integer number of electrons. The usual LDA and GGA approaches yield a total en-

ergy curve with unphysical curvature for non-integer occupations and a false minimum. The self-interaction of the partially occupied Kohn-Sham orbitals is not treated properly by the functionals and that gives a nonlinear contribution to the total energy with respect to number of electrons. The DFT+U correction compensates for this discrepancy once the numerical value of the U parameter is set equal to the curvature of the respective LDA or GGA energy profile.

In summary, the Hubbard U parameter can be regarded as the *unphysical* curvature, shown in Fig. 2.3, of the exchange-correlation functional energy as a function of the number of electrons, which in turn is related to the incorrect treatment of self-interaction of the non-integer electrons injected into the system.

2.3 Thermoelectric effect

2.3.1 Seebeck effect

The Seebeck effect is the conversion of heat directly into electricity at the junction of different types of metal. Seebeck made his discovery in 1821. He observed that when a metallic compass needle is placed between two different conductors, linked by junctions at their extremities and under a temperature gradient, the needle is deflected. This was because the electron energy levels in each metal shifted differently and a voltage difference between the junctions created an electrical current and therefore a magnetic field around the wires. Seebeck did not recognise initially that there was an electric current involved, so he called the phenomenon the thermomagnetic effect. It was later discovered that a difference in the electric potential appears at the junction of two materials when subject to a temperature gradient. The Seebeck effect is mainly used in thermocouples for accurate temperature measurements.

The Seebeck coefficient, or thermoelectric power (thermopower), of a material can be defined as [30]:

$$S = -\frac{\Delta V}{\Delta T}, \tag{2.13}$$

where S is the Seebeck coefficient, ΔT shows the temperature difference between the two ends of the material, and ΔV denotes the thermoelectric voltage seen at the terminals. The minus sign comes from the fact that the voltage gradient in the material always points against the temperature gradient.

2.3.2 Peltier effect

The Peltier effect could be considered as the opposite of the Seebeck effect. In 1834, Peltier discovered that a temperature gradient would appear at the junctions of two different materials when voltage was applied. In other words, when a current is flowing through the junctions, one junction absorbs heat while the other generates it. The magnitude of the produced and absorbed heat at the junction, when current is applied, is given by the Peltier coefficient:

$$Q = \Pi I, \tag{2.14}$$

where Q is the produced or absorbed heat, I is the electric current and Π is the Peltier coefficient. The Peltier effect could be used in heat pumps. As current is driven through the material, some of the junctions absorb heat, while others lose heat. This phenomenon is the basics of thermoelectric coolers.

Figure 2.4 illustrates the schematics of devices based on both effects. Left diagram shows a thermocouple, while right diagram shows the circuit of a thermoelectric cooling device.

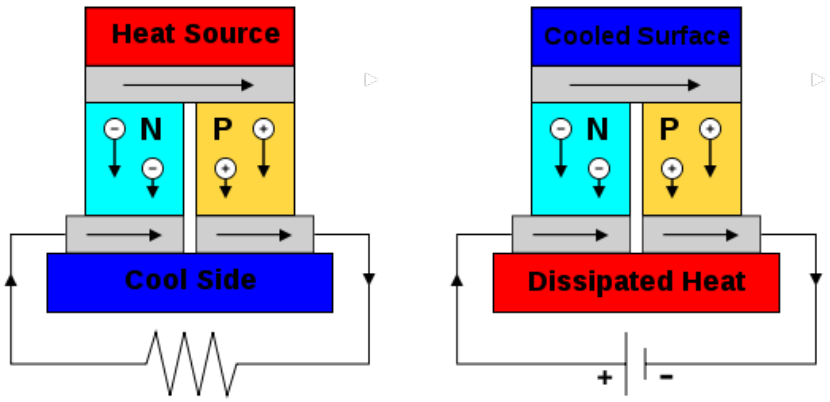

Figure 2.4: A thermoelectric circuit composed of materials of different Seebeck coefficient (p-doped and n-doped semiconductors), configured as a thermoelectric generator (left) and thermoelectric cooler (right). If the load resistor at the bottom of the left diagram is replaced with a voltmeter then the circuit functions as a temperature-sensing thermocouple [131].

2.3.3 Thompson effect

In 1851, Lord Kelvin predicted and observed that both Seebeck and Peltier effects are related. When a single type of material is traversed by an electric current it develops a temperature gradient and exchanges heat with the envi-

ronment. Inversely, an electric current is generated when a material is under a temperature gradient with heat flowing through. This phenomenon is called the Thomson effect. The main difference with the Peltier and Seebeck effects is that the Thomson effect involves only one material and no junction is required.

The importance of the the Thomson effect comes from the possible various applications. On one hand, thermoelectric materials could be used as refrigerators in many devices which require precise temperature regulation. On the other hand, converting heat into electricity would improve the efficiency of modern devices and solve some of the issues related to the harmfulness of current energy sources.

2.3.4 Thermoelectric figure of merit

The quality of thermoelectric materials is measured by a dimensionless quantity called "figure of merit" [30]:

$$ZT = \frac{S^2\sigma T}{\kappa_{tot}} = \frac{S^2\sigma T}{\kappa_{el} + \kappa_{latt}}, \tag{2.15}$$

where σ is the electrical conductivity, T is the temperature, S is the Seebeck coefficient and κ_{tot} is the total thermal conductivity, which is the sum of the electronic thermal conductivity κ_{el} and the lattice thermal conductivity κ_{latt}. The numerator $S^2\sigma$ is called power factor. Materials with a high power factor are able to generate more energy and do more work, but this does not mean they are more efficient.

In order to understand why ZT is so important for devices, it is necessary to look at the equation for maximum efficiency:

$$\eta_{\max} = \frac{T_H - T_C}{T_H} \frac{\sqrt{1+Z\bar{T}} - 1}{\sqrt{1+Z\bar{T}} + \frac{T_C}{T_H}}, \tag{2.16}$$

where $\eta_{\max}$ is the maximum efficiency, T_H and T_C is the temperature at the hot and cold junction, respectively, and $\bar{T}$ is the average temperature. It can be seen just by inspecting the equation, that the only way to increase $\eta_{\max}$ is by having $T_H = -T_C$, which is meaningless, or by improving the ZT value by a substantial amount.

The figure of merit can be optimised by reducing the the thermal conductivity. The problem is κ_{el} and σ are related by the Wiedemann-Franz law:

$$\frac{\kappa_{el}}{\sigma} = LT, \tag{2.17}$$

with L being the Lorenz factor equivalent to 2.4×10^{-8} WΩK^{-2}. In other words, it is almost impossible to optimise ZT by simply increasing its power factor or by decreasing the electronic thermal conductivity. Fortunately, the total thermal conductivity is the sum of two components and there exist different strategies which could minimise the lattice thermal conductivity.

In summary, the key ingredients for the most effective TE materials are high Seebeck coefficient, high electrical conductivity and low thermal conductivity. In the next few sections, we will go through the theory needed for calculating these quantities.

2.4 Boltzmann transport equation

2.4.1 Electron solution

The Boltzmann transport theory is the main tool for calculating thermoelectric properties. The fundamental assumption in deriving the Boltzmann transport equation (BTE) is that there exists a distribution function $f_{\mathbf{k}}(\mathbf{r},t)$ which measures the occupation number of electrons in the neighbourhood of $\boldsymbol{r}$ at time t. At thermal equilibrium, electrons are distributed according to Fermi-Dirac statistics $f^0_{\mathbf{k}}$. The evolution of the distribution function with time can be considered as the sum of three terms – a diffusion term, an electric field term and a scattering term. The total rate of change of the distribution function must vanish in the steady state of heat flow through the sample. Thus, the most general form of the Boltzmann transport equation is given by [132]:

$$\frac{df_{\mathbf{k}}}{dt} = \left.\frac{\partial f_{\mathbf{k}}}{\partial t}\right|_{\text{diff}} + \left.\frac{\partial f_{\mathbf{k}}}{\partial t}\right|_{\text{el.field}} + \left.\frac{\partial f_{\mathbf{k}}}{\partial t}\right|_{\text{scatt}} = 0. \tag{2.18}$$

Then Eqn. 2.18 can be rearranged with the scattering term being put on the right hand side [133]:

$$-\mathbf{v}_{\mathbf{k}}\frac{\partial f_{\mathbf{k}}}{\partial \mathbf{r}} - \frac{e}{\hbar}\left(\mathbf{E} + \frac{1}{c}\mathbf{v}_{\mathbf{k}} \times \mathbf{H}\right)\frac{\partial f_{\mathbf{k}}}{\partial \mathbf{k}} = -\left.\frac{\partial f_{\mathbf{k}}}{\partial t}\right|_{\text{scatt}}. \tag{2.19}$$

The first two terms in Eqn. 2.19 are the diffusion and electric field terms with the time dependence being transferred to $\mathbf{r}$ and $\mathbf{k}$, respectively. The velocity of the electrons is given with $\mathbf{v}_{\mathbf{k}}$, whereas $\mathbf{E}$ and $\mathbf{H}$ denote the electric and

magnetic field, respectively. The electron charge is given by e, the speed of light by c and $\hbar$ stands for the reduced Planck constant. It can be seen that the first two terms do not contain a lot of unknowns and can be solved. On the other hand, the precise form of the scattering term remains somewhat undefined. It is possible to do some analysis on the collisions and describe the transition probabilities (P) of electrons moving back and forth from state $\mathbf{k}$ to $\mathbf{k}'$:

$$\begin{aligned} P_{\mathbf{k}}^{\mathbf{k}'} d\mathbf{k}' &= f_{\mathbf{k}}(1 - f_{\mathbf{k}'}) Q_{\mathbf{k}}^{\mathbf{k}'} d\mathbf{k}', \\ P_{\mathbf{k}'}^{\mathbf{k}} d\mathbf{k}' &= f_{\mathbf{k}'}(1 - f_{\mathbf{k}}) Q_{\mathbf{k}'}^{\mathbf{k}} d\mathbf{k}', \end{aligned} \tag{2.20}$$

where $Q_{\mathbf{k}}^{\mathbf{k}'} = Q_{\mathbf{k}'}^{\mathbf{k}}$ is the intrinsic transition rate which can be calculated with Fermi's golden rule. The scattering term can be written as the difference between the probabilities given in Eqn. 2.20. When the brackets are expanded higher order terms cancel out and we are left with first order terms. The next step involves subtracting the equilibrium distributions for states $\mathbf{k}$ and $\mathbf{k}'$ from their respective perturbed distributions in the scattering term. This is possible because the equilibrium distribution is stationary with respect to time. The interesting physics in our system is only due to the deviation from equilibrium. We would also assume that the deviation from equilibrium is very small, which allows us to substitute $f_{\mathbf{k}}$ with $f_{\mathbf{k}}^0$ on the left hand side of Eqn. 2.19. As a result, the linearised BTE has the following form:

$$-\mathbf{v}_{\mathbf{k}} \frac{\partial f_{\mathbf{k}}^0}{\partial T} \nabla T - \mathbf{v}_{\mathbf{k}} e \frac{\partial f_{\mathbf{k}}^0}{\partial \varepsilon} \mathbf{E} = \int \left[(f_{\mathbf{k}} - f_{\mathbf{k}}^0) - (f_{\mathbf{k}'} - f_{\mathbf{k}'}^0) \right] Q_{\mathbf{k}}^{\mathbf{k}'} d\mathbf{k}', \tag{2.21}$$

where ε represents the eigenenergy of the electrons. As already mentioned, the right hand side of Eqn. 2.21 can be solved with the help of Fermi's golden rule. In practice, however, this is very complicated and requires very expensive calculations. Therefore, it is crucial to assume that only the deviation from equilibrium is the reason for the transport properties of the system. We also need to define a constant which shows us how often we move away from equilibrium. This constant is called the relaxation time of the electrons (τ) and the Boltzmann transport equation within the relaxation time approximation is given by:

$$-\mathbf{v}_{\mathbf{k}} \frac{\partial f_{\mathbf{k}}^0}{\partial T} \nabla T - \mathbf{v}_{\mathbf{k}} e \frac{\partial f_{\mathbf{k}}^0}{\partial \varepsilon} \mathbf{E} = \frac{f_{\mathbf{k}} - f_{\mathbf{k}}^0}{\tau}. \tag{2.22}$$

Now it becomes trivial to rearrange Eqn. 2.22 for $f_{\mathbf{k}}$. It also becomes apparent that the distribution function is proportional to τ and the final results would

heavily depend on what relaxation time value we choose to use.

The thermoelectric properties of a given system can be obtained from the electric and heat current density equations:

$$j = \int e\mathbf{v}_{\mathbf{k}} f_{\mathbf{k}} \frac{d^3\mathbf{k}}{8\pi^3}, \tag{2.23}$$

$$q = \int (\varepsilon - \mu)\mathbf{v}_{\mathbf{k}} f_{\mathbf{k}} \frac{d^3\mathbf{k}}{8\pi^3}, \tag{2.24}$$

where j is the electric current density, q is the heat flux, ε is the electron energy and μ is the chemical potential. When $f_{\mathbf{k}}$ is substituted into the equations above, one obtains the following set of equations:

$$\begin{bmatrix} K_0 & \frac{1}{eT}K_1 \\ \frac{1}{e}K_1 & \frac{1}{e^2T}K_2 \end{bmatrix} \begin{bmatrix} \mathbf{E} \\ -\nabla T \end{bmatrix} = \begin{bmatrix} j \\ q \end{bmatrix}, \tag{2.25}$$

where K_n is given by [103]:

$$K_n = e^2 \int \sigma(\varepsilon) \left(-\frac{\partial f^0_{\mathbf{k}}}{\partial \varepsilon} \right) (\varepsilon - \mu)^n d\varepsilon, \tag{2.26}$$

$$\sigma(\varepsilon) = \tau \int \mathbf{v}_{\mathbf{k}} \mathbf{v}_{\mathbf{k}} \delta(\varepsilon - \varepsilon_{\mathbf{k}}) \frac{d^3\mathbf{k}}{8\pi^3}. \tag{2.27}$$

Notice that Eqn. 2.25 is presented in a matrix notation. The matrix which acts on the electric field and the temperature gradient gives information on the thermoelectric properties of the system. One can obtain the electrical and thermal conductivity from the diagonal of the matrix, whereas the off-diagonal terms show the relation between temperature and electrical field, which is exactly the definition of the Seebeck coefficient (S) [100, 103, 133]:

$$\sigma = K_0 = \int \sigma(\varepsilon) \left(-\frac{\partial f^0_{\mathbf{k}}}{\partial \varepsilon} \right) d\varepsilon, \tag{2.28}$$

$$S = \frac{1}{eT}\frac{K_1}{K_0} = \frac{1}{eT} \frac{\int \sigma(\varepsilon) \left(-\frac{\partial f^0_{\mathbf{k}}}{\partial \varepsilon} \right) (\varepsilon - \mu) d\varepsilon}{\int \sigma(\varepsilon) \left(-\frac{\partial f^0_{\mathbf{k}}}{\partial \varepsilon} \right) d\varepsilon}, \tag{2.29}$$

$$\kappa^0 = \frac{K_2}{e^2T} = \int \sigma(\varepsilon) \left(-\frac{\partial f^0_{\mathbf{k}}}{\partial \varepsilon} \right) (\varepsilon - \mu)^2 d\varepsilon. \tag{2.30}$$

The value of σ in Eqn. 2.28 is obtained when the temperature gradient in Eqn. 2.25 is set to zero from the simple relation $j = K_0\mathbf{E}$. The Peltier coefficient (Π), shown in Eqn. 2.14, can be obtained from the ratio of q and j, again at $\nabla T = 0$. The Seebeck coefficient in Eqn. 2.29 is obtained when the relation between $\mathbf{E}$ and ∇T is investigated at $j = 0$. The electrical thermal conductivity κ^0 defined in Eqn. 2.30 is obtained at $j \neq 0$. However, the electron thermal conductivity is always measured for $j = 0$. Thus, by substituting $\mathbf{E} = S\nabla T$ in the heat current density equation, we get [100, 103, 134]:

$$q = S^2\sigma T\nabla T + \kappa^0(-\nabla T) = \kappa^0(1 - \frac{S^2\sigma T}{\kappa^0})(-\nabla T), \tag{2.31}$$

which means that the electron thermal conductivity in real measurements is κ_{el}:

$$\kappa_{el} = \kappa^0 - S^2\sigma T. \tag{2.32}$$

It is evident from Eqn. 2.26 that the relaxation time plays a very important role in the computation of thermoelectric properties. And even though S should not depend on τ, the constituent components do change, which further highlights how important it is to obtain a proper estimate of the relaxation time for a given system.

2.4.2 Phonon solution

The process of solving the Boltzmann transport equation for phonons is very similar to the electron example discussed in the previous section. There are, however, a few important differences which we need to discuss.

In the phonon BTE, there is no electric field term like in Eqn. 2.18, which leaves us only with the diffusion and scattering terms. As a result, phonons contribute only to the lattice thermal conductivity and do not have a major contribution to the electric transport. The phonon distribution function f_λ obeys the Bose-Einstein statistics since the particles are bosons. The subscript λ denotes the phonon branch and the position in reciprocal space, similar to the index $\mathbf{k}$ in $f_\mathbf{k}$. The intrinsic lattice thermal conductivity κ_{latt} is then calculated as [114]:

$$\kappa_{latt} = \frac{1}{k_\mathrm{B}T^2\Omega N}\sum_\lambda \mathbf{v}_\lambda \mathbf{F}_\lambda(\hbar\omega)^2 f_\lambda^0(1 + f_\lambda^0), \tag{2.33}$$

$$\mathbf{F}_\lambda = \tau_\lambda^0(\mathbf{v}_\lambda + \Delta_\lambda), \tag{2.34}$$

where f_λ^0 is the equilibrium phonon distribution, $\mathbf{v}_\lambda$ is the phonon velocity for a given mode, Δ_λ is a measure of the deviation from the relaxation time approximation prediction, $\hbar$ is the reduced Planck constant, ω is the phonon frequency, Ω is the unit cell volume and N is the number of the grid points used for the calculation. It can be seen by comparison that the terms in the phonon Eqn. 2.33 and the electron Eqn. 2.30 match very well to each other, e.g. $f_\lambda^0(1+f_\lambda^0)$ corresponds to the electron $(\frac{\partial f_\mathbf{k}^0}{\partial \varepsilon})$, both consist a squared energy and velocity terms, etc. The main difference, however, is in the treatment of the relaxation time.

Remember that while solving the BTE for electrons, we made an approximation that τ is constant since the the transition rate $Q_\mathbf{k}^{\mathbf{k}'}$ was very difficult to compute. The electron-electron scattering interactions needed for the electron τ require very large simulation cells, which makes them prohibitively expensive. Unlike the electron τ, the phonon relaxation time depends on the two- and three-phonon processes, which decay quicker with respect to distance, and can be modelled more easily.

The phonon relaxation time, which we will call τ_λ^0 in this section, is computed by taking into account the two- and three-phonon scattering rates which are estimated directly from Fermi's golden rule. The scattering matrix elements needed for Fermi's golden rule are obtained from the third-order force constants, which are briefly discussed in Section 2.1.2. The additional Δ_λ term in Eqn. 2.34 offers a way of estimating how much τ_λ^0 deviates from the relaxation time approximation. The value Δ_λ is computed in a self-consistent way and depends on both the $\mathbf{F}_\lambda$ function and the transition rates, which in turn depend on phonon frequencies [114].

In summary, the phonon distribution function, velocity and frequency can be computed from the second-order force constants, while the τ_λ^0 and Δ_λ terms can be calculated from the third-order force constants. As a result, it is possible to model fairly accurately the intrinsic lattice thermal conductivity of a system entirely from first principles.

2.5 Quicker ways of calculating the lattice thermal conductivity

While the solution of the phonon Boltzmann transport equation yields the most rigorous estimate of the intrinsic lattice conductivity, it is by no means a cheap calculation which can be used to screen different materials. In com-

parison, Slack showed that for nonmetallic crystals in the temperature range $T \geq \Theta_D$, where Θ_D is the Debye temperature, the intrinsic lattice thermal conductivity (in W/m·K) can be estimated from [107, 135]:

$$\kappa_{latt} = A \frac{\Theta_D^3 V_a^{1/3} m_{av}}{\gamma^2 n^{2/3} T}, \tag{2.35}$$

where V_a, m_{av}, γ and n are the volume per atom (in Å^3), the average atomic mass (in amu), the Grüneisen parameter and the number of atoms in the unit cell, respectively. The parameter A is given by the following equation [108, 136]:

$$A = \frac{2.43 \times 10^{-6}}{1 - \frac{0.514}{\gamma} + \frac{0.228}{\gamma^2}}. \tag{2.36}$$

The two important parameters in this model are the Debye temperature, which can be considered as a cut-off temperature associated with the Debye cut-off frequency, and the Grüneisen parameter, which is a measure of the anharmonicity of the system. In other words, Θ_D and γ play roles similar to the distribution function and the relaxation time in the Boltzmann transport equation.

Using the elastic properties

The study conducted by Jia *et al.* showed that Eqn. 2.35 can be solved by knowing the elastic properties of the material. The averaged sound velocity v_{av} can be calculated from the velocities of the longitude v_L and shear v_T waves [108]:

$$v_L = \sqrt{\frac{B_H + (4/3)G_H}{\rho}}, \qquad v_T = \sqrt{\frac{G_H}{\rho}}, \qquad v_{av} = \left[\frac{1}{3}\left(\frac{1}{v_L^3} + \frac{2}{v_T^3}\right)\right]^{-\frac{1}{3}}, \tag{2.37}$$

where B_H, G_H and ρ are the bulk modulus, shear modulus and the density of the compound, respectively. Then the Debye temperature Θ_D can be calculated using the velocity of sound:

$$\Theta_D = \frac{\hbar}{k_B} v_{av} \left(\frac{6\pi^2 n}{V_a}\right)^{\frac{1}{3}}, \tag{2.38}$$

where $\hbar$ and k_B are the reduced Planck constant and Boltzmann constant.

The final parameter needed for estimating κ_{latt} from Eqn. 2.35 is the Grüneisen parameter γ and it can be obtained from the Poisson ratio ν in the following way:

$$\gamma = \frac{3}{2}\left(\frac{1+\nu}{2-3\nu}\right), \qquad \nu = \frac{1-2(v_{\mathrm{T}}/v_{\mathrm{L}})^2}{2-2(v_{\mathrm{T}}/v_{\mathrm{L}})^2}. \tag{2.39}$$

This model works relatively well for rock-salt structures but overestimates the value of γ for zincblende and wurtzite crystals [108]. The main advantage of this approach is the lack of expense of the calculation since it becomes free if the elastic constants are already known. An improvement can be made by looking at how the bulk and shear moduli change with respect to volume but that increases the computational cost and detracts from quickly testing a given material.

Using the quasi-harmonic approximation

Alternatively, one can use the quasi-harmonic approximation (QHA) to obtain Θ_{D} and γ. The QHA is a simple approach which accounts for the anharmonic effects by assuming the harmonic approximation at any given crystal geometry, even if it does not correspond to the equilibrium structure. There are many different models which are based on analysing a 'volume versus energy' curve in order to fit an equation of state and then give an estimate of quantities like heat capacity, Debye temperature and Grüneisen parameter [137]. The main drawback of the QHA is that the more reliable the results are, the more detailed the input needs to be, which makes the computational cost in some cases comparable to solving the Boltzmann transport equation.

2.6 Considering extrinsic defects

One of the most difficult tasks in modelling the lattice thermal conductivity is simulating the contributions of crystal lattice imperfections, like grain boundaries and point defects. Such calculations are often extremely demanding to compute. Instead we can use a simplified approach in which we find the intrinsic lattice thermal conductivity (κ_{int}) of a perfect crystal from Eqn. 2.33 and assume that it is proportional to the phonon relaxation time.

The total phonon relaxation time τ_{tot} is a combination of different scattering rates from different contributions and is calculated using Matthiessen's rule:

$$\tau_{tot}^{-1} = \tau_{3P}^{-1} + \tau_{GB}^{-1} + \tau_{PD}^{-1} + \tau_{EP}^{-1}, \tag{2.40}$$

where the subscripts 3P (three-phonon processes), GB (grain boundaries), PD (point defects) and EP (electron-phonon interaction) indicate the sort of interaction which contributes to the the final scattering rate.

The intrinsic lattice thermal conductivity, which is obtained by solving the phonon BTE (Eqn. 2.33), depends only on τ_{3P} as we simulate a perfect crystal. Hence all additional contributions need be included separately.

2.6.1 Grain boundaries

We can make the assumption that scattering events due to grains happen every time a phonon passes through a grain boundary. Thus, the distance which the phonons travel before scattering is equal to the grain size (L_{GB}). It should be noted that not all grains are of the same size or shape in real structures. Therefore, the grain size L_{GB}, which is defined here, represents an effective grain size rather than a distribution. The grain size can be estimated by multiplying the phonon velocity (v) and the time needed by the phonons to travel through the grain for the scattering to occur (τ_{GB}). If this relation is rearranged with respect to τ_{GB} then the relaxation time due to grain boundaries is given as:

$$\tau_{GB}^{-1} = v/L_{\mathrm{GB}}. \tag{2.41}$$

The phonon BTE result (κ_{int}) can be approximated to be proportional to τ_{3P} ($\kappa_{int} \propto constant \times \tau_{3P}$). When the contribution of grain boundary scattering is included alongside the phonon BTE result, τ_{tot} is calculated using $\tau_{tot}^{-1} = \tau_{3P}^{-1} + \tau_{GB}^{-1}$. In such a case, the value of the lattice thermal conductivity with the effect of the grain boundaries (κ_{GB}) can be expressed as:

$$\kappa_{GB} = \frac{\kappa_{int}}{1 + \frac{\lambda_{mfp}}{L_{\mathrm{GB}}}}, \tag{2.42}$$

where λ_{mfp} is the mean free path of phonons. Although convenient, using a single value for λ_{mfp} is rather unreasonable because not all phonons travel with the same velocity, nor do they have the same relaxation time, nor the same contribution to the total thermal conductivity (κ_{int}). Instead we can differentiate the phonon BTE result for lattice thermal conductivity accumulation with respect to λ_{mfp}. This gives us information on the lattice thermal conductivity ($\kappa_{int}^{'}$) of phonons with a given mean free path ($\lambda_{mfp}^{'}$). Then Eqn. 2.42 is applied

to every λ'_{mfp} and its respective κ'_{int} with the final result being integrated back to obtain κ_{GB}.

2.6.2 Point defects

Doping introduces point defects into the structure and the lattice thermal conductivity with point defects included (κ_{PD}) can be calculated using the empirical Klemens' equation[138]:

$$\kappa_{PD} = \kappa_{GB}\left(\frac{\omega_0}{\omega_m}\right)\arctan\left(\frac{\omega_m}{\omega_0}\right), \tag{2.43}$$

$$\frac{\omega_0}{\omega_m} = \sqrt{\frac{4\gamma^2 k_B T}{3\pi G_H V_a x_a}}\frac{M}{\Delta M}, \tag{2.44}$$

where κ_{GB} is the lattice thermal conductivity obtained at the previous stage. It could also be κ_{int} if one does not want to consider grain boundaries. The Debye and point defects frequency cut-off are given by ω_m and ω_0, respectively. The other parameters γ, G_H, V_a and x_a represent the Grüneisen parameter, shear modulus, volume per atom and doping concentration per atom in the unit cell. The mass of the host atom is given by M, whereas the mass difference between the host atom and the dopant atom is given by ΔM.

For the above two equations, Klemens makes an assumption that only phonons with high group velocity make a substantial contribution to thermal conductivity. He uses the Debye model and computes the lattice thermal conductivity by considering only the acoustic phonons, which can have a frequency from zero to the Debye frequency ω_m. For point defects it is possible to define a cut-off frequency ω_0, which affects the mean free path of phonons. Klemens obtains Eqn. 2.43 by considering the mean free path due to the two frequencies (ω_m and ω_0) and the ω_0/ω_m ratio, which shows to what extent point defects affect the frequency of acoustic phonons in the Debye model.

2.6.3 Electron-phonon interaction

The computation of the electron-phonon interaction from first principles is expensive. However, a more empirical, but tested, approach based on the Callaway model [139, 140] can be used to gain an insight of how the electron-phonon interaction affects the lattice thermal conductivity in terms of temperature and doping concentration. The relaxation time due to electron-phonon interaction satisfies [141]:

$$\tau_{EP}^{-1} = C\omega^2, \tag{2.45}$$

where C is given by [142]:

$$C = \frac{4nm^* v_e \lambda_e}{15\rho v^2}, \tag{2.46}$$

where ω is the phonon frequency, n is the doping concentration, m^* is the effective mass, v_e is the electron velocity, λ_e is the mean free path of the electrons, ρ is the mass density, and v is the phonon velocity. In principle, the value of C can be calculated from first principles. In practice, however, the value of v_e and λ_e is related to the electron relaxation time, which is modelled to be constant with respect to doping. Therefore, estimating a parameter, which aims to show how doping affects the electron-phonon interaction, with a relaxation time, which is modelled to be insensitive to doping, would lead to a significant inaccuracy in the final results. Instead, experimental results can be used to obtain a value proportional to C. Then the doping dependency ($C \propto n$) and temperature dependency ($C \propto T^{-1/2}$) are included in the model.

2.7 Constant relaxation time approximation

The electron relaxation time (τ) is a measure of how often there are scattering events affecting the free propagation of the carriers. In the constant relaxation time approximation, the value of τ is fixed with respect to the chemical potential. The constant τ can be expressed in terms of the mobility of the charge carriers (μ) and their effective mass (m^*). In the Drude model this relation is given by:

$$\tau = \frac{\mu m^*}{e}, \tag{2.47}$$

where e is the charge of an electron. Looking at the equation above one can be left with the wrong impression that heavy but mobile charge carriers can increase the time between scattering events. In fact, the deformation potential theory introduced by Bardeen and Shockley [102] shows quite the opposite behaviour in which light charge carriers are preferable for obtaining longer relaxation time.

There are three major components needed in order to calculate μ. These are the deformation potential energy, effective mass and elastic constants. The expression for the mobility of the charge carriers is given as:

$$\mu = \frac{2\sqrt{2\pi}e\hbar^4 c_{ii}}{3(k_B T)^{\frac{3}{2}} m^{*\frac{5}{2}} \lambda_{DP}^2}, \tag{2.48}$$

where $\hbar$ is the reduced Planck constant, c_{ii} is the lattice elastic constant ($i = 1,2,3$), k_B is the Boltzmann constant, T is the temperature and λ_{DP} is the deformation potential energy.

The next three subsections discuss how to calculate the variables in Eqn. 2.48. Before proceeding, it needs to be noted that the Bardeen and Shockley theory works for cubic isotropic materials. For the purposes of this thesis such an approximation is reasonable. For anisotropic materials, however, one needs to refer to the generalised theory by Herring and Vogt [143], in which c_{ii} and λ_{DP} values depend on the direction of propagation.

2.7.1 Deformation potential energy

If we have a gradually varying electrostatic potential, which is superimposed on the periodic potential of the crystal lattice, then we can neglect the periodic potential and calculate the motion of the charge carriers in the gradually varying potential. As a prerequisite condition, the change in the gradually varying potential in one period needs to be small compared to the periodic potential.

Bardeen and Shockley extended the idea to effective potentials which are generated by the change in the position of the band edges of the valence band maximum and conduction band minimum due to a gradually varying dilation [102]. Such a varying potential is referred to as the deformation potential and for cubic isotropic systems it is given by:

$$\lambda_{DP} = \frac{dE_{edge}}{d\delta_\alpha}, \tag{2.49}$$

where E_{edge} is the valence band maximum or conduction band minimum and δ_α is the uniaxial strain along the α direction, which is conveniently chosen to be in the direction of the lattice vector a and is defined as:

$$\delta_\alpha = \left.\frac{a - a_0}{a_0}\right|_{\alpha=a}, \tag{2.50}$$

where a_0 is the equilibrium lattice constant and a is the dilated lattice vector.

2.7.2 Effective mass

The presence of a periodic potential in solids makes particles respond to forces in a different manner when compared to the response of free particles in a vacuum. The effective mass (m^*) is a simplification which aims to compensate for this discrepancy by treating the electrons and holes as free particles but with modified masses.

The effective mass tensor is defined as:

$$\left(\frac{1}{m^*}\right)_{ij} = \frac{1}{\hbar^2}\frac{\partial^2 E_n(\mathbf{k})}{\partial \mathbf{k}_i \partial \mathbf{k}_j}, \quad i,j = x,y,z \tag{2.51}$$

where indices i and j denote the x, y and z directions in reciprocal space and $E_n(\mathbf{k})$ is the dispersion relation for a given electronic band with a number n. The distinction between holes and electrons comes from the sign of $E_n(\mathbf{k})$. Particles with negative mass are regarded as holes which are moving through a sea of electrons, similar to air bubbles in a bottle of water.

Depending on the axes' direction the effective mass can be longitudinal (m_l^*) or transverse (m_t^*). The averaging of the three directions is rather straightforward but depends on type of the calculation. For density of states calculations the effective mass is obtained via the geometric mean and is defined as:

$$m_{dos}^* = \sqrt[3]{g^2 m_l^* m_t^* m_t^*}, \tag{2.52}$$

where m_{dos}^* is the density of states effective mass and g is the number of conduction band minima, called valleys. Equation 2.52 reduces to $m_{dos}^* = m^*$ if the band gap is direct at the Γ-point. For conductivity calculations the harmonic mean is used to find the average. The conductivity effective mass (m_{cond}^*) is given by:

$$m_{cond}^* = \frac{3}{\frac{1}{m_l^*} + \frac{1}{m_t^*} + \frac{1}{m_t^*}}. \tag{2.53}$$

When calculating the effective mass of holes, one needs to consider that the energy levels at the top of valence band are often degenerate, which leads to the presence of a heavy holes (*hh*) band and light holes (*lh*) band. The nature of the holes is determined by the dispersion of the bands, with the flatter band being responsible for the heavy holes. Both *hh* and *lh* contribute to the scattering processes, hence a combined mass is needed in order to find τ. We know from Eqn. 2.47 and 2.48 that $\tau \propto 1/m^{*\frac{3}{2}}$ and that the relaxation time is a measure of the frequency of scattering events. Therefore, we can define the combined

effective mass as being equal to:

$$m_h^* = \left(m_{hh}^{*\frac{3}{2}} + m_{lh}^{*\frac{3}{2}}\right)^{\frac{2}{3}}, \tag{2.54}$$

where m_h^* is the effective mass of holes.

2.7.3 Elastic constants

According to Bardeen and Shockley, the mobility of electrons and holes in non-polar semiconductors and insulators is determined by interactions with the acoustic phonon branches in the system and by scattering due to impurities or other defects. In the limit where the doping is small and does not introduce a lot of impurities, classical rather than quantum statistics may be applied to the conduction electrons. In this case, the charge carriers interact only with acoustic phonon modes of comparably long wavelength. The properties of these phonon branches can be deduced from the elastic constants.

Given that the cubic elastic constants c_{11}, c_{12} and c_{44} are obtained from first principles, the values of c_{ii} along different directions of propagation can be expressed as:

$$\begin{aligned}
&(100) \quad c_{ii} = c_{11}, \\
&(110) \quad c_{ii} = \frac{1}{2}(c_{11} + c_{12} + 2c_{44}), \\
&(111) \quad c_{ii} = \frac{1}{3}(c_{11} + 2c_{12} + 4c_{44}).
\end{aligned} \tag{2.55}$$

For isotropic systems the discrepancy between c_{ii} values for different directions is relatively small and can be neglected when calculating the mobility. The shear modulus of a cubic system can also be calculated from the elastic constants [144]:

$$\begin{aligned}
G_V &= \frac{c_{11} - c_{12} + 3c_{44}}{5}, \\
G_R &= \frac{5(c_{11} - c_{12})c_{44}}{4c_{44} + 3(c_{11} - c_{12})}, \\
G_H &= \frac{G_V + G_R}{2},
\end{aligned} \tag{2.56}$$

where G_V and G_R are Voigt's [145] and Reuss's [146] approximations, respectively, and G_H is Hill's proposed mean arithmetic value of the former two to

reflect the real properties of the system [147].

The bulk modulus B of a cubic system is defined as [148]:

$$B_H = B_G = B_V = \frac{c_{11} + 2c_{12}}{3}. \tag{2.57}$$

In the cubic case the three approximations are equal to each other.

2.8 Future outlook for modelling electron-phonon coupling

The theoretical framework presented in this chapter is sufficient for the full scale modelling of thermoelectric materials from first principles. However, this does not mean that it cannot be improved or developed furthermore in order to predict thermoelectric results which depend less on cross-checks with experimental data.

Sections 2.7 and 2.6.3, which discuss the constant relaxation time approximation and the phonon-electron coupling, are excellent candidates for such improvements. In these cases, the interaction between charge carriers and lattice vibrations is either omitted or extracted from experimental data.

In a very recent study Sohier *et al.* [149] shows how the electron-phonon coupling (EPC) can be used with the electron Boltzmann transport equation (BTE) to obtain a value for the electron relaxation time. The EPC process is reminiscent of how phonons interact. For example, if a longitudinal vibration compresses or expands the lattice at a given point, the effective electrostatic potential at that point, which acts on electrons, is also changed. Thus, there exist the possibility of scattering [150]. The Sohier *et al.* approach works for 2D materials and is very analogous to the solution of the phonon BTE, as discussed in Section 2.4.2. Instead of the third-order force constant for the phonon solution, the electron transition rates ($P_{\mathbf{k}\mathbf{k}'}$) are computed from the EPC matrix elements. As a result, one can obtain the scattering time within the energy relaxation-time approximation (eRTA):

$$\frac{1}{\tau_{\mathrm{eRTA}}(\mathbf{k})} = \sum_{\mathbf{k}'} P_{\mathbf{k}\mathbf{k}'} \frac{1 - f^0(\mathbf{k}')}{1 - f^0(\mathbf{k})}, \tag{2.58}$$

where f^0 denotes an equilibrium distribution function for states $\mathbf{k}$ and $\mathbf{k}'$.

While elegant, the solution of Eqn. 2.58 is computationally demanding and not fully implemented in the various DFT codes as of writing. Once this obstacle

is overcome one will be able to use a more accurate model of the electronic τ, which depends on the chemical potential. In addition, the EPC contribution to the lattice thermal conductivity can also be included to the final results. All that will lead to a more realistic and rigorous full-scale modelling from first principles of the thermoelectric materials.

Chapter 3

Methodology

The computational workflow can be described as a staged process which involves obtaining properties of materials from an *ab initio* runs and then using them as an input in more specialised programs. This is done multiple times until all components of the thermoelectric 'figure of merit' equation are found.

This chapter will serve as a guide of how the study was conducted and how the results can be reproduced. It will present the software needed to solve the theoretical framework discussed in Chapter 2 and will highlight the key parameters or assumptions which were used in the working process.

3.1 Calculating the properties of materials from first principles

The density function theory (DFT) calculations in this project were performed with the CASTEP program, which is a leading code using a plane wave basis set to calculate the properties of materials from first principles [123]. CASTEP can simulate a wide range of properties of material proprieties including energetics, structure at the atomic level, vibrational properties, electronic response properties and many others.

3.1.1 Setting up a CASTEP calculation

To perform a DFT simulation with CASTEP one needs to create two input files. The first one is called *seedname.cell* and contains information about lattice vectors, ionic positions, symmetry operations, pseudopotentials, Hubbard U values and a Monkhorst-Pack **k**-points mesh [151], which can sample the Brillouin zone on an equally spaced grid or along a given path.

The second input file is called *seedname.param*. It is used to specify parameters like cut-off energy, exchange-correlation functional and other settings, which depend on the task and the system of interest. These could include specifications about optimisation methods, convergence criteria, spin polarisation, spin-orbit coupling, semi-empirical dispersion correction, etc.

3.1.1.1 Key convergence parameters

There are two key parameters which need to be converged extremely well when one starts investigating a new system. These are the cut-off energy and the **k**-point sampling.

Since the particles in the DFT calculation are in a periodically-repeating environment, the wavefunction in the Kohn-Sham equation can be written as a Bloch wave $\psi_{\mathbf{k}}(\mathbf{r}) = e^{i\mathbf{k}\cdot\mathbf{r}}u_{\mathbf{k}}(\mathbf{r})$, where $u_{\mathbf{k}}(\mathbf{r})$ is a periodic function with the same periodicity as the crystal. The periodic Bloch function can be expressed as plane waves in Fourier series $u_{\mathbf{k}}(\mathbf{r}) = \sum_{\mathbf{G}} c_{\mathbf{Gk}} e^{i\mathbf{G}\cdot\mathbf{r}}$, where **G** is a reciprocal lattice vector [132, 152]. In principle, an infinite number of **G** vectors is needed in order to obtain the precise form of the Bloch function. In practice, however, the coefficients $c_{\mathbf{Gk}}$ become small when **G** is large and the series can be truncated. Thus, we form a basis set with plane waves with wave vector lengths less than some maximum value of **G**. In calculations the basis set is input in terms of an energy cut-off value which is the energy of an electron in a periodic box as the unit cell and a plane wave wavefunction with wave vector of length **G** maximum, i.e. $E^{cut} = \frac{\hbar^2}{2m}|\mathbf{G}|^2$.

Therefore, when we define a cut-off energy in the calculation, we set a maximum value for **G**. The usual way of checking if the truncation of the Fourier series is good enough is to expand the number of the included Fourier components by increasing the cut-off energy and check that little is affected. As a rule of thumb the cut-off energy is considered converged when the change in the energy of the system per atom is less than a couple of meV.

Calculations also require integrating the periodic functions of the Bloch wave vector **k** over the entire Brillouin zone, i.e. the specific region of reciprocal-space which is closest to the origin. However, it is possible to use only a finite number of **k**-points if these are selected in a way which appropriately samples the reciprocal space. The Brillouin zone in CASTEP is sampled via a Monkhorst-Pack **k**-points mesh (an evenly spaced grid) [151]. The number of **k**-points is gradually converged by increasing the density of the grid. The convergence criterion is the same as for the cut-off energy and the **k**-points sampling is considered sufficient when the change in the energy of the system

per atom is less than a couple of meV.

3.1.1.2 Periodic boundary conditions and cell size

CASTEP uses periodic boundary conditions and infinite systems are approximated to a small part called a *unit cell*. Using periodic boundary conditions means that particles are enclosed in a box, which is virtually replicated to infinity by rigid translation in all directions, completely filling the space. However, only the particles in the box are effectively simulated. In the presence of defects or surfaces, finite size effects can occur. This means that defects or surfaces can interact with their own virtual copies. Such an effect can be reduced by increasing the defect-defect distance or the vacuum distance between surfaces.

In terms of defects, the usual approach involves creating a *supercell*, which contains the defect surrounded by a region of bulk crystal. Due to boundary conditions the new super structure contains an array of defects rather than a single defect. It is important to include enough bulk solid in the supercell to prevent the defects in neighbouring cells from interacting with each other [152]. Although it seems that a bigger supercell will guarantee 'better' results, that is not always the case. The convergence of defect calculations in supercells needs to be done methodically [153]. This includes converging carefully the cut-off energy and the **k**-points grid with respect to the quantity which is being measured, i.e. defect formation energy or forces between atoms. It is also considered that the best systematic way to treat defects is to consider the defect density for each different supercell symmetry separately as it can have a directionality effect. Once the symmetry with the best convergence is found, the next step relies on geometry optimisation. If the defect is isolated from its virtual copy, then there should be a region in the supercell where the structure is bulk-like. We can assume that neighbouring atoms form shells around the defect. In that way, we can assess the convergence of the defect structure by considering the relative displacement of successive shells of atoms in a fixed volume calculation. If the displacement between the relaxed and unrelaxed defect systems of the largest allowed shell, i.e. the one which is equidistant from the defect and its virtual copy, is larger than some predefined tolerance, then a bigger supercell is needed.

In terms of surfaces and thermoelectric calculations, and in addition to the methodical approach discussed above, one might check how the density of states are affected by the size of the vacuum region. It is important that the vacuum regions are wide enough so that faces of adjacent crystal slabs do not interact across the vacuum in a way which affects the thermoelectric properties.

3.1.2 Types of DFT calculations

The type of the DFT calculation, called 'task' in CASTEP, is specified in *seedname.param*. Here we will focus mainly on the tasks which are relevant to computing the electronic thermoelectric properties: energy and force calculations, geometry optimisation and spectral calculations.

3.1.2.1 Energy calculations

The procedure for self-consistent electronic minimisation in CASTEP is similar to the one described in Fig. 2.1 in Section 2.1. The old and new density are mixed until the change in the total energy reaches the convergence criteria. This type of calculation is performed at the start of every run before initialising another task. It is also used on its own when one starts investigating a new material. Then the cut-off energy and the **k**-point sampling are converged by running a set of simple total energy calculations. Both parameters are considered well converged when the total energy varies less than a few milli-electron volts per atom.

The benefit of the energy runs is that they are relatively cheap and allow the user to investigate a snapshot of the crystal structure. Thus, one can compare energies between different experimental configurations, screen for possible doping sites or check structural stability.

In terms of thermoelectric properties, computing the total energy for a range of different volumes can allows us to calculate the lattice thermal conductivity via the quasi-harmonic approximation as discussed in Section 2.5. This can be done with the help of the Gibbs2 program by fitting an equation of state to the precomputed data [137]. The energy calculations can also be used to analyse the forces between atoms in different perturbed configurations and obtain the third-order force constants, which are crucial for solving the phonon Boltzmann transport equation.

3.1.2.2 Geometry optimisation

Geometry optimisation is used to refine the lattice parameters and ionic coordinates of a crystal structure. The essence of the calculation is for the ions and electrons in the supercell to be moved around step-wise until the forces on the atoms and the change in total energy between steps fall below some predefined convergence tolerance. The ionic positions are optimised using quasi-Newton methods, which are a class of hill-climbing optimisation techniques that seek

a stationary point of a function. The curvature of the function is described by a square matrix of second-order partial derivatives, which is called a Hessian matrix.

The geometry optimisation process involves moving ions into new positions by using a geometry optimisation algorithm. Then the electronic configuration is optimised using conjugated gradients method, an algorithm for the numerical solution of particular systems of linear equations. Afterwards the total energy of the system is compared with previous configurations and it is checked if forces fall within the predefined tolerance limits. If the structure is not optimised, the process returns to the starting point and generates a new set of ionic positions. This cycle is performed until the forces fall within the tolerance limit and the energy should then be at a local minimum.

The geometry optimisation algorithms used in this project are the Broyden-Fletcher-Goldfarb-Shanno (BFGS) algorithm [154] and its limited memory version LBFGS [155]. BFGS was the default algorithm until CASTEP v18. It uses the fractional atomic positions and cell strains as the variables for optimisation. It looks for a state of minimum enthalpy (fixed cell) or zero force and stress (variable cell). BFGS allows for both variable and fixed cell calculations. While BFGS is reasonably fast and robust, it can require a lot of memory for large systems and therefore the limited memory version LBFGS is the default choice from CASTEP v18 onwards.

In terms of thermoelectric calculations, structures which are not geometry optimised could lead to instability when calculating lattice dynamics or unrealistic charge carrier mobility when computing the electron relaxation time. It is important to note that the crystal structure should be relaxed whenever the exchange-correlation functional or the pseudopotentials need to be changed.

3.1.2.3 Spectral calculations

The spectral task in CASTEP allows the user to take the converged wavefunction, as described in Section 3.1.2.1, and use it to compute the eigenstates on a denser **k**-points grid for a density of states (DOS) calculation or along a specified path for a band structure calculation. The calculated eigenvalues and **k**-points coordinates are placed in a file called *seedname.bands*, which requires further post-processing.

Band structure

The band structure is calculated along a path of high symmetry points which are defined in *seedname.cell*. The visualisation of *seedname.bands* and the type of the band gap are done by the Perl script *dispersion.pl*, which is distributed as part of the CASTEP package. The band structure calculation is crucial in determining the electron relaxation time by computing the deformation potential of the system and the effective mass of the charge carriers.

Density of states

Density of states are computed similarly to the band structure but on an equally spaced **k**-points grid rather than a path. The post-processing needs to be more sophisticated and can be done with a program called OptaDOS [156]. It is a code for calculating optical, core-level excitation spectra along with full, partial and joint electronic density of states (DOS). One of the nice features of the program is the adaptive DOS broadening. This means that OptaDOS adds weight to the states depending on how localised they are, i.e. flat bands yield more states than dispersive ones. Thus, allowing for better DOS plots with a coarser **k**-points sampling. OptaDOS can also report the type of the band gap, its magnitude and the position of the valence band maximum and conduction band minimum.

For this project, we are interested in the full and partial density of states since it allows us to see the type of the material, predict some of its thermoelectric properties and see which atomic species are responsible for the electronic transport. In terms of thermoelectric calculations, CASTEP density of states data are used as an input for the program which solves the electron Boltzmann transport equation.

3.2 Computing the electronic thermoelectric properties

The program which was used to compute the electronic thermoelectric properties is called BoltzTraP [100]. The Seebeck coefficient, electronic thermal conductivity and electrical conductivity are obtained within the constant relaxation time approximation by solving the Boltzmann transport equation. The program relies on smooth Fourier interpolations of the band energies. Group

velocities are calculated as derivatives of the energies; therefore, the band energies must be well resolved. This could be achieved only if a very dense **k**-points grid is used in density of states calculations.

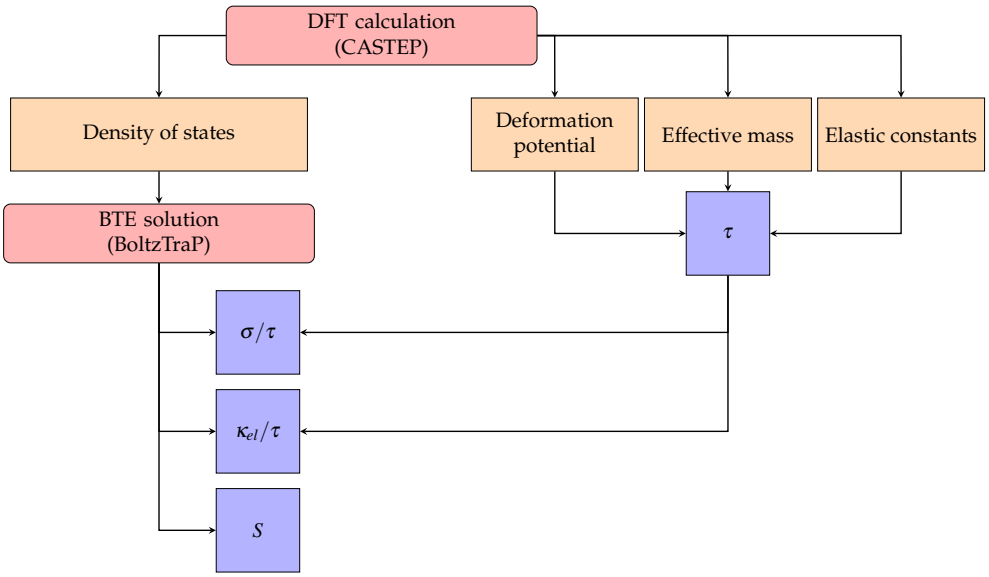

Figure 3.1: Workflow for calculating the electronic thermoelectric properties. Red boxes illustrate different type of software used, orange boxes show the intermediate stages and blue boxes show final results.

Figure 3.1 summarises the workflow for obtaining the electronic thermoelectric properties. BoltzTraP is interfaced with CASTEP via a Python script called *castep2boltz.py*. Both the script and the program can handle spin-polarised and spin-orbit coupling cases. The prerequisites for the script are the eigenenergies from *seedname.bands* and the crystal structure from *seedname.castep*. The latter informations is used to harness the symmetry operations of the system. Settings needed for obtaining the thermoelectric properties in the left section of Fig. 3.1 are discussed below, while the computation of the relaxation time is explained in Section 3.3.

3.2.1 Performing a BoltzTraP calculation

BoltzTraP input parameters are defined in a file called *seedname.intrans* and the user can tweak them to their preference. The most common parameters which need modification include the temperature range, temperature step and doping levels. In BoltzTraP the term 'doping' refers to chemical doping. Instead of adding electrons to the simulation, the program calculates the electron thermoelectric properties for a given energy level which corresponds the Fermi energy if the system had a given amount of additional of electrons or holes.

One of the special BoltzTraP features which is implemented in the program is

the possibility of adding a scissors operator when solving the BTE. first principles calculations often predict an unrealistic band gap. Thus, the ability to manually set the band gap size becomes very useful for testing different scenarios, especially for materials for which there is no definite agreement between theory and experiments, e.g. Fe_2VAl full-Heusler alloys.

The last feature worth discussing is the ability to add a relaxation time estimate to the calculation. Such calculations were not performed in this project since it would have required including experimental data. However, the development of the field along with the discussed in Section 2.6.3 electron-phonon coupling, would enable more accurate estimates of the relaxation time from first principles. Thus, the ability to include relaxation time values to the BoltzTraP calculation will become extremely useful.

3.2.2 Successor of BoltzTraP

It is worth pointing out that BoltzTraP was superseded in 2018 by a newer version called BoltzTraP2 [103]. The new code is distributed as a free Python3 library and offers all features of the old program but is better prepared to visualise output data. It can also load relaxation time values obtained via the electron-phonon coupling for each individual eigenstate. BoltzTraP2 does not rely on external interfaces to work with other DFT codes. Instead internal loaders are used to analyse the input intelligently and decided how the data need to be loaded. CASTEP is part of the supported programs and can be used along with BolzTraP2 but for consistency purposes all calculations in this project were performed with the first version of BoltzTraP.

3.3 Computing the relaxation time

The electron relaxation time (τ), present in the right section of Fig. 3.1, is calculated using the deformation potential theory, which is discussed in Section 2.7. The deformation potential is obtained from a set of band structure calculations in which the energy values of the valence band maximum (VBM) and conduction band minimum (CBM) are measured when the unit cell is dilated or contracted along one direction. Elastic constants are computed with the help of two scripts *generate_strain.py* and *elastics.py*, which are distributed with the CASTEP software. The first script generates a set of *seedname.cell* files deformed according to the appropriate strain pattern. Each .cell file corresponds to a different CASTEP calculation. Once all calculations are done, the second

script can extract the forces between atoms and estimate the elastic constants.

3.3.1 Effective mass effects

The effective mass of the charge carriers is computed with the help of an external program called 'Effective mass calculator' (EMC) [157], which was modified to work with CASTEP. The program uses finite difference method to evaluate energy derivatives numerically. It calculates the derivatives from a 3- or 5-point stencil around a given **k**-point. Therefore, the code requires as an input the VBM or CBM **k**-point coordinates, the respective band index and the spacing between the **k**-points in the pattern. Once the list of **k**-points is generated, the user needs to include it in the *seedname.cell* file and perform a band structure calculation. Once the calculation is done, the EMC code is used again to estimate the charge carrier effective mass.

There are two aspects of the calculation which need to be considered carefully. The first one is the spacing between the **k**-points in the pattern. It is not a bad practice to test several values and check how the parabola described by the pattern points matches the shape of the whole band in the band structure. If the spacing is too small, the charge carriers will be too light. If the spacing is tto wide, the charge carriers will be too heavy The second parameter worth paying attention to is the band index. If the input unit cell is not an elementary unit cell, then band folding will be present. As a result, light hole band and heavy hole band need not be next to each other in terms of indices.

3.3.2 Drawbacks of constant relaxation time approximation

Despite being the most widely used approach, there are some drawbacks to the present τ scheme, which need to be mentioned. The most prominent one is the lack of dependence on the chemical potential. Regardless of the doping levels, the relaxation time remains constant. This further highlights why implementing ways for obtaining τ from the electron-phonon coupling is considered very important. In addition, current models do not consider how point defects and grain boundaries affect the movement of the electrons. Including all defects directly to the DFT calculations would make them very expensive.

3.4 Lattice thermal conductivity

The software package used to calculate the lattice thermal conductivity (κ_{latt}) is called ShengBTE [114]. It can solve the Boltzmann transport equation for phonons by knowing the second- and third-order force constants of the system. The program computes converged sets of phonon scattering rates and uses them to obtain κ_{latt} along with other related quantities, such as the relaxation time and Grüneisen parameter. ShengBTE harnesses the symmetries of the system to make calculations more efficient and is able to deal with isotropic as well as anisotropic crystals. Additionally, the ShengBTE implementation does not rely entirely on the constant relaxation time approximation, but rather uses an iterative method for finding the phonon τ. The theoretical explanation is given in Section 2.4.2.

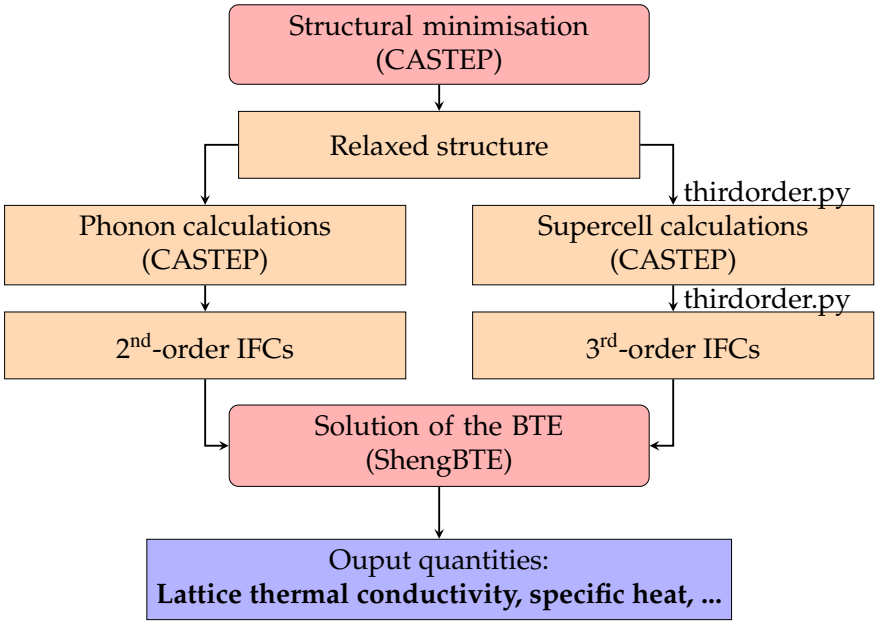

Figure 3.2: Workflow for thermal conductivity calculations using a real-space supercell approach for force constants. Red boxes represent starting points for DFT and BTE calculations, orange boxes show the intermediate stages, computer programs are denoted in brackets and blue boxes show the final output. The script thirdorder.py is part of the ShengBTE program.

The computation workflow for obtaining the lattice thermal conductivity is given in Fig. 3.2. Here we will discuss the input settings needed by ShengBTE, while the methodology for obtaining the force constants is discussed in the next two subsections.

ShengBTE and CASTEP are linked with a program called *castep2shengbte.py*. It is a Python script which creates two files – one with control settings and one containing second-order force constants. The control file contains information about the crystal structure, phonon **q**-point grid, referred as supercell,

temperature steps and range, number of ShengBTE integration grid planes and a parameter called *scaleboard*. One of the computational tricks used in ShengBTE is that Dirac delta distributions arising from conservation of energy can be approximated by a Gaussian function. The Gaussian smearing is controlled by the *scaleboard* parameter. According to the authors the default value ($scaleboard = 1$) is theoretically guaranteed to work, but significant speedups can sometimes be achieved by reducing it. Literature results, even for the same material, should be analysed carefully without knowing the *scaleboard* value since it represents a compromise between speed and accuracy. The other parameter which affects the speed of the ShengBTE run is the number of integration grid planes. This is analogous to the **k**-points mesh in CASTEP and also needs to be converged systematically.

3.4.1 Modelling second-order interatomic force constants

In this section we will follow the process of calculating the second-order force constant with CASTEP. It was discussed in Section 2.1.2 that the dynamical matrix can be obtained in several ways. CASTEP contains implementations of both the finite-displacement supercell approach and the density-functional perturbation theory method. In either case, having a fully relaxed crystal structure is absolutely mandatory, otherwise the phonon calculation might fail to complete or phonon frequencies might indicate mechanical instability.

3.4.1.1 Finite-displacement supercell approach

The finite-displacement approach is based on displacing the atoms by a small amount from their equilibrium position and numerically differentiating the forces between them. The condition that the displacements are necessarily periodic with the simulation cell makes only the phonons at the Γ-point meaningful. This limitation in reciprocal space can be overcome by increasing the size of the system in real space, hence using a supercell. The size of the supercell is guided by how quickly the force constant matrix decays with respect to interatomic distance. The assumption is that after a given cut-off radius R_c the force constants are small and can be neglected. Due to periodicity, the size of the supercell L needs to be $L > 2R_c$, where it is the best to imagine that a virtual sphere with a radius R_c illustrates the range of the force constants. Therefore, a cubic supercell is the best option for capturing the most interactions in the smallest volume possible.

The computational workflow includes includes two key steps. The first one,

as already mentioned, is to relax the crystal structures. The second step is to decide the size of the supercell. It is preferable to start with a big supercell calculation as CASTEP allows you to later decrease the cut-off radii, test different values and determine if a smaller supercell is also usable. In general, the drawback of the supercell approach is that even a small primitive unit cell of 2 atoms, would result in a relatively big supercell, i.e. a $4 \times 4 \times 4$ supercell will contain 128 atoms. Transforming a non-cubic cell to a cubic one could also increase the number of atoms. In general, DFT calculations scale as $O(N^3)$, where N is the system size, and the computation time can become extremely long.

3.4.1.2 Density-functional perturbation theory method

Alternatively, one could use the density-functional perturbation theory (DFPT) method to calculate the force constants. Unlike in the finite-displacement approach, here we compute the response wavefunction ($\frac{d\Psi}{d\lambda}$), where λ is atomic displacement. One of the benefits of DFPT, as implemented in CASTEP, is that one can calculate phonon modes at the Γ-point and elsewhere equally easy [158]. The calculation is performed by adding a list of **q**-points to the *seedname.cell* file, without generating a supercell. In this case, the **q**-points grid defines the cut-off range of the interatomic interactions. For example, the force constants computed on a $4 \times 4 \times 4$ **q**-point grid using the DFPT method are equivalent to the force constants obtained in a $4 \times 4 \times 4$ supercell using the finite-displacement approach. In this project the DFPT method was employed for computing the second-order force constants.

In terms of scaling, having more **q**-points is better than having more atoms in the simulation cell. Nevertheless, calculations aside from the Γ-point are more demanding due to decreased symmetry. The DFPT method also requires using norm-conserving pseudopotentials. Inside a certain core cut-off radius, where the pseudized part of the potential is, the norm of each pseudo-wavefunction needs to be identical to its corresponding all-electron wavefunction. The wavefunction is varying very quickly when the potential is very attractive, i.e. close to the nuclei, which means that large **G** components (discussed in Section 3.1.1.1), are needed to describe this region of space. Therefore, the DFPT method requires a higher plane wave basis set cut-off energy, which increases furthermore the computational cost. As a result, it becomes impractical to use a very dense **q**-points grid due to the norm-conserving pseudopotentials. The other types of calculations in this project can be performed with ultrasoft pseudopotentials, which relax the norm-conserving constraint, and thus require a smaller **G** and lower cut-off energy.

In a solid, the interactions between atoms have a finite range and decay rapidly to zero. Specifically, the elements of the force constant matrix in Eqn. 2.7 decrease as $1/r^5$ with interatomic distance [159]. A pragmatic way of checking the convergence of the interatomic force constants is by comparing the phonon dispersion and density of states curves for different **q**-points grids. Whenever qualitative changes stop occurring, it can be concluded the force constants are converged. Figure 3.3 shows an example of how the dispersion curve of NbFeSb converges when the density of the **q**-points mesh is gradually increased. The unconverged force constants on the $2 \times 2 \times 2$ mesh are often being used in the literature [109, 160], which highlights that in some cases accuracy sacrifices need to be made due to the computational costs.

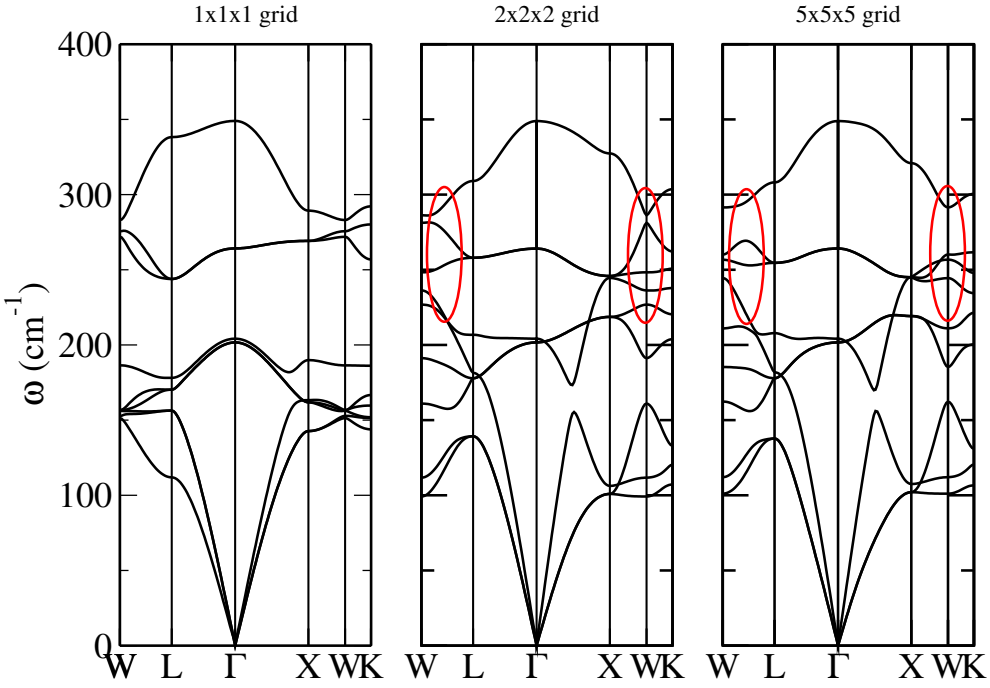

Figure 3.3: Illustration of how the phonon dispersion of NbFeSb gradually convergences when the **q**-points mesh is increased from a $1 \times 1 \times 1$ to $5 \times 5 \times 5$ grid. Notice the differences in the W-L regions (red ellipses) between the $2 \times 2 \times 2$ and $5 \times 5 \times 5$ meshes despite both data sets being Fourier interpolated on a similar denser grid.

A detailed dispersion, like in Fig. 3.3, or density of states plot requires thousands of **q**-points, which contradicts the fact that we are using a relatively coarse grid. The quickly decaying force constants and the smoothly varying phonon frequencies with a wavevector **q** allow CASTEP to use Fourier interpolation to generate dynamical matrices on an arbitrarily fine grid or line sample in reciprocal space. Thus, it becomes possible to obtain high quality results on a coarse **q**-point grid.

3.4.2 Computing the anharmonicity of the system

The third-order force constants are computed using the finite-displacement supercell approach. The calculation process is as follows. A program called *thirdorder.py*, part of the ShengBTE suite, creates a set of supercells containing atoms with perturbed positions. Then CASTEP computes the forces between atoms in all possible configurations in separate runs by using an energy calculation, as explained in Section 3.1.2.1. Afterwards, *thirdorder.py* gathers the forces from the CASTEP output and constructs the third-order force constants. It should be noted that the default energy tolerance for the electronic minimisation in the energy calculations must be reduced below the default value and set on par with the default value used in the DFPT calculations. Otherwise, noise will dominate the third-order force constants.

All aspects of the supercell approach discussed in Section 3.4.1.1 still need to be considered. The advantages here are that third-order force constants are expected to decay even quicker, hence, a smaller supercell is required. Having multiple independent configurations means that parallelisation on a supercomputer can be done very easily. CASTEP also allows reusing the equilibrium electron density as a starting point for new runs, which can reduce the computation time by 20%. As an example and in terms of CPU time, 15k CPU hours are needed for the computation of the second-order force constants of NbFeSb with the conventional cubic cell, while the third-order force constants require 12k CPU hours. A similar system but with a reduced symmetry ($Nb_{0.25}Ta_{0.75}FeSb$) requires 45k and 36k CPU hours for the second- and third-order force constants, respectively. There are a couple of drawbacks when computing the third-order force constants with the finite-displacement supercell approach and an external program. For example, *thirdorder.py* neglects the symmetries in some cases which leads to a few identical runs in the set. There is also no easy way of going for one big calculation and then checking how the force constants change by decreasing the interaction cut-off radius. At the end, computing third-order force constants of a small system can prove even more computationally demanding than calculating its second-order force constants. Nevertheless, obtaining such set of results is fundamental for the accurate modelling of the intrinsic lattice thermal conductivity from first principles.

3.5 List of developed software

This section discusses the developed software as part of the research. A short summary is presented in Table 3.1. The table footnotes provide links to the

Table 3.1: Summary of developed scripts and loaders.

Interface name	Short description	Code snippets
castep2boltz.py[1]	CASTEP to BoltzTraP interface	Listing B.1
castep2shengbte.py[2]	CASTEP to ShengBTE interface	Listing B.2
castep2almabte.py[3]	CASTEP to almaBTE interface	Listing B.3
thirdorder_castep.py[4]	Script for computing 3rd-order force constants with CASTEP. Part of the *thirdorder.py* package	Listing B.4
gb2shengbte.py[5]	Computes grain boundaries effect on lattice thermal conductivity	Listing B.5
CASTEP loader for *emc.py*[6]	Function which allows using *emc.py* with CASTEP	Listing B.6
CASTEP loader for BoltzTraP2[7]	Added CASTEP support for Python3 module BoltzTraP2	Listing B.7

[1] https://github.com/ganphys/castep2boltz
[2] https://github.com/ganphys/castep2shengbte
[3] https://github.com/ganphys/castep2shengbte/blob/master/castep2almabte.py
[4] https://bitbucket.org/sousaw/thirdorder/src/master/thirdorder_castep.py
[5] https://github.com/ganphys/castep2shengbte/blob/master/gb2shengbte.py
[6] https://github.com/afonari/emc/blob/master/emc.py
[7] https://gitlab.com/sousaw/BoltzTraP2

webpage of the every program. Examples with code snippets are given as listings in Appendix B.

The *castep2boltz.py*, *castep2shengbte.py* and *castep2almabte.py* scripts were written by me. They allow CASTEP users to compute the desired transport properties with CASTEP and the BoltzTraP, ShengBTE and almaBTE programs. Parts of the scripts are shown in Listings B.1, B.2 and B.3.

The *thirdorder_castep.py* interface is now part of the *thirdorder.py* package, which can compute the third-order force constants using the finite-displacement supercell approach. I wrote the following functions in the CASTEP interface: 'read_CASTEP_cell', 'gen_CASTEP_supercell', 'write_CASTEP_cell' and 'normalize_CASTEP_supercell'. The rest of *thirdorder_castep.py* script along with the 'read_forces' and 'build_unpermutation' functions was also adapted by me to work with CASTEP. Example of 'gen_CASTEP_supercell' can be seen in Listing B.4.

I wrote a short program *gb2shengbte.py* which estimates the effect of grain boundaries on the lattice thermal conductivity as computed by ShengBTE. The program code is shown in Listing B.5.

The *emc.py* is an effective mass calculator which was developed by Alexandr Fonari and Christopher Sutton [157]. The function 'parse_bands_CASTEP' in the *emc.py* script was written by me. It adds support for CASTEP. The part of

the effective mass calculator which contains the CASTEP loader is shown in Listing B.6.

BoltzTraP2 is a Python3 module which can be used to solve the Boltzmann transport equation for electrons. The CASTEP loader for BoltzTraP2 was written by me. The loader includes the 'CASTEPLoader' class and the functions '_get_CASTEPsystemname', 'read_CASTEP_bands' and 'read_CASTEP_output'. An example of 'CASTEPLoader' and '_get_CASTEPsystemname' is given in Listing B.7.

Chapter 4

Computing the electronic thermoelectric properties of Heusler alloys

4.1 Background

Fe_2VAl is a full Heusler-type intermetallic compound which has been extensively studied as a potential thermoelectric material due to its ecologically friendly properties and earth abundance of Fe, V and Al [161–164]. Fe_2VAl alloys have a very large power factor comparable to some of the best thermoelectrics, e.g. Bi_2Te_3. However, their thermal conductivity, which is about 10 times higher than Bi_2Te_3, results in a small thermoelectric figure of merit (ZT) [54, 165]. The high thermal conductivity of Fe_2VAl is phonon dominated and provides much room for improvement of ZT, hence several theoretical and experimental studies which aim to optimise the thermal conductivity (κ) as well as the Seebeck coefficient (S) and electrical conductivity (σ) have been conducted in the past two decades [162, 163, 166–168].

The majority of the thermoelectric properties can be calculated from the density of states (DOS), the conductivity tensor and the group velocity of the electrons [100]. Therefore, it is important to obtain a proper electronic structure in order to calculate the transport properties correctly. In the case of Fe_2VAl, bulk band structure calculations [166, 169–174] consistently predict the presence of an *indirect* pseudo band gap at the Fermi level. In contrast to these predictions, experimental measurements of Fe_2VAl alloys show typical behaviour for *direct* band gap semiconductors with hole carriers. Photoelectronic spectroscopy [161, 175] and optical conductivity measurements [176] confirm the existence of a pseudo band gap without taking into account the $\mathbf{k}$-dependence

and hence cannot distinguish between direct and indirect gaps. These studies show that the widely accepted and theoretically predicted level of E_F in the band structure of Fe_2VAl cannot explain both the experimentally measured hole carrier concentration [177] and the lack of temperature dependence in optical conductivity [176]. Moreover, recent ARPES measurements of off-stoichiometric Fe_2VAl alloys mapped the **k**-dependence and showed that no conduction bands are crossing the Fermi level at the X high symmetry point in the irreducible Brillouin zone [178], once again disagreeing with the theoretically predicted band structure [171, 172, 174, 179, 180].

In addition, current theoretical band modelling underestimates the maximum value of the Seebeck coefficient and cannot explain its asymmetry with respect to doping [166]. Several studies have tried to explain the magnitude of S (for both n- and p-type doping) by modifying the electron-electron exchange-correlation functional [171] or by including the Hubbard U [172]. In all cases the calculations failed to model the asymmetric behaviour of the Seebeck coefficient and thus overestimated the maximum value of S for p-type semiconductor. In this work, we show that conduction bands responsible for the p-type behaviour of Fe_2VAl come from Fe rather than V, and as a result the experimentally measured values of the Seebeck coefficient can be reproduced. This is accomplished only if a larger Hubbard U term is added to V than to Fe. We also thoroughly investigate the band structure of Fe_2VAl, describe how the bands fold when the size of the simulation cell is changed and demonstrate how an apparent lack of periodicity in the conduction bands can be removed by the inclusion of the Hubbard U. Also, the Hubbard U model can predict the asymmetry in the Seebeck coefficient, i.e. the dependence of S on the chemical potential.

4.2 Calculations setup

4.2.1 Crystal structure of Fe_2VAl

Heusler alloys have chemical formula X_2YZ, where X and Y are transition metals and Z is a main group element. Calculations were performed on the ordered $L2_1$ structure of Fe_2VAl, which is shown in Fig. 4.1. The structure is face-centred cubic, having space group $Fm\bar{3}m$ (225). There are four Fe_2VAl formula units (f.u.) in the cubic unit cell, with Fe atoms reside at (1/4, 1/4, 1/4) and (3/4, 3/4, 3/4), Al at (1/2, 1/2, 1/2) and V at (0, 0, 0). A primitive rhombohedral unit cell, which contains 1 f.u., can be extracted from the cubic cell. Bulk properties of Heusler alloys are usually calculated with a primitive unit cell,

whereas doped systems are investigated with a supercell in order to obtain the desired doping concentration.

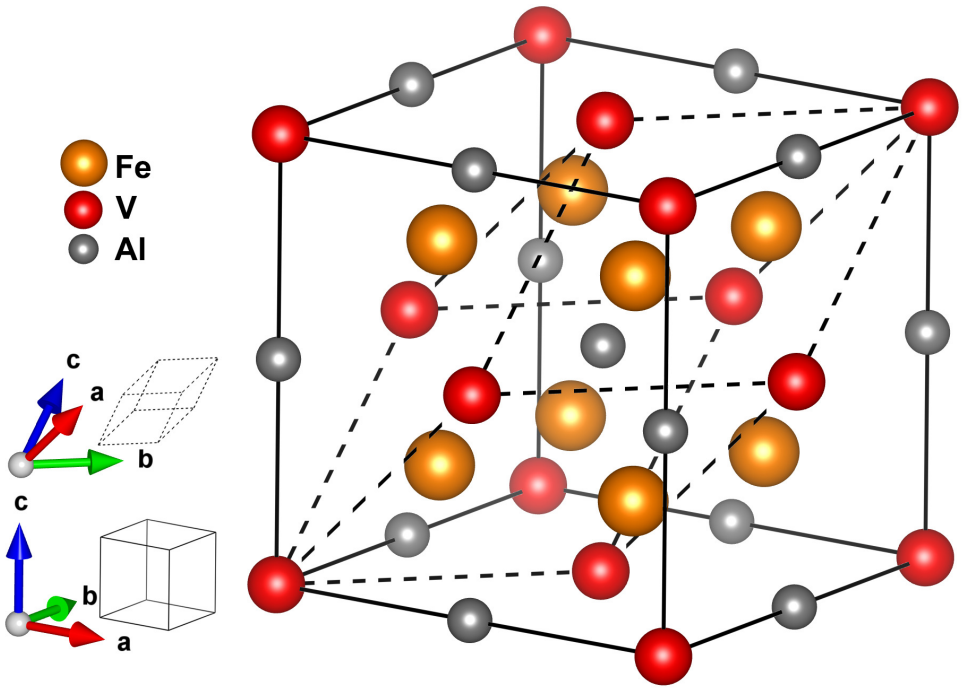

Figure 4.1: Schematic of the cubic (solid lines) and rhombohedral (dashed lines) Fe_2VAl unit cell. Fe atoms (orange) reside at (1/4, 1/4, 1/4) and (3/4, 3/4, 3/4), Al (grey) at (1/2, 1/2, 1/2) and V (red) at (0, 0, 0).

4.2.2 Density functional theory calculations settings

The first principles calculations were performed with the CASTEP [123] code and a GGA-PBE exchange-correlation functional [126]. On-the-fly ultrasoft pseudopotentials (C9 set) were used with a plane-wave cut-off energy of 700 eV with a grid scale of size 2.0. The Brillouin zone was sampled using a MonkhorstPack [151] grid with a $24 \times 24 \times 24$ **k**-points mesh (equivalent to **k**-points spacing of 0.013 2πÅ^{-1}) for the rhombohedral unit cell. Spin-orbit coupling was included for the rhombohedral cells but did not influence the final results significantly and therefore was not considered for the other cases. The structure was fully optimized until pressure and energy were converged to 0.01 GPa and 0.02 meV/atom, respectively. Transport properties were calculated using the semi-classical Boltzmann transport formalism as implemented in the BoltzTraP code [100]. The eigenenergies required for the transport properties were calculated with a $48 \times 48 \times 48$ **k**-points mesh. Density of states (DOS) and partial density of states (PDOS) were analysed using the OptaDOS code [156].

4.2.3 Theoretical expectations

Theoretically, the relation between the thermoelectric figure of merit, ZT, and S, σ, and κ, is given by Eqn. 4.1:

$$ZT = \frac{S^2 \sigma T}{\kappa}. \tag{4.1}$$

One of the requirements for a good thermoelectric material is the presence of a rapid change in the density of states across the Fermi level (E_F). This could be explained with the formula for the Seebeck coefficient S (T) for metallic systems at a given temperature T [181]:

$$S(T) = \frac{\pi^2 {k_B}^2 T}{3(-e)} \left(\frac{\partial \ln \sigma(E)}{\partial E} \right)_{E=E_F}. \tag{4.2}$$

Considering that the electrical conductivity $\sigma(E)$ is proportional to the density of states, $N(E)$, it could be shown with Eqn. 4.2 that a steep slope, $\partial N(E)/\partial E$, near E_F, would result in a large Seebeck coefficient and better ZT. Thus, semiconductors whose DOS varies rapidly on either side of the band gap are considered as promising candidates for efficient new thermoelectric materials.

4.3 Electronic structure

We start by presenting the electronic properties and band structure of Fe_2VAl using a primitive rhombohedral cell without the inclusion of the Hubbard U on any of the atoms. After relaxation, the optimized lattice constant of the primitive rhombohedral cell was found to be 4.03 Å (equivalent to 5.70 Å for a cubic cell). The obtained lattice constant is smaller than the experimental value of 5.76 Å [161, 180] by 1%, similar to other DFT studies [166, 169, 179]. Spin-polarised calculations showed that Fe_2VAl is nonmagnetic, in good agreement with other theoretical [175, 182] and experimental [161, 169] studies.

Fig. 4.2(a) and (b) show the band structure of Fe_2VAl in the irreducible Brillouin zone and the contribution of the V and Fe d-orbitals to the total DOS near E_F, respectively. Fig. 4.2(a) shows the small overlap between the bottom of the conduction band (X-point) and the top of the valence band (Γ-point), which is typical for semimetals. The small indirect overlap between them leads to the formation of a pseudo band gap with a magnitude of -0.13 eV, in good agreement with other DFT studies [166, 169, 179, 183]. Fig. 4.2(b) illustrates several important points. First, states below E_F are due to Fe d-orbital

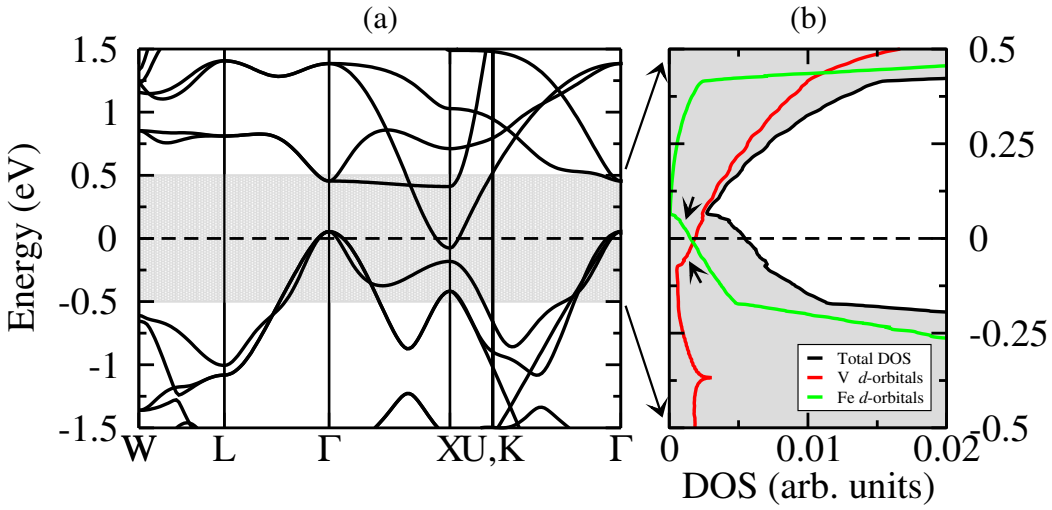

Figure 4.2: Band structure of Fe_2VAl (a) and the contribution of Fe and V *d*-orbitals to the total DOS near the Fermi level (b). The small arrows in (b) show the symmetry problem.

electrons, whereas states above E_F are mainly due to V *d*-orbital electrons. Secondly, the change of DOS near E_F is symmetric, illustrated by the arrows in Fig. 4.2(b). According to Eqn. 4.2 this symmetry would also be imposed on the Seebeck coefficient, consistent with previous theoretical predictions [166]. This predicted symmetry is contrary to the experimentally observed asymmetry of S [54]. Therefore, the similarity in the dispersion of the valence and conduction bands in Fig. 4.2(a), which is also responsible for the change in DOS near E_F, does not correspond to experimental results [163, 184].

4.4 Lack of periodicity in conduction bands and a possible solution

It has been argued in the literature that doping Fe_2VAl changes the position of the pseudo band gap [166, 167]. Next we show that the shift of the pseudo gap is not a result of doping but merely a consequence of the change of the size of the simulation cell. Fig. 4.3 presents (i) the band structure of the primitive rhombohedral cell along the W-X-L-Γ-X-W path, (ii) the band structure obtained with a cubic cell and (iii) a $2 \times 2 \times 2$ rhombohedral supercell. The band structure in Fig. 4.3(ii) can be obtained from Fig. 4.3(i) by folding the right X-point onto the Γ-point and overlaying the X-W section on top of the new Γ-X section. The R-Γ region in Fig. 4.3(ii) can be obtained by folding the W-X-L-Γ section along the L-point towards the Γ-point so that the X-point goes again on top of the Γ-point. The band structure in Fig. 4.3(iii) is obtained by folding the R-Γ section in Fig. 4.3(ii) to the right and overlaying an X-K region from

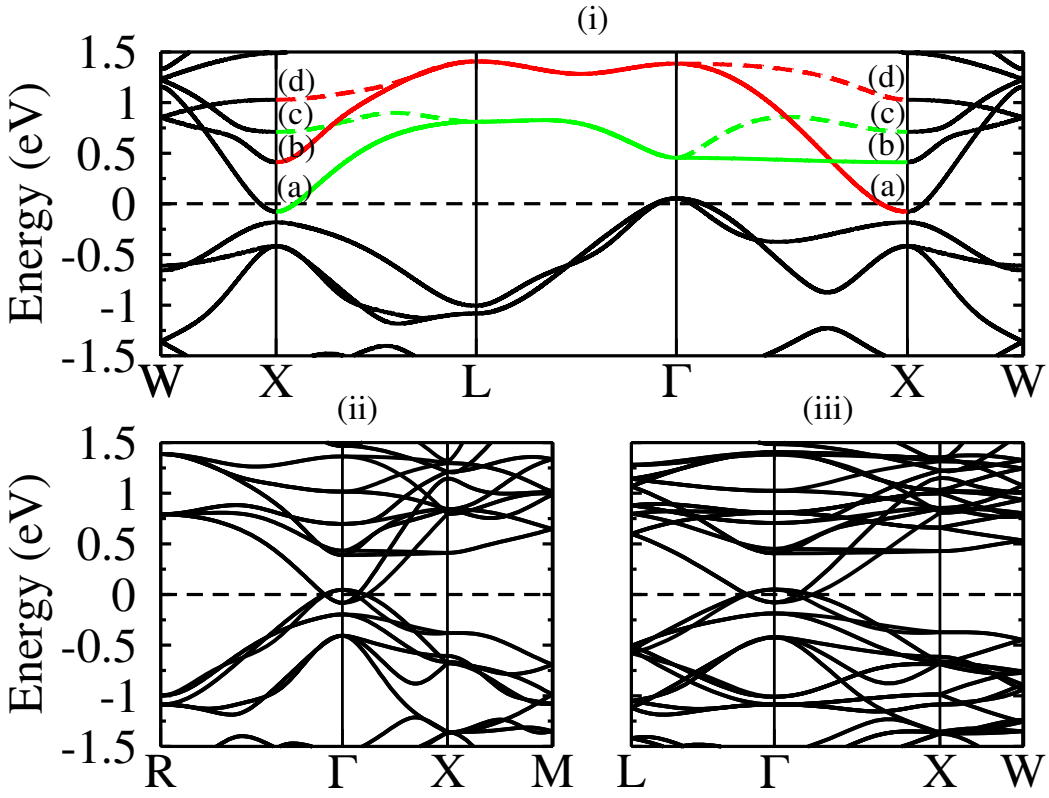

Figure 4.3: Fe_2VAl band structure of a primitive rhombohedral unit cell (i), cubic unit cell (ii) and $2 \times 2 \times 2$ rhombohedral unit cell (iii). Fermi level is indicated with a horizontal dashed line. The orbital character for each conduction band *exactly* at the X-point in (i) is labelled as (a) V $d_{x^2-y^2}$, (b) Fe $d_{x^2-y^2}$, (c) Fe d_{z^2} and V d_{xz}, (d) Fe d_{z^2}. The green (solid and dashed) bands illustrate the starting (a) and (c) positions at the left X-point and the possible final (b) and (c) positions at the right X-point. The red (solid and dashed) bands illustrate the starting (b) and (d) positions at the left X-point and the possible final (a) and (d) positions at the right X-point. Visual illustration of labels (a)-(d) is shown in Fig. 4.4 (a)-(d).

the primitive cell onto the Γ-X region in Fig. 4.3(iii). Therefore, the change in the position of the pseudo band gap is due to band folding rather than doping, and can be seen in this undoped material.

Fig. 4.3(i) also reveals a lack of periodicity within the calculated band structure when plotted along the X-L-Γ-X path. The two X-points are equivalent and form a closed path. Hence the bands along this path are expected to return to the same eigenvalues. However, this is not the case, as illustrated by the red and green coloured bands in Fig. 4.3(i). Note that the colours of the bands do not represent their orbital character but rather aim to make them distinguishable for the reader and illustrate the interrupted periodicity. Our calculations showed that this lack of periodicity is observed with both PBE and LDA exchange-correlation functionals. We would further like to emphasise that the reason we call the pure PBE band structure anomalous is because it is in quali-

tative disagreement with the experimental evidence (thermoelectric response); it is of course perfectly possible for a material to have such features in its band structure, but in this case they arise because of the spurious self-interaction inherent in standard PBE calculations (and LDA) and disappear with even the modest Hubbard U potentials used in this work.

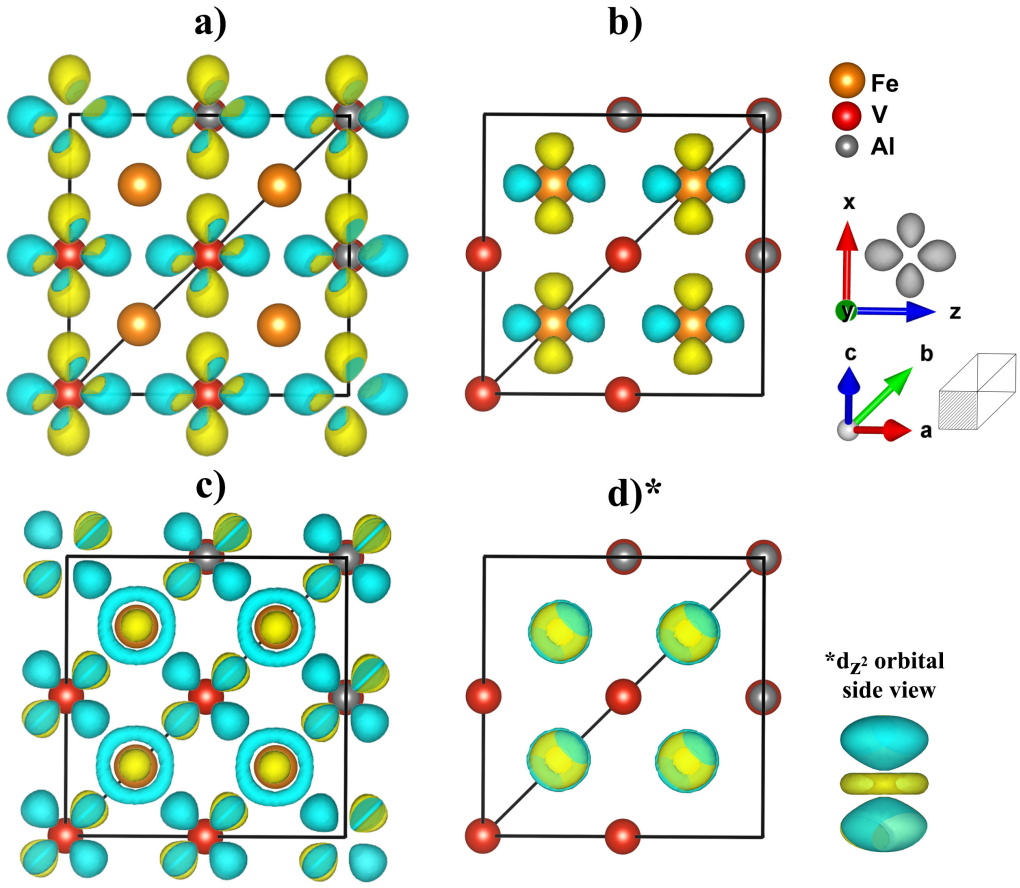

Figure 4.4: Wave functions of the bottom four conduction bands *only* at the X-point, shown in Fig. 4.3(i)(bands 'a'–'d'). The yellow and blue colours represent different wave function phase. Different shapes represent different d-orbitals. Subfigure (a) shows the $d_{x^2-y^2}$ orbitals around V (band 'a' in Fig. 4.3(i)), subfigure (b) shows $d_{x^2-y^2}$ orbitals around Fe (band 'b'), subfigure (c) shows a hybrid Fe d_{z^2} and V d_{xz} orbitals (band 'c'), and subfigure (d) shows Fe d_{z^2} orbitals (band 'd'). The coordinate systems of the orbitals and the unit cell are illustrated with a grey schematic of an orbital and a shaded area of the rhombohedral cell, respectively. The orbitals are plotted with respect to a cubic coordinate system with the y-axis coming out of the plane.

We proceed by plotting and analysing the conduction bands at the X-point in conjunction with the wave functions in real space, superimposed on the atomic positions in the cell (Fig. 4.4). For better visualisation, the primitive rhombohedral cell was extended to occupy the same region of space as a $2 \times 2 \times 2$ rhombohedral supercell. For simplicity, only a portion of the cell, indicated by the

dashed area next to the rhombohedral coordinate system in Fig. 4.4, is shown. The labels (a)-(d) in Fig. 4.3 correspond to the images shown in Fig. 4.4(a)-(d). Our calculations also showed that the only crossing point between the 'red' and 'green' band in Fig. 4.3(i) happens in a region where there is almost no hybridisation in the bands, thus the periodicity problem remains unexplained. The given representation is in agreement with another DFT study [172].

Fig. 4.3 and 4.4 indicate that the electrons need to go along the X-L-Γ-X path twice to return to the same starting energy and band. That is, if one starts at positions (a) or (b) at the left and right X-points (which are identical due to Brillouin zone periodicity) in Fig. 4.3(i), it becomes impossible to reach the same eigenenergy at the Γ-point. The bottom conduction bands have V-Fe hybridisation character as one moves away from the X-points, thus it becomes difficult to pinpoint exactly whether Fe or V is the reason for the lack of periodicity in them. Recent ARPES measurements [178] managed to map the top valence bands in Fe_2VAl. Our results agree well with the ARPES mapping and show that these bands are entirely due to Fe. The top valence bands are also responsible for the *p*-type behaviour and magnitude of the Seebeck coefficient, which could be modelled well even within the standard DFT framework. It has been also shown in a recent DFT+DMFT study [185] that the V site displays stronger orbital-localised states than the Fe site. The requirement for a double periodicity in reciprocal space, the agreement between theory and experiments on the Fe bands dispersion and *p*-type peak Seebeck coefficient magnitude, along with the results from the DFT+DMFT study give enough reasons and good motivation for applying an additional on-site Coulomb term *only* to V in the form of the Hubbard U, while leaving Fe untouched.

4.5 Testing the Hubbard model on Fe_2VAl

Next we present the results of the Fe_2VAl band structure with the inclusion of the U parameter only on V. Fig. 4.5 shows how the band structure changes when U_V = 1.0, 2.0, 2.75 and 3.0 eV is added. The inclusion of U_V modifies mostly the bottom conduction band at the X-point, as expected and in agreement with another study [172]. The general trend presented in Fig. 4.5(a)-(d) shows that the eigenvalue of the bottom conduction band at the X-point moves upwards with the increase of U_V. Looking specifically at the X-L section of the band structure, the bottom conduction band (green) moves upwards up to U_V = 2.75 eV. An increase of U_V above 2.75 eV stops affecting the movement of the bottom conduction band (green), while the band above (red) starts moving upwards. As a result, the lack of periodicity disappears for all U_V values

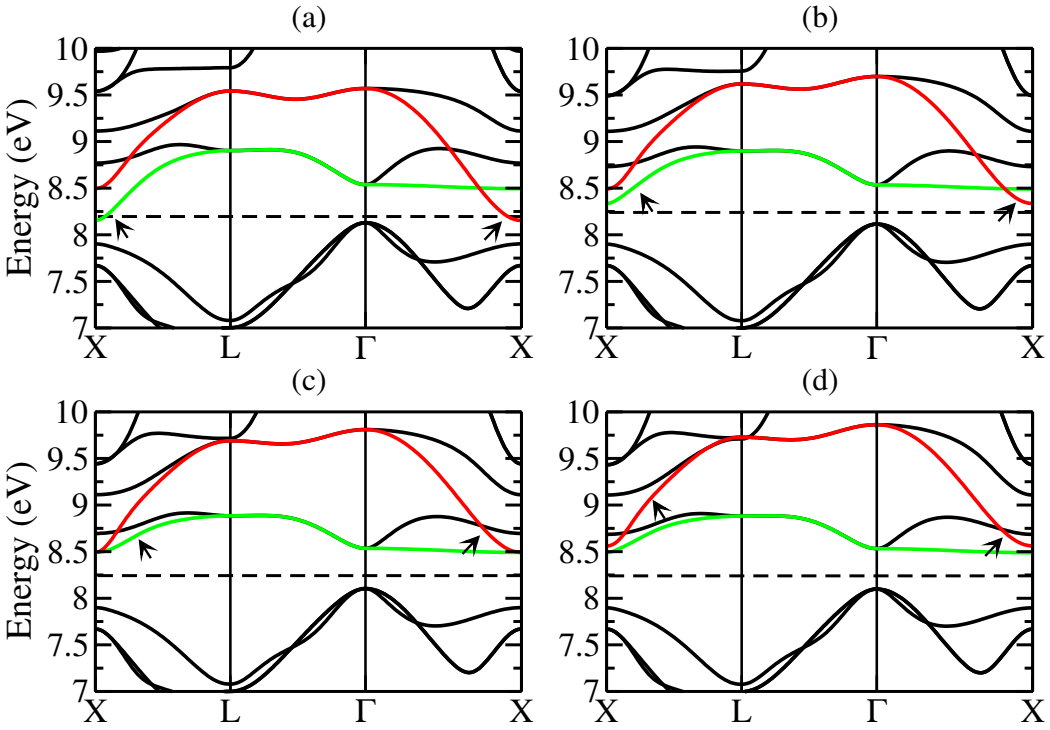

Figure 4.5: Band structure of Fe_2VAl along the X-L-Γ-X path with U_V of 1.0 eV(a), 2.0 eV(b), 2.75 eV(c), 3.0 eV(d). Fermi level is represented by a dashed horizontal line. Arrows indicate which bands are being pushed upwards. The colour of the bands is for illustration purposes and shows that the lack of periodicity is no longer present in (c) and (d).

$>$ 2.75 eV. In addition, the green band in the Γ-X section, which for this region specifically is due to Fe, becomes the major contributor to the conduction states. The flat dispersion of the Fe band in the Γ-X section results in a sharp change in DOS, thus eliminating the symmetry problem outlined in Fig. 4.2. This result agrees very well with the recent DFT+DMFT study [185] which also reports the lifting of the DFT-based symmetry.

As discussed above we demonstrate that the values of U_V larger than 2.75 eV overcome the DOS symmetry and band structure lack of periodicity problems. The precise value of U_V is difficult to determine without experimental data which maps the dispersion of the V conduction bands in Fe_2VAl, which to the best of our knowledge is not available at present. In order to remain as close as possible to the original PBE exchange-correlation functional the smallest value of U_V (2.75 eV), which solves the problems discussed above, was used for transport properties calculations.

The inclusion of the Hubbard U only on V opens a large band gap of 0.4 eV. This value of the band gap results in an overestimate of S maxima when compared to the experimental results [163]. As indicated by the more accurate DFT+DMFT method [185] the band gap is a lot smaller at low temperatures.

Therefore, a scissors operator was added to the thermoelectric calculations in order to correct for the significant increase in S. The scissors operator set the difference between the top conduction and valence bands to 0.04 eV and 0.2 eV at the Γ- and X-points, respectively, with an overall (indirect) band gap value of 0 eV. This zero-band gap semiconductor model is also implied by experimental studies [184].

4.6 Electronic thermoelectric properties

Considering the Hubbard U on V and the scissors operator correction we calculated the thermoelectric properties of Fe_2VAl at room temperature. The calculated values of S, σ/τ and κ_{el}/τ within PBE and PBE + Δ, with Δ = U + scissors operator, are presented in Fig. 4.6. The Seebeck coefficient maxima obtained within PBE (Fig. 4.6(a), black line) are 58 and -52 μV/K for p- and n-type, respectively. This is in good agreement with other theoretical studies [166, 171, 172, 186], but as expected disagrees with experimental results [54, 184]. In contrast, the maximum values of S obtained within PBE + Δ (Fig. 4.6(a), green line) yield 76 and -158 μV/K for p- and n-type, respectively. These results capture the asymmetry in the variation of S and are now in good agreement with the experimental results [162, 163]. The values of σ/τ and κ_{el}/τ (Fig. 4.6(b) and (c)) within the constant relaxation time approximation are presented in Table 4.1. The value of τ (Table 4.1) is obtained by fitting the theoretical value of $1/\sigma$ to the experimental one of 0.75 mΩcm [184, 187].

Table 4.1: Values of σ/τ, κ_{el}/τ and τ obtained within PBE and PBE + Δ.

	σ/τ $(\Omega^{-1}m^{-1}s^{-1})$	κ_{el}/τ $(Wm^{-1}K^{-1}s^{-1})$	τ (s)
PBE	1.14×10^{19}	1.23×10^{14}	1.17×10^{-14}
PBE + Δ	0.82×10^{19}	1.50×10^{14}	1.62×10^{-14}

Our calculations also showed that the theoretically obtained maxima of S heavily depend on the strength of the scissors operator, in agreement with other studies [171, 172]. A small variation of 30 meV in the magnitude of the band gap (set at 0 eV in the present calculations) moves the maximum of S across the whole experimental range, especially for the n-type semiconductor. Therefore, the uncertainty in the experimental [54, 162, 163] measurements of S makes it difficult to determine the precise value of the band gap. Furthermore, we also note that the valence bands at the X-point (Fig. 4.5(d)) are slightly lower in energy compared to ARPES measurements [178]. As shown in this study, the bands dispersion determines the magnitude and the symmetry of the Seebeck

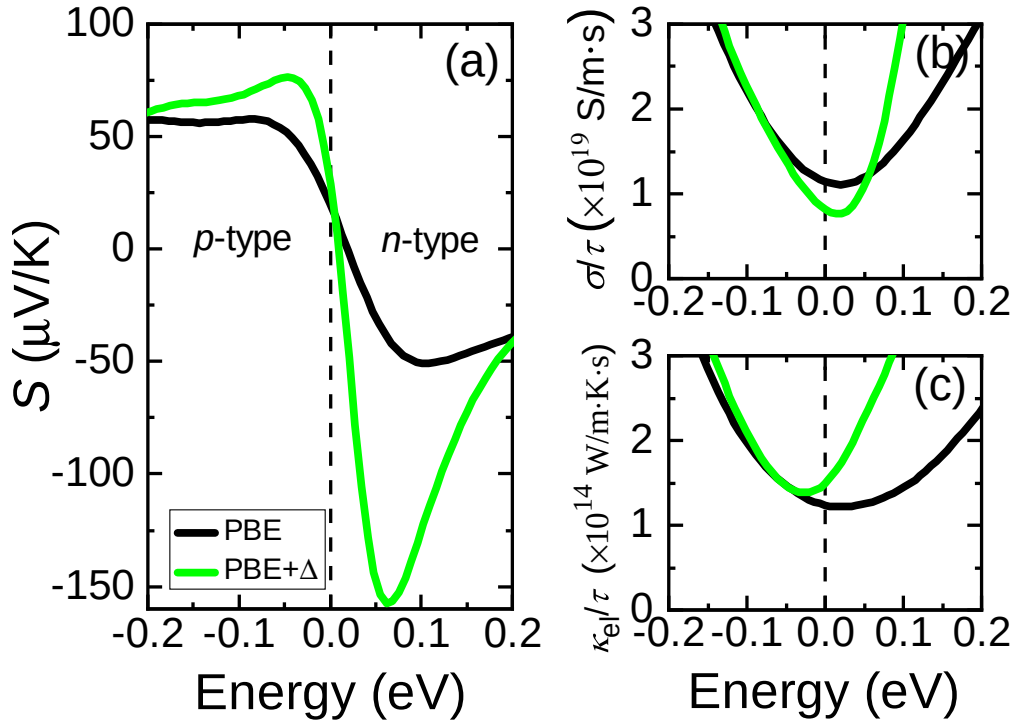

Figure 4.6: Thermoelectric properties of Fe_2VAl at T=300 K. Black and green solid lines represent results obtained within PBE and PBE + Δ, respectively; Δ represents U + scissors operator. Fermi level is indicated by a vertical dashed line at 0 eV. The subfigures show the Seebeck coefficient (a), electrical conductivity (b) and the electronic thermal conductivity (c).

coefficient. Therefore, a small increase in the energy of the bands at the X-point would increase the *p*-type and decrease the *n*-type values of S, putting them in even better agreement with experimental data.

Next we show a further comparison between our theoretical prediction and experimental results in Fig. 4.7. Subfigure (a) shows the power factor computed with PBE (black) and PBE + Δ (green). We compare *n*-type *PF* performance to the reported experimental values (horizontal dashed lines) between 5.0–5.5 $mW/m{\cdot}K^2$ [162, 188] for $Fe_2VAl_{1-x}Si_x$ with $x = 0.1$. We obtain a new value for τ by fitting the theoretical value of $1/\sigma$ to the experimental one of 0.35 mΩcm for $x = 0.1$ in $Fe_2VAl_{1-x}Si_x$ [162]. Chemical doping of $x = 0.1$ corresponds to an energy of 0.09 eV above the Fermi level in the PBE + Δ model. Compared to τ values in Table 4.1 the relaxation time increases by 65% for PBE and decreases by 27% for PBE + Δ. A reduction in τ is the expected behaviour as dopants increase the scattering rates. Regarding the power factor we see that the *n*-type peak for the PBE + Δ curve agrees very well with experimental results and falls within the experimental range marked by the horizontal dashed lines. Figure 4.7(b) compares the Seebeck coefficient obtained via PBE

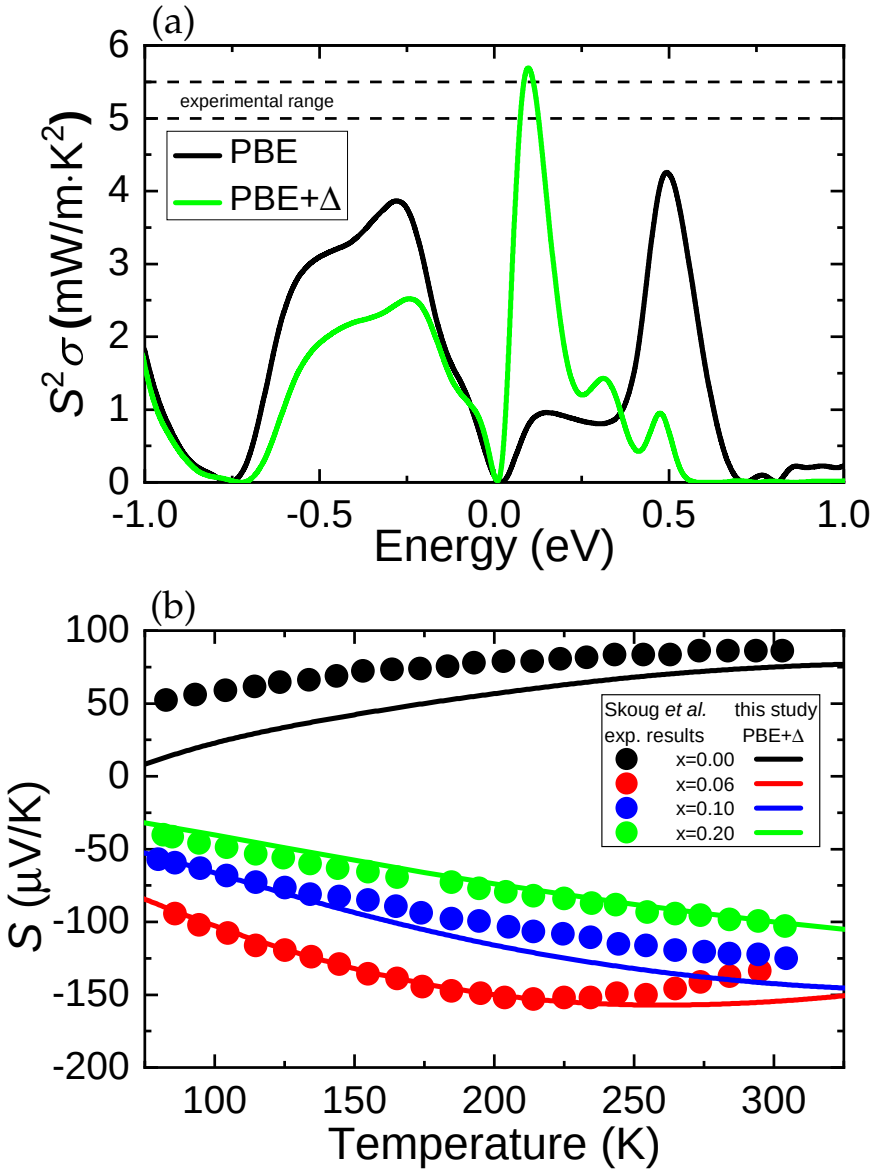

Figure 4.7: Power factor (a) of Fe_2VAl at T=300 K for PBE (black) and PBE + Δ (green); Δ represents U + scissors operator. Horizontal dashed lines show the experimental range for the power factor. Comparing S (b) obtained with PBE + Δ and experimental measurements at different doping levels [162].

+ Δ to experimental results for doping concentrations of 0, 6, 10 and 20% additional electrons per formula unit [162]. The good agreement between our prediction and experimental measurements means that the PBE + Δ method not only captures correctly the maximum values of the Seebeck peaks for *p*- and *n*-type semiconductor but also model properly their position and spread along the chemical potential.

4.7 Applying the Hubbard model to Fe and V

We know from other studies [172] that having a larger Hubbard U on Fe than V does not result in an asymmetric S. Based on our calculations we find that the U value on V needs to be at least 2.75 eV in order to make the conduction bands periodic and recreate the asymmetry in S. In principle, this suggests that the Hubbard U on V needs to be 2.75 eV higher than the U on Fe but does not indicate what would happen if $U_{\mathrm{Fe}} > 0$. As we are using a very pragmatic approach to the problem we would like to investigate if the difference of 2.75 eV remains the same when we apply the Hubbard U model to both V and Fe with $U_{\mathrm{V}} > U_{\mathrm{Fe}}$.

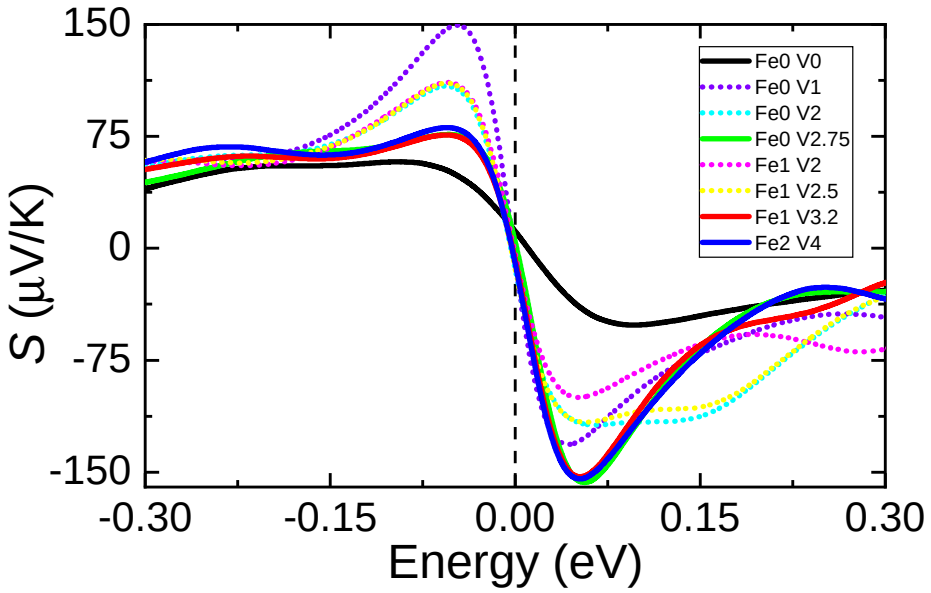

Figure 4.8: Comparing how different Hubbard U settings on Fe and V affect S of Fe_2VAl at T=300 K. Solid curves show cases when conduction bands are periodic. Dotted curves represent cases when conduction bands are non periodic.

Figure 4.8 shows the Seebeck coefficient when there is a Hubbard U on both V and Fe, with $U_{\mathrm{V}} > U_{\mathrm{Fe}}$. We have set the band gap to 0 eV for all cases when it had a positive value. Results are presented with dotted and solid curves. Dotted curves do not exhibit the expected asymmetry of S. We noted that in all dotted cases bottom conduction bands exhibited the periodicity problem. In contrast, solid curves all agree with each other and recreate the asymmetric behaviour of S, similarly to the result shown in Fig. 4.6(a). In addition to our initial settings of $U_{\mathrm{Fe}} = 0$ eV and $U_{\mathrm{V}} = 2.75$ eV (green curve), other successful attempts included $U_{\mathrm{Fe}} = 1$ eV and $U_{\mathrm{V}} = 3.2$ eV (red curve), and $U_{\mathrm{Fe}} = 2$ eV and $U_{\mathrm{V}} = 4$ eV (blue curve). The difference between Fe and V gradually falls down to 2 eV when we add the Hubbard U to the Fe atoms. We noted that all

solid curve examples belong to cases in which the bottom conduction bands are periodic. Based on Fig. 4.8 results we can conclude that even with $U_{\mathrm{Fe}} > 0$ eV the Seebeck coefficient of Fe_2VAl can exhibit the expected experimental asymmetric behaviour as long as the localisation on V atoms is stronger and conduction bands are periodic.

One might wonder whether the PBE + Δ approach would remain applicable for more challenging structures where no experimental data is available. For simple doping, e.g. with Si or Ge, the states around E_{F} remain unaffected and the parameters used in this study will be the same. For off-stoichiometric compounds, it was shown experimentally by Nishino and Tamada [163] that the asymmetry in S is always present. As our method does not affect the valence states in Fe_2VAl, the magnitude of the p-type peak of S could be used as a guide to deduce the value of the scissors operator for more complicated structures. Alternatively, if the power factor is used as a reference point, then the scissor operator becomes less significant since for any positive value of the band gap, S and σ changes compensate each other and yield no net change in PF. In most cases, the aim of more challenging modifications of Fe_2VAl is to reduce the lattice thermal conductivity, and our approach provides a very cheap way of checking whether the rest of the thermoelectric properties are affected. Our method makes it obvious that Fe_2VAl is a special compound which is hard to model within the conventional DFT/DFT+U framework. Analysis of the results should be done with care and for more challenging structures it would be appropriate to check the accuracy of the results with a higher level of theory, e.g. the more expensive but more accurate DFT+DMFT method.

4.8 Conclusions

In summary, our calculations show that in simple DFT the bottom conduction bands in Fe_2VAl lack periodicity. The inclusion of $U_{\mathrm{V}} > 2.75$ eV resolves the problem, modifies the bands dispersion and changes the order of the bottom conduction bands from V to Fe being at the bottom. As a result, the experimentally observed asymmetry in S could be theoretically reproduced. Furthermore, Fe_2VAl was modelled as a zero-band gap semiconductor by adding a scissors operator to the transport calculations. Thus, the maxima of S become +76 and -158 µV/K for p- and n-type, respectively, in good agreement with experimental results [163]. The ability of our approach to model simultaneously the p- and n-type sides around E_{F} provides a good starting point for understanding the Fe_2VAl thermoelectric properties, as well as further studies which may include structure modifications or movement along the chemical

potential in pursuit of a better thermoelectric figure of merit (ZT). We note that this should be accompanied by a very careful interpretation and analysis of the results, especially for more challenging structures.

Chapter 5

Thermoelectric properties of half-Heusler compounds

The results discussed in this chapter have been published in [189].

5.1 Background

In this chapter we focus on NbFeSb and TaFeSb, which are half-Heusler intermetallic compounds. NbFeSb has recently attracted a lot of attention as a potential thermoelectric material due to its ecologically friendly properties and the relatively high earth abundance of Nb and Fe. NbFeSb alloys are reported to have a large power factor of up to 10 $mW/(m{\cdot}K^2)$ [140], beating some of the best thermoelectrics, e.g. Bi_2Te_3. However, their thermal conductivity is also a lot higher than Bi_2Te_3 [140, 190, 191]. The high thermal conductivity of NbFeSb is phonon dominated and this provides much room for improvement of the current thermoelectric figure of merit maximum of ZT=1. As the thermoelectric figure of merit is given by the equation $ZT = S^2\sigma T/\kappa$, several theoretical and experimental studies aim to optimise the thermal conductivity (κ), the Seebeck coefficient (S) and the electrical conductivity (σ) [55, 105, 106, 109, 140, 190, 192–194]. This optimisation is done by p-type doping with Ti, Hf and Zr for Nb or Sn for Sb. Such an approach maximises the power factor by fine tuning of the doping levels and decreases the lattice thermal conductivity by enhancing the phonon scattering due to the mass difference between the dopant and host atoms. To date, the best NbFeSb results are obtained by Ti-doping [140] due to the large mass difference between Ti and Nb. The mass difference can be further enhanced if Nb is substituted with a heavier but chemically similar element like Ta, which is something that has not yet been thoroughly investigated.

The first aim of this study is to compute the lattice thermal conductivity (κ_{latt}) of NbFeSb using the semi-classical Boltzmann Transport Equation (BTE) and compare the obtained theoretical thermoelectric (TE) results to experimental measurements. The second aim is to use the same approach and calculate the TE properties of a compound very similar to NbFeSb, namely TaFeSb. A theoretical study by Bhattacharya and Madsen [105] reports that TaFeSb is a stable compound which can also be doped with Ti in a similar way to NbFeSb. A very recent experimental study by Zhu *et al.* [195] investigates extensively the phase stability of the compound and provides an XRD pattern after the successful experimental synthesis of TaFeSb. The main interest in TaFeSb comes from the fact that it has the same number of valence electrons as NbFeSb, while Ta has almost twice the mass of Nb. This suggests that TaFeSb should have the same good electronic TE properties as NbFeSb. In addition, the heavier Ta should also lead to an increase in the scattering strength in doped TaFeSb due to point defects and thus decrease κ_{latt}. As a result, TaFeSb may be expected to have a significantly higher ZT than NbFeSb but until now there have been no full-scale theoretical studies on the pure TaFeSb compound to confirm this hypothesis. Zeeshan *et al*. [160] investigates the thermoelectric properties of TaFeSb but without computing the electron relaxation time or including the additional phonon scattering mechanisms. Another recent study conducted by Yu *et al*. [193] investigates the effect of Ta but in NbFeSb systems. Hence, this is clearly a very hot topic and there is a strong need for a full study of the thermoelectric properties of TaFeSb.

The results are split into two sections. The first one presents the calculations on the TE properties of NbFeSb. We start by following the well-established procedure of using BoltzTraP [100] to obtain the electronic properties of the material and then solve the phonon BTE using ShengBTE [114]. Furthermore, we build upon the method proposed by Hong *et al*. [109] for the inclusion of point defects and introduce the contributions of grain boundaries and electron-phonon interaction to the lattice thermal conductivity of NbFeSb. To the best of our knowledge, this is the first instance when the lattice thermal conductivity of NbFeSb is calculated by solving the BTE and including all these additional contributions. For this reason, the results are thoroughly compared to the available experimental data. The second section follows a similar layout but is focused on TaFeSb and the observed improvements in TE properties with respect to NbFeSb.

It is worth pointing out that BolzTraP calculates the TE properties at different doping levels by changing the chemical potential implicitly and hence the dopant atoms are not explicitly included. For this reason, the p-type com-

pounds in electronic properties section are referred simply as NbFeSb and TaFeSb. However, the computation of the change in the lattice thermal conductivity due to point defects requires knowledge of the atomic mass of the dopant atoms. In this case, the structures are referred as $Nb_{1-x}Ti_xFeSb$ and $Ta_{1-x}Ti_xFeSb$, with Ti being used for the *p*-type doping.

5.2 Computational settings

5.2.1 Electronic thermoelectric properties

The first principles calculations were performed with the CASTEP [123] code and the generalized gradient approximation Perdew–Burke–Ernzerhof (GGA-PBE) exchange-correlation functional [126]. On-the-fly ultrasoft pseudopotentials (C9 set) [196] were used with a plane-wave cut-off energy of 700 eV with a grid scale of size 2.0. A cubic unit cell, corresponding to four elementary rhombohedral cells, was used for all simulations. The Brillouin zone was sampled using a MonkhorstPack grid [151] with an $8 \times 8 \times 8$ **k**-points mesh (equivalent to **k**-points spacing of 0.021 2πÅ^{-1}). The structure was fully optimized until pressure and energy were converged to 0.1 GPa and 0.02 meV/atom, respectively. Density of states (DOS) and partial density of states (PDOS) were analysed using the OptaDOS code [156].

Electronic transport properties were calculated using the semi-classical Boltzmann transport formalism as implemented in the BoltzTraP code [100]. The electronic eigenenergies required for the transport properties were calculated with CASTEP on a $48 \times 48 \times 48$ **k**-points mesh, which was later interpolated on a 5 times denser mesh in BoltzTraP. The simulated half-Heusler alloys are isotropic and the Seebeck coefficient S, electrical conductivity σ and electron thermal conductivity κ_{el} can be evaluated as the average of the trace of the respective tensors. The final results are obtained as a function of the temperature (T) for 37 fixed doping levels from $n_h = 10^{18}$ cm^{-3} to $n_h = 10^{22}$ cm^{-3}. BoltzTraP calculates both electrical and electron thermal conductivity as σ/τ and κ_{el}/τ where τ is the relaxation time. We use the deformation potential (DP) theory to compute τ [102].

5.2.2 Lattice thermal conductivity

The lattice thermal conductivity was calculated by solving the phonon BTE in ShengBTE, which as inputs requires the second order force constants (usually

just called the 'force constants') and the anharmonicity (third order force constants) of the system. The second order force constants were obtained with CASTEP using density-functional perturbation theory (DFPT) [158]. The calculations used the GGA-PBE exchange-correlation functional [126], on-the-fly norm-conserving pseudopotentials (NCP17 set) and a plane-wave cut-off energy of 2000 eV with a grid scale of size 2.0. The Brillouin zone was sampled using a MonkhorstPack [151] grid with an $5 \times 5 \times 5$ **k**-points mesh (equivalent to **k**-points spacing of 0.034 2πÅ^{-1}). A **q**-point grid of the same size and spacing was used for calculating the second order force constants.

The third order force constants were calculated using the finite-displacement supercell approach. The set of supercells and the reconstruction of the force constants was performed by the *thirdorder.py* script that is supplied with the ShengBTE package. The *ab initio* calculations were done using CASTEP. The settings for these runs included: on-the-fly ultrasoft pseudopotentials (C9 set), a plane-wave cut-off energy of 600 eV with a grid scale of size 2.0 and a very fine energy per atom convergence tolerance of 2×10^{-10} eV. The size of the supercells in the set containing 332 jobs corresponded to a $2 \times 2 \times 2$ cubic supercell containing 96 atoms. The interactions up to the third nearest neighbour were computed, which corresponds to a cut-off radius $R_c = 0.545$ nm.

In addition to the force constants, the ShengBTE *CONTROL* file requires a few more convergence parameters to be defined. In our case, a $9 \times 9 \times 9$ grid of planes in reciprocal space and a *scalebroad* of 1.0 were enough to converge the lattice thermal conductivity.

ShengBTE computes the intrinsic lattice thermal conductivity κ_{int} due to 3P (three-phonon) processes. We have also included the effect of GB (grain boundaries), PD (point defects) and EP (electron-phonon) interaction to the lattice thermal conductivity.

5.3 NbFeSb

5.3.1 Electronic structure

NbFeSb is a half-Heusler compound, which has a composition of XYZ, where X and Y are transition metals and Z is a main group element. The crystal structure is face-centred cubic, having space group $F\bar{4}3m$ (216). The lattice constant is calculated to be 5.96 Å, which agrees well with the experimental value of 5.95 Å [55]. The band structure and density of states (DOS) are presented in Fig. 5.1. The figure shows that the conduction band minimum (CBM) is at

the Γ-point, whereas the valence band maximum (VBM) is positioned at the L-point. The magnitude of the formed indirect band gap (ε_g) is 0.53 eV, which is in an excellent agreement with other theoretical [106, 109, 140] (ε_g = 0.52 and 0.53 eV) and experimental [140] (ε_g = 0.51 eV) studies. The partial DOS show that Fe and Nb are the main contributors to states around the Fermi level. This means that the power factor is mainly affected by Fe and Nb rather than Sb.

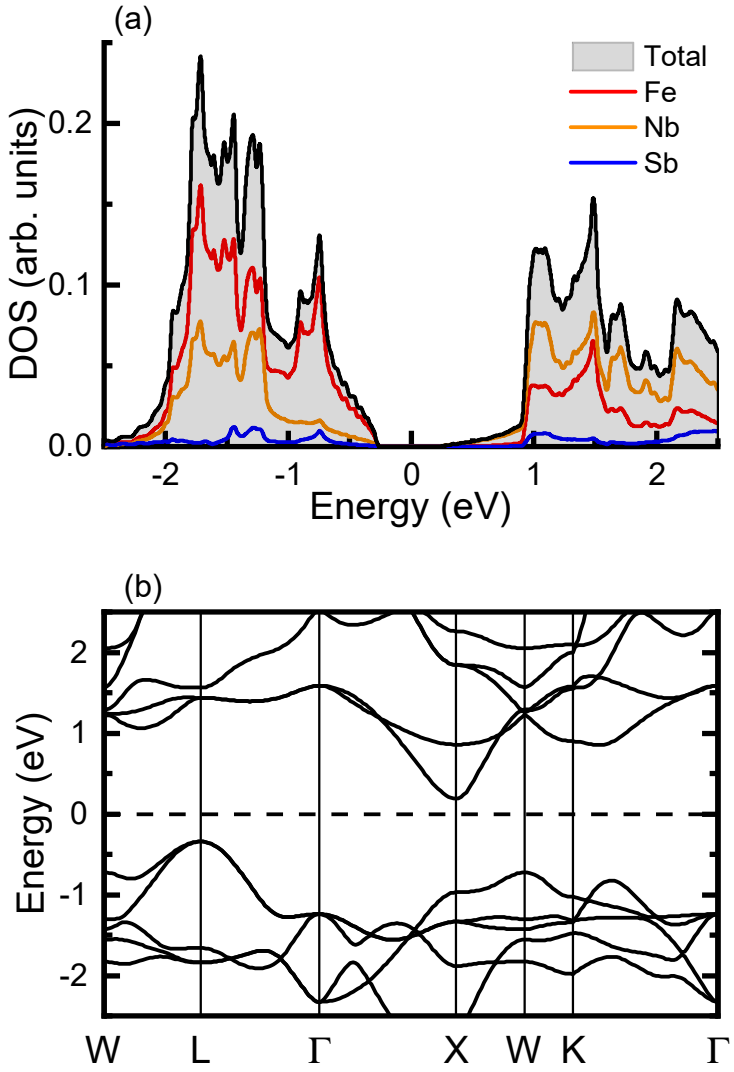

Figure 5.1: Density of states (a) and band structure (b) graphs of NbFeSb.

5.3.2 Electronic thermoelectric properties

The parameters needed to calculate the electron relaxation time of NbFeSb are given in Table 5.1. These include the deformation potential (V_{DP}), effective mass of the charge carriers (m^*), carrier mobility (μ) and relaxation time (τ). The elastic constants are given in Table 5.3 in Section 5.4.4. The values

Table 5.1: Parameters needed for electron and hole τ calculations of NbFeSb. These include the deformation potential (V_{DP}), effective mass of charge carriers (m^*), carrier mobility (μ) and relaxation time (τ) at 300 K for electrons and holes.

Carrier type	V_{DP} (eV)	m^* (m_e)	μ ($cm^2V^{-1}s^{-1}$)	τ (fs)
holes	-13.98	1.65	28.02	26.23
electrons	-14.53	0.35	1243.93	247.54

of the parameters obtained for holes are slightly higher, but within the margin of error, than the ones obtained experimentally by He *et al*. [140] and Fu *et al*. [55] The experimental measurements have been performed on doped systems which exhibit structural defects. Therefore, a slight overestimate is to be expected when the results are compared to the modelled perfect bulk system. To the best of our knowledge there are no experimental results on the electron parameters. However, the electron values presented in Table 5.1 agree extremely well with the theoretical prediction of Hong *et al*. [109] The magnitude of the deformation potential constant for holes ($V_{DP} = -13.98$ eV) is lower than the one for electrons ($V_{DP} = -14.53$ eV). This can be explained by the different dispersion of the valence and conduction bands. The bottom conduction band is more dispersive than the top valence band, and the applied strain has a smaller effect on the flatter bands. Due to the difference in the dispersion of the bands, the effective mass of electrons m^*_{el}=0.35(m_e) is much smaller than that of the holes m^*_h=1.65(m_e). This results in a much lower mobility ($\mu_h = 28.02$ $cm^2V^{-1}s^{-1}$) of the heavier holes and a lower relaxation time of $\tau_h = 26.23$ fs at 300 K. This value of the relaxation time, with the included temperature dependence of $\tau \propto 1/T^{3/2}$ is used to post-process the results obtained from BoltzTraP for the *p*-type behaviour of NbFeSb.

The thermoelectric properties of *p*-type NbFeSb are shown in Fig. 5.2. All quantities agree very well with results obtained in the other theoretical studies [106, 109]. It can be seen that the Seebeck coefficient (top left graph) reaches values up of 700 μV/K at low temperature (around 300 K) and at extremely small doping levels (between 0.04 and 0.004% hole concentration). When the doping concentration is increased to the experimental values of x = 0.04 ($n_h = 8 \times 10^{20} cm^{-3}$) the Seebeck coefficient becomes 129 μV/K and 266 μV/K at 300 K and 1000 K, respectively. These values are slightly lower than the experimental results obtained by Fu *et al*. [55] (S = 150 μV/K and 285 μV/K at 300 K and 1000 K, respectively) and He *at al*. [140] (S = 175 and 300 μV/K at 300 and 1000 K, respectively). It is worth mentioning, however, that a lower doping level in the theoretical model of $n_h = 6 \times 10^{20} cm^{-3}$ (x = 0.03) yields identical results to the experimental ones obtained for x = 0.04 by Fu *et al*. [55] This could mean

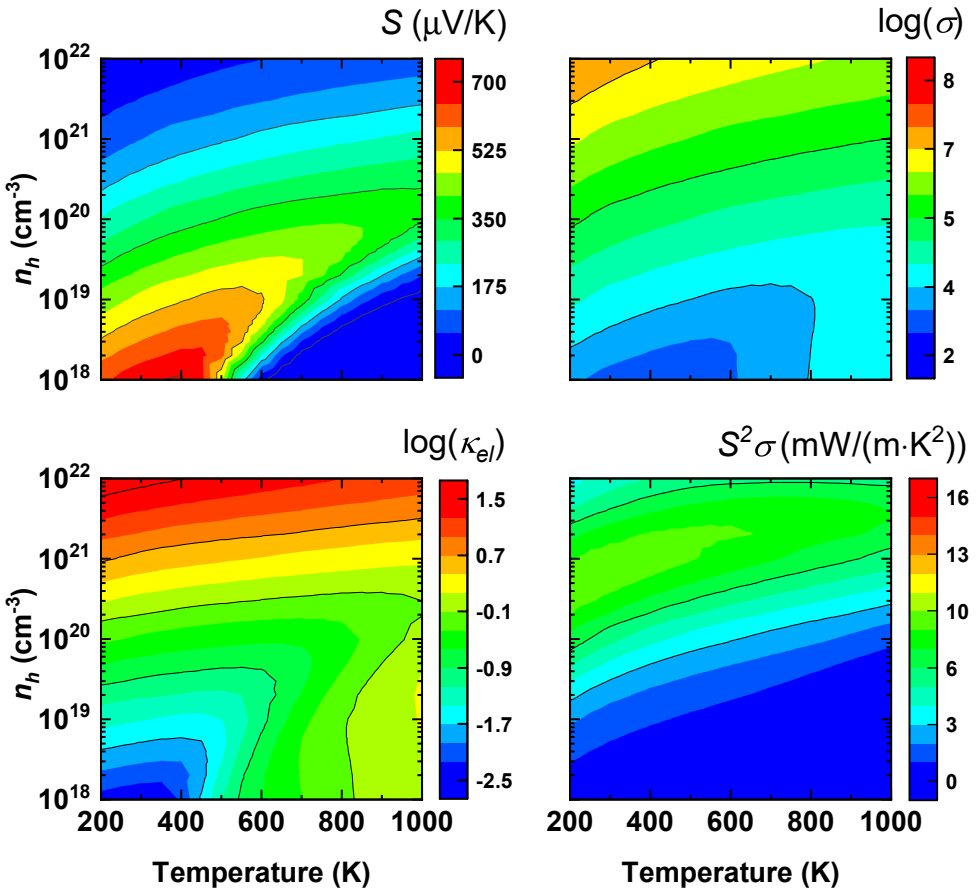

Figure 5.2: Colour maps of the electronic TE properties of *p*-type NbFeSb. The magnitude of the electrical conductivity σ (top right) and electronic thermal conductivity κ_{el} (bottom left) is given on a log scale. A maximum power factor (bottom right) value of PF = 9.15 mW/(m·K^2) is obtained at 300 K and $n_h = 7 \times 10^{20}$cm^{-3} (x = 0.037).

that an x = 0.04 does not strictly correspond to 8×10^{20}cm^{-3} hole concentration in the experimental samples, and some of the holes could be compensated. The presence of defects can be responsible for such a compensation. For example, other studies on NbFeSb state that anti-phase boundaries make NbFeSb n-type semiconductor [197]. Therefore, it is not unreasonable to assume that the presence of grain boundaries, vacancies, dislocations and anti-site defects can tweak the electronic structure in such a way that some of the holes to be compensated in experimental samples. In fact, Fu *et al.* [55] results show that a doping level of x = 0.04 corresponds more to $n_h = 6 \times 10^{20}$cm^{-3} rather than $n_h = 8 \times 10^{20}$cm^{-3}, as the theory suggests. For simplicity, however, we use the theoretical relation between x and n_h ($volume = x/n_h$), where the volume is theoretically calculated to be 52.86×10^{-24}cm^3.

The electrical conductivity σ and electronic thermal conductivity κ_{el} also agree

very well with other theoretical studies [106, 109], but are slightly larger than found in experiment [55, 140]. There are a few reasons for this discrepancy. As already mentioned, the carrier mobility of the perfect crystal is expected to be higher than μ of the doped compounds, hence τ and σ are also larger. Second, the temperature dependence of τ is no longer proportional to $T^{-3/2}$ at temperature < 450 K [55, 140]. Finally, the constant relaxation time approximation lacks dependence on the chemical potential, which means that additional scattering events are not captured when the doping levels are increased. Thus, σ and κ_{el} tend to be overestimated at high doping levels. Nevertheless, the current model for τ is a computationally inexpensive approach that allows us to calculate values for σ and κ_{el}, which agree relatively well with both theoretical and experimental studies.

The highest value of the power factor $PF = S^2\sigma$ is obtained at $n_h = 7 \times 10^{20}\text{cm}^{-3}$ (x = 0.037) and yields PF = 9.15 and 5.23 mW/(m·K^2) at 300 K and 1000 K, respectively. This result is very close to the key result of He *et al.* [140] study of PF = 10.6 mW/(m·K^2) at room temperature and $x \approx 0.05$. In general, the power factor values remain consistent with the experimental measurements up to $n_h = 2 \times 10^{21}\text{cm}^{-3}$ (x = 0.1). Beyond that value, the theoretical prediction starts to overestimate the experimental results by values up to ≈ 2 mW/(m·K^2) when one reaches x = 0.3. Such behaviour is also noticed by the other theoretical studies mentioned before. The reason for this could be either the constant relaxation time approximation, or the fact that the heavy doping significantly changes the electronic structure of the system. However, as shown experimentally, NbFeSb exhibits its best thermoelectric performance at around x = 0.05, and this region is accurately modelled by the current theoretical approach.

5.3.3 Lattice thermal conductivity

The phonon density of states (DOS) are presented in Fig. 5.3. The data is in a good agreement with the results obtained by Hong *et al.* [109] and Zeeshan *et al*. [160] and as there are no imaginary frequencies the structure is mechanically stable. The phonon DOS can be split into three regions. The first one is at low frequency, $\omega < 170$ cm^{-1} where the lattice vibrations are primarily due to Sb atoms. The dominant contributor to the phonon DOS for $170 < \omega < 230$ cm^{-1} is Nb, whereas for $\omega > 230$ cm^{-1} lattice vibrations are predominantly due to Fe with a small contribution from Nb. The Nb atomic vibrations have the biggest frequency spread among the constituents of the material. In addition, the mass difference between Nb and the dopant atoms (here assumed to be Ti) leads to an increase in the scattering strength. Thus, the lattice ther-

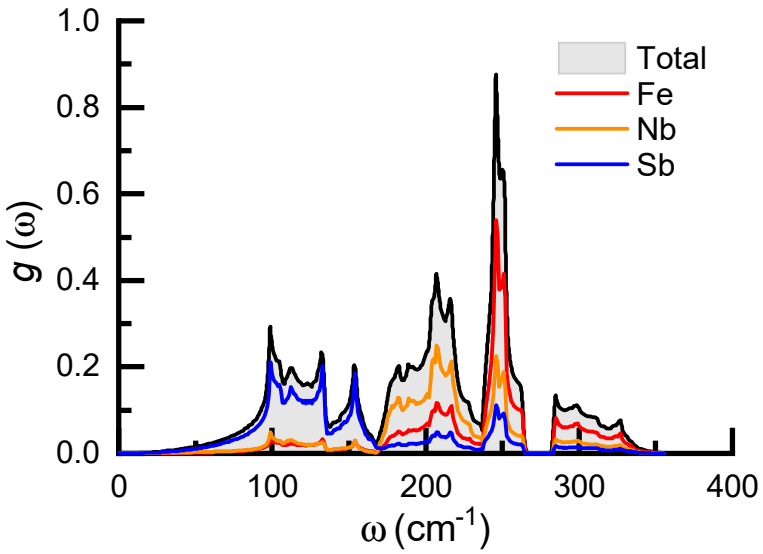

Figure 5.3: Phonon density of states of NbFeSb.

mal conductivity κ_{latt} of NbFeSb can be reduced significantly by doping. Our results show the clear presence of a phonon gap at $\omega \approx 275$ cm^{-1}, something which is not observed either by Hong *et al.* or Zeeshan *et al.* [160] The reason for this discrepancy comes from the choice of the **q**-point grid for the phonon calculations. The phonon DOS converges slowly and the gap only becomes apparent when the **q**-point mesh is at least $3 \times 3 \times 3$ or equivalently a spacing of 0.056 2πÅ^{-1} .

Next we focus on the estimated value for the lattice thermal conductivity and how different contributions affect it. The intrinsic value of κ_{latt} obtained from ShengBTE is 21.82 and 6.49 Wm^{-1}K^{-1} at 300 and 1000 K, respectively. This agrees very well with the theoretical result obtained by Hong *et al.* [109] but is a bit higher than the experimental measurements [55, 140]. The main reasons for this discrepancy is the fact that there are no defects such as grain boundaries, point defects or dopant atoms in the modelled structure. To correct this, we include the effect of all mentioned impurities by using Klemens' model [198] and calculating the impact on the intrinsic value obtained from ShengBTE.

5.3.3.1 Grain boundaries

The study conducted by He *at al.* reports that the size of the grain boundaries in NbFeSb varies between 0.3 and 4.5 μm, depending on the hot pressing temperature. Figure 5.4 shows how the lattice thermal conductivity of phonons with a given mean free path changes at room temperature when grain boundaries are included in the theoretical model. The graph illustrates the effect of grain boundaries (L_{GB}) by considering two different average sizes of L_{GB} = 4.5

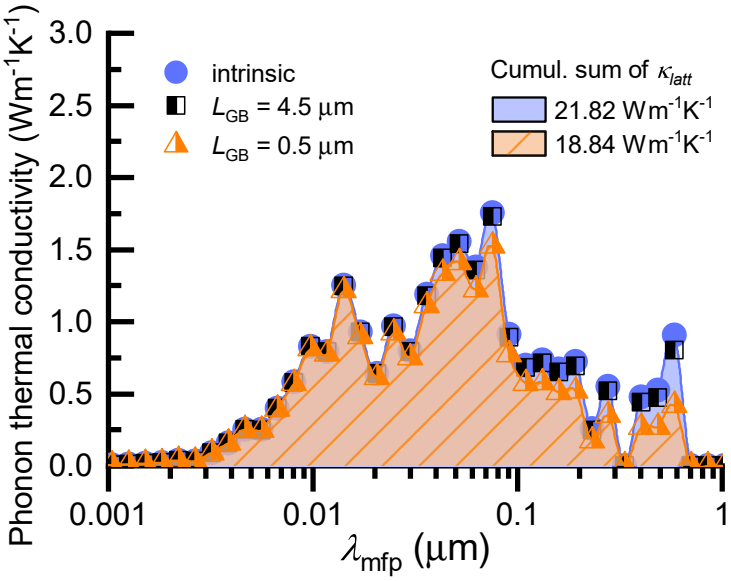

Figure 5.4: The impact of grain boundaries on the lattice thermal conductivity of NbFeSb at 300 K.

and 0.5 μm. Blue circles represent the intrinsic values of κ_{latt} and it can be seen that L_{GB} = 4.5 μm, illustrated with black and white squares, have an almost negligible impact on κ_{latt}. However, there is a noticeable change in κ_{latt} when the size of the grain boundaries is reduced to 0.5 μm (orange triangles), and the accumulated value of κ_{latt} becomes 18.84 $Wm^{-1}K^{-1}$. For completeness, L_{GB} = 0.3 μm was also tested and yielded a result of κ_{latt} = 17.59 $Wm^{-1}K^{-1}$ at 300 K. Both results for L_{GB} = 0.3 and 0.5 μm are within the margin of error of the experimental value of $\kappa_{latt} \approx 17$ $Wm^{-1}K^{-1}$ (undoped NbFeSb, 12% relative error).

5.3.3.2 Point defects and electron-phonon interaction

To complete the calculation, we include the effect of point defects and electron-phonon interaction to κ_{latt}. The computation of the electron-phonon interaction requires knowledge of the electron τ. The lack of doping level dependence in the constant relaxation time approximation makes it unsuitable for calculating the electron-phonon contribution. The experimental data from the He *et al.* study, including the temperature and doping dependencies, was used in accordance to the theoretical model and is discussed in more details in Section 2.6.3. Figure 5.5(a) shows how the lattice thermal conductivity of $Nb_{1-x}Ti_xFeSb$ is reduced when all contributions are included. The results are presented for doping x = 0.05 and the best match to the experimental data is obtained with L_{GB} = 0.5 μm. Figure 5.5(b) compares κ_{latt} when all contributions have been added to the experimental results. The computed values for the lattice thermal

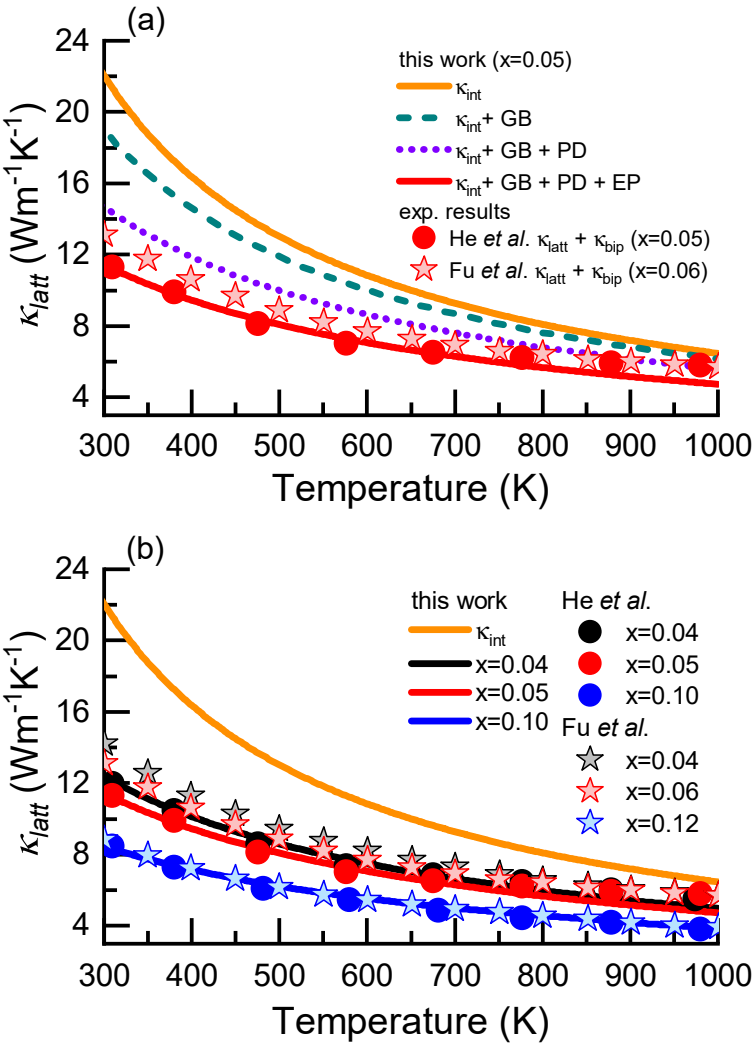

Figure 5.5: Figure (a) shows the contribution of grain boundaries GB, point defects PD and electron-phonon interaction EP to the lattice thermal conductivity κ_{int} of NbFeSb. Figure (b) compares the theoretical prediction of this study (solid lines) for $Nb_{1-x}Ti_xFeSb$ with L_{GB} = 0.5 μm to the experimental results (stars and circles).

conductivity agree very well with the experimental study, particularly with the He *et al*. study at temperature up to 700 K. There is a slight underestimate of the theoretical value of κ_{latt} at higher temperature for x=0.04 and x=0.05. This can be explained by the lack of a bipolar thermal conductivity (κ_{bip}) term in the calculations. In order to compute that, one needs to calculate a value for the electron relaxation time which depends on the doping level. Therefore, using the constant relaxation time approximation to compute κ_{bip} would yield inaccurate results. However, as it can be seen in Figure 5.5(b), the contribution of κ_{bip} is sufficiently small that the computed values are still in a good agreement with the experimental measurements.

5.3.4 Thermoelectric figure of merit

Figure 5.6 presents the final results on the thermoelectric figure of merit ZT for the p-type $Nb_{1-x}Ti_xFeSb$. A comparison between ZT values obtained in this study and the experimental data is shown in Figure 5.6(a). There is a good agreement up to T = 650 K between our results and the measurements conducted by He *et al*. The overestimate of ZT above this temperature for x = 0.04 and 0.05 can be explained by the missing κ_{bip} term in the lattice thermal con-

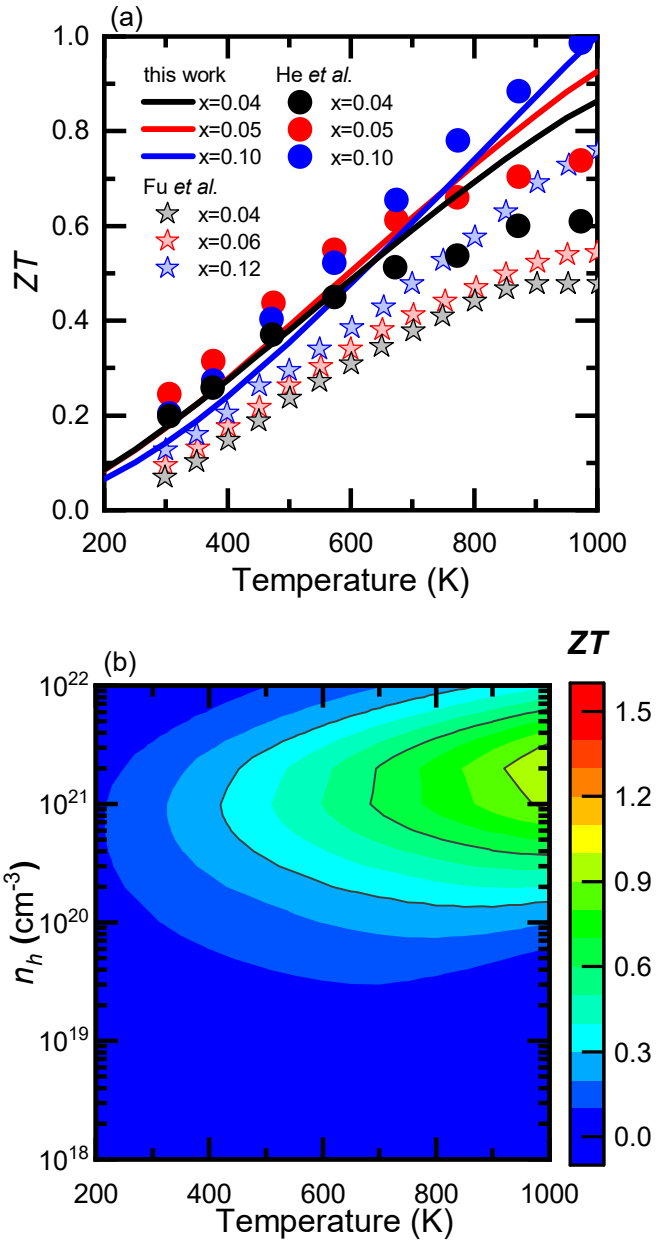

Figure 5.6: Comparison between our theoretical results and experimental measurements on p-type NbFeSb at x = 0.04, 0.05 and 0.10 (a). Colour map of p-type ZT with respect to the charge carrier concentration and temperature (b), with a maximum ZT of 1 at $n_h = 2 \times 10^{21}$ cm $^{-3}$ (x=0.1) and T = 1000 K.

ductivity. This has already been discussed in the previous section and explains why the agreement between the experimental and theoretical results at high temperatures improves with the increase of the doping concentration. Additionally, the limitations of the constant relaxation time approximation, e.g. no dependence on the chemical potential and no inclusion of the extrinsic scattering mechanisms, can easily add up and lead to the observed discrepancies at lower temperatures.

The results in this study slightly overestimate ZT when compared to Fu *et al*. [55] However, as with the lattice thermal conductivity results, there is a mismatch between the experimental results presented by He *et al*. and Fu *et al*. The latter uses a much lower annealing temperature, and so the density of the grain boundaries in the sample is expected to be higher. This further confirms that the constant relaxation time approximation could play a major role along with the bipolar term in the discrepancy between the theoretical and experimental results. The sample preparation in the Fu *et al*. study influences both the electrical and thermal conductivity, and as a consequence, the measured ZT values are expected to be a bit lower than the ones obtained in our calculations.

The colour map in Fig. 5.6(b) shows that NbFeSb remains most efficient at high temperature, despite the big power factor of PF = 9.3 mW/(m·K^2) at 300 K. The p-doped NbFesb displays its best figure of merit ($ZT \approx 1.0$) at T = 1000 K and high doping levels between x = 0.05 and 0.10, corresponding to $n_h = 1 \times 10^{21}$ and 2×10^{21} cm^{-3}. This result is typical for half-Heusler alloys [53] and illustrates that a reduction of κ_{latt} can significantly enhance the thermoelectric performance of similar half-Heusler alloys.

5.4 TaFeSb

5.4.1 Electronic structure

The crystal structure of TaFeSb is very similar to NbFeSb with the only difference being the atomic species on the X-site. The lattice constant is calculated to be 5.95 Å. The band structure and density of states (DOS) are presented in Fig. 5.7. The band gap of TaFeSb is calculated to be 0.86 eV, close to the value $\varepsilon_g = 0.93eV$ computed by Bhattachrya and Madsen [105]. It can be seen that the valence bands and DOS near the Fermi level remain almost unchanged when compared to NbFeSb. This suggests that the p-type S, σ and κ_{el} should exhibit the same behaviour as in NbFeSb, leaving the relaxation time as the

determining factor for any change in the electronic TE properties.

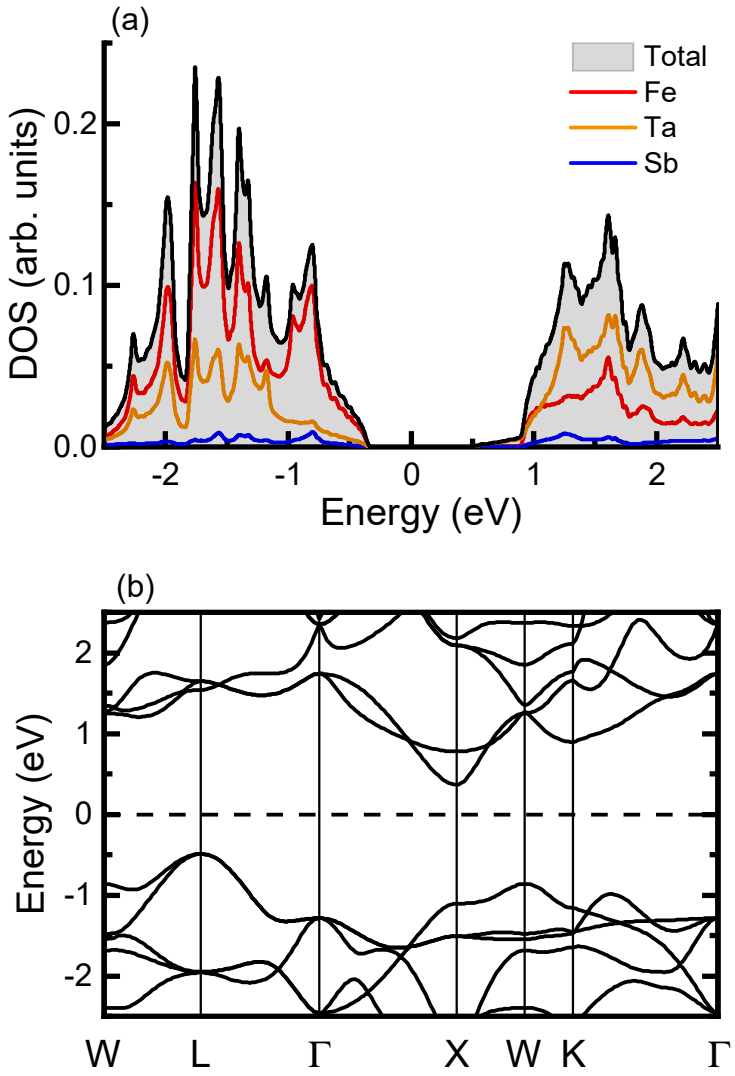

Figure 5.7: Density of states (a) and band structure (b) graphs of TaFeSb.

5.4.2 Electronic thermoelectric properties

The relaxation time along with the parameters necessary for its calculation are shown in Table 5.2. There is a noticeable reduction in the deformation potential values for both holes $V_{DP} = -11.06$ eV (-13.98 eV for NbFeSb) and electrons $V_{DP} = -11.81$ eV (-14.53 eV for NbFeSb). This means that stress has less effect on the electronic structure of TaFeSb. In addition, a slight reduction in the effective mass is also observed, with $m_h^* = 1.57(m_e)$. As a result, the mobility of the holes and relaxation time are increased to $\mu_h = 53.11$ cm^{2}V^{-1}s^{-1} and $\tau_h = 47.32$ fs.

Table 5.2: Parameters needed for electron and hole τ calculations of TaFeSb. These include the deformation potential constant (V_{DP}), effective mass of charge carriers (m^*), carrier mobility (μ) and relaxation time (τ) at 300 K for electrons and holes.

Carrier type	V_{DP} (eV)	m^* (m_e)	μ ($cm^2V^{-1}s^{-1}$)	τ (fs)
holes	−11.06	1.57	53.11	47.32
electrons	−11.81	0.38	1629.74	350.26

Next we present the electronic TE properties of TaFeSb in the form of colour maps in Fig. 5.8. The colour maps investigate a very wide doping and temperature range and might not be intuitive for comparison purposes. For that reason, we also provide 2D plots in Fig. 5.9, which compare the electronic properties of TaFeSb and NbFeSb for the common doping levels of x = 0.04, 0.05 and 0.10. The value of the *p*-type Seebeck coefficient for x=0.05 is calculated to be

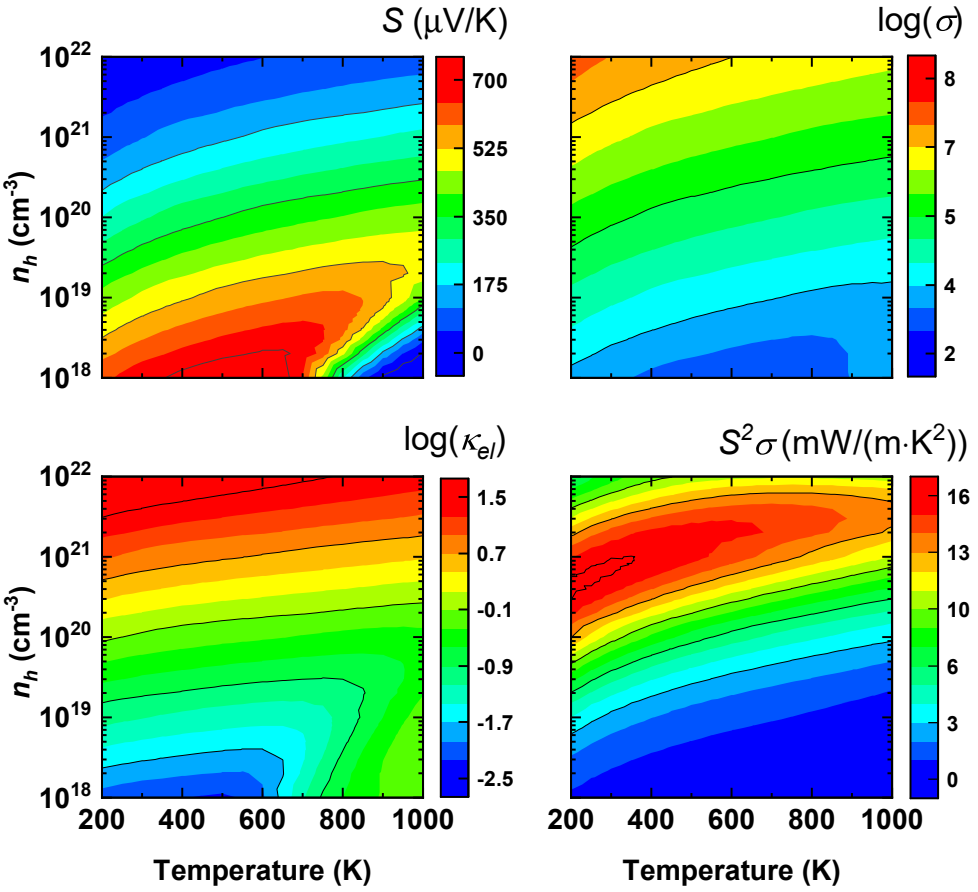

Figure 5.8: Colour maps of the electronic TE properties of *p*-type TaFeSb. The magnitude of the electrical conductivity σ (top right) and electronic thermal conductivity κ_{el} (bottom left) is given on a log scale. A maximum power factor (bottom right) value of PF = 16.11 mW/(m·K^2) is obtained at 300 K and $n_h = 7 \times 10^{20}$ cm^{-3} (x = 0.037).

113.81 and 247.5 μV/K at 300 and 1000 K, respectively. The change in S with respect to the NbFeSb results for the same doping concentration is less than 1%, which is expected due to the similarity in the valence bands of both materials. On the other hand, the bigger band gap in TaFeSb results in a bigger p-type S at a very low doping concentration and temperature around 600 K. This is visualised with an increase of the red area in Fig. 5.8(a) when compared to NbFeSb in Fig. 5.2(a). The results confirm that not only does TaFeSb exhibit a competitive Seebeck coefficient around the experimentally investigated doping levels, but also shows a significant improvement at very low n_h and moderate T.

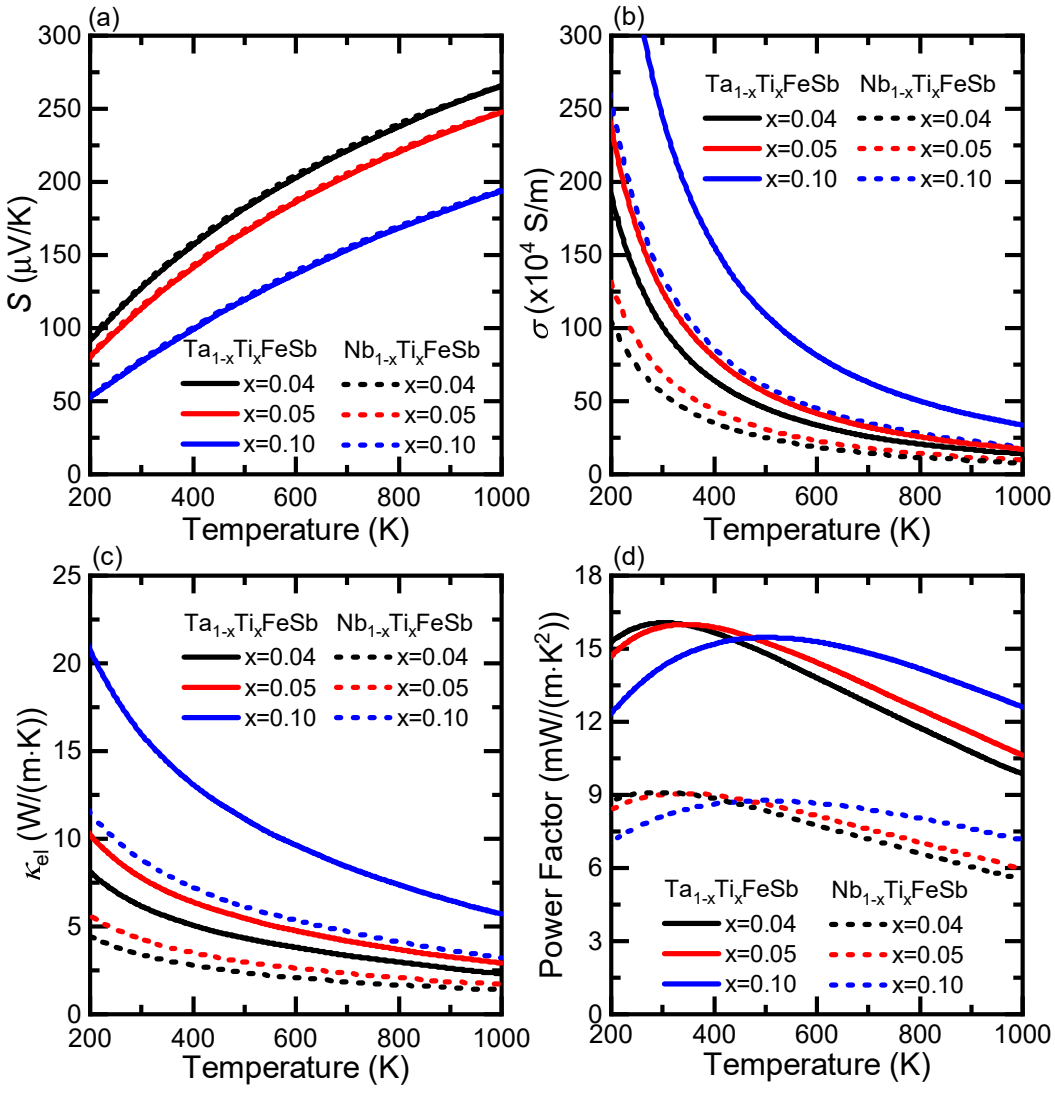

Figure 5.9: Comparison of the thermoelectric properties of TaFeSb and NbFeSb for x = 0.04, 0.05 and 0.10. The subfigures compare the Seebeck coefficient (a), electrical conductivity (b), electronic thermal conductivity (c), and power factor (d).

The results obtained from BoltzTraP for σ and κ_{el} predict a behaviour analogous to the changes observed for p-type S. Therefore, the increase of τ (holes),

which is $\approx 80\%$, yields a significant improvement in σ, and an increase in κ_{el}. The increase of σ leads to an astonishing power factor of $PF \approx 16$ mW/(m·K^2) at room temperature and x=0.03-0.05. For comparison, the power factor of NbFeSb is estimated to be 9-10 mW/(m·K^2), while the maximum value for Fe_2VAl is measured to be 5.5 mW/(m·K^2) [54]. The compounds based on the already established TE material Bi_2Te_3 have a power factor between 1.5 and 6 mW/(m·K^2) [191, 199, 200]. The improvement in PF of TaFeSb over NbFeSb is maintained over a wide range of doping levels from $n_h = 10^{20}$ cm^{-3} to $n_h = 2 \times 10^{21}$ cm^{-3} and at higher temperatures (compare Fig. 5.8(d) and Fig. 5.2(d) and note the unchanged ranges). In summary, TaFeSb has a significantly better electronic TE performance than NbFeSb due to the increased band gap and higher mobility of the charge carriers.

5.4.3 Lattice thermal conductivity

The phonon density of states of TaFeSb, presented in Fig. 5.10, show a close resemblance to the NbFeSb results. There are no imaginary frequencies and so this structure is also mechanically stable. The data is again in a very good agreement with the results obtained by Zeeshan *et al.* [160] The low frequency region is up to 150 cm^{-1} and is dominated by Sb. The intermediate region between 150 and 220 cm^{-1} is due to Ta, instead of Nb. The last region is dominated by Fe atomic vibrations and occupies the high frequencies up to 350 cm^{-1}. It is also noticeable that a gap is formed in between the regions dominated by Ta and Fe. Our calculations show that the intrinsic value of κ_{latt} is 20.57 and 5.75 Wm^{-1}K^{-1} at 300 and 1000 K, respectively. This is slightly lower

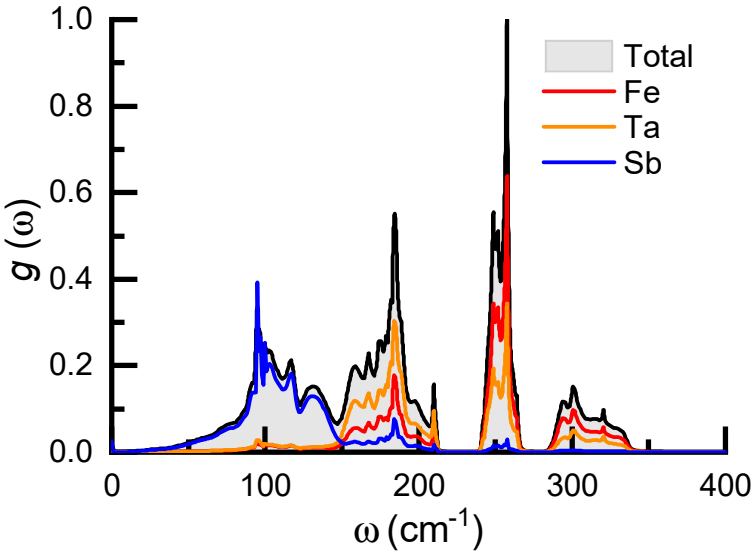

Figure 5.10: Phonon density of states of TaFeSb.

than the NbFeSb results and can be accounted for by the gap between Ta and Fe in Fig. 5.10.

5.4.3.1 Grain boundaries

The effect of grain boundaries on κ_{latt} of TaFeSb at 300 K is shown in Fig. 5.11. Grain boundaries of size 4.5 μm have an almost negligible effect on the lattice thermal conductivity. When their size is reduced to 0.5 μm κ_{latt} is computed to be 17.63 $Wm^{-1}K^{-1}$. Although a similar behaviour was noticed in NbFeSb, the presence of an additional gap in the phonon DOS of TaFeSb leads to a different phonon mean free path λ_{mfp} distribution. A common dip in the phonon thermal conductivity is observed for both TaFeSb and NbFeSb between 0.3 and 0.4 μm. This can be explained by the common gap in the phonon DOS at $\omega \approx 275$ cm^{-1}. However, whilst the Ta-Fe gap in TaFeSb leads to an extra dip at 0.08 μm, this has a small effect as phonons with λ_{mfp} less than 0.3 μm contribute less to the total lattice thermal conductivity. Despite this difference, grain boundaries of the same size seem to reduce κ_{latt} in both TaFeSb and NbFeSb by a similar amount. This means that the change in the phonon mean free path distribution has an effect only on the intrinsic value of κ_{latt} but little impact on the effect of grain boundaries.

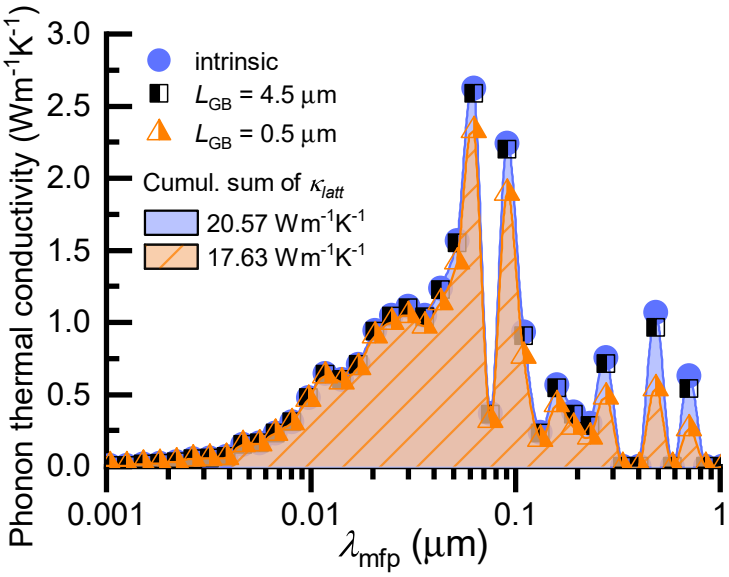

Figure 5.11: The impact of grain boundaries on the lattice thermal conductivity of TaFeSb at 300 K.

5.4.3.2 Point defects and electron-phonon interaction

Next we proceed by adding the contribution of the point defects due to Ti doping. The major difference between TaFeSb and NbFeSb is in the atomic

mass of the X element. The mass of Ta is 180.95 amu, whereas Nb is significantly lighter with a mass of 92.906 amu. One of the crucial parameters in the Klemens model [198] for the thermal conductivity of systems with point defects is the mass difference between the dopant atom (Ti) and the atoms which are substituted (Ta or Nb): a larger mass difference results in a greater reduction in the lattice thermal conductivity. Therefore, the lattice thermal conductivity of $Ta_{1-x}Ti_xFeSb$ is expected to be affected significantly by the Ti dopants. Fig. 5.12(a) illustrates this point by comparing the $Ta_{1-x}Ti_xFeSb$ and $Nb_{1-x}Ti_xFeSb$ results. It is indeed seen that the reduction in κ_{latt} of the Ta-based compound due to point defects (Ti doping) is much more significant.

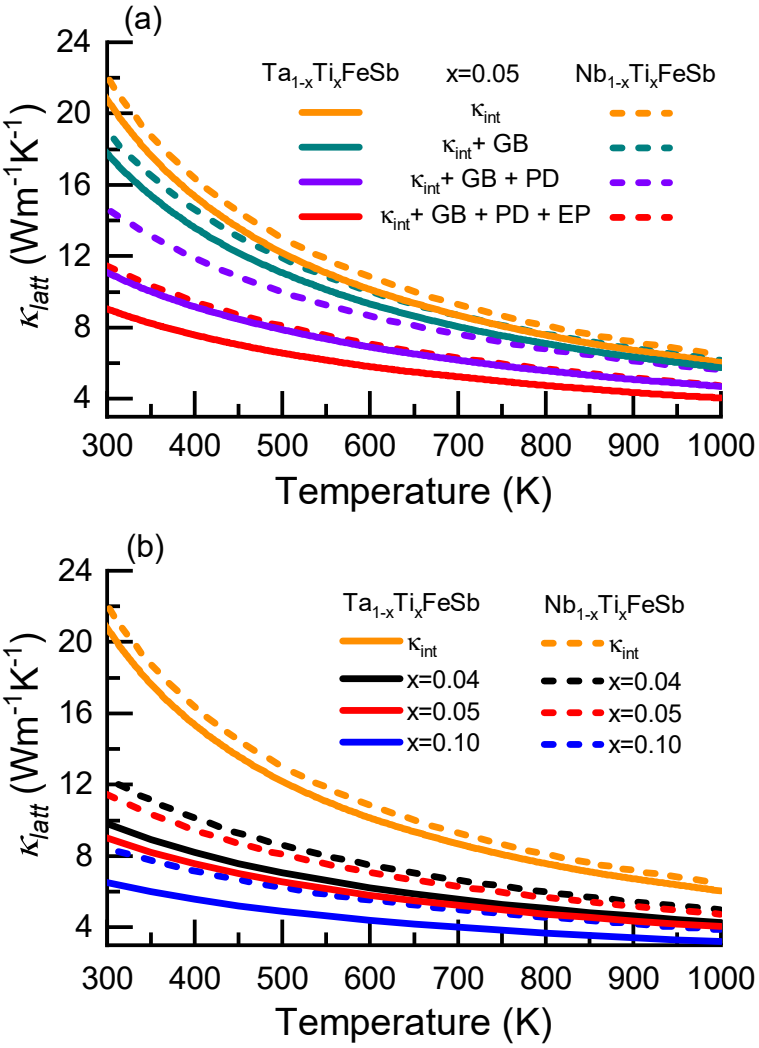

Figure 5.12: Figure (a) compares the lattice thermal conductivity of $Ta_{1-x}Ti_xFeSb$ (solid lines) and $Nb_{1-x}Ti_xFeSb$ (dashed lines) when the contribution of grain boundaries GB, point defects PD and electron-phonon interaction EP are added. The biggest change occurs when the contribution from point defects is added to the Ta-based compound. Figure (b) compares κ_{latt} with all contributions included at different doping levels.

For $Nb_{1-x}Ti_xFeSb$ the lattice thermal conductivity is reduced by 23% and 9% at 300 K and 1000 K, respectively, when the point defects are included. For $Ta_{1-x}Ti_xFeSb$ these numbers increase to 37% and 18% at 300 K and 1000 K, respectively.

The last contribution which needs to be added is the electron-phonon interaction. As already described, it is meaningless to use the constant relaxation time approximation to compute the electron-phonon interaction. For that reason, experimental data was used earlier to obtain a value for the NbFeSb compound. Unfortunately, there are no experimental measurements which can be used to extract a value for the electron-phonon contribution in TaFeSb. For practical purposes and because of the similarity in the electronic structure and phonon DOS between TaFeSb and NbFeSb, we will use the electron-phonon contribution which was extracted for NbFeSb. In the worst case, such an approximation would lead to an overestimate of κ_{latt} and an underestimate of the ZT of TaFeSb rather than the opposite.

The lattice thermal conductivity of $Ta_{1-x}Ti_xFeSb$ and $Nb_{1-x}Ti_xFeSb$ at different doping levels with all contributions included is shown in Fig. 5.12(b). The trend shows that κ_{latt} of the Ta-based compound is lower at all doping levels. At x=0.05, κ_{latt} is lower by 21% (κ_{latt}=8.99 $Wm^{-1}K^{-1}$) and 15% (κ_{latt}=4.04 $Wm^{-1}K^{-1}$) at 300 K and 1000 K, respectively. At x=0.10, the reduction is 23% (κ_{latt}=8.43 $Wm^{-1}K^{-1}$) and 18% (κ_{latt}= 3.20 $Wm^{-1}K^{-1}$) at 300 K and 1000 K, respectively. The improvement of 15-23%, as already discussed, comes from the slightly lower intrinsic value of κ_{latt} for TaFeSb and the bigger mass difference between Ta and Ti. There is also a noticeable similarity of the lattice thermal conductivity of $Ta_{1-x}Ti_xFeSb$ at x=0.05 and that of $Nb_{1-x}Ti_xFeSb$ at x=0.10. This hints that TaFeSb might require less doping than NbFeSb to reach its maximum ZT value.

5.4.4 Alternative ways of computing the intrinsic lattice thermal conductivity

As discussed before, the intrinsic lattice thermal conductivity can be calculated in several ways. Here we compare the results obtained for NbFeSb and TaFeSb by solving the phonon BTE (ShengBTE) and Slack's equation. For Slack's equation, we use the approach suggested by Jia *et al*. [108], where Θ_D and γ are calculated from the bulk and shear moduli. These results are presented in Table 5.3. We also compare the NbFeSb results to the one obtained by Hong *et al*., who employed the quasi-harmonic approximation (QHA) to calculate Θ_D and γ before solving the Slack's equation. In terms of speed, Jia *et al*. approach is

the fastest one, followed by QHA method, while the phonon BTE remains last.

Table 5.3: Elastic constants, bulk (B_H) and shear (G_H) moduli of NbFeSb and TaFeSb. The longitudinal, transverse and average phonon velocities are given by v_L, v_T, v_{av}, respectively. Grüneisen parameter and Debye temperature are given by γ and Θ_D. Experimental results are taken from Tavassoli *et al.* [190], where the data is obtained via Resonant Ultrasound Spectroscopy (RUS) at room temperature.

Compound	NbFeSb (this work)	NbFeSb (exp RUS [190])	TaFeSb (this work)
c_{11} (GPa)	311.5	-	326.8
c_{12} (GPa)	94.3	-	100.3
c_{44} (GPa)	66.0	-	77.6
B_H (GPa)	166.7	156	175.8
G_H (GPa)	80.7	81	89.6
v_L (m/s)	5 674	5 597	5 115
v_T (m/s)	3 082	3 099	2 818
v_{av} (m/s)	3 438	3 452	3 140
γ [from phonon BTE]	1.76	-	1.79
γ [from elastic moduli]	1.72	-	1.64
Θ_D (K)	393.4	394	359.5

We can see in Fig. 5.13 that all tested methods yield relatively close results for NbFeSb, with the largest difference between the values of κ_{int} being 11% at room temperature. The TaFeSb results, however, show a difference up to 27% at room temperature, which will have a noticeable impact on the rest of the ZT calculations.

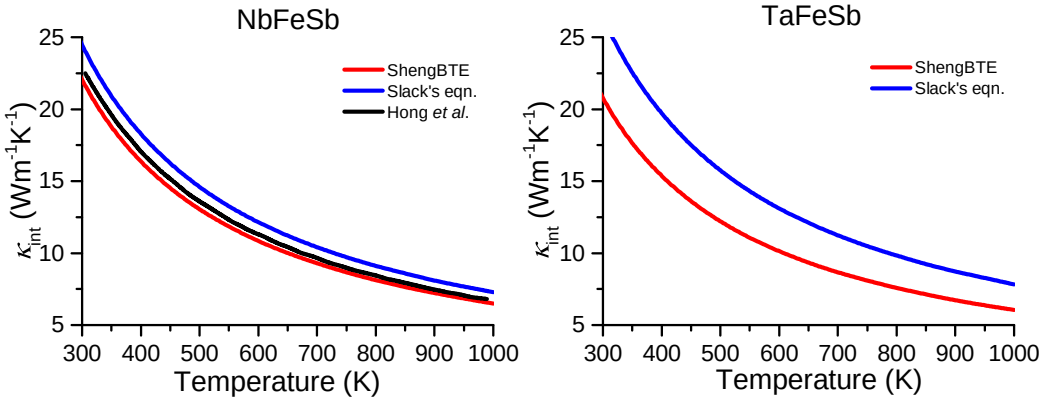

Figure 5.13: Comparison of the intrinsic lattice thermal conductivity of NbFeSb (left) and TaFeSb (right) when obtained by solving the phonon BTE and the Slack's equation.

Our analysis suggests the larger discrepancy in the TaFeSb results is mainly due to the different Grüneisen parameter (a measure of the anharmonicity of the system) obtained using ShengBTE or the elastic moduli, as shown in Table 5.3. Therefore, it can be concluded that Slack's equation offers a rather

inexpensive way of calculating the lattice thermal conductivity of NbFeSb, but a more sophisticated approach, like the phonon BTE, is required to calculate accurately the anharmonicity and the lattice thermal conductivity of TaFeSb.

5.4.5 Comparison between *ZT* of *p*-type TaFeSb and NbFeSb

Finally, we present the results on *ZT* of $Ta_{1-x}Ti_xFeSb$ and compare them to the $Nb_{1-x}Ti_xFeSb$ results. Fig. 5.14 shows that the maximum thermoelectric figure

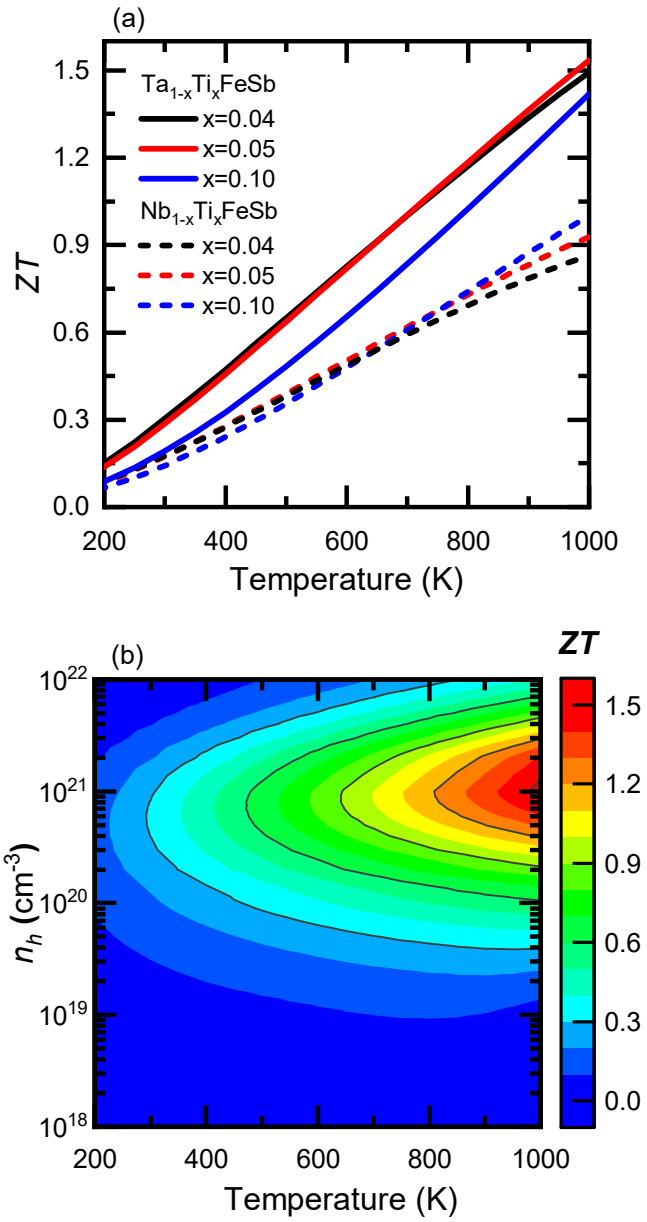

Figure 5.14: Comparison between *p*-type TaFeSb and NbFeSb at x = 0.04, 0.05 and 0.10 (a). Subfigure (b) is a colour map which shows the *ZT* of *p*-type TaFeSb with respect to the charge carrier concentration and temperature, with a maximum *ZT* of 1.53 at $n_h = 1 \times 10^{21}\text{cm}^{-3}$ (x=0.05) and T = 1000 K.

of merit is obtained at T=1000 K, x=0.05 and is equal to ZT=1.53. For comparison the maximum ZT value for $Nb_{1-x}Ti_xFeSb$ is only 1.01, and at x=0.10. Fig. 5.14(a) shows that $Ta_{1-x}Ti_xFeSb$ exhibits higher ZT across the entire temperature range and at all doping levels. The main difference to $Nb_{1-x}Ti_xFeSb$ is that there is a 50% increase in ZT and that the peak is achieved at x=0.05 rather than x=0.10, which is in agreement with the prediction made in the lattice thermal conductivity section.

The colour map in Fig. 5.14(b) reveals a broad area between 800 and 1000 K, and x=0.02 and x=0.15 in which the ZT of $Ta_{1-x}Ti_xFeSb$ is higher than 1.2. At moderate temperature (500–700 K) the ZT value drops to ≈ 1, which is still considered as an excellent TE result. Even at room temperature, the TE figure of merit (ZT=0.3) is almost 2 times bigger than that of NbFeSb (ZT=0.17). The wide range of conditions, which result in a good ZT value, suggests that p-type TaFeSb can indeed be used as a novel material for efficient thermoelectric devices.

5.5 Conclusions

We have conducted a thorough study of the thermoelectric properties of p-type NbFeSb and TaFeSb. In addition to solving the Boltzmann transport equations for electrons and phonon with *ab initio* inputs, several approximations were also included in the process. These are the constant relaxation time approximation with no dependence on the chemical potential due to doping, the choice of grain boundary size and the inclusion of the electron-phonon interaction based on experimental data. This multi-step procedure needs to be executed with caution, and so at each step the results have been thoroughly compared to the available experimental measurements. We would like to point out that although the results in this study look promising and are consistent with the expectations, one should not use the presented theoretical framework lightly on fully unknown compounds. The key feature of this study was to preserve the chemical environment of NbFeSb and change it slightly to TaFeSb in a way that the empirical Klemens' equation is still applicable.

In summary, the NbFeSb results agree extremely well with multiple theoretical and experimental studies. The same procedure was then used to perform a full-scale computation on the TE properties of TaFeSb. The results have shown that both compounds exhibit high power factor at room temperature and have a good thermoelectric figure of merit at high temperatures. At 1000 K we find PF = 9 mW/(m·K^2) and ZT = 1 for NbFeSb and PF = 16 mW/(m·K^2) and ZT =

1.5 for TaFeSb. The higher atomic mass of Ta (compared to Nb) increases the scattering strength in Ti-doped TaFeSb, which reduces the lattice thermal conductivity of the compound. At the same time, *p*-type charge carries in TaFeSb exhibit higher mobility and relaxation time, which increases the power factor. The net result is a material with an amazing power factor of 16 $mW/(m{\cdot}K^2)$ and ZT value which is approximately 50% better than that of NbFeSb.

In conclusion, TaFeSb not only appears to be a better TE material than NbFeSb, but it also opens a new path of TE optimisation of materials based on the two alloys. In theory, an alloy based on $Nb_{1-x}Ta_xFeSb$ should exhibit good electrical properties due to the similarities in the electronic structure of NbFeSb and TaFeSb. At the same time, the mass difference between Nb and Ta should create additional scattering centres which would suppress the lattice thermal conductivity even before doping, and so the final doped compound should exhibit an even higher ZT value. This is further hinted by a very recent experimental study by Yu *et al*. [193], which reports the successful synthesis of $Nb_{1-x}Ta_xFeSb$ alloys and a measured ZT of up to 1.6.

Chapter 6

Complex optimisation of electronic thermoelectric properties

6.1 Introduction

There are multiple mechanisms which can be used to optimise the thermoelectric performance. The best thermoelectric candidates usually exhibit excellent electronic properties but high thermal conductivity. Lattice vibrations are responsible for the majority of the heat transport in semiconductors. Therefore, most optimisation techniques aim to disrupt the lattice heat transport by introducing scattering centres, i.e. making the structure as complex as possible. As a side effect this could lead to a reduction in the electronic thermoelectric performance, thus yielding no net improvement in the figure of merit.

So far we have focused on computing the properties of bulk materials with simple unit cells which contain only a few atoms. In this chapter, we will change the approach and test more complex structures. We will include the structural modifications due to the various optimisation techniques explicitly into the first principles calculations. The number of simulated atoms will increase an order of magnitude from 4-12 in the bulk cases to 48-120 for the superstructures. The computation time scales cubically with the number of electrons and while density of states calculations remain feasible, force constants calculations become extremely demanding. Nevertheless, we know that all thermoelectric optimisation techniques discussed in Section 1.5 ruin the perfect crystal lattice and affect negatively the lattice thermal conductivity. Therefore, we will focus only on the electronic properties and see how affected they are by the structural modifications. Superstructures also make calculating electron relaxation time (τ) computationally very demanding. For that reason and due to the lack of chemical potential dependence in the deformation potential

theory, we will assume a constant value of $\tau = 10^{-14}$ s for all BoltzTraP results in this chapter. This will not only make the computation time manageable, but will also allow us also to draw a comparison between different compounds entirely based on the changes in their density of states.

The optimisation techniques which we test in this chapter include doping, planar defects and size reduction. In terms of materials, we revisit the Heusler alloys and investigate various Bi_2Te_3 structures. Results are split into three main sections. First we investigate how doping changes the Seebeck coefficient (S), electrical conductivity (σ), electronic thermal conductivity (κ_{el}) and power factor (PF). This involves testing both cases with and without changing the number of valence electrons. The second section investigates how antiphase boundaries modify the electronic thermoelectric (TE) properties of both Fe_2VAl and Bi_2Te_3. The final section reveals some very interesting results on the thermoelectric properties on Bi_2Te_3 thin films.

6.2 Effects of doping thermoelectric compounds

6.2.1 Doping Fe_2VAl with Si, Ge and Sn

We start by looking at the simplest case, which is explicitly doping Fe_2VAl with group IV elements: Si, Ge and Sn. Calculations were performed on the ordered $L2_1$ structure of Fe_2VAl in a hexagonal unit cell. The usage of the hexagonal cell allows for an uniform distribution of the dopant atoms in a superstructure which contains only 48 atoms. In case of a cubic supercell, the number of atoms would have been 128. The bulk structure contains 3 formula units while the doped systems are investigated with $2 \times 2 \times 1$ supercells containing 12 formula units. Dopants substitute 1 Al atom in the supercell which corresponds to a doping concentration of x=0.083 in the n-type $Fe_2VAl_{1-x}Z_x$ (Z=Si, Ge or Sn).

First principles calculations were performed with the CASTEP code [123] and a GGA-PBE exchange-correlation functional [126]. On-the-fly ultrasoft pseudopotentials (C9 set) were used with a plane-wave cut-off energy of 700 eV and a grid scale of size 2.0. The Brillouin zone was sampled using a Monkhorst-Pack grid [151] with a **k**-points spacing of $0.05\ 2\pi\text{Å}^{-1}$. The ionic positions were fully relaxed until forces between atoms were less than 0.01 eV/Å. Transport properties were calculated using BoltzTraP [100]. Density of states were computed on a much denser **k**-points grid of spacing $0.008\ 2\pi\text{Å}^{-1}$. The Hubbard U model was not used in this set of calculations. The main motivation behind this decision was to see whether dopants can affect on their own the symmetry of

the Seebeck coefficient and bring it closer to the experimental expectations [54].

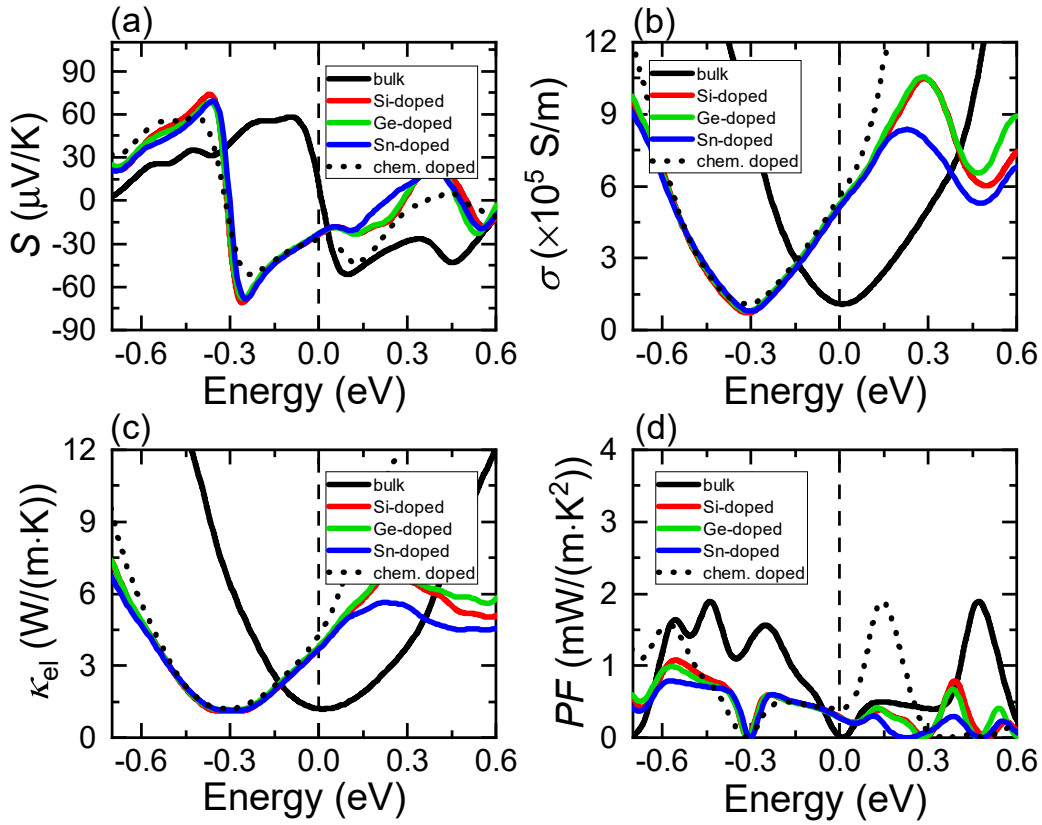

Figure 6.1: Electronic thermoelectric properties of doped Fe_2VAl at T=300 K. S, σ, κ_{el} and PF are given in subfigures (a)–(d). Bulk results are given in black, while Si-, Ge- and Sn-doped results are in red, green and blue, respectively. Dotted line simulates chemical doping. Dashed line corresponds to the Fermi level.

The electronic thermoelectric properties of the explicitly doped Fe_2VAl at T= 300 K are shown in Fig. 6.1. Fermi level is given with a vertical dashed line at 0 eV. Results above and below the Fermi level correspond to n- and p-type doping, respectively. Looking at Fig. 6.1(a) we notice that there is a very small change in the shape of S. The absolute maximum for n- and p-type doping changes from around $-/+55$ μV/K for the bulk structure to around $-/+70$ μV/K for the doped compounds. The difference is cause by the reduction of the pseudo gap from -0.13 to -0.11 eV. While the states introduced by the dopants have a small effect, they do not lead to the experimentally observed asymmetric behaviour of the Seebeck coefficient. The other noticeable difference is that the Fermi level has been shifted by the same amount when doping with Si, Ge and Sn. We see that in all cases a change of 0.3 eV corresponds to doping with x=0.083 additional electrons per formula unit. This agrees well with expectations since all dopants introduce only one additional electron to the system. When comparing the doped compounds to the bulk, we should note that the region between -0.3 and $+0.3$ eV for the bulk corre-

sponds to the region between -0.6 and 0 eV for the doped structures. This is highlighted by the dotted line, which is obtained via chemical doping, i.e. setting the Fermi level in the bulk at an energy level which yields a doping concentration of x=0.083. Apart from the small change in S, the BoltzTraP chemical doping matches very well the explicit doping in that area.

When we look at σ and κ_{el} in Fig. 6.1(b) and (c) we notice that there is a small decrease in the absolute minimum of both quantities, which is expected since we had an increase in the Seebeck maximum value. It can also be seen that in both cases the increase of σ and κ_{el} above the Fermi level does not follow the trend predicted by the bulk material. It seems that heavier doping would have a reduced positive effect on both types of conductivity. The power factor in Fig. 6.1(d) shows that all doped compounds exhibit similar behaviour between -0.3 and 0 eV, which is in a good agreement with the bulk prediction for the region between 0 and $+0.3$ eV. The similarities between the Si- and Ge-doped results agree well with the experimental observations made by Nishino and Deguchi [187].

While we could not reproduce the experimental asymmetry in the Seebeck coefficient of Fe_2VAl by explicitly doping the material, we observed that Si, Ge and Sn modify the electronic properties of the Heulser alloy in an identical way. It can be noted that the doping concentration of x=0.083 is slightly beyond the optimal efficiency and lower doping levels would be more beneficial. Taking into account the reduction of the total lattice thermal conductivity due to the mass-difference scattering strength and that Sn is the heaviest among the investigated dopants we can expect that $Fe_2VAl_{1-x}Sn_x$ will exhibit the highest ZT of the three cases.

6.2.2 Transitioning from NbFeSb to TaFeSb

The next optimisation technique which we investigate involves some heavy doping. It does not attempt to make the semiconductor n- or p-type but rather keep its neutral bulk properties. In other words, we will be trying to find a new starting compound, which can be tuned later on. We have investigated the half-Heusler alloys NbFeSb and TaFeSb in Chapter 5. They both exhibit excellent p-type thermoelectric properties with the main difference being that TaFeSb exhibits larger hole relaxation time and lower lattice thermal conductivity due to the heavier Ta atom. Since Nb and Ta have the same number of valence electrons and both NbFeSb and TaFeSb have almost identical lattice constants, it will be interesting to investigate if mixing them would result in a stable structure which keeps the excellent thermoelectric properties. In this

chapter we test the thermoelectric properties of $Nb_{1-x}Ta_xFeSb$ with x=0, 0.25, 0.50, 0.75 and 1.

In terms of computation, we kept using the GGA-PBE exchange-correlation functional and the on-the-fly ultrasoft pseudopotentials from the C9 set. The plane-wave cut-off energy was 700 eV with a grid scale of size 2.0. The Brillouin zone sampling was done on a mesh with **k**-points spacing of 0.021 2πÅ^{-1}. Spectral calculations were performed on a denser mesh with **k**-points spacing of 0.007 2πÅ^{-1}.

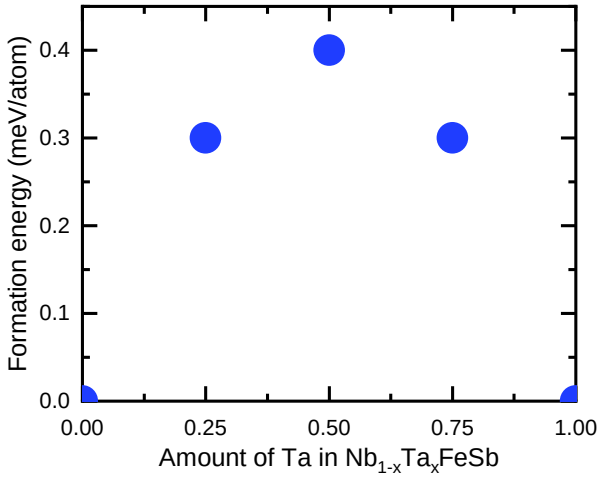

Figure 6.2: Formation energy of $Nb_{1-x}Ta_xFeSb$.

We show the formation energy of the intermediate compounds with respect to the stable NbFeSb and TaFeSb in Fig. 6.2. The formation energy is computed using Eqn. 6.1:

$$\Delta E_{\text{form}} = E(Nb_{1-x}Ta_xFeSb) - ((1-x) \times E(NbFeSb) + x \times E(TaFeSb)). \quad (6.1)$$

Despite all values being positive, the scale on y-axis (meV/atom) suggests that we might be close the noise level within the DFT calculation.

Figure 6.3 shows the electronic thermoelectric properties of $Nb_{1-x}Ta_xFeSb$. The power factor of these half-Heusler alloys is at its maximum around room temperature and therefore we plot the data at T=300 K. The maximum value of the Seebeck coefficient increases gradually with the concentration of Ta. The other quantities σ, κ_{el} and PF are described by similar curves which are have an off-set along the x-axis. Such behaviour can be explained by the fact that these materials have similar band structures but different band gaps. In fact, the band gap of NbFeSb is 0.53 eV and increases linearly with the concentra-

tion of Ta up to 0.93 eV for TaFeSb.

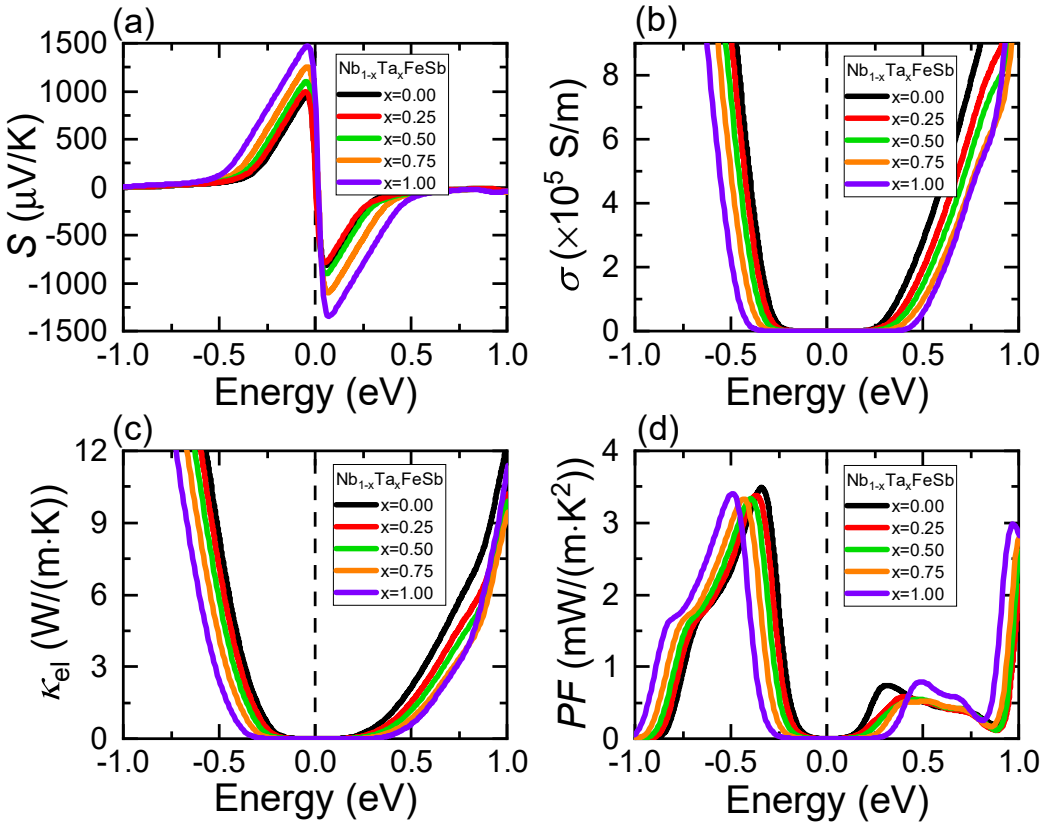

Figure 6.3: Electronic thermoelectric properties of $Nb_{1-x}Ta_xFeSb$ at T=300 K. S, σ, κ_{el} and PF are given in subfigures (a)–(d). Different doping concentrations of x = 0, 0.25, 0.50, 0.75 and 1 are given in black, red, green, orange and violet, respectively. Dashed line corresponds to the Fermi level.

The only difference between the $Nb_{1-x}Ta_xFeSb$ compounds is in the band gap and in this case it is more convenient if we change the x-axis from energy to number of additional electrons per formula unit, as if the compounds were doped with another material (Y), e.g. $(Nb_{1-x}Ta_x)_{1-y}Y_yFeSb$. Figure 6.4 illustrates the thermoelectric properties of $Nb_{1-x}Ta_xFeSb$ if we make it *p*-type (negative additional electrons) or *n*-type (positive additional electrons). We see that *p*-type thermoelectric properties of all $Nb_{1-x}Ta_xFeSb$ alloys are identical when using similar hole relaxation time. The *n*-type side is different though. It shows that the compounds with more Ta exhibit much higher *n*-type power factor when there are more than 0.1 additional electrons per formula unit.

One of the advantages of the intermediate $Nb_{1-x}Ta_xFeSb$ (x=0.25, 0.50 and 0.75) compounds is that the mixture of Nb and Ta introduces additional scattering centres which should decrease the intrinsic lattice thermal conductivity. The fact that the compounds are stable and the mixing does not ruin the *p*-type electronic thermoelectric properties suggests that $Nb_{1-x}Ta_xFeSb$ can exhibit *p*-type ZT values which are even higher than that of TaFeSb (ZT=1.5).

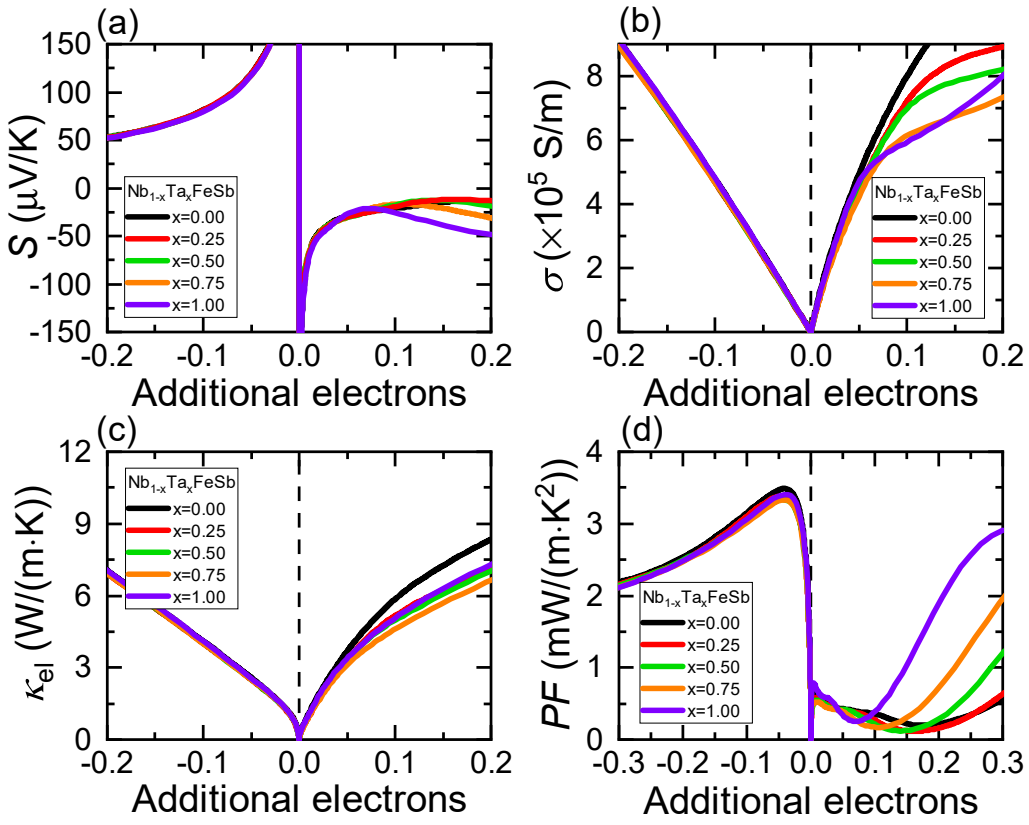

Figure 6.4: $Nb_{1-x}Ta_xFeSb$ electronic thermoelectric properties at 300 K with respect to additional electrons per formula unit. S, σ, κ_{el} and PF are given in subfigures (a)–(d).

In addition, the n-type results reveal a surprising trend which suggests that TaFeSb might exhibit very good n-type thermoelectric properties. Considering how scattering centres affect the lattice thermal conductivity in the mixed compounds, $Nb_{0.25}Ta_{0.75}FeSb$ might posses the best n-type ZT among the investigated group of half-Heusler alloys.

6.3 Modelling planar defects in thermoelectric compounds

The next optimisation mechanism which we test is based on planar defects. In theory, they should act as a wall which scatters phonons more effectively than charge carriers. In this section we investigate how anti-phase grain boundaries (APBs) affect the electronic thermoelectric properties of Fe_2VAl and Bi_2Te_3.

6.3.1 Anti-phase boundary in Fe_2VAl

We start by looking at Fe_2VAl. We use a hexagonal unit cell to model the APB, shown in Fig. 6.5. There are usually two boundaries due to periodic boundary conditions in this type of calculations. Here, however, the stacking in the hexagonal cell allows us to remove one Fe atom and return to the expected order at the cell boundary. Therefore, instead of two boundaries there is only one APB along the c-axis of the hexagonal cell and the height of the unit cell determines the separation between the APBs.

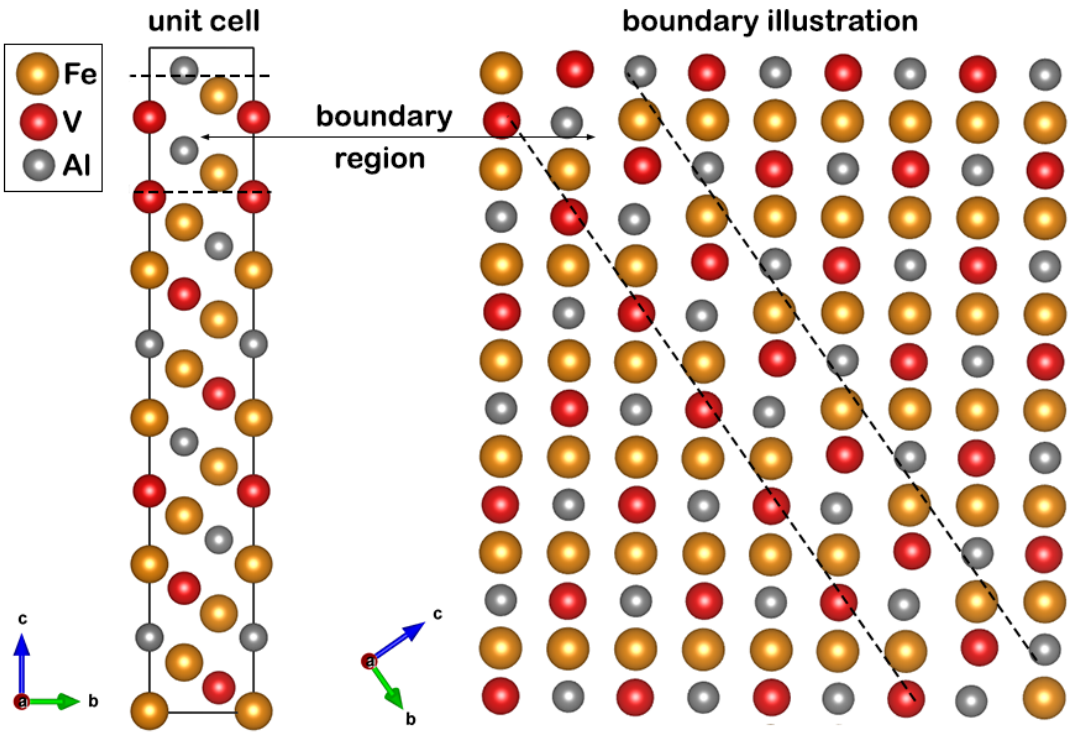

Figure 6.5: Illustration of the anti-phase boundary in Fe_2VAl.

Anti-phase boundaries can be considered as an array of antisite defects. This can be seen in the boundary illustration in Fig. 6.5, where Fe and V-Al layers swap places within the boundary. One speculations for the discrepancy between theory and experiments regarding S asymmetry is the presence of antisite defects in Fe_2VAl [178, 201]. Therefore, we will use the same computational settings as in Section 6.2.1 (again without Hubbard U) and test how APBs affect the electronic thermoelectric properties. The separation between APBs in Fe_2VAl is reported to be around 100 nm in experimental studies [202, 203]. Such a calculation would require a simulation with more than a thousand atoms. Instead we focus on three manageable cases in which the boundaries are separated by 1.2, 2.2 or 4.2 nm. The height of the hexagonal unit cell without any stacking faults is 1 nm.

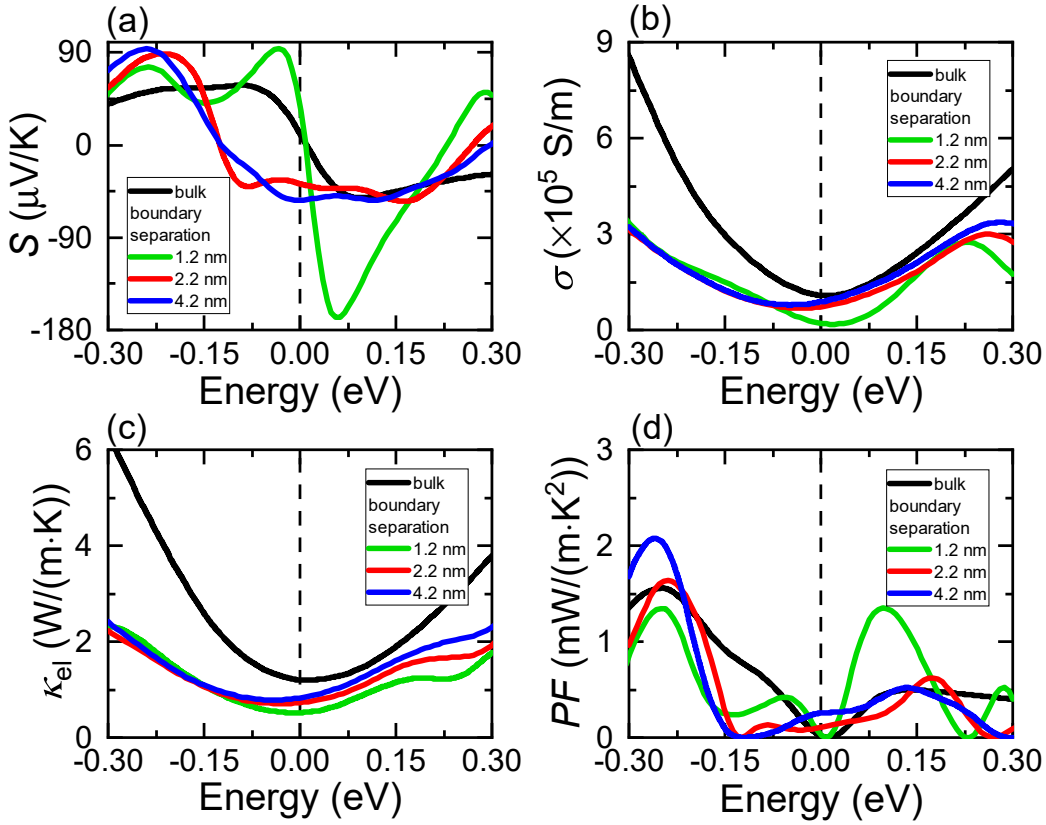

Figure 6.6: Effect of the anti-phase boundary on the electronic thermoelectric properties of Fe_2VAl at T=300 K. S, σ, κ_{el} and PF are given in subfigures (a)–(d). Dashed line corresponds to the Fermi level.

The electronic thermoelectric properties are shown in Fig. 6.6. Looking at the Seebeck coefficient we see that there is a huge difference in the maximum values when the boundaries are only 1.2 nm across each other. The shape of the curve is asymmetric and the maximum S for p- and n-type becomes $+95$ and -170 μV/K, respectively. When we increase the separation between the APBs to 2.2 and 4.2 nm, the maximum n-type values of S decrease drastically and return to the bulk values of -55 μV/K. On the p-type side both maxima remain above $+90$ μV/K though. The other interesting finding is that for 2.2 and 4.2 nm boundary separation the Fermi level looks shifted towards the n-type. Such behaviour is rather similar to the results reported in recent study which states that APBs make NbFeSb n-type semiconductor [197]. Regarding σ we see that decreasing the density of the APBs brings the electrical conductivity closer to bulk values for n-type semiconductor but leaves them much lower for p-type. The electrical thermal conductivity remains below the bulk values in all cases. Power factor behaviour is rather interesting. We see that the best n-type performance is obtained when the APBs separation is only 1.2 nm but would require light doping of approximately 0.03–0.04 additional electrons per formula unit. The energy range in Fig. 6.6 corresponds to having a

maximum of -0.2 to $+0.2$ additional electrons per formula unit. The 2.2 and 4.2 nm cases look somewhat similar thus we focus on the 4.2 nm APBs. In this case we see that *PF* has a finite value of 0.2 mW/m·K^2 at the Fermi level, which does not require further doping to be achieved. This comes from the fact that σ remains close to the bulk values at the Fermi level but S is enhanced to -55 μV/K. Regardless of the finite *PF* at the Fermi level, Fig. 6.6(d) shows that *n*-type doping does not further improve the *PF* of the 2.2 and 4.2 nm APBs and leave their performance on par with bulk.

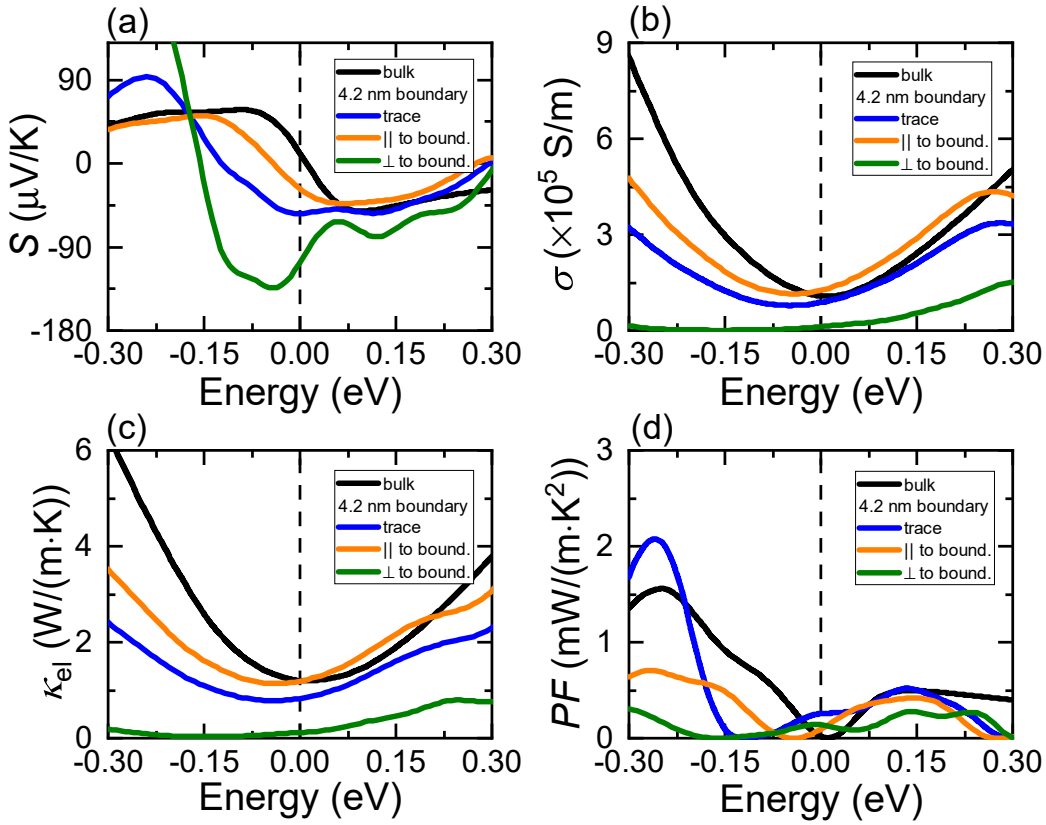

Figure 6.7: Difference in the electronic thermoelectric properties for the 4.2 nm boundary in planes parallel (∥, orange curve) and perpendicular (⊥, green curve) to the boundary. Bulk isotropic properties are in black, whereas the trace for the boundary properties is in blue. S, σ, κ_{el} and *PF* are given in sub-figures (a)–(d). Dashed line corresponds to the Fermi level.

Up until now we have not considered that anti-phase boundaries make our material anisotropic. Figure 6.7 shows the difference in the electronic thermoelectric properties for the 4.2 nm boundary in planes parallel (orange curve) and perpendicular (green curve) to the APB. We see that there is a big difference in S when moving along the two directions. The Seebeck coefficient almost overlaps with the bulk values when we are in the plane parallel to the APB, with the main difference being a slight shift of the Fermi level towards the *n*-type side. The value of S along the perpendicular direction is much higher at the Fermi level while the curve does not show any resemblance to the shape of

S in the bulk isotropic case. In terms of conductivity, APBs act as expected and completely ruin σ and κ_{el} in the plane perpendicular to the boundary. Results along the parallel plane are bulk-like but shifted towards the n-type side, similar to the Seebeck coefficient. In terms of PF, the perpendicular plane exhibits higher value at the Fermi level than the parallel plane. This result is rather counter-intuitive, especially considering the low values of σ illustrated by the green curve in Fig. 6.7(b).

Anti-phase grain boundaries have a significant impact on the electronic thermoelectric properties of Fe_2VAl. We have seen that n-type properties are considerably improved when the APB concentration is very high (1.2 nm). The asymmetry in S is also present. While such high density is not reported experimentally, it creates an interesting opportunity for nanostructuring and stability investigations. Lower APB densities exhibit n-type semiconductor properties. In the plane parallel to the APB with separation of 4.2 nm, S, σ seem to be converging towards the bulk values. In contrast, the results in the plane perpendicular to the APB remain inconclusive, especially considering that our modelled APB separation of 4.2 nm is much shorter than the experimentally measured values of 100 nm and that the shape of S in Fig. 6.7(a) is qualitatively very different to the bulk one. Taking into account that the experimental APB separation is much longer than in our model and that we did not observe an asymmetric behaviour in S for the boundary separations of 2.2 and 4.2 nm, it seems very unlikely that anti-phase boundaries are responsible for the asymmetry in the Seebeck coefficient of Fe_2VAl.

6.3.2 Anti-phase boundary in Bi_2Te_3

We have already discussed that Bi_2Te_3 is the most widely used thermoelectric material. It has a trigonal crystal structure with space group $R\bar{3}m$ (166). Each repetition of the formula unit creates a layered structure, called quintuple layer (QL), in a sequence of Te(1)-Bi-Te(2)-Bi-Te(1), where 1 and 2 denote two different chemical states for the anions. Quintuple layers are weakly bonded to each other via the van der Waals forces, which means that during growth the structure is susceptible to the formation of grain boundaries. There are reports which suggest that grain boundaries have a positive effect on the p- and n-type thermoelectric properties of Bi_2Te_3[75, 76]. One hypothesis is that the positive effect is due to the presence of charged donor-like defects arising from an antisite altering at the grain boundary. Here, we test whether anti-phase boundaries can give rise to a similar behaviour.

To model the APBs we use a hexagonal unit cell with experimental lattice con-

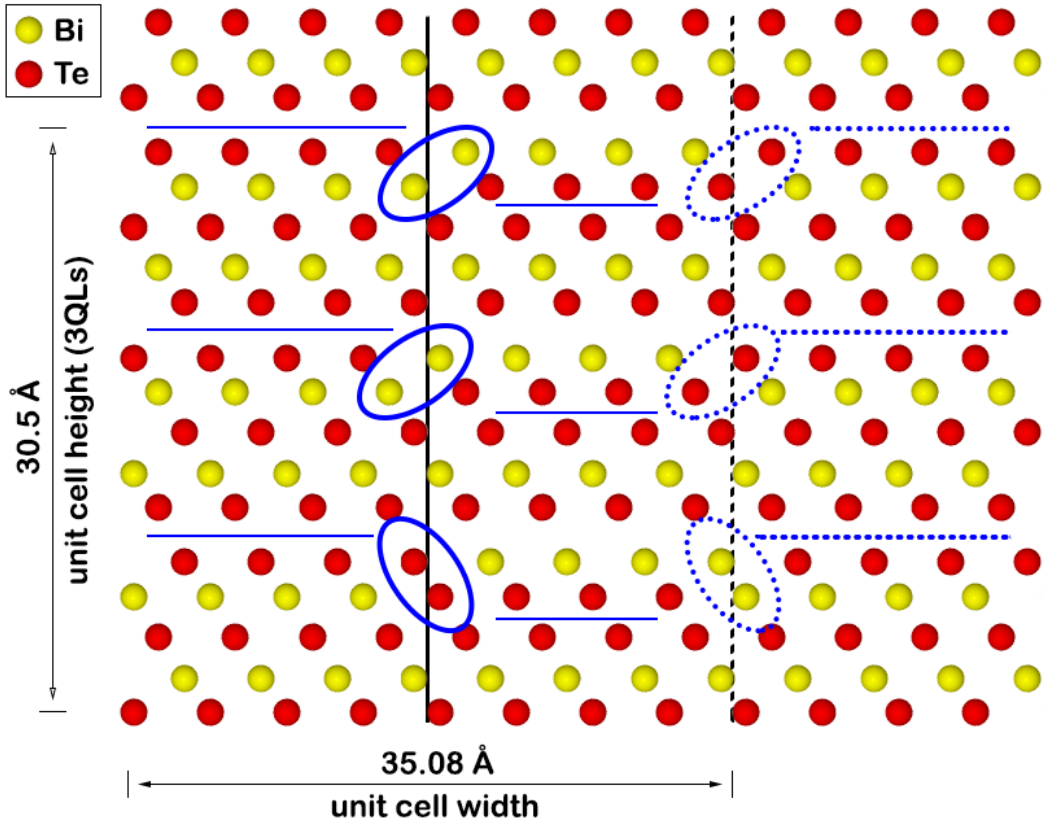

Figure 6.8: Modelling anti-phase boundary in Bi_2Te_3. Solid shapes are within the unit cell, dashed ones are due to periodic boundary conditions. Vertical lines show the position of anti-phase boundaries. Horizontal lines visualise the order of QLs.

stants of a=b=4.39 Å and c=30.49 Å, and distance between the atoms Bi-Te_1 = 3.04 Å, Bi-Te_2 = 3.24 Å and Te_1-Te_2= 3.72 Å [204]. The APBs are illustrated in Fig. 6.8. They were formed by expanding the unit cell 8 times along the a-axis and rigidly shifting half of the structure by $\pm 3/5$ of QL along the c-axis. This creates two APBs. One is in the middle of the cell with 2 Bi-Bi pairs and 1 Te-Te pair (highlighted with solid shapes in the figure). The other is at the end of the cell with 1 Bi-Bi pair and 2 Te-Te pairs (highlighted with dashed shapes in the figure). The distance between the APBs is effectively 17.54 Å, half of the cell width. The superstructure contains 120 atoms and was not further relaxed.

Calculations were performed using the GGA-PBE exchange-correlation functional and ultrasoft pseudopotentials with spin-orbit coupling. The plane-wave cut-off energy was 600 eV. The Brillouin zone sampling for the electronic minimisation was done on a mesh with **k**-points spacing of 0.053 2πÅ^{-1}. Spectral calculations were performed on a much denser mesh with **k**-points spacing of 0.0066 2πÅ^{-1}. An interpolation factor (lpfac) of 10 was used for the BoltzTraP calculations.

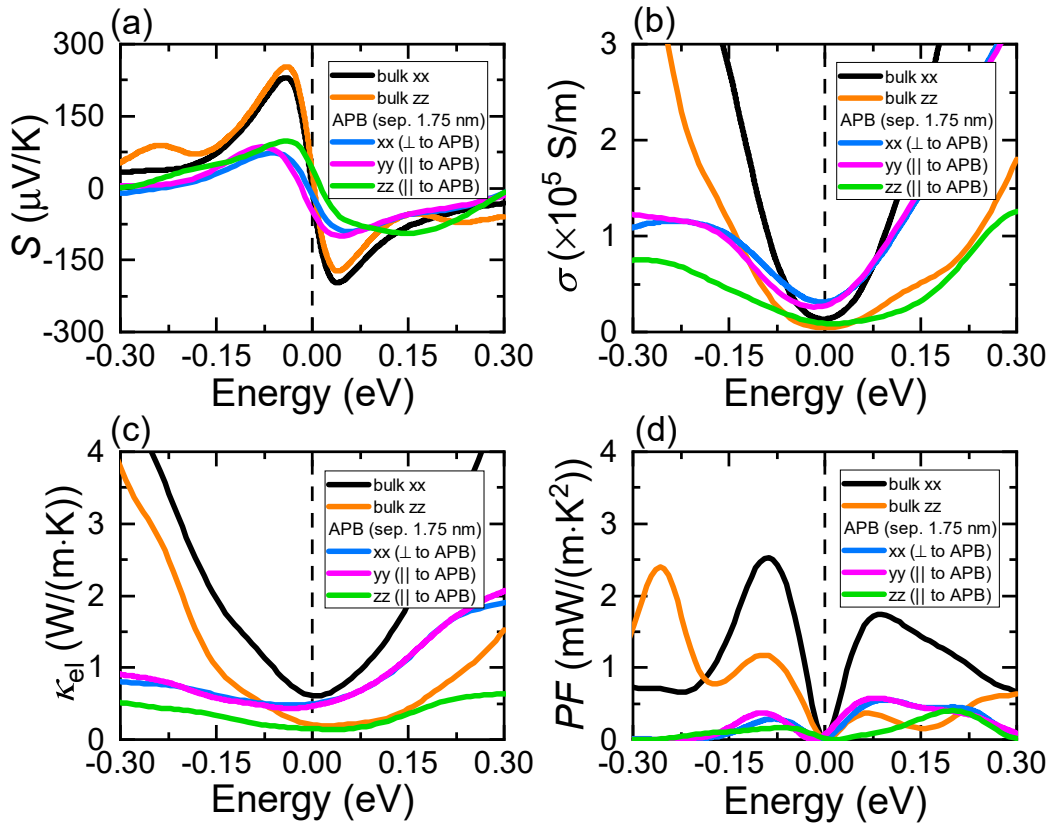

Figure 6.9: Effect of the anti-phase boundary on the electronic thermoelectric properties of Bi_2Te_3 at T=300 K. S, σ, κ_{el} and PF are given in subfigures (a)–(d). Dashed line corresponds to the Fermi level.

We compare the electronic thermoelectric properties of bulk Bi_2Te_3 to the results with APBs in Fig. 6.9. The layered structure of Bi_2Te_3 makes its thermoelectric properties anisotropic. For the bulk there are two different directions which are parallel to the vdW gaps (xx or yy) and perpendicular to the vdW gaps (zz). For the APB we need to consider that the boundary ruins the periodicity along the a-vector, which means that the xx (perpendicular to APB) and yy (parallel to APB) directions are no longer equivalent.

Bulk results with S up to $+254$ μV/K for p-type and -200 μV/K for n-type and PF of 2.55 mW/m·K^2 for p-type and 1.73 mW/m·K^2 for n-type agree qualitatively well with the accepted theoretical prediction for Bi_2Te_3 [100, 133]. Regarding the APB, we note that it has a negative effect on the p-type thermoelectric properties with PF falling below 0.5 mW/m·K^2 in all directions. The power factor on the n-type side is slightly higher, with maximum values of 0.6 mW/m·K^2 along xx and yy. This is comparable to the bulk n-type PF of 0.4 mW/m·K^2 along the zz direction. Based on these results, APBs have an equal negative effect along all directions. Results along xx and yy axes appear to be very similar, despite the two directions being perpendicular and parallel to the boundaries.

The initial impression from our investigation is that APBs ruin the electronic thermoelectric properties of Bi_2Te_3. Based on Fig. 6.9 it looks as if the Fermi level remains unchanged and that the semiconductor is around the charge neutrality point, where there is no excess of charge carriers. Thermoelectric properties also appear to be negatively affected on the *n*- and *p*-type sides. This slightly contradicts expectations based on experimental results [75, 76, 205], which suggest that nanostructuring and grain boundaries can be used to improve the thermoelectric performance. We need to note, however, that the experimentally reported grain size is in the range between 50–200 nm, whereas the distance between APBs in our model is only 1.75 nm. The study by Bae *et al.* [205] reports that the thermoelectric properties of Bi_2Te_3 not only improve but also switch between *n*- and *p*-type when the grain size reaches 150 nm. This suggests the APBs density in our model needs to be reduced by two orders of magnitude before we can observe an improvement in the thermoelectric properties of Bi_2Te_3. Such a calculation is prohibitively expensive at the moment. Therefore, we will change our approach and test another optimisation mechanism on Bi_2Te_3. One which goes in the oposite direction in terms of modelling and aims to reduce the size of the structure. In the next section we investigate the thermoelectric properties of Bi_2Te_3 thin films.

6.4 Electronic thermoelectric properties of a few quintuple layers of Bi_2Te_3

One of the great features of Bi_2Te_3 is that the quintuple layers (QLs) can be mechanically exfoliated due to the weak van der Waals forces which bond the layers together. Therefore, it is possible to tune the thickness of Bi_2Te_3 samples and produce thin films. We know that conducting states should be present at the surface of the films since Bi_2Te_3 is a topological insulator. We have also already seen that the electronic thermoelectric properties of bulk Bi_2Te_3 are anisotropic. Thus, it will be interesting to investigate how the electronic thermoelectric properties of Bi_2Te_3 thin films changes with thickness size.

We use the same computational settings as in Section 6.3.2 with one major difference regarding geometry optimisation. This time we relax both the lattice constants and ionic positions for the bulk and only the ionic positions for the thin films. Semi-empirical dispersion correction [206] was used to take into account the vdW interaction between the QLs. After the geometry optimisation the hexagonal lattice constants for bulk Bi_2Te_3 were found to be a=b= 4.43 Å and c = 30.53Å. These results are in a good agreement with other theoretical

studies [207, 208] but longer than the experimental values which we used for the APB study. A vacuum gap of 10 Å is used to separate the films. Thin film thickness varies from 1 QL to 4 QLs (0.8–3.8 nm).

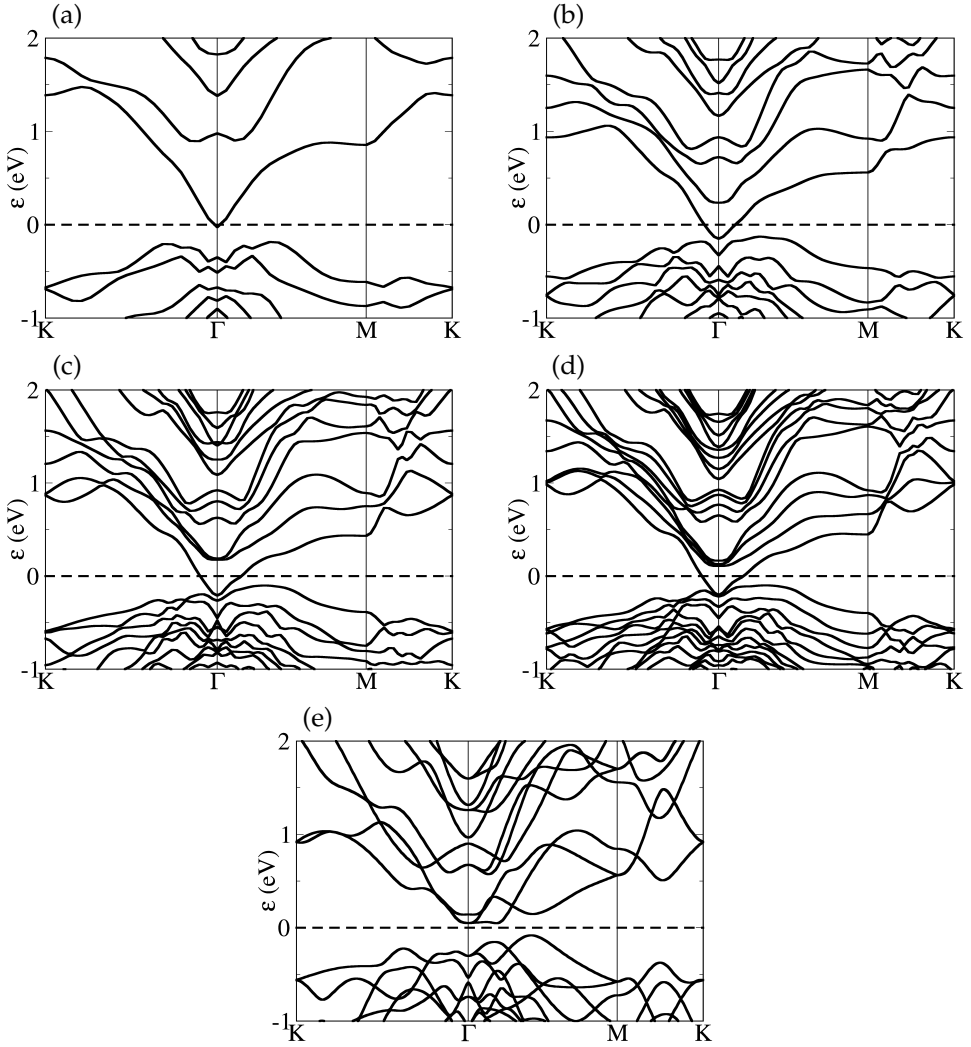

Figure 6.10: Bandstructure of Bi_2Te_3 thin films – (a) 1 QL, (b) 2 QLs, (c) 3 QLs, (d) 4 QLs, (e) bulk.

First we look at the band structure of the thin films and compare it to the bulk in Fig. 6.10. We see that gradually a Dirac cone is formed when we increase the thin film thickness. As the number of layers increases going from (a) to (d), the bottom conduction band gets closer to the top valence band, which closes the band gap present in 1 QL. We can also see that as the thickness increases bands arising from atoms inside the material represent more and more the bulk-like band structure. A direct comparison can be made between Fig. 6.10(c) and (e). Both structures are made of 3 QLs, but the Dirac cone is missing in subfigure (e) since bulk material lacks the surface states. A prominent band gap is only present in 1 QL (0.18 eV) and in the bulk (0.09 eV). These results are within the range of other theoretical predictions [93, 207, 209–211], which ar-

gue that the band gap in 1 QL can be between 0.09 and 0.39 eV. Our prediction for the band gap in bulk yields a value which is also smaller than the experimental band gap of 0.15 eV. It is worth mentioning that the band gap of bulk Bi_2Te_3 with experimental lattice constants and ionic positions, as modelled in Section 6.3.2, is also 0.09 eV. Therefore, the discrepancy between the experimental and theoretical value cannot be explained by the mismatch between the experimental and theoretical lattice constants.

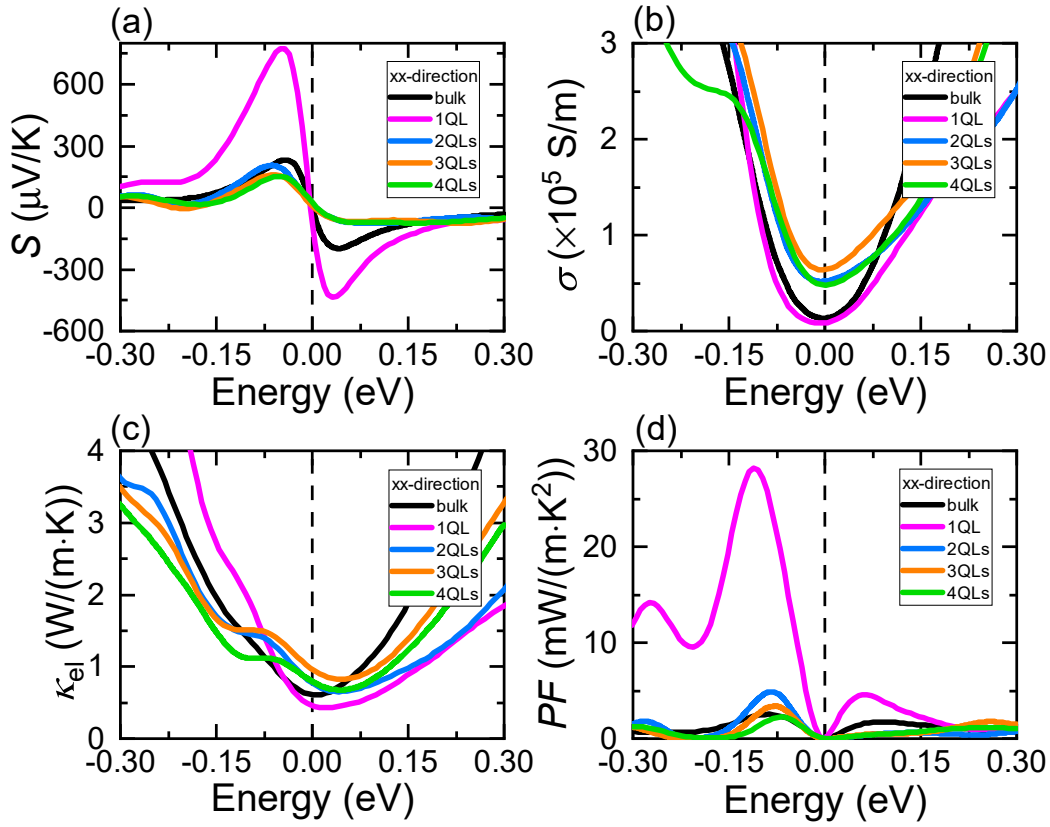

Figure 6.11: Bi_2Te_3 thin films thermoelectric properties along xx direction. S, σ, κ_{el} and PF are given in subfigures (a)–(d). Dashed line corresponds to the Fermi level.

Next we investigate the electronic thermoelectric properties of Bi_2Te_3 thin films. The results are split into two. Figure 6.11 shows the results along the xx direction, which is parallel to the film (in-plane), whereas Fig. 6.12 shows the zz direction (out-of-plane), which is perpendicular to the film. When we look at S in Fig. 6.11(a) we notice that there is an enormous increase in the power factor of 1 QL for both p- and n-type with maxima of $+780$ and -440 μV/K, respectively. We can account the increase to the wider band gap in the 1 QL thin film than in the bulk. When we increase the thickness of our thin films the band gap closes and the p-type S gradually becomes worse than that of the bulk. On the n-type side S is always worse than in bulk for anything more than 1 QL. The electrical conductivity of 1 QL of Bi_2Te_3 along the xx direction remains qualita-

tively similar to the bulk on the *p*-type side but start to fall below it for *n*-type semiconductor. This result differs from our observation on $Nb_{1-x}Ta_xFeSb$ in Section 6.2.2 which showed that for identical electronic structures with a different band gap an increase in the S is compensated by a decrease in σ and features no net gain in PF. Therefore, we can assume that in addition to the different band gap size of 1 QL and bulk, there is a considerable difference in the band structure, especially below the Fermi level. That is something which is not immediately obvious when comparing the band structures in Fig. 6.10(a) and (e). The electrical conductivity of 2-4 QLs is higher than that of the bulk on the *p*-type side and up to 0.07 eV on the *n*-type side. Such behaviour is expected due to the formation of the Dirac cone when more QLs are added. The structure with the highest σ is the thin film with 3 QLs.

Electronic thermal conductivity of 1 QL changes from being higher to lower than κ_{el} of the bulk at -0.04 eV. Thicker films all have lower κ_{el} than bulk apart from the region between -0.1 and 0.05 eV. The most interesting change in the electronic thermoelectric properties along the xx directions is seen in PF. The in-plane *p*-type PF maximum of 1 QL and 2 QLs is 10 and 2 times, respectively, higher than the bulk PF. The maxima occur at energy levels which correspond to doping levels, which introduce 4-6% extra holes per formula unit. The improvement gradually decays and returns to bulk values as we increase the thickness of the thin films to 4 QLs. On the *n*-side there is an improvement only on for 1 QL, whereas 2-4 QLs exhibit worse PF than bulk.

Before drawing any conclusions regarding the performance of Bi_2Te_3 thin films we will have a look at the thermoelectric properties along the zz direction. We see in Fig. 6.12(a) that the Seebeck coefficient for 1 and 2 QLs remains higher than the bulk S on the *p*-type side, while 3 and 4 QLs thin films have S which is lower. On the *n*-type side all thin films exhibit S which is lower than the Seebeck coefficient of bulk Bi_2Te_3. Thin films have $\times 10^5$ lower σ and κ_{el} along the zz direction when compared to the xx direction and bulk zz values. This shows that reducing the dimensions of Bi_2Te_3 by tuning the number of QLs has an enormous impact on the out-of-plane conductivity. We show the PF along the zz direction in Fig. 6.12(d). In all cases, the PF is 4-5 orders of magnitude lower than the bulk and in-plane results. Curiously, the worst performing thin film contains 3 QLs. It is a rather special case, which contains the same number of QLs as in the bulk unit cell but with a vacuum gap. It will be interesting to see how a further increase in the thickness will affect the out-of-plane thermoelectric properties and whether cases with $3N$ QLs, where N is an integer, will exhibit odd behaviour.

Our investigation showed that Bi_2Te_3 thin films up to 4 QLs can only be utilised

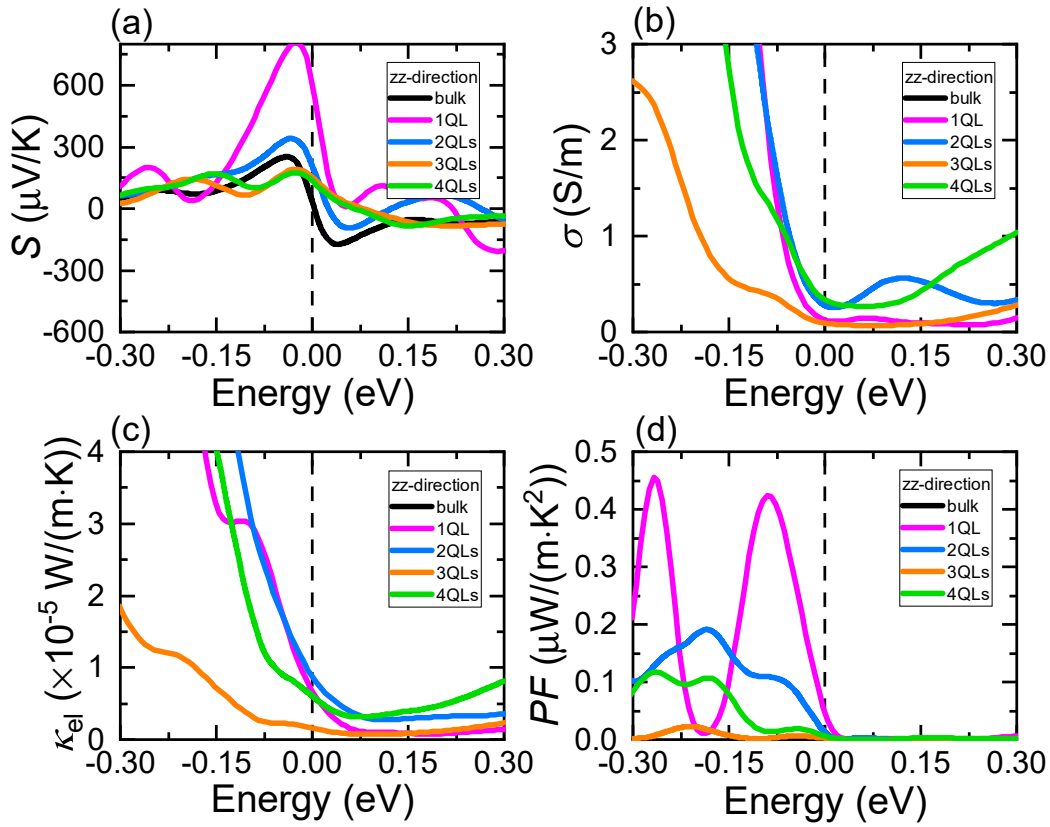

Figure 6.12: Bi_2Te_3 thin films thermoelectric properties along zz direction for S (a), σ (b), κ_{el} (c) and PF (d). Dashed line corresponds to the Fermi level.

for their in-plane thermoelectric properties. Therefore, when talking about the electronic thermoelectric properties of thin films we will refer to our results along the xx direction. Results showed that when the thickness of Bi_2Te_3 is reduced to 1 or 2 QLs there is a considerable gain in the p-type PF, which is in agreement with other theoretical predictions [93, 210]. An improvement in the thermoelectric properties of Bi_2Te_3 thin films has also been reported experimentally even for films with thickness of 1 μm [212]. The thickness of the thin films can be reduced mechanically down to 8 nm by using adhesive tape [213]. Despite the impressive experimental results, thickness of 8 nm corresponds to 9 QLs which is significantly thicker than all of our test cases. Therefore, it remains to be seen if the theoretically predicted excellent thermoelectric properties for 1 and 2 QLs (0.8 and 1.8 nm) can be observed experimentally.

6.5 Conclusions

In this chapter we tested three different optimisation techniques and showed in a qualitative way how they change the electronic thermoelectric properties of Fe_2VAl, NbFeSb, TaFeSb and Bi_2Te_3. The first optimisation technique showed

how doping affects the electronic thermoelectric properties with and without changing the number of charge carriers. In Fe_2VAl, we explicitly *n*-type doped the structure with Si, Ge or Sn. Results show that the change in the thermoelectric properties agrees well with the expectations if we were to chemically dope the bulk material in BoltzTraP. We also see that the explicit doping of Fe_2VAl does not make *S* asymmetric around the Fermi level, as predicted by experiments. In $Nb_{1-x}Ta_xFeSb$, we do not change the number of valence electrons but rather introduce scattering centres by mixing NbFeSb and TaFeSb. Results show that all mixed compounds exhibit identical *p*-type thermoelectric properties to the parent compounds and that mixing has no negative effect. On the *n*-type side we notice that *PF* increases with the concentration of Ta. Considering that the lattice thermal conductivity is reduced in more complex structures due to the presence of more scattering centres, we suspect that $Nb_{0.25}Ta_{0.75}FeSb$ might exhibit the best *n*-type *ZT* among the investigated half-Heusler alloys.

With the second optimisation mechanism we have added anti-phase boundaries to Fe_2VAl and Bi_2Te_3 bulk structures. Our results for Heusler alloy show that APBs are not responsible for the experimentally observed asymmetry in *S*. We note that APBs in Fe_2VAl lead to an *n*-type semiconductor behaviour and have a relatively small negative effect on the thermoelectric performance. In Bi_2Te_3 anti-phase boundaries affect negatively the electronic thermoelectric properties of the material, which contradicts the experimental measurements. Nevertheless, it must be noted that the separation between the boundaries in our models is much shorter than the experimentally reported values.

The last optimisation technique which have tried is to reduce the size of Bi_2Te_3. We have investigated the band structure and tested the electronic thermoelectric properties of Bi_2Te_3 thin films up to 4 QLs. Our results show that 1 QL and 2 QLs exhibit an in-plane *p*-type *PF* which is 10 and 2 times, respectively, higher than bulk. These predictions agree well with other theoretical results and present an exciting opportunity for experimental realisation.

In summary, we have shown that heavy doping with elements which have the same number of valence electrons as the host atom can be successfully employed to retain the electronic thermoelectric properties of the compound and thus potentially improve its *ZT*. We have also seen that adding anti-phase boundaries with very high density has an overall negative effect on the thermoelectric performance. Finally, we have obtained our best improvement of the thermoelectric properties by reducing the thickness of Bi_2Te_3 down to 1 or 2 QLs. Both cases suggest an impressive increase in *PF* for *p*-type semiconductor.

Chapter 7

Conclusions

In this thesis, we have used first principle calculations to investigate the properties of thermoelectric materials. We started by giving an overview of the thermoelectric field. This included looking at the different thermoelectric devices, applications, materials and optimisation techniques. Then we proceeded to the theoretical background and the methodology needed to repeat the experiments.

Our first set of results was presented in Chapter 4. We investigated the Seebeck coefficient of Fe_2VAl and analysed the reasons for the discrepancy between the theoretical predictions and experimental measurements on the symmetry of S around the Fermi level. Our pragmatic modelling approach suggested that the Hubbard U model can resolve the problem by applying a larger U value on V than Fe d-orbitals.

In Chapter 5, we focused on half-Heusler alloys. We computed all thermoelectric properties of NbFeSb and showed that experimental ZT values can be obtained by considering the effects of grain boundaries, point defects and electron-phonon interactions on the lattice thermal conductivity. Furthermore, we substituted Nb with Ta, a heavier element which has the same number of valence electrons. The proposed TaFeSb alloy proved to be stable and exhibit a higher ZT than NbFeSb due to its lower lattice thermal conductivity after doping.

In Chapter 6, we focused on testing various optimisation techniques. We computed explicitly the effects of dopants, anti-phase boundaries and size reduction. The systems of interest included Fe_2VAl, $Nb_{1-x}Ta_xFeSb$ and Bi_2Te_3. We gave a qualitative comparison between the electronic thermoelectric properties of the bulk structures and the modified ones. Results showed that doping and anti-phase boundaries are not responsible for the asymmetry in the Seebeck coefficient of Fe_2VAl. In addition, anti-phase boundaries had a negative impact

on the electronic thermoelectric properties of the full-Heusler alloy. Similar results were obtained for anti-phase boundaries in Bi_2Te_3. We must note that for both structures the modelled boundary density was much higher than in experiments. In contrast, two other thermoelectric optimisation approaches proved very successful. We saw that mixing NbFeSb with TaFeSb does not affect the *p*-type thermoelectric properties, which is beneficial for obtaining a higher ZT in the mixed compounds. Additionally, the *n*-type thermoelectric properties were gradually improved by increasing the concentration of Ta in $Nb_{1-x}Ta_xFeSb$. The best improvement in this chapter was observed when we reduced the thickness of Bi_2Te_3 thin films to 1 QL. We saw how reducing the dimensionality of a structure can benefit its thermoelectric properties and that the *p*-type power factor of 1 QL of Bi_2Te_3 is 10 times higher than in bulk.

One of the background goals of this project was to develop a set of tools which can be used by the CASTEP community to calculate the thermoelectric properties of any material. Although we did not focus on the coding and development process, the wide variety of results on different structures and properties showed that the task has been completed successfully. Hence, the computational workflow and the interfaces between CASTEP and the other programs can be used to perform a full-scale computation of the thermoelectric properties of other interesting materials too.

7.1 Future work

The current stage of this project presents many possible directions for future improvements and research. One of the most difficult parameters to calculate is the electron relaxation time τ. The level of theory used in this thesis does not consider how τ depends on the chemical potential and how grain boundaries and point defects affect charge carriers scattering frequency. A possible solution to these problems is the electron-phonon coupling (EPC) approach discussed in Section 2.6.3, which can be used to obtain a more accurate estimate of τ with respect to the chemical potential. The effects of boundaries and defects can be estimated using superstructures. Adding CASTEP support to the BoltzTraP2 program was the first step towards using the more realistic EPC model. The second version of the transport programs accepts τ values obtained via the electron-phonon coupling as an input. Once the EPC calculation of τ becomes fully implemented into CASTEP, thermoelectric calculation will become a lot more realistic.

The overall computational workflow for calculating the thermoelectric prop-

erties can also be simplified. As of now, the user needs to interfere at almost every stage of the calculation, especially when there is more than one program involved. Building a framework which automates the process can prove extremely useful. It will reduce the down time between different computational stages and will make thermoelectric calculation more user friendly.

In terms of materials and optimisation techniques, we have seen that mixed half-Heusler alloys like $Nb_{0.25}Ta_{0.75}FeSb$ have the potential to exhibit not only excellent *p*-type but also *n*-type thermoelectric properties. Recent studies also suggested that anti-phase boundaries have a positive impact on the *n*-type NbFeSb properties [197]. Testing how boundaries affect the electronic properties of our mixed half-Heusler alloys presents an excellent opportunity for further research. It will also be very interesting to compute the lattice thermal conductivity of these potential superstructures.

Thin films made of Bi_2Te_3 are another option for research. Some of the optimisation mechanisms which we have not explored in this project involve straining the structure or introducing vacancies. Such modifications will affect the relaxation time of the charge carries. In such a case, it will be essential to employ the more accurate EPC method for calculating τ. Thin films, especially with 1 or 2 QLs, are excellent candidates for such investigation since they are relatively easy to model and more importantly have the potential to exhibit amazing thermoelectric properties.

Appendix A

Preferential sites in the van der Waals gaps of Mn-doped Bi_2Te_3

The space in the van der Waals (vdW) gaps could be used to utilise Bi_2Te_3. Therefore, doping it with manganese (Mn) is one possibility which gives interesting but controversial results [214–216]. The aim of this study was to support experimental results and determine where Mn prefers to sit in the vdW gaps. In this case, we are not interested in the electronic structure and spin-orbit coupling (SOC) is not included. The initial tests showed that SOC does not play an important role with respect to relative energy differences between different configurations.

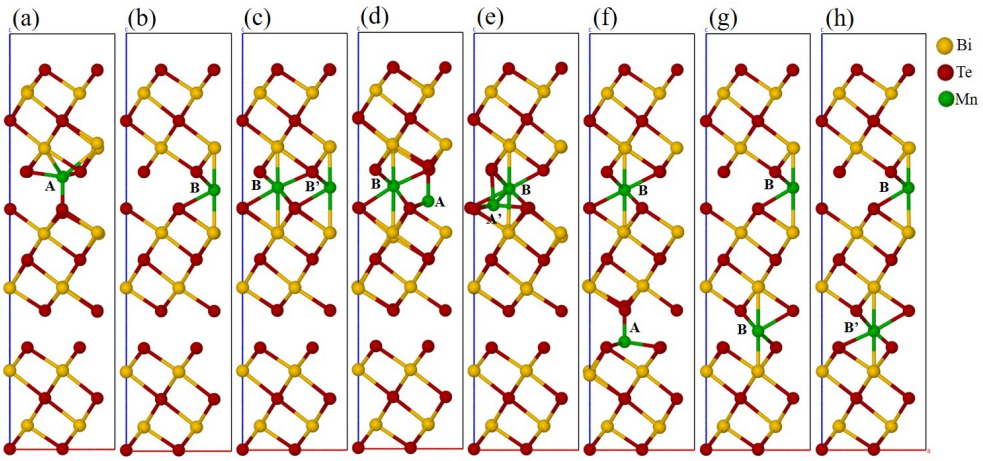

Figure A.1: Simulation models of Bi_2Te_3 with 1 (a) and (b) Mn atom (4%), and 2 (c)-(h) Mn atoms (7.7%) placed in the vdW gaps. Tetrahedral and octahedral sites in the vdW gaps are labelled as (A) and (B), respectively. Their alternatives which gives different bond lengths between Mn atoms are denoted with (A′) and (B′).

Calculations from first principles were performed with CASTEP. A $2 \times 2 \times 1$ supercell with fixed lattice parameters was fully relaxed for two different dop-

ing concentrations of 4 and 7.7%. Internal atomic positions were fully optimised until the force on each atom is less than 0.05 eV/Å and the total energy converges within 0.02 meV/atom. The Brillouin zone was sampled using a **k**-points grid with spacing of 0.04 2πÅ^{-1}. On-the-fly ultrasoft pseudopotentials (C9 set) were used with a plane-wave cut-off energy of 500 eV. In Figure A.1(a) and (b) a single Mn atom (4%) is present at the interstitial sites and occupies the tetrahedral (A) and octahedral (B) sites, respectively. The configuration with Mn adsorption on the B site for 4% was found to be more favourable in energy by 0.19 eV than that on the A site. This is consistent with other experimental and theoretical studies [214, 215]. The total magnetic moments are -4.38 and $+4.20$ μ_B for the A and B cases, respectively.

For the higher concentration of 7.7%, multiple configurations needed to be considered as the two Mn atoms can occupy the A or B sites either in the same, or in different van der Waals gaps, as shown in Figure A.1(c)–(h). In the $2 \times 2 \times 1$ supercell there are two pairs of inequivalent A and B sites, and the second sites were denoted as A′ and B′. Mn remained preferable to the B sites regardless of the gap which was occupied. On the other hand, it was noted that the configuration with the lowest energy was obtained when two Mn atoms were in the same gap occupying the B and B′ sites.

	Mn arrangement	Magnetic moment (μ_B)	Energy difference (eV)
Same gap			
(c)	B–B′	$+4.10$ $+4.10$	Lowest energy
(d)	B–A	-3.60 -4.19	$+0.056$
(e)	B–A′	$+4.45$ -4.19	$+0.363$
Different gap			
(f)	B–A	-2.17 -2.17	$+0.328$
(g)	B–B	$+4.12$ $+4.12$	$+0.146$
(h)	B–B′	-4.12 $+4.12$	$+0.141$

Table A.1: Energy and magnetic moments for different arrangements of Mn in the van der Waals gaps. Subsections (c) - (h) correspond to the illustrations given in Figure A.1.

The results, as shown in Table A.1, suggest that when the doping concentration is increased, Mn prefers to stay in the same van der Waals gap on the available octahedral sites rather than move to the next gap. In terms of magnetic moment, the two most favourable configurations (B–B′ and B–A in the same gap) were found to be ferromagnetic with values of +4.10 +4.10 μ_B and -3.60 -4.19 μ_B for each Mn atom, respectively.

Appendix B

Code snippets from developed software

CASTEP to BoltzTraP interface snippet

```
#=================================================================#
#              Create the <seedname>.struct file                  #
#=================================================================#
    # First line is a comment, name of the structure in this case.
    f_struct = prefix + '\n'

    # Crystal lattice from <seedname>.bands file
    for i in range(3):
      for j in range(3):
        f_struct += str(unit_cell[i][j]) + ' '
      f_struct +='\n'

    # Check if symmetry operations and spglib are present
    if symmetry is True and has_spglib:
      f_struct += str(len(symm_ops_spglib)) + '\n'
      for i in range(int(len(symm_ops_spglib))):
        for j in range(3):
          for k in range(3):
            f_struct += str(symm_ops_spglib[i][j][k]) + ' '
        f_struct += '\n'


    # If there are no symmetry operations, append an identity matrix
    # to the .struct file. BoltzTraP doesn't run otherwise.
    elif symmetry is False or not has_spglib:
      f_struct += '1' + '\n'
      f_struct += '1 0 0 0 1 0 0 0 1'

```

```
29
30      f = open(struct_file, 'w')
31      f.write(f_struct)
32      f.close()
```

Listing B.1: Part of the *castep2boltz.py* interface, which shows how the structure file is created.

CASTEP to ShengBTE interface snippet

```
1  #=================================================================#
2  #           Gather info from <seedname>.castep file               #
3  #=================================================================#
4      # Get unit cell from <seedname>.castep.
5      lat_vectors = []
6      for index, line in enumerate(castep_data):
7           if 'Real Lattice(A)' in line:
8                start = index + 1
9                for j in range (3):
10                    lat_vectors.append(
11                         [float(castep_data[start].split()[0]),
12                          float(castep_data[start].split()[1]),
13                          float(castep_data[start].split()[2])])
14                    start += 1
15               break # avoid double counting
16
17     # Species names
18     species_names = []
19     for index, line in enumerate(castep_data):
20          if ' Mass of species in AMU' in line:
21               start1 = index + 1
22               for j1 in range (int(species)):
23                    species_names.append(str(castep_data[start1].split()
       [0]))
24                    start1 += 1
25               break # avoid double counting
26
27     # Species coordinates
28     positions = []
29     for index, line in enumerate(castep_data):
30          if 'Cell Contents' in line:
31               for i in range(0, ions):
32                    positions.append([str(castep_data[index+10+i].
       split()[1]),
33                    float(castep_data[index+10+i].split()[3]),
34                    float(castep_data[index+10+i].split()[4]),
35                    float(castep_data[index+10+i].split()[5])])
```

```
36                break # avoid double counting
```

Listing B.2: Part of the *castep2shengbte.py* interface, which shows how the script gathers information about the lattice vectors of the unit cell, species names and their coordinates.

CASTEP to almaBTE interface snippet

```
1  #=================================================================#
2  #                    Create input for almaBTE                     #
3  #=================================================================#
4      # _metadata
5      f = open ('_metadata', 'w')
6      f_meta = 'Compound: %s' %str(prefix) + '\n'
7      f_meta += '2nd IFC supercell: (n1,n2,n3) = %s '%str(nx) + '%s '%
       str(ny) + '%s' %str(nz) + '\n'
8      f_meta += "3rd IFC supercell: (n1',n2',n3', cutoff) = {} {} {}
       {}".format(args.supercell[0], args.supercell[1], args.supercell
       [2], args.cutoff)
9      f.write(f_meta)
10     f.close()
11
12     # FORCE_CONSTANTS
13     f = open('FORCE_CONSTANTS', 'w')
14     f_struct = '%6s' %str(nx*ny*nz*ions) + '\n'
15     for key1 in sorted(ifc_for_sheng):
16        f_struct += str(key1) + '\n'
17        for m in range(3):
18          for l in range (3):
19            f_struct += '%22s' %str("{0:.15f}".format(ifc_for_sheng[
       key1][0][m][l]))
20          f_struct += '\n'
21     f.write(f_struct)
22     f.close()
```

Listing B.3: Snippet from the *castep2almabte.py* interface which shows how the *_metadata* and *FORCE_CONSTANTS* files are created. This interface is identical to *castep2shengbte.py* with the only difference being the format of the output.

thirdorder_castep.py code snippet

```
1  #=================================================================#
2  #                    Generate supercells                          #
3  #=================================================================#
4  def gen_CASTEP_supercell(CASTEP_cell, na, nb, nc):
5      """
```

```
    Create a dictionary similar to the first argument but describing
    a
    supercell.
    """
    nruter = dict()
    nruter["na"] = na
    nruter["nb"] = nb
    nruter["nc"] = nc
    nruter["lattvec"] = np.array(CASTEP_cell["lattvec"])
    nruter["lattvec"][:, 0] *= na
    nruter["lattvec"][:, 1] *= nb
    nruter["lattvec"][:, 2] *= nc
    nruter["elements"] = copy.copy(CASTEP_cell["elements"])
    nruter["numbers"] = na * nb * nc * CASTEP_cell["numbers"]
    nruter["positions"] = np.empty(
        (3, CASTEP_cell["positions"].shape[1] * na * nb * nc))
    pos = 0
    for pos, (k, j, i, iat) in enumerate(
            itertools.product(
                xrange(nc),
                xrange(nb),
                xrange(na), xrange(CASTEP_cell["positions"].shape
[1]))):
        nruter["positions"][:, pos] = (
            CASTEP_cell["positions"][:, iat] + [i, j, k]) / [na, nb,
 nc]
    nruter["types"] = []
    for i in xrange(na * nb * nc):
        nruter["types"].extend(CASTEP_cell["types"])
    return nruter
```

Listing B.4: Part of the *thirdorder_castep.py* script, which shows the function which generates the supercells needed for the computation of the third-order force constants.

Program which computes the reduction in the lattice thermal conductivty due to grain boundaries

```
import numpy as np
import sys
import os

L_gb = float(sys.argv[1]) # in [m]
list_of_folders =[x[0] for x in os.walk(".")]
final_data={}

```

```
for folder in range(1,len(list_of_folders)):
  file_path = str(list_of_folders[folder]) + '/BTE.
   cumulative_kappa_scalar'
  L_mfp, k_int = np.loadtxt(fname=file_path, unpack=True)
        temperature = ''
  for i in range(3, (len(list_of_folders[folder])-1)):
        temperature += str(list_of_folders[folder][i])
  # contribution of each data point to k_int
  k_int_cont = np.empty([len(k_int)])
  for i in range(0, len(k_int)):
    if i == 0:
      k_int_cont[i] = k_int[i] - 0.0
          else:
      k_int_cont[i] = k_int[i] - k_int[i-1]
  # apply gb formula to each data point
  k_gb = np.empty([len(k_int_cont)])
  for i in range(0, len(k_int_cont)):
    k_gb[i] = k_int_cont[i]/(1 + (L_mfp[i]*1e-9)/L_gb) # convert
   L_mfp from [nm] to [m]
  k_gb_cumul = np.sum(k_gb)
  final_data[int(temperature)] = k_gb_cumul
final_data = sorted(final_data.items())
print '# L_gb = ' + '%s' %str(L_gb) + ' m'
print '# Temp[K] kappa_with_gb[W/m*K]'
for key in final_data:
  print key[0], key[1]
```

Listing B.5: A short program which computes the reduction in the lattice thermal conductivty as computed by ShengBTE due to grain boundaries.

Snippet from the Effective mass calculator showing the CASTEP loader

```
#=================================================================#
#                      Parse <seedname>.bands                     #
#=================================================================#
def parse_bands_CASTEP(eigenval_fh, band, diff2_size, debug=False):

    # Number of k-points X
    nkpt = int(eigenval_fh.readline().strip().split()[3])
    # Number of spin components X
    spin_components = float(eigenval_fh.readline().strip().split()
   [4])
    # Number of electrons X.00 Y.00
    tmp = eigenval_fh.readline().strip().split()
    if spin_components == 1:
        nelec = int(float(tmp[3]))
```

```
        n_electrons_down = None
    elif spin_components == 2:
        nelec = [float(tmp[3])]
        n_electrons_down = int(float(tmp[4]))
    # Number of eigenvalues X
    nband = int(eigenval_fh.readline().strip().split()[3])
    energies = []
    # Get eigenenergies and unit cell from .bands file
    while True:
        line = eigenval_fh.readline()
        if not line:
            break
        #
        if 'Spin component 1' in line:
            for i in range(1, nband + 1):
                energy = float(eigenval_fh.readline().strip())
                if band == i:
                    energies.append(energy)
    return energies
```

Listing B.6: The function from the *emc.py* program, which parses the CASTEP *seedname.bands* file.

Snippet from the CASTEP Loader for BoltzTraP2

```
#====================================================================#
#                   CASTEP Loader for BoltzTraP2                     #
#====================================================================#
class CASTEPLoader:
    """Loader for CASTEP calculations."""

    def __init__(self, directory):
        if not isinstance(directory, str):
            raise LoaderError("this loader only works with
    directories")
        castepname = _get_CASTEPsystemname(directory)
        if castepname is None:
            raise LoaderError("cannot determine a CASTEP system name
    ")
        structfn = castepname + ".castep"
        energyfn = castepname + ".bands"
        with BoltzTraP2.misc.dir_context(directory):
            BoltzTraP2.misc.info("CASTEP system name:", castepname)
            if not os.path.isfile(energyfn):
                raise ValueError("energy file not found")
            (self.atoms, magmom,
             fict_magmom) = BoltzTraP2.io.read_CASTEP_output(
    structfn)
```

```
21              BoltzTraP2.misc.info("lattice:", self.atoms.get_cell().T
    )
22              (self.fermi, self.castep_fermi_mismatch, self.dosweight,
23               self.kpoints, self.ebands, self.nelect,
24               mommat) = BoltzTraP2.io.read_CASTEP_bands(energyfn)
25
26              # Non-collinear spin-polarised runs don't use symmetry
    in CASTEP.
27              # Hubbard U calculations with symmetry are not
    compatible with
28              # BoltzTraP2 at the moment.
29              # In both cases, use fictitious magmom instead to break
    the symmetry.
30              if fict_magmom is not None:
31                  self.magmom = fict_magmom
32              else:
33                  self.magmom = magmom
34              # mommat is not implemented at the moment
35              if mommat is not None:
36                  self.mommat = mommat
37          self.sysname = castepname
38
39  register_loader("CASTEP", CASTEPLoader)
40
41  def _get_CASTEPsystemname(dirname):
42      """Try to guess the CASTEP system name corresponding to a
    directory."""
43      with BoltzTraP2.misc.dir_context(dirname):
44          filenames = sorted(
45              [i for i in glob.glob("*.castep") if os.path.isfile(i)])
46          if not filenames:
47              return None
48          if len(filenames) > 1:
49              logging.warning(
50                  "there is more than one .castep file in the
    directory"
51                  " - using the first one")
52      return os.path.splitext(os.path.basename(filenames[0]))[0]
```

Listing B.7: Snippet from the Python3 BoltzTraP2 module, which shows the CASTEP loader.

Bibliography

[1] R. He, G. Schierning, and K. Nielsch, "Thermoelectric Devices: A Review of Devices, Architectures, and Contact Optimization," *Advanced Materials Technologies*, vol. 3, p. 1700256, Apr. 2018. 18, 19, 20

[2] M. Hodes, "Optimal Pellet Geometries for Thermoelectric Power Generation," *IEEE Transactions on Components and Packaging Technologies*, vol. 33, pp. 307–318, June 2010. 18

[3] X. C. Xuan, K. C. Ng, C. Yap, and H. T. Chua, "Optimization of two-stage thermoelectric coolers with two design configurations," *Energy Conversion & Management*, vol. 43, pp. 2041–2052, Oct. 2002. 18

[4] S. Oki and R. O. Suzuki, "Performance Simulation of a Flat-Plate Thermoelectric Module Consisting of Square Truncated Pyramid Elements," *Journal of Electronic Materials*, vol. 46, pp. 2691–2696, May 2017. 18

[5] H. Ali, A. Z. Sahin, and B. S. Yilbas, "Thermodynamic analysis of a thermoelectric power generator in relation to geometric configuration device pins," *Energy Conversion & Management*, vol. 78, pp. 634–640, Feb. 2014. 18

[6] B. S. Yilbas and H. Ali, "Thermoelectric generator performance analysis: Influence of pin tapering on the first and second law efficiencies," *Energy Conversion & Management*, vol. 100, pp. 138–146, Aug. 2015. 18

[7] Y. Shi, D. Mei, Z. Yao, Y. Wang, H. Liu, and Z. Chen, "Nominal power density analysis of thermoelectric pins with non-constant cross sections," *Energy Conversion & Management*, vol. 97, pp. 1–6, June 2015. 18

[8] A. Fabián-Mijangos, G. Min, and J. Alvarez-Quintana, "Enhanced performance thermoelectric module having asymmetrical legs," *Energy Conversion & Management*, vol. 148, pp. 1372–1381, Sept. 2017. 18

[9] X. F. Zheng, C. X. Liu, Y. Y. Yan, and Q. Wang, "A review of thermoelectrics research – Recent developments and potentials for sustainable

and renewable energy applications," *Renewable and Sustainable Energy Reviews*, vol. 32, pp. 486–503, Apr. 2014. 19, 21, 23, 25, 26

[10] J. Garcia, D. A. L. Ramos, M. Mohn, H. Schlörb, N. P. Rodriguez, L. Akinsinde, K. Nielsch, G. Schierning, and H. Reith, "Fabrication and Modeling of Integrated Micro-Thermoelectric Cooler by Template-Assisted Electrochemical Deposition," *ECS Journal of Solid State Science and Technology*, vol. 6, pp. N3022–N3028, Jan. 2017. 19

[11] A. Boyer and E. Cissé, "Properties of thin film thermoelectric materials: application to sensors using the Seebeck effect," *Materials Science and Engineering B*, vol. 13, pp. 103–111, Mar. 1992. 19

[12] H. Bottner, J. Nurnus, A. Gavrikov, G. Kuhner, M. Jagle, C. Kunzel, D. Eberhard, G. Plescher, A. Schubert, and K. . Schlereth, "New thermoelectric components using microsystem technologies," *Journal of Microelectromechanical Systems*, vol. 13, pp. 414–420, June 2004. 19

[13] O. Bubnova, Z. U. Khan, A. Malti, S. Braun, M. Fahlman, M. Berggren, and X. Crispin, "Optimization of the thermoelectric figure of merit in the conducting polymer poly(3,4-ethylenedioxythiophene)," *Nature Materials*, vol. 10, pp. 429–433, June 2011. 20

[14] O. Bubnova, Z. U. Khan, H. Wang, S. Braun, D. R. Evans, M. Fabretto, P. Hojati-Talemi, D. Dagnelund, J.-B. Arlin, Y. H. Geerts, S. Desbief, D. W. Breiby, J. W. Andreasen, R. Lazzaroni, W. M. Chen, I. Zozoulenko, M. Fahlman, P. J. Murphy, M. Berggren, and X. Crispin, "Semi-metallic polymers," *Nature Materials*, vol. 13, pp. 190–194, Feb. 2014. 20

[15] K. T. Settaluri, H. Lo, and R. J. Ram, "Thin Thermoelectric Generator System for Body Energy Harvesting," *Journal of Electronic Materials*, vol. 41, pp. 984–988, June 2012. 20

[16] F. Suarez, A. Nozariasbmarz, D. Vashaee, and M. C. Öztürk, "Designing thermoelectric generators for self-powered wearable electronics," *Energy & Environmental Science*, vol. 9, pp. 2099–2113, June 2016. 20

[17] M. Wahbah, M. Alhawari, B. Mohammad, H. Saleh, and M. Ismail, "Characterization of Human Body-Based Thermal and Vibration Energy Harvesting for Wearable Devices," *Emerging and Selected Topics in Circuits and Systems, IEEE Journal on*, vol. 4, pp. 354–363, 09 2014. 20

[18] G. Min and D. M. Rowe, "Ring-structured thermoelectric module," *Semiconductor Science and Technology*, vol. 22, p. 880, June 2007. 20

[19] S. Funahashi, J. Guo, H. Guo, K. Wang, A. L. Baker, K. Shiratsuyu, and C. A. Randall, "Demonstration of the cold sintering process study for the densification and grain growth of ZnO ceramics," *Journal of the American Ceramic Society*, vol. 100, pp. 546–553, Feb. 2017. 21

[20] N. F. Güler and R. Ahiska, "Design and testing of a microprocessor-controlled portable thermoelectric medical cooling kit," *Applied Thermal Engineering*, vol. 22, pp. 1271–1276, Aug. 2002. 21, 27

[21] D. Bhatia, S. Bairagi, S. Goel, and M. Jangra, "Pacemakers charging using body energy," *Journal of Pharmacy & Bioallied Sciences*, vol. 2, pp. 51–54, Jan. 2010. 21, 27

[22] D. Malathi and K. Sabitha, "Battery less thermo electric energy harvesting generator for implantable medical electronic devices," *Biomedical Research*, 2018. 22

[23] J. C. Bass, N. B. Elsner, and F. A. Leavitt, "Performance of the 1 kw thermoelectric generator for diesel engines," *AIP Conference Proceedings*, vol. 316, pp. 295–298, Aug. 1994. 22

[24] K. Ikoma, M. Munekiyo, K. Furuya, M. Kobayashi, H. Komatsu, and K. Shinohara, "Thermoelectric Generator for Gasoline Engine Vehicles Using Bi_2Te_3 Modules," *Journal of the Japan Institute of Metals*, vol. 63, no. 11, pp. 1475–1478, 1999. 22

[25] D. M. Rowe, "Thermoelectric waste heat recovery as a renewable energy source," *International Journal of Innovations in Energy Systems and Power*, vol. 1, no. 1, pp. 13–23, 2006. 22

[26] J. LaGrandeur, D. Crane, and A. Eder, "Vehicle Fuel Economy Improvement through Thermoelectric Waste Heat Recovery." 2005 Diesel Engine Emissions Reduction (DEER) Conference, Aug. 2008. 22

[27] C. B. Vining, "An inconvenient truth about thermoelectrics," *Nature Materials*, vol. 8, pp. 83–85, Feb. 2009. 23, 29

[28] D. M. Rowe, "Thermoelectrics, an environmentally-friendly source of electrical power," *Renewable Energy*, vol. 16, pp. 1251–1256, Jan. 1999. 23

[29] D. T. Crane and L. E. Bell, "Progress Towards Maximizing the Performance of a Thermoelectric Power Generator," in *2006 25th International Conference on Thermoelectrics*, pp. 11–16, Aug. 2006. 23

[30] D. M. Rowe, *CRC Handbook of Thermoelectrics*. CRC Press, July 1995. 24, 27, 53, 55

[31] G. Bennett, "Space Nuclear Power: Opening the Final Frontier," in *4th International Energy Conversion Engineering Conference and Exhibit (IECEC)*, International Energy Conversion Engineering Conference (IECEC), American Institute of Aeronautics and Astronautics, June 2006. 24

[32] J. W. Stevens, "Optimal design of small ΔT thermoelectric generation systems," *Energy Conversion & Management*, vol. 42, pp. 709–720, Apr. 2001. 24

[33] P. Fan, Z.-H. Zheng, Z.-K. Cai, T.-B. Chen, P.-J. Liu, X.-M. Cai, D.-P. Zhang, G.-X. Liang, and J.-T. Luo, "The high performance of a thin film thermoelectric generator with heat flow running parallel to film surface," *Applied Physics Letters*, vol. 102, p. 033904, Jan. 2013. 24, 27

[34] R. H. Redus, A. C. Huber, and J. A. Pantazis, "Improved thermoelectrically cooled X/γ-ray detectors and electronics," *Nuclear Instruments & Methods in Physics Research Section A: Accelerators, Spectrometers, Detectors and Associated Equipment*, vol. 458, pp. 214–219, Feb. 2001. 25, 27

[35] G. Bale, A. Holland, P. Seller, and B. Lowe, "Cooled CdZnTe detectors for X-ray astronomy," *Nuclear Instruments & Methods in Physics Research Section A: Accelerators, Spectrometers, Detectors and Associated Equipment*, vol. 436, pp. 150–154, Oct. 1999. 25, 27

[36] J. Lofy and L. E. Bell, "Thermoelectrics for environmental control in automobiles," in *Twenty-First International Conference on Thermoelectrics, 2002. Proceedings ICT '02.*, pp. 471–476, Aug. 2002. 25, 27

[37] T. Caillat, J.-P. Fleurial, and A. Borshchevsky, "Development of high efficiency thermoelectric generators using advanced thermoelectric materials," *AIP Conference Proceedings*, vol. 420, pp. 1647–1651, Jan. 1998. 26

[38] T. Kajikawa, "Overview of thermoelectric power generation technologies in Japan," in *Thermoelectrics Application Meeting of the US Office of Energy Efficiency and Renewable Energy*, 2011. 26, 27

[39] D. M. Rowe, ed., *Proceedings of 19th International Conference on Thermoelectrics*. Babrow Press, May 2001. 26

[40] A. Killander and J. C. Bass, "A stove-top generator for cold areas," in *Fifteenth International Conference on Thermoelectrics. Proceedings ICT '96*, pp. 390–393, Mar. 1996. 26, 27

[41] G. Min and D. M. Rowe, ""Symbiotic" application of thermoelectric conversion for fluid preheating/power generation," *Energy Conversion & Management*, vol. 43, pp. 221–228, Jan. 2002. 27

[42] X. F. Zheng, Y. Y. Yan, and K. Simpson, "A potential candidate for the sustainable and reliable domestic energy generation–Thermoelectric cogeneration system," *Applied Thermal Engineering*, vol. 53, pp. 305–311, May 2013. 27

[43] X. Qiu, "Determination of Bisphenol A Using Chemiluminescence Combined with Flow Injection," in *2012 International Conference on Biomedical Engineering and Biotechnology*, pp. 1315–1317, May 2012. 27

[44] X. F. Zheng, C. X. Liu, and Y. Y. Yan, "Investigations on an oriented cooling design for thermoelectric cogenerations," *Journal of Physics: Conference Series*, vol. 395, p. 012062, Nov. 2012. 27

[45] K. Matsubara and M. Matsuura, "Thermoelectric applications to vehicles," in *Thermoelectrics Handbook: Macro to Nano*, ch. 52, CRC Press, 2005. 27

[46] A. Zevalkink, D. M. Smiadak, J. L. Blackburn, A. J. Ferguson, M. L. Chabinyc, O. Delaire, J. Wang, K. Kovnir, J. Martin, L. T. Schelhas, T. D. Sparks, S. D. Kang, M. T. Dylla, G. J. Snyder, B. R. Ortiz, and E. S. Toberer, "A practical field guide to thermoelectrics: Fundamentals, synthesis, and characterization," *Applied Physics Reviews*, vol. 5, p. 021303, June 2018. 29

[47] L. E. Bell, "Cooling, heating, generating power, and recovering waste heat with thermoelectric systems," *Science*, vol. 321, pp. 1457–1461, Sept. 2008. 29

[48] J. He and T. M. Tritt, "Advances in thermoelectric materials research: Looking back and moving forward," *Science*, vol. 357, Sept. 2017. 29, 30, 32, 33, 34

[49] S. Twaha, J. Zhu, Y. Yan, and B. Li, "A comprehensive review of thermoelectric technology: Materials, applications, modelling and performance improvement," *Renewable and Sustainable Energy Reviews*, vol. 65, pp. 698–726, Nov. 2016. 31

[50] G. J. Snyder, M. Christensen, E. Nishibori, T. Caillat, and B. B. Iversen, "Disordered zinc in Zn_4Sb_3 with phonon-glass and electron-crystal thermoelectric properties," *Nature Materials*, vol. 3, pp. 458–463, July 2004. 31

[51] Y. Mozharivskyj, A. O. Pecharsky, S. Bud'ko, and G. J. Miller, "A Promising Thermoelectric Material: Zn_4Sb_3 or $Zn_{6-\delta}Sb_5$. Its Composition, Structure, Stability, and Polymorphs. Structure and Stability of $Zn_{1-\delta}Sb$," *Chemistry of Materials*, vol. 16, pp. 1580–1589, Apr. 2004. 31

[52] T. Uemura, K. Akai, K. Koga, T. Tanaka, H. Kurisu, S. Yamamoto, K. Kishimoto, T. Koyanagi, and M. Matsuura, "Electronic structure and thermoelectric properties of clathrate compounds $Ba_8Al_xGe_{46-x}$," *Journal of Applied Physics*, vol. 104, p. 013702, July 2008. 32

[53] M. Rull-Bravo, A. Moure, J. F. Fernández, and M. Martín-González, "Skutterudites as thermoelectric materials: revisited," *RSC Advances*, vol. 5, pp. 41653–41667, May 2015. 32, 114

[54] Y. Nishino, "Development of thermoelectric materials based on Fe_2VAl Heusler compound for energy harvesting applications," *IOP Conference Series: Materials Science and Engineering*, vol. 18, no. 14, p. 142001, 2011. 32, 49, 87, 91, 96, 118, 128

[55] C. Fu, T. Zhu, Y. Liu, H. Xie, and X. Zhao, "Band engineering of high performance p-type FeNbSb based half-Heusler thermoelectric materials for figure of merit $zT > 1$," *Energy & Environmental Science*, vol. 8, pp. 216–220, Dec. 2014. 33, 102, 105, 107, 108, 109, 110, 114

[56] C. Fu, S. Bai, Y. Liu, Y. Tang, L. Chen, X. Zhao, and T. Zhu, "Realizing high figure of merit in heavy-band p-type half-Heusler thermoelectric materials," *Nature Communications*, vol. 6, p. 8144, Sept. 2015. 33

[57] C. Fu, T. Zhu, Y. Pei, H. Xie, H. Wang, G. J. Snyder, Y. Liu, Y. Liu, and X. Zhao, "High Band Degeneracy Contributes to High Thermoelectric Performance in p-Type Half-Heusler Compounds," *Advanced Energy Materials*, vol. 4, p. 1400600, Dec. 2014. 33

[58] L.-D. Zhao, S.-H. Lo, Y. Zhang, H. Sun, G. Tan, C. Uher, C. Wolverton, V. P. Dravid, and M. G. Kanatzidis, "Ultralow thermal conductivity and high thermoelectric figure of merit in SnSe crystals," *Nature*, vol. 508, pp. 373–377, Apr. 2014. 33

[59] L.-D. Zhao, G. Tan, S. Hao, J. He, Y. Pei, H. Chi, H. Wang, S. Gong, H. Xu, V. P. Dravid, C. Uher, G. J. Snyder, C. Wolverton, and M. G. Kanatzidis, "Ultrahigh power factor and thermoelectric performance in hole-doped single-crystal SnSe," *Science*, vol. 351, pp. 141–144, Jan. 2016. 33

[60] K. Peng, X. Lu, H. Zhan, S. Hui, X. Tang, G. Wang, J. Dai, C. Uher, G. Wang, and X. Zhou, "Broad temperature plateau for high ZTs in heavily doped p-type SnSe single crystals," *Energy & Environmental Science*, vol. 9, pp. 454–460, Feb. 2016. 33

[61] A. T. Duong, V. Q. Nguyen, G. Duvjir, V. T. Duong, S. Kwon, J. Y. Song, J. K. Lee, J. E. Lee, S. Park, T. Min, J. Lee, J. Kim, and S. Cho, "Achieving ZT=2.2 with Bi-doped n-type SnSe single crystals," *Nature Communications*, vol. 7, p. 13713, Dec. 2016. 33

[62] J. He, Y. Liu, and R. Funahashi, "Oxide thermoelectrics: The challenges, progress, and outlook," *Journal of Materials Research*, vol. 26, pp. 1762–1772, Aug. 2011. 34

[63] K. Koumoto, Y. Wang, R. Zhang, A. Kosuga, and R. Funahashi, "Oxide Thermoelectric Materials: A Nanostructuring Approach," *Annual Review of Materials Research*, vol. 40, pp. 363–394, June 2010. 34

[64] T. Zhu, L. Hu, X. Zhao, and J. He, "New Insights into Intrinsic Point Defects in V_2VI_3 Thermoelectric Materials," *Advancement of Science*, vol. 3, p. 1600004, July 2016. 35

[65] J. Yang, L. Xi, W. Qiu, L. Wu, X. Shi, L. Chen, J. Yang, W. Zhang, C. Uher, and D. J. Singh, "On the tuning of electrical and thermal transport in thermoelectrics: an integrated theory–experiment perspective," *NPJ Computational Materials*, vol. 2, p. 15015, Feb. 2016. 35

[66] A. Ghasemi, D. Kepaptsoglou, A. I. Figueroa, G. A. Naydenov, P. J. Hasnip, M. I. J. Probert, Q. Ramasse, G. van der Laan, T. Hesjedal, and V. K. Lazarov, "Experimental and density functional study of Mn doped Bi_2Te_3 topological insulator," *APL Materials*, vol. 4, p. 126103, Dec. 2016. 35

[67] Y. Pei, A. D. LaLonde, N. A. Heinz, X. Shi, S. Iwanaga, H. Wang, L. Chen, and G. J. Snyder, "Stabilizing the optimal carrier concentration for high thermoelectric efficiency," *Advanced Materials*, vol. 23, pp. 5674–5678, Dec. 2011. 36

[68] Y. Pei, H. Wang, Z. M. Gibbs, A. D. LaLonde, and G. J. Snyder, "Thermopower enhancement in $Pb_{1-x}Mn_xTe$ alloys and its effect on thermoelectric efficiency," *NPG Asia Materials*, vol. 4, p. e28, Sept. 2012.

[69] Y. Pei, X. Shi, A. LaLonde, H. Wang, L. Chen, and G. J. Snyder, "Convergence of electronic bands for high performance bulk thermoelectrics," *Nature*, vol. 473, pp. 66–69, May 2011. 36

[70] Y. Tang, Z. M. Gibbs, L. A. Agapito, G. Li, H.-S. Kim, M. B. Nardelli, S. Curtarolo, and G. J. Snyder, "Convergence of multi-valley bands as the electronic origin of high thermoelectric performance in $CoSb_3$ skutterudites," *Nature Materials*, vol. 14, pp. 1223–1228, Dec. 2015. 36

[71] W. Liu, X. Tan, K. Yin, H. Liu, X. Tang, J. Shi, Q. Zhang, and C. Uher, "Convergence of Conduction Bands as a Means of Enhancing Thermoelectric Performance of *n*-Type $Mg_2Si_{1-x}Sn_x$ Solid Solutions," *Physical Review Letters*, vol. 108, p. 166601, Apr. 2012. 36

[72] Y. Chen, C. M. Jaworski, Y. B. Gao, H. Wang, T. J. Zhu, G. J. Snyder, J. P. Heremans, and X. B. Zhao, "Transport properties and valence band feature of high-performance $(GeTe)_{85}(AgSbTe_2)_{15}$ thermoelectric materials," *New Journal of Physics*, vol. 16, p. 013057, Jan. 2014. 36

[73] G. Tan, F. Shi, S. Hao, H. Chi, L.-D. Zhao, C. Uher, C. Wolverton, V. P. Dravid, and M. G. Kanatzidis, "Codoping in SnTe: Enhancement of Thermoelectric Performance through Synergy of Resonance Levels and Band Convergence," *Journal of the American Chemical Society*, vol. 137, pp. 5100–5112, Apr. 2015. 36

[74] S. I. Kim, K. H. Lee, H. A. Mun, H. S. Kim, S. W. Hwang, J. W. Roh, D. J. Yang, W. H. Shin, X. S. Li, Y. H. Lee, G. J. Snyder, and S. W. Kim, "Thermoelectrics. Dense dislocation arrays embedded in grain boundaries for high-performance bulk thermoelectrics," *Science*, vol. 348, pp. 109–114, Apr. 2015. 36

[75] B. Poudel, Q. Hao, Y. Ma, Y. Lan, A. Minnich, B. Yu, X. Yan, D. Wang, A. Muto, D. Vashaee, X. Chen, J. Liu, M. S. Dresselhaus, G. Chen, and Z. Ren, "High-Thermoelectric Performance of Nanostructured Bismuth Antimony Telluride Bulk Alloys," *Science*, vol. 320, pp. 634–638, May 2008. 36, 136, 139

[76] P. Puneet, R. Podila, M. Karakaya, S. Zhu, J. He, T. M. Tritt, M. S. Dresselhaus, and A. M. Rao, "Preferential Scattering by Interfacial Charged De-

fects for Enhanced Ehermoelectric performance in Few-layered *n*-type Bi_2Te_3," *Scientific Reports*, vol. 3, p. 3212, Nov. 2013. 36, 136, 139

[77] A. Shakouri, "Recent Developments in Semiconductor Thermoelectric Physics and Materials," *Annual Review of Materials Research*, vol. 41, pp. 399–431, Aug. 2011. 36

[78] K. Biswas, J. He, Q. Zhang, G. Wang, C. Uher, V. P. Dravid, and M. G. Kanatzidis, "Strained endotaxial nanostructures with high thermoelectric figure of merit," *Nature Chemistry*, vol. 3, pp. 160–166, Feb. 2011. 36

[79] L.-D. Zhao, S. Hao, S.-H. Lo, C.-I. Wu, X. Zhou, Y. Lee, H. Li, K. Biswas, T. P. Hogan, C. Uher, C. Wolverton, V. P. Dravid, and M. G. Kanatzidis, "High thermoelectric performance via hierarchical compositionally alloyed nanostructures," *Journal of the American Chemical Society*, vol. 135, pp. 7364–7370, May 2013. 36

[80] K. Biswas, J. He, I. D. Blum, C.-I. Wu, T. P. Hogan, D. N. Seidman, V. P. Dravid, and M. G. Kanatzidis, "High-performance bulk thermoelectrics with all-scale hierarchical architectures," *Nature*, vol. 489, pp. 414–418, Sept. 2012. 36, 37

[81] W. Xie, J. He, H. J. Kang, X. Tang, S. Zhu, M. Laver, S. Wang, J. R. D. Copley, C. M. Brown, Q. Zhang, and T. M. Tritt, "Identifying the specific nanostructures responsible for the high thermoelectric performance of $(Bi,Sb)_2Te_3$ nanocomposites," *Nano Letters*, vol. 10, pp. 3283–3289, Sept. 2010. 36

[82] A. I. Hochbaum, R. Chen, R. D. Delgado, W. Liang, E. C. Garnett, M. Najarian, A. Majumdar, and P. Yang, "Enhanced thermoelectric performance of rough silicon nanowires," *Nature*, vol. 451, pp. 163–167, Jan. 2008. 36

[83] X. Ji, B. Zhang, Z. Su, T. Holgate, J. He, and T. M. Tritt, "Nanoscale granular boundaries in polycrystalline $Pb_{0.75}Sn_{0.25}$ Te: an innovative approach to enhance the thermoelectric figure of merit," *physica status solidi (a)*, vol. 206, pp. 221–228, Feb. 2009. 36

[84] C. J. Vineis, A. Shakouri, A. Majumdar, and M. G. Kanatzidis, "Nanostructured thermoelectrics: big efficiency gains from small features," *Advanced Materials*, vol. 22, pp. 3970–3980, Sept. 2010. 37

[85] J.-F. Li, W.-S. Liu, L.-D. Zhao, and M. Zhou, "High-performance nanostructured thermoelectric materials," *NPG Asia Materials*, vol. 2, p. 152, Oct. 2010. 37

[86] L. D. Hicks and M. S. Dresselhaus, "Thermoelectric figure of merit of a one-dimensional conductor," *Physical Review B*, vol. 47, pp. 16631–16634, June 1993. 37

[87] L. D. Hicks and M. S. Dresselhaus, "Effect of quantum-well structures on the thermoelectric figure of merit," *Physical Review B*, vol. 47, pp. 12727–12731, May 1993. 37

[88] K. v. Klitzing, G. Dorda, and M. Pepper, "New Method for High-Accuracy Determination of the Fine-Structure Constant Based on Quantized Hall Resistance," *Physical Review Letters*, vol. 45, pp. 494–497, Aug 1980. 37

[89] X.-L. Qi and S.-C. Zhang, "The quantum spin Hall effect and topological insulators," *Physics Today*, vol. 63, pp. 33–38, Jan. 2010. 38

[90] M. Z. Hasan and C. L. Kane, "Colloquium: Topological insulators," *Reviews of Modern Physics*, vol. 82, pp. 3045–3067, Nov. 2010. 38

[91] L. Müchler, H. Zhang, S. Chadov, B. Yan, F. Casper, J. Kübler, S.-C. Zhang, and C. Felser, "Topological Insulators from a Chemist's Perspective," *Angewandte Chemie, International Edition*, vol. 51, pp. 7221–7225, July 2012. 38

[92] H. Zhang, C.-X. Liu, X.-L. Qi, X. Dai, Z. Fang, and S.-C. Zhang, "Topological insulators in Bi_2Se_3, Bi_2Te_3 and Sb_2Te_3 with a single Dirac cone on the surface," *Nature Physics*, vol. 5, p. 438, May 2009. 38

[93] G. Zhou and D. Wang, "Few-quintuple Bi_2Te_3 nanofilms as potential thermoelectric materials," *Scientific Reports*, vol. 5, p. 8099, Jan. 2015. 38, 140, 143

[94] J. Liang, L. Cheng, J. Zhang, H. Liu, and Z. Zhang, "Maximizing the thermoelectric performance of topological insulator Bi_2Te_3 films in the few-quintuple layer regime," *Nanoscale*, vol. 8, pp. 8855–8862, Apr. 2016. 38

[95] P. Wei, J. Yang, L. Guo, S. Wang, L. Wu, X. Xu, W. Zhao, Q. Zhang, W. Zhang, M. S. Dresselhaus, and J. Yang, "Minimum Thermal Conductivity in Weak Topological Insulators with Bismuth-Based Stack Structure," *Advanced Functional Materials*, vol. 26, pp. 5360–5367, Aug. 2016. 38

[96] B. Qiu and X. Ruan, "Thermal conductivity prediction and analysis of few-quintuple Bi_2Te_3 thin films: A molecular dynamics study," *Applied Physics Letters*, vol. 97, p. 183107, Nov. 2010. 38

[97] R. D. Reeves, L. A. Crosser, G. E. Chester, and J. J. Hill, "Thermoelectric property enhancement via pore confinement in template grown bismuth telluride nanowire arrays," *Nanotechnology*, vol. 28, p. 505401, Dec. 2017. 39

[98] B. L. Davis and M. I. Hussein, "Nanophononic metamaterial: thermal conductivity reduction by local resonance," *Physical Review Letters*, vol. 112, p. 055505, Feb. 2014. 39

[99] H. Honarvar and M. I. Hussein, "Two orders of magnitude reduction in silicon membrane thermal conductivity by resonance hybridizations," *Physical Review B*, vol. 97, p. 195413, May 2018. 39

[100] G. K. H. Madsen and D. J. Singh, "BoltzTraP. A code for calculating band-structure dependent quantities," *Computer Physics Communications*, vol. 175, pp. 67–71, July 2006. 40, 58, 59, 76, 87, 89, 103, 104, 127, 138

[101] G. Pizzi, D. Volja, B. Kozinsky, M. Fornari, and N. Marzari, "An updated version of BoltzWann: A code for the evaluation of thermoelectric and electronic transport properties with a maximally-localized Wannier functions basis," *Computer Physics Communications*, vol. 185, pp. 2311–2312, Aug. 2014. 40

[102] J. Bardeen and W. Shockley, "Deformation Potentials and Mobilities in Non-Polar Crystals," *Physics Review*, vol. 80, pp. 72–80, Oct. 1950. 40, 65, 66, 104

[103] G. K. H. Madsen, J. Carrete, and M. J. Verstraete, "BoltzTraP2, a program for interpolating band structures and calculating semi-classical transport coefficients," *Computer Physics Communications*, vol. 231, pp. 140–145, Oct. 2018. 40, 58, 59, 78

[104] F. VanGessel, J. Peng, and P. W. Chung, "A review of computational phononics: the bulk, interfaces, and surfaces," *Journal of Materials Science*, vol. 53, pp. 5641–5683, Apr. 2018. 40

[105] S. Bhattacharya and G. K. H. Madsen, "A novel p-type half-Heusler from high-throughput transport and defect calculations," *Journal of Materials Chemistry*, vol. 4, pp. 11261–11268, Dec. 2016. 40, 102, 103, 114

[106] T. Fang, S. Zheng, H. Chen, H. Cheng, L. Wang, and P. Zhang, "Electronic structure and thermoelectric properties of p-type half-Heusler compound NbFeSb: a first-principles study," *RSC Advances*, vol. 6, pp. 10507–10512, Jan. 2016. 40, 102, 106, 107, 109

[107] G. A. Slack, "Nonmetallic crystals with high thermal conductivity," *The Journal of Physics and Chemistry of Solids*, vol. 34, pp. 321–335, Jan. 1973. 40, 61

[108] T. Jia, G. Chen, and Y. Zhang, "Lattice thermal conductivity evaluated using elastic properties," *Physical Review B*, vol. 95, p. 155206, Apr. 2017. 40, 41, 61, 62, 121

[109] A. J. Hong, L. Li, R. He, J. J. Gong, Z. B. Yan, K. F. Wang, J.-M. Liu, and Z. F. Ren, "Full-scale computation for all the thermoelectric property parameters of half-Heusler compounds," *Scientific Reports*, vol. 6, p. 22778, Mar. 2016. 40, 83, 102, 103, 106, 107, 109, 110

[110] T. Tadano, Y. Gohda, and S. Tsuneyuki, "Anharmonic force constants extracted from first-principles molecular dynamics: applications to heat transfer simulations," *Journal of Physics: Condensed Matter*, vol. 26, p. 225402, June 2014. 41

[111] J. Carrete, B. Vermeersch, A. Katre, A. van Roekeghem, T. Wang, G. K. H. Madsen, and N. Mingo, "almaBTE: A solver of the space–time dependent Boltzmann transport equation for phonons in structured materials," *Computer Physics Communications*, vol. 220, pp. 351–362, Nov. 2017. 41

[112] A. Chernatynskiy and S. R. Phillpot, "Phonon Transport Simulator (PhonTS)," *Computer Physics Communications*, vol. 192, pp. 196–204, July 2015. 41

[113] A. Togo, L. Chaput, and I. Tanaka, "Distributions of phonon lifetimes in Brillouin zones," *Physical Review B*, vol. 91, p. 094306, Mar. 2015. 41

[114] W. Li, J. Carrete, N. A. Katcho, and N. Mingo, "ShengBTE: a solver of the Boltzmann transport equation for phonons," *Computer Physics Communications*, vol. 185, p. 17471758, 2014. 41, 59, 60, 80, 103

[115] A. J. H. McGaughey, A. Jain, H.-Y. Kim, and B. Fu, "Phonon properties and thermal conductivity from first principles, lattice dynamics, and the Boltzmann transport equation," *Journal of Applied Physics*, vol. 125, p. 011101, Jan. 2019. 41

[116] K. Schwarz and P. Blaha, "Solid state calculations using WIEN2k," *Computational Materials Science*, vol. 28, pp. 259–273, Oct. 2003. 41

[117] X. Gonze, B. Amadon, P.-M. Anglade, J.-M. Beuken, F. Bottin, P. Boulanger, F. Bruneval, D. Caliste, R. Caracas, M. Côté, T. Deutsch, L. Genovese, P. Ghosez, M. Giantomassi, S. Goedecker, D. R. Hamann, P. Hermet, F. Jollet, G. Jomard, S. Leroux, M. Mancini, S. Mazevet, M. J. T. Oliveira, G. Onida, Y. Pouillon, T. Rangel, G.-M. Rignanese, D. Sangalli, R. Shaltaf, M. Torrent, M. J. Verstraete, G. Zerah, and J. W. Zwanziger, "ABINIT: First-principles approach to material and nanosystem properties," *Computer Physics Communications*, vol. 180, pp. 2582–2615, Dec. 2009. 41

[118] J. M. Soler, E. Artacho, J. D. Gale, A. García, J. Junquera, P. Ordejón, and D. Sánchez-Portal, "The SIESTA method for ab initio order-N materials simulation," *Journal of Physics: Condensed Matter*, vol. 14, p. 2745, Mar. 2002. 41

[119] G. Kresse and J. Furthmüller, "Efficiency of ab-initio total energy calculations for metals and semiconductors using a plane-wave basis set," *Computational Materials Science*, vol. 6, pp. 15–50, July 1996. 41

[120] P. Giannozzi, S. Baroni, N. Bonini, M. Calandra, R. Car, C. Cavazzoni, D. Ceresoli, G. L. Chiarotti, M. Cococcioni, I. Dabo, A. Dal Corso, S. de Gironcoli, S. Fabris, G. Fratesi, R. Gebauer, U. Gerstmann, C. Gougoussis, A. Kokalj, M. Lazzeri, L. Martin-Samos, N. Marzari, F. Mauri, R. Mazzarello, S. Paolini, A. Pasquarello, L. Paulatto, C. Sbraccia, S. Scandolo, G. Sclauzero, A. P. Seitsonen, A. Smogunov, P. Umari, and R. M. Wentzcovitch, "QUANTUM ESPRESSO: a modular and open-source software project for quantum simulations of materials," *Journal of Physics: Condensed Matter*, vol. 21, p. 395502, Sept. 2009. 41

[121] A. A. Mostofi, J. R. Yates, G. Pizzi, Y.-S. Lee, I. Souza, D. Vanderbilt, and N. Marzari, "An updated version of wannier90: A tool for obtaining maximally-localised Wannier functions," *Computer Physics Communications*, vol. 185, pp. 2309–2310, Aug. 2014. 41

[122] R. Dovesi, A. Erba, R. Orlando, C. M. Zicovich-Wilson, B. Civalleri, L. Maschio, M. Rérat, S. Casassa, J. Baima, S. Salustro, and B. Kirtman, "Quantum-mechanical condensed matter simulations with CRYSTAL," *Wiley Interdisciplinary Reviews: Computational Molecular Science*, vol. 8, p. e1360, July 2018. 41

[123] S. J. Clark, M. D. Segall, C. J. Pickard, P. J. Hasnip, M. I. J. Probert, K. Refson, and M. C. Payne, "First principles methods using CASTEP," *Zeitschrift für Kristallographie - Crystalline Materials*, vol. 220, pp. 567–570, Jan. 2005. 42, 71, 89, 104, 127

[124] P. Hohenberg and W. Kohn, "Inhomogeneous Electron Gas," *Physics Review*, vol. 136, pp. B864–B871, Nov. 1964. 45

[125] W. Kohn and L. J. Sham, "Self-Consistent Equations Including Exchange and Correlation Effects," *Physics Review*, vol. 140, pp. A1133–A1138, Nov. 1965. 45

[126] J. P. Perdew, K. Burke, and M. Ernzerhof, "Generalized Gradient Approximation Made Simple," *Physical Review Letters*, vol. 77, pp. 3865–3868, Oct. 1996. 47, 89, 104, 105, 127

[127] S. Baroni, S. de Gironcoli, A. Dal Corso, and P. Giannozzi, "Phonons and related crystal properties from density-functional perturbation theory," *Reviews of Modern Physics*, vol. 73, pp. 515–562, July 2001. 49

[128] M. Cococcioni and S. de Gironcoli, "Linear response approach to the calculation of the effective interaction parameters in the LDAU method," *Physical Review B*, vol. 71, p. 035105, Jan. 2005. 51, 52

[129] J. Hubbard and B. H. Flowers, "Electron correlations in narrow energy bands," *Proceedings of the Royal Society of London. Series A, Mathematical and Physical Sciences*, Nov. 1963. 51

[130] V. I. Anisimov, VI, J. Zaanen, and O. K. Andersen, "Band theory and Mott insulators: Hubbard U instead of Stoner I," *Physical Review B*, vol. 44, pp. 943–954, July 1991. 51

[131] Wikipedia, "Thermoelectric effect — Wikipedia, the free encyclopedia," 2016. [Online; accessed 27-May-2016]. 54

[132] N. W. Ashcroft and N. David Mermin, *Solid State Physics*. Holt, Rinehart and Winston, 1 edition ed., 1976. 56, 72

[133] T. J. Scheidemantel, C. Ambrosch-Draxl, T. Thonhauser, J. V. Badding, and J. O. Sofo, "Transport coefficients from first-principles calculations," *Physical Review B*, vol. 68, p. 125210, Sept. 2003. 56, 58, 138

[134] I. Terasaki, *Thermodynamics of thermoelectric device*, ch. 10. 2005. 59

[135] D. T. Morelli, V. Jovovic, and J. P. Heremans, "Intrinsically Minimal Thermal Conductivity in Cubic I-V-VI_2 Semiconductors," *Physical Review Letters*, vol. 101, p. 035901, July 2008. 61

[136] H. Xie, X. Gu, and H. Bao, "A relaxation time model for efficient and accurate prediction of lattice thermal conductivity," Nov. 2018. 61

[137] A. Otero-de-la Roza, D. Abbasi-Pérez, and V. Luaña, "Gibbs2: A new version of the quasiharmonic model code. II. Models for solid-state thermodynamics, features and implementation," *Computer Physics Communications*, vol. 182, pp. 2232–2248, Oct. 2011. 62, 74

[138] P. G. Klemens, "Theory of Thermal Conduction in Thin Ceramic Films," *International Journal of Thermophysics*, vol. 22, pp. 265–275, Jan. 2001. 64

[139] J. Callaway, "Model for Lattice Thermal Conductivity at Low Temperatures," *Physics Review*, vol. 113, pp. 1046–1051, Feb. 1959. 64

[140] R. He, D. Kraemer, J. Mao, L. Zeng, Q. Jie, Y. Lan, C. Li, J. Shuai, H. S. Kim, Y. Liu, D. Broido, C.-W. Chu, G. Chen, and Z. Ren, "Achieving high power factor and output power density in p-type half-Heuslers $Nb_{1-x}Ti_xFeSb$," *Proceedings of the National Academy of Sciences of the United States of America*, vol. 113, pp. 13576–13581, Nov. 2016. 64, 102, 106, 107, 109, 110

[141] X. Shi, Y. Pei, G. Jeffrey Snyder, and L. Chen, "Optimized thermoelectric properties of $Mo_3Sb_{7x}Te_x$ with significant phonon scattering by electrons," *Energy & Environmental Science*, vol. 4, pp. 4086–4095, Sept. 2011. 64

[142] J. Yang, D. T. Morelli, G. P. Meisner, W. Chen, J. S. Dyck, and C. Uher, "Influence of electron-phonon interaction on the lattice thermal conductivity of $Co_{1-x}Ni_xSb_3$," *Physical Review B*, vol. 65, no. 9, 2002. 65

[143] C. Herring and E. Vogt, "Transport and Deformation-Potential Theory for Many-Valley Semiconductors with Anisotropic Scattering," *Physics Review*, vol. 101, pp. 944–961, Feb. 1956. 66

[144] O. M. Abid, S. Menouer, A. Yakoubi, H. Khachai, S. B. Omran, G. Murtaza, D. Prakash, R. Khenata, and K. D. Verma, "Structural, electronic, elastic, thermoelectric and thermodynamic properties of the NbMSb half heusler (M=Fe, Ru, Os) compounds with first principle calculations," *Superlattices and Microstructures*, vol. 93, pp. 171–185, May 2016. 68

[145] W. Voigt, *Lehrbuch der kristallphysik (mit ausschluss der kristalloptik)*. Leipzig; Berlin: B.G. Teubner, 1928. 68

[146] A. Reuss, "Berechnung der fließgrenze von mischkristallen auf grund der plastizitätsbedingung für einkristalle," *ZAMM. Zeitschrift fur Angewandte Mathematik und Mechanik. Journal of Applied Mathematics and Mechanics*, vol. 9, no. 1, pp. 49–58, 1929. 68

[147] R. Hill, "The Elastic Behaviour of a Crystalline Aggregate," *Proceedings of the Physical Society. Section A*, vol. 65, p. 349, Dec. 2002. 69

[148] S. Al-Qaisi, M. S. Abu-Jafar, G. K. Gopir, R. Ahmed, S. Bin Omran, R. Jaradat, D. Dahliah, and R. Khenata, "Structural, elastic, mechanical and thermodynamic properties of Terbium oxide: First-principles investigations," *Results in Physics*, vol. 7, pp. 709–714, Jan. 2017. 69

[149] T. Sohier, D. Campi, N. Marzari, and M. Gibertini, "Mobility of two-dimensional materials from first principles in an accurate and automated framework," *Physical Review Materials*, vol. 2, p. 114010, Nov. 2018. 69

[150] J. M. Ziman, "ELECTRON-PHONON INTERACTION," in *Electrons and Phonons*, Oxford: Oxford University Press, 2001. 69

[151] H. J. Monkhorst and J. D. Pack, "Special points for Brillouin-zone integrations," *Physical Review B*, vol. 13, pp. 5188–5192, June 1976. 71, 72, 89, 104, 105, 127

[152] M. C. Payne, M. P. Teter, D. C. Allan, T. a. Arias, and J. D. Joannopoulos, "Iterative minimization techniques for *ab initio* total-energy calculations: molecular dynamics and conjugate gradients," *Reviews of Modern Physics*, vol. 64, no. 4, 1992. 72, 73

[153] M. I. J. Probert and M. C. Payne, "Improving the convergence of defect calculations in supercells: An ab initio study of the neutral silicon vacancy," *Physical Review B*, vol. 67, p. 075204, Feb. 2003. 73

[154] B. G. Pfrommer, M. Côté, S. G. Louie, and M. L. Cohen, "Relaxation of Crystals with the Quasi-Newton Method," *Journal of Computational Physics*, vol. 131, pp. 233–240, Feb. 1997. 75

[155] R. H. Byrd, J. Nocedal, and R. B. Schnabel, "Representations of quasi-Newton matrices and their use in limited memory methods," *Mathematical Programming. A Publication of the Mathematical Programming Society*, vol. 63, pp. 129–156, Jan. 1994. 75

[156] A. J. Morris, R. J. Nicholls, C. J. Pickard, and J. R. Yates, "OptaDOS: A tool for obtaining density of states, core-level and optical spectra from electronic structure codes," *Computer Physics Communications*, vol. 185, pp. 1477–1485, May 2014. 76, 89, 104

[157] A. Fonari and C. Sutton, "Effective mass calculator." `https://github.com/afonari/emc`, 2012. 79, 85

[158] K. Refson, P. R. Tulip, and S. J. Clark, "Variational density-functional perturbation theory for dielectrics and lattice dynamics," *Physical Review B*, vol. 73, p. 155114, Apr. 2006. 82, 105

[159] X. Gonze and C. Lee, "Dynamical matrices, born effective charges, dielectric permittivity tensors, and interatomic force constants from density-functional perturbation theory," *Physical Review B*, vol. 55, pp. 10355–10368, Apr. 1997. 83

[160] M. Zeeshan, T. Nautiyal, J. van den Brink, and H. C. Kandpal, "FeTaSb and FeMnTiSb as promising thermoelectric materials: An ab initio approach," *Physical Review Materials*, vol. 2, p. 065407, June 2018. 83, 103, 109, 110, 118

[161] Y. Nishino, M. Kato, S. Asano, K. Soda, M. Hayasaki, and U. Mizutani, "Semiconductorlike Behavior of Electrical Resistivity in Heusler-type Fe_2VAl Compound," *Physical Review Letters*, vol. 79, pp. 1909–1912, Sept. 1997. 87, 90

[162] E. J. Skoug, C. Zhou, Y. Pei, and D. T. Morelli, "High Thermoelectric Power Factor Near Room Temperature in Full-Heusler Alloys," *Journal of Electronic Materials*, vol. 38, pp. 1221–1223, July 2009. 87, 96, 97, 98

[163] Y. Nishino and Y. Tamada, "Doping effects on thermoelectric properties of the off-stoichiometric Heusler compounds $Fe_{2-x}V_{1+x}Al$," *Journal of Applied Physics*, vol. 115, p. 123707, Mar. 2014. 87, 91, 95, 96, 100

[164] H. Miyazaki, M. Inukai, and Y. Nishino, "Effect of Ta substitution on the electronic structure of Heusler-type Fe_2VAl-based alloy," *Journal of Applied Physics*, vol. 120, p. 125106, Sept. 2016. 87

[165] M. Vasundhara, V. Srinivas, and V. V. Rao, "Low-temperature electrical transport in Heusler-type $Fe_2V(AlSi)$ alloys," *Journal of Physics: Condensed Matter*, vol. 17, pp. 6025–6036, Sept. 2005. 87

[166] H. Al-Yamani and B. Hamad, "Thermoelectric Properties of Fe_2VAl and $Fe_2V_{0.75}M_{0.25}Al$ (M = Mo, Nb, Ta) Alloys: First-Principles Calculations,"

Journal of Electronic Materials, vol. 45, pp. 1101–1114, Feb. 2016. 87, 88, 90, 91, 96

[167] C. Venkatesh, S. K. Srivastava, and V. V. Rao, "First principle investigations on boron doped Fe_2VAl Heusler alloy," *Physica B: Condensed Matter*, vol. 448, pp. 237–243, Sept. 2014. 91

[168] M. Mikami, M. Inukai, H. Miyazaki, and Y. Nishino, "Effect of Off-Stoichiometry on the Thermoelectric Properties of Heusler-Type Fe_2VAl Sintered Alloys," *Journal of Electronic Materials*, vol. 45, pp. 1284–1289, Mar. 2016. 87

[169] G. Y. Guo, G. A. Botton, and Y. Nishino, "Electronic structure of possible 3d 'heavy-fermion' compound," *Journal of Physics: Condensed Matter*, vol. 10, p. L119, Jan. 1999. 87, 90

[170] D. J. Singh and I. I. Mazin, "Electronic structure, local moments, and transport in Fe_2VAl," *Physical Review B*, vol. 57, pp. 14352–14356, June 1998.

[171] D. I. Bilc and P. Ghosez, "Electronic and thermoelectric properties of Fe_2VAl: The role of defects and disorder," *Physical Review B*, vol. 83, pp. 1–4, May 2011. 88, 96

[172] D. Do, M.-S. Lee, and S. D. Mahanti, "Effect of onsite Coulomb repulsion on thermoelectric properties of full-Heusler compounds with pseudogaps," *Physical Review B*, vol. 84, p. 125104, Sept. 2011. 88, 94, 96, 99

[173] A. Bansil, S. Kaprzyk, P. E. Mijnarends, and J. Toboła, "Electronic structure and magnetism of $Fe_{3-x}V_xX$ (X = Si , Ga, and Al) alloys by the KKR-CPA method," *Physical Review B*, vol. 60, pp. 13396–13412, Nov. 1999.

[174] M. Weinert and R. E. Watson, "Hybridization-induced band gaps in transition-metal aluminides," *Physical Review B*, vol. 58, pp. 9732–9740, Oct. 1998. 87, 88

[175] K. Soda, H. Murayama, K. Shimba, S. Yagi, J. Yuhara, T. Takeuchi, U. Mizutani, H. Sumi, M. Kato, H. Kato, Y. Nishino, A. Sekiyama, S. Suga, T. Matsushita, and Y. Saitoh, "High-resolution soft x-ray photoelectron study of density of states and thermoelectric properties of the Heusler-type alloys $(Fe_{2/3}V_{1/3})_{100-y}Al_y$," *Physical Review B*, vol. 71, p. 245112, June 2005. 87, 90

[176] H. Okamura, J. Kawahara, T. Nanba, S. Kimura, K. Soda, U. Mizutani, Y. Nishino, M. Kato, I. Shimoyama, I, H. Miura, K. Fukui, K. Nakagawa, H. Nakagawa, and T. Kinoshita, "Pseudogap formation in the intermetallic compounds $(Fe_{1-x}V_x)_3Al$," *Physical Review Letters*, vol. 84, pp. 3674–3677, Apr. 2000. 87, 88

[177] M. Kato, Y. Nishino, S. Asano, and S. Ohara, "Electrical resistance anomaly and Hall effect in $(Fe_{1-x}V_x)_3Al$ alloys," *Journal of the Japan Institute of Metals*, vol. 62, no. 7, pp. 669–674, 1998. 88

[178] K. Soda, S. Harada, T. Hayashi, M. Kato, F. Ishikawa, Y. Yamada, S. Fujimori, and Y. Saiyoh, "Angle-Resolved Photoemission Analysis of Electronic Structures for Thermoelectric Properties of Off-Stoichiometric $Fe_{2-x}V_{1+x}Al$ Alloys," *Materials Transactions*, vol. 57, no. 7, pp. 1040–1044, 2016. 88, 94, 96, 133

[179] M. Kumar, T. Nautiyal, and S. Auluck, "First-principles calculations of electronic and optical properties of $Fe_{3-x}V_xAl$ (x=0–3) compounds," *Journal of Physics: Condensed Matter*, vol. 21, p. 446001, Nov. 2009. 88, 90

[180] E. Shreder, S. Streltsov, A. Svyazhin, A. Lukoyanov, and V. Anisimov, "Electronic structure and physical properties of Fe_2MAl (M = Ti ,V ,Cr) Heusler alloys," in *Proceedings of the Third Moscow International Symposium on Magnetism*, pp. 7–10, 2005. 88, 90

[181] S. N. F. Mott and H. Jones, *The Theory of the Properties of Metals and Alloys*. Courier Corporation, 1958. 90

[182] I. Galanakis, P. Mavropoulos, and P. H. Dederichs, "Electronic structure and Slater–Pauling behaviour in half-metallic Heusler alloys calculated from first principles," *Journal of Physics D: Applied Physics*, vol. 39, p. 765, Feb. 2006. 90

[183] R. Weht and W. E. Pickett, "Excitonic correlations in the intermetallic Fe_2VAl," *Physical Review B*, vol. 58, pp. 6855–6861, Sept. 1998. 90

[184] M. Vasundhara, V. Srinivas, and V. Rao, "Electronic transport in Heusler-type $Fe_2VAl_{1-x}M_x$ alloys (M = B, In, Si)," *Physical Review B*, vol. 77, no. 22, p. 224415, 2008. 91, 96

[185] O. Kristanovski, R. Richter, I. Krivenko, A. I. Lichtenstein, and F. Lechermann, "Quantum many-body intermetallics: Phase stability of Fe_3Al and small-gap formation in Fe_2VAl," *Physical Review B*, vol. 95, p. 045114, Jan. 2017. 94, 95

[186] B. Xu, Y. Wang, W. Zhao, and Y. Yan, "Thermoelectric properties of Heusler-type compound $Fe_2V_{1-x}Nb_xAl$," *Journal of Applied Physics*, vol. 110, p. 013530, July 2011. 96

[187] Y. Nishino, S. Deguchi, and U. Mizutani, "Thermal and transport properties of the Heusler-type $Fe_2VAl_{1-x}Ge_x$ $(0 \leq x \leq 0.20)$ alloys: Effect of doping on lattice thermal conductivity, electrical resistivity, and Seebeck coefficient," *Physical Review B*, vol. 74, pp. 1–6, Sept. 2006. 96, 129

[188] H. Kato, M. Kato, Y. Nishino, U. Mizutani, and S. Asano, "Effect of Silicon Substitution on Thermoelectric Properties of Heusler-type Fe_2VAl Alloy," *Journal of the Japan Institute of Metals*, vol. 65, no. 7, pp. 652–656, 2001. 97

[189] G. A. Naydenov, P. J. Hasnip, V. K. Lazarov, and M. I. J. Probert, "Huge power factor in p-type half-Heusler alloys NbFeSb and TaFeSb," *Journal of Physics: Materials*, vol. 2, p. 035002, June 2019. 102

[190] A. Tavassoli, F. Failamani, A. Grytsiv, G. Rogl, P. Heinrich, H. Müller, E. Bauer, M. Zehetbauer, and P. Rogl, "On the Half-Heusler compounds $Nb_{1-x}\{Ti,Zr,Hf\}_xFeSb$: Phase relations, thermoelectric properties at low and high temperature, and mechanical properties," *Acta Materialia*, vol. 135, pp. 263–276, Aug. 2017. 102, 122

[191] F. Wu, W. Wang, X. Hu, and M. Tang, "Thermoelectric properties of I-doped n-type Bi_2Te_3-based material prepared by hydrothermal and subsequent hot pressing," *Progress in Natural Science: Materials International*, vol. 27, pp. 203–207, Apr. 2017. 102, 118

[192] T. Fang, S. Zheng, T. Zhou, L. Yan, and P. Zhang, "Computational prediction of high thermoelectric performance in p-type half-Heusler compounds with low band effective mass," *Physical Chemistry Chemical Physics*, vol. 19, pp. 4411–4417, Feb. 2017. 102

[193] J. Yu, C. Fu, Y. Liu, K. Xia, U. Aydemir, T. C. Chasapis, G. J. Snyder, X. Zhao, and T. Zhu, "Unique Role of Refractory Ta Alloying in Enhancing the Figure of Merit of NbFeSb Thermoelectric Materials," *Advanced Energy Materials*, vol. 8, Jan. 2018. 103, 125

[194] X. Zhang, Y. Wang, Y. Yan, C. Wang, G. Zhang, Z. Cheng, F. Ren, H. Deng, and J. Zhang, "Origin of high thermoelectric performance of $FeNb_{1-x}Zr/Hf_xSb_{1-y}Sn_y$ alloys: A first-principles study," *Scientific Reports*, vol. 6, p. 33120, Sept. 2016. 102

[195] H. Zhu, J. Mao, Y. Li, J. Sun, Y. Wang, Q. Zhu, G. Li, Q. Song, J. Zhou, Y. Fu, R. He, T. Tong, Z. Liu, W. Ren, L. You, Z. Wang, J. Luo, A. Sotnikov, J. Bao, K. Nielsch, G. Chen, D. J. Singh, and Z. Ren, "Discovery of TaFeSb-based half-Heuslers with high thermoelectric performance," *Nature Communications*, vol. 10, p. 270, Jan. 2019. 103

[196] K. Lejaeghere *et al.*, "Reproducibility in density functional theory calculations of solids," *Science*, vol. 351, p. aad3000, Mar. 2016. 104

[197] D. Hobbis, R. P. Hermann, H. Wang, D. S. Parker, T. Pandey, J. Martin, K. Page, and G. S. Nolas, "Structural, Chemical, Electrical, and Thermal Properties of n-Type NbFeSb," *Inorganic Chemistry*, vol. 58, pp. 1826–1833, Feb. 2019. 108, 134, 147

[198] F. L. Madarasz and P. G. Klemens, "Reduction of lattice thermal conductivity by point defects at intermediate temperatures," *International Journal of Thermophysics*, vol. 8, pp. 257–262, Mar. 1987. 110, 120

[199] J.-H. Kim, J.-Y. Choi, J.-M. Bae, M.-Y. Kim, and T.-S. Oh, "Thermoelectric Characteristics of n-Type Bi_2Te_3 and p-Type Sb_2Te_3 Thin Films Prepared by Co-Evaporation and Annealing for Thermopile Sensor Applications," *Materials Transactions*, vol. 54, no. 4, pp. 618–625, 2013. 118

[200] S. V. Ovsyannikov, V. V. Shchennikov, G. V. Vorontsov, A. Y. Manakov, A. Y. Likhacheva, and V. A. Kulbachinskii, "Giant improvement of thermoelectric power factor of Bi_2Te_3 under pressure," *Journal of Applied Physics*, vol. 104, p. 053713, Sept. 2008. 118

[201] S. Bandaru, A. Katre, J. Carrete, N. Mingo, and P. Jund, "Influence of Antisite Defects on the Thermoelectric Properties of Fe_2VAl," *Nanoscale and Microscale Thermophysical Engineering*, pp. 1–10, July 2017. 133

[202] S. Maier, L. Perri'ere, J. Bourgon, E. Leroy, M. Beaudhuin, and E. Alleno, "Phonon scattering by antiphase boundaries in Fe_2VAl." The 37th Annual International and 16th European Conference on thermoelectrics, 2018. 133

[203] E. Alleno, "Review of the Thermoelectric Properties in Nanostructured Fe_2VAl," *Metals*, vol. 8, p. 864, Oct. 2018. 133

[204] "Bismuth telluride (Bi_2Te_3) crystal structure, chemical bond, lattice parameters (including data for related compounds)," in *Non-Tetrahedrally Bonded Elements and Binary Compounds I* (O. Madelung, U. Rössler, and M. Schulz, eds.), pp. 1–4, Berlin, Heidelberg: Springer Berlin Heidelberg, 1998. 137

[205] C. Bae, T. Böhnert, J. Gooth, S. Lim, S. Lee, H. Kim, S. Heimann, S. Schulz, H. Shin, and K. Nielsch, "Thermopower engineering of Bi_2Te_3 without alloying: the interplay between nanostructuring and defect activation," *Semiconductor Science and Technology*, vol. 29, p. 064003, May 2014. 139

[206] E. R. McNellis, J. Meyer, and K. Reuter, "Azobenzene at coinage metal surfaces: Role of dispersive van der Waals interactions," *Physical Review B*, vol. 80, no. 20, p. 205414, 2009. 139

[207] F. Zahid and R. Lake, "Thermoelectric properties of Bi_2Te_3 atomic quintuple thin films," *Applied Physics Letters*, vol. 97, p. 212102, Nov. 2010. 140

[208] J. Zhang, H. J. Liu, L. Cheng, J. Wei, J. Shi, X. F. Tang, and C. Uher, "Enhanced thermoelectric performance of a quintuple layer of Bi_2Te_3," *Journal of Applied Physics*, vol. 116, p. 023706, July 2014. 140

[209] C.-X. Liu, H. Zhang, B. Yan, X.-L. Qi, T. Frauenheim, X. Dai, Z. Fang, and S.-C. Zhang, "Oscillatory crossover from two-dimensional to three-dimensional topological insulators," *Physical Review B*, vol. 81, p. 041307, Jan. 2010. 140

[210] J. Maassen and M. Lundstrom, "A computational study of the thermoelectric performance of ultrathin Bi_2Te_3 films," *Applied Physics Letters*, vol. 102, p. 093103, Mar. 2013. 143

[211] S. Sharma and U. Schwingenschlögl, "Thermoelectric Response in Single Quintuple Layer Bi_2Te_3," *ACS Energy Letters*, vol. 1, pp. 875–879, Oct. 2016. 140

[212] M. Winkler, X. Liu, J. D. König, S. Buller, U. Schürmann, L. Kienle, W. Bensch, and H. Böttner, "Electrical and structural properties of Bi_2Te_3 and Sb_2Te_3 thin films grown by the nanoalloying method with different deposition patterns and compositions," *Journal of Materials Chemistry*, vol. 22, pp. 11323–11334, May 2012. 143

[213] C. I. Fornari, P. H. O. Rappl, S. L. Morelhão, T. R. F. Peixoto, H. Bentmann, F. Reinert, and E. Abramof, "Preservation of pristine Bi_2Te_3 thin film topological insulator surface after *ex situ* mechanical removal of Te capping layer," *APL Materials*, vol. 4, p. 106107, Oct. 2016. 143

[214] J. Růžička, O. Caha, V. Holý, H. Steiner, V. Volobuiev, A. Ney, G. Bauer, T. Duchoň, K. Veltruská, I. Khalakhan, V. Matolín, E. F. Schwier, H. Iwasawa, K. Shimada, and G. Springholz, "Structural and electronic proper-

ties of manganese-doped Bi_2Te_3 epitaxial layers," *New Journal of Physics*, vol. 17, p. 013028, Jan. 2015. 148, 149

[215] Y. Li, X. Zou, J. Li, and G. Zhou, "Ferromagnetism and topological surface states of manganese doped Bi_2Te_3: insights from density-functional calculations," *The Journal of Chemical Physics*, vol. 140, p. 124704, Mar. 2014. 149

[216] J.-M. Zhang, W. Ming, Z. Huang, G.-B. Liu, X. Kou, Y. Fan, K. L. Wang, and Y. Yao, "Stability, electronic, and magnetic properties of the magnetically doped topological insulators Bi_2Se_3, Bi_2Te_3, and Sb_2Te_3," *Physical Review B*, vol. 88, p. 235131, Dec. 2013. 148